

The Kinematics and Dynamics of Complex Crater Collapse

Auriol Stephen Prenter Rae

Department of Earth Science and Engineering
Imperial College London

Submitted for the degree of Doctor of Philosophy
and Diploma of Imperial College

July 2018

Abstract

Large impact craters collapse to form complex structures, with zones of structural uplift that can be expressed topographically as central peaks and/or peak-rings internal to the crater rim. The formation of these structures requires transient strength reduction in the target material, but the process that facilitates this strength reduction is unknown. More fundamentally, descriptions of how structural uplifts, particularly peak-rings, are emplaced lack the quantitative details needed to constrain models of large impact crater formation. This thesis describes aspects of the formation of complex impact structures in an attempt to constrain the mechanism that facilitates crater collapse.

The approach adopted in this research was to combine geological observations of large impact structures; field geology, core logging, petrography, and petrophysics, with the results of numerical impact simulations. More specifically, this thesis focusses upon the Clearwater Lake impact structures and the Chicxulub impact structure as case studies to understand complex crater collapse. The results presented demonstrate that the block model of acoustic fluidisation provides a realistic description of the rheology of rocks during crater collapse. Nonetheless, observational support for the block model of acoustic fluidisation, or indeed, any single currently proposed transient weakening mechanism, is lacking. Deformation during crater collapse is dominated by cataclasites which occur on a variety of scales, while the lubrication of faults by frictional melts and/or intrusions of impact melt and breccia may only have a significant effect during the late-stages of crater modification.

The research carried out in this thesis demonstrates numerous ways in which geological and geophysical observations can be combined with numerical impact simulations to understand cratering and constrain the process of crater collapse. The methods include using observationally constrained shock pressures, geophysical data, and most significantly, the structural history of rocks in impact craters.

Acknowledgements

The work in this thesis would not have been possible without the support of many people. First and foremost, my supervisors Jo Morgan and Gareth Collins, who were always supportive, available, and perhaps most important of all, trusted me to pursue my own ideas. I could not have wished for better supervisors. Additionally, I am extremely grateful to Richard Grieve and Gordon Osinski, who introduced me to the fascinating world of Canadian impact structures and supported my later endeavours.

A large part of this thesis uses the iSALE shock physics code — for this, I am grateful to the developers. In particular, Tom Davison, who was always available to help with my coding-related problems. Additionally, many in the impact modelling community — Kai Wünnemann, Jay Melosh, and Kat Miljkovic — have always been supportive and provided useful discussions, comments, and criticisms.

Part III of this thesis concerns the Chicxulub crater and IODP-ICDP Expedition 364. I am extremely grateful to have been involved in the expedition and to have had such excellent collaborators: Michael Poelchau, Ulrich Riller, Brendon Hall, Ludovic Ferrière, Erwan Le Ber, Johanna Lofi, Gail Christeson, and Sean Gulick. Additionally, I wish to thank all of the excellent scientists within the science party and ECORD: Elise Chenot, Phillippe Claeys, Charles Cockell, Marco Coolen, Catalina Gebhardt, Kazuhisa Goto, Sophie Green, Heather Jones, David Kring, Chris Lowery, Claire Mellett, Ruben Ocampo-Torres, Ligia Perez-Cruz, Annemarie Pickersgill, Cornelia Rasmussen, Mario Rebolledo-Vieyra, Honami Sato, Jan Smit, David Smith, Sonia Tikoo, Naotaka Tomioka, Jaime Urrutia-Fucugauchi, Michael Whalen, Axel Wittmann, Long Xiao, Kosei Yamaguchi, and William Zylberman.

During the summer of 2017, I had the pleasure of being a Visiting Scientist at Curtin University, during which time I had the pleasure to collaborate, in both the field and the lab, with Aaron Cavosie, Nick Timms, Timmons Erickson, Kat Miljkovic, and Thomas Kenkmann. I would particularly like to thank Kat for helping to organise my visit and the work that I carried out.

Finally, I would like to thank my friends, for still being there.

Declaration of Originality and Copyright

I, Auriol Stephen Prenter Rae, hereby declare that the intellectual content of this thesis is the product of my own work, unless otherwise stated and/or referenced. Additional intellectual contribution to the work in this thesis has been duly acknowledged.

The copyright of this thesis rests with the author and is made available under a Creative Commons Attribution Non-Commercial No Derivatives licence. Researchers are free to copy, distribute or transmit the thesis on the condition that they attribute it, that they do not use it for commercial purposes and that they do not alter, transform or build upon it. For any reuse or redistribution, researchers must make clear to others the licence terms of this work

Contents

1	Introduction	1
1.1	Objectives	3
1.2	Thesis Structure	3
I	Background and Methods	5
2	Background	6
2.1	The Impact Cratering Process	6
2.1.1	Contact and Compression	6
2.1.2	Excavation	10
2.1.3	Modification	10
2.2	Complex Crater Collapse	12
2.3	The Geology and Geophysics of Complex Craters	17
2.3.1	Impactites	17
2.3.2	Physical Properties	23
3	Methods	24
3.1	Observational Methods	24
3.1.1	Core Logging and Field Observations	24
3.1.2	Petrography	24
3.2	Numerical Methods	29
3.2.1	The iSALE Shock Physics Code	30

3.2.2	Material Models	36
II	The Clearwater Lake Impact Structures	44
4	Introduction to the Clearwater Lake Impact Structures	45
5	Constraining the Parameters of Transient Weakening during Crater Collapse using Observations of Shock Metamorphism and Deformation: The West Clearwater Lake Impact Structure	49
5.1	Introduction	49
5.2	Methods	49
5.2.1	Samples	49
5.2.2	Shock Barometry	50
5.2.3	Numerical Modelling	50
5.3	Results	51
5.3.1	Observations	51
5.3.2	Numerical Modelling	61
5.4	Discussion	62
5.4.1	Shock Barometry	67
5.4.2	Original Crater Morphology	69
5.4.3	The Block Model Implementation of Acoustic Fluidisation	70
5.5	Summary	72
6	Characterisation of Deformation during Complex Crater Formation: The East Clearwater Lake Impact Structure	74
6.1	Introduction	74
6.2	Methods	74
6.2.1	Core Logging	74
6.2.2	Optical Microscopy	75
6.2.3	Electron Microscopy	75

6.2.4	Numerical Modelling	76
6.3	Results	77
6.3.1	Core Logging	77
6.3.2	Optical Microscopy	79
6.3.3	Electron Microscopy	83
6.3.4	Numerical Simulations	88
6.4	Discussion	93
6.4.1	Deformation during Central Peak Formation	93
6.4.2	Numerical Modelling	95
6.5	Conclusions	96
III	The Chicxulub Impact Structure	99
7	Introduction to the Chicxulub Impact Structure	100
8	Stress and Strain during Complex Crater Formation: Linking Models with Observations	104
8.1	Introduction	104
8.2	Stress and Strain during Shock and Deformation	104
8.2.1	Strain Quantification	106
8.2.2	Stress Quantification	111
8.3	Results	113
8.3.1	Shock and Decompression	115
8.3.2	Transient Cavity Formation	118
8.3.3	Modification	122
8.3.4	Accumulated Deformation throughout Cratering	128
8.4	Discussion	128
8.4.1	Comparison to Observations from the Chicxulub Peak-Ring . . .	129

8.5	Conclusions	133
9	Shock, Fracturing, Porosity, and Gravity at the Chicxulub Impact Structure: Impact Cratering on the μm - km Scale	134
9.1	Introduction	134
9.2	Data Sets	134
9.2.1	Geophysical and Petrophysical data	134
9.2.2	Shock Barometry	137
9.2.3	SEM Imaging and Analysis	139
9.2.4	The iSALE Shock Physics Code	141
9.3	Results	141
9.3.1	Petrophysical Data Sets	141
9.3.2	Shock Barometry	142
9.3.3	SEM Imaging and Analysis	147
9.3.4	EBSD Analysis	151
9.3.5	Numerical Simulations	156
9.4	Discussion	160
9.4.1	Orientation of Fractures	164
9.5	Conclusions	169
IV	Conclusions	170
10	Conclusions	171
10.1	Summary of Findings	171
10.1.1	Modification-Related Deformation	171
10.1.2	Transient Weakening	172
10.1.3	Shock Metamorphism	172
10.1.4	Methods to Constrain Numerical Impact Models	173

10.2 Perspectives	174
Appendices	192
A The Universal Stage and Shocked Quartz	193
A.1 The Basics	194
A.2 Preparing the Microscope for U-Stage Installation	194
A.3 Setting a Thin Section	195
A.4 Calibration of the U-Stage	195
A.5 Measuring Quartz PDFs and Peak Shock Pressure	196
A.6 Notes and Troubleshooting	198
B iSALE inputs	200
C Supplementary Universal-Stage Data	207
C.1 West Clearwater Lake	207
C.2 East Clearwater Lake	207
D Supplementary BSE Images and Analysis	216
D.1 East Clearwater Lake	216
D.2 Chicxulub	239
E Supplementary EDS Results	250
F Comparison of Chicxulub Numerical Simulations	264
G Comparison of Stress-Strain Paths of Lagrangian Pseudo-Cells within the Chicxulub Peak-Ring	267
H Supplementary EBSD Maps	271

List of Figures

1.1	Size-morphology progression of craters	2
2.1	Rock failure in a compressive wave	7
2.2	Types of stress wave	9
2.3	Pressure, stress, and particle velocity cross section of a shock wave	11
2.4	The dependence of gravity on the simple to complex transition	13
2.5	Intact and damaged strength profiles of rocks as a function of pressure .	14
2.6	Thermal softening and the thermal effect of shock	16
2.7	Impactite classification	18
2.8	Fault rock classification	19
2.9	Schematic cross-sections of a simple and complex crater	22
3.1	Schematic diagram of the iSALE mesh geometry	33
3.2	Comparison between Eulerian and Lagrangian calculations	34
4.1	Map of Clearwater Lake, and the locations of drill cores and field samples	46
5.1	Macroscopic products of impact deformation at West Clearwater Lake .	54
5.2	Lithological logs of Holes 1-63, 3-63, 4-63, 4a-63, and 5-63 from West Clearwater Lake	55
5.3	Microphtographs of shock indicators at West Clearwater Lake	57
5.4	Map of shock distribution at West Clearwater Lake	59
5.5	Shock distribution at West Clearwater Lake as a function of radial and vertical distance	60

5.6	PDF sets per grain and estimated peak shock pressure of West Clearwater Lake samples	61
5.7	The effect of varying acoustic fluidisation parameters on the morphology and shock distribution of the final crater at West Clearwater Lake	63
5.8	Shock pressures in simulated drill cores through the numerical simulations at varying acoustic fluidisation parameters at West Clearwater Lake	64
5.9	Shock pressures in simulated slices through the numerical simulations at varying acoustic fluidisation parameters at West Clearwater Lake	65
5.10	Comparison between modelled shock pressures and observed shock pressures at West Clearwater Lake	66
6.1	Log of Hole 1-64 from East Clearwater Lake	80
6.2	QAP diagram of East Clearwater Lake samples	81
6.3	Deformation structures in East Clearwater Lake samples observed by optical microscopy	82
6.4	Quantitative analysis by location within a cataclasite in Sample 1-64-2206	86
6.5	Grain- and pore-size distributions of cataclasite in Sample 1-64-2206	87
6.6	Stitched BSE SEM images of deformation zones in East Clearwater Lake samples	89
6.7	BSE SEM images of deformation features in East Clearwater Lake samples	90
6.8	Numerical simulation of the formation of the East Clearwater Lake structure	91
6.9	Modelled peak shock pressures in Hole 1-64	92
6.10	Modelled porosity distribution and resultant gravity signal at East Clearwater Lake	94
6.11	Comparison between East and West Clearwater Lake models and shock attenuation	97
7.1	Geophysically constrained cross section of upper 20 km of the Chicxulub impact structure	101
7.2	Bouguer Gravity Map, velocity structure of the Chicxulub peak-ring, and stratigraphic log of Hole M0077A	102

8.1	Schematic representation of a Lagrangian pseudo-cell	108
8.2	Selected timesteps of the presented Chicxulub simulation. The target is comprised of three layers; Sedimentary Rock (Grey), Granitic Basement (Pink), and Mantle (Purple). A grid of tracer particles is shown to highlight the sub-crater deformation. Additionally, in the first frame, a), the provenance of impact melt and the peak-ring is shown in green and red respectively. The impact melt and peak-ring material is then tracked throughout the steps b) - f). The location of a single pseudo-cell (white) is shown throughout the simulation.	114
8.3	Strain path of the Lagrangian pseudo-cell during shock and decompression	116
8.4	Stresses experienced by the Lagrangian pseudo-cell during shock and decompression	117
8.5	Stress orientations and magnitudes during shock and decompression . . .	119
8.6	Strain path of the Lagrangian pseudo-cell during transient cavity growth	120
8.7	Stress orientation and magnitude during transient cavity growth	121
8.8	Strain stages during modification	123
8.9	Quantification of strain during the phases of crater modification	124
8.10	Flinn-Ramsay Diagram of strain ellipsoids corresponding to each phase of peak-ring formation	126
8.11	Stress magnitudes and pressure through time during crater modification	127
8.12	Total volumetric and shear strains through time	129
9.1	Residual Bouguer gravity map of the crater	136
9.2	Average radial gravity profile of the Chicxulub structure	137
9.3	IODP-ICDP Expedition 364 density and porosity data	138
9.4	Physical property measurements of the granitic rocks recovered during Expedition 364	143
9.5	Shock deformation at the Chicxulub impact structure	144
9.6	Estimated peak shock pressures and number of PDFs per grain in Hole M0077A	146
9.7	Porosity measurements determined by SEM image analysis	148

9.8	Types of porosity demonstrated in within Chicxulub Samples	149
9.9	Intra-granular fractures within granitic minerals of the Chicxulub peak-ring	150
9.10	Pore orientation-frequency distributions for each of the analysed thin sections from the Chicxulub peak-ring	152
9.11	Comparison of a BSE image of a sample from Hole M0077A with its pore orientation-frequency distribution	154
9.12	Strain on the grain-scale, EBSD analysis of shocked target rocks.	155
9.13	Planar elements in alkali feldspar.	157
9.14	Comparison of observed and modelled porosity and gravity signals of the Chicxulub simulation	158
9.15	The distribution of porosity within the Chicxulub peak-ring	163
9.16	Fracture formation during shock	165
9.17	Rotation of fractures during modification	167
9.18	Comparison of observed and modelled shock pressures in the Chicxulub peak-ring	168
A.1	Transmitted cross-polarised light photomicrographs of quartz PDFs from the West Clearwater Impact Structure	193
A.2	Schematic diagram of a universal stage	194
D.1	Transect analysis of 1-64-544a	217
D.2	Grain size-frequency distribution of 1-64-544a	218
D.3	Pore size-frequency distribution of 1-64-544a	218
D.4	Transect analysis of 1-64-544b	219
D.5	Grain size-frequency distribution of 1-64-544b	220
D.6	Pore size-frequency distribution of 1-64-544b	220
D.7	Transect analysis of 1-64-972	221
D.8	Grain size-frequency distribution of 1-64-972	222
D.9	Pore size-frequency distribution of 1-64-972	222
D.10	Transect analysis of 1-64-1090	223

D.11	Grain size-frequency distribution of 1-64-1090	224
D.12	Pore size-frequency distribution of 1-64-1090	224
D.13	Transect analysis of 1-64-1223	225
D.14	Grain size-frequency distribution of 1-64-1223	226
D.15	Pore size-frequency distribution of 1-64-1223	226
D.16	Transect analysis of 1-64-1617	227
D.17	Grain size-frequency distribution of 1-64-1617	228
D.18	Pore size-frequency distribution of 1-64-1617	228
D.19	Transect analysis of 1-64-2140	229
D.20	Grain size-frequency distribution of 1-64-2140	230
D.21	Pore size-frequency distribution of 1-64-2140	230
D.22	Transect analysis of 1-64-2206a	231
D.23	Grain size-frequency distribution of 1-64-2206a	232
D.24	Pore size-frequency distribution of 1-64-2206a	232
D.25	Transect analysis of 1-64-2206b	233
D.26	Grain size-frequency distribution of 1-64-2206b	234
D.27	Pore size-frequency distribution of 1-64-2206b	234
D.28	Transect analysis of 1-64-2763a	235
D.29	Grain size-frequency distribution of 1-64-2763a	236
D.30	Pore size-frequency distribution of 1-64-2763a	236
D.31	Transect analysis of 1-64-2763b	237
D.32	Grain size-frequency distribution of 1-64-2763b	238
D.33	Pore size-frequency distribution of 1-64-2763b	238
D.34	Stitched BSE image of 364-77-A-95-R-3-27-29	240
D.35	Pore size-frequency distribution of Sample 364-77-A-95-R-3-27-29	240
D.36	Pore orientation distribution of Sample 364-77-A-95-R-3-27-29	240
D.37	Stitched BSE image of 364-77-A-104-R-1-24-26	241

D.38 Pore size-frequency distribution of Sample 364-77-A-104-R-1-24-26	241
D.39 Pore orientation distribution of Sample 364-77-A-104-R-1-24-26	241
D.40 Stitched BSE image of 364-77-A-121-R-1-75-77	242
D.41 Pore size-frequency distribution of Sample 364-77-A-121-R-1-75-77	242
D.42 Pore orientation distribution of Sample 364-77-A-121-R-1-75-77	242
D.43 Stitched BSE image of 364-77-A-132-R-1-22-24	243
D.44 Pore size-frequency distribution of Sample 364-77-A-132-R-1-22-24	243
D.45 Pore orientation distribution of Sample 364-77-A-132-R-1-22-24	243
D.46 Stitched BSE image of 364-77-A-150-R-1-53-55	244
D.47 Pore size-frequency distribution of Sample 364-77-A-150-R-1-53-55	244
D.48 Pore orientation distribution of Sample 364-77-A-150-R-1-53-55	244
D.49 Stitched BSE image of 364-77-A-204-R-1-07-09	245
D.50 Pore size-frequency distribution of Sample 364-77-A-204-R-1-07-09	245
D.51 Pore orientation distribution of Sample 364-77-A-204-R-1-07-09	245
D.52 Stitched BSE image of 364-77-A-219-R-1-22-24	246
D.53 Pore size-frequency distribution of Sample 364-77-A-219-R-1-22-24	246
D.54 Pore orientation distribution of Sample 364-77-A-219-R-1-22-24	246
D.55 Stitched BSE image of 364-77-A-250-R-1-41-43	247
D.56 Pore size-frequency distribution of Sample 364-77-A-250-R-1-41-43	247
D.57 Pore orientation distribution of Sample 364-77-A-250-R-1-41-43	247
D.58 Stitched BSE image of 364-77-A-276-R-1-17-19	248
D.59 Pore size-frequency distribution of Sample 364-77-A-276-R-1-17-19	248
D.60 Pore orientation distribution of Sample 364-77-A-276-R-1-17-19	248
D.61 Stitched BSE image of 364-77-A-301-R-2-30-32	249
D.62 Pore size-frequency distribution of Sample 364-77-A-301-R-2-30-32	249
D.63 Pore orientation distribution of Sample 364-77-A-301-R-2-30-32	249

E.1	EDS data from 1-64-543a	251
E.2	EDS data from 1-64-543b	252
E.3	EDS data from 1-64-543c	253
E.4	EDS data from 1-64-544a	254
E.5	EDS data from 1-64-544b	255
E.6	EDS data from 1-64-544c	256
E.7	EDS data from 1-64-544d	257
E.8	EDS data from 1-64-846a	258
E.9	EDS data from 1-64-846b	259
E.10	EDS data from 1-64-1357	260
E.11	EDS data from 1-64-1617	261
E.12	EDS data from 1-64-2763a	262
E.13	EDS data from 1-64-2763b	263
F.1	Comparison of iSALE Chicxulub simulations	265
F.2	Comparison of iSALE Chicxulub simulations with previously published cross-section.	266
G.1	Locations of selected and alternative Lagrangian pseudo-cells	268
G.2	Comparison of strains recorded by alternative Lagrangian pseudo-cells . .	269
G.3	Comparison of stresses recorded by alternative Lagrangian pseudo-cells .	270
H.1	EBSD maps of Sample 364-77-A-104-R-1-24-26	272
H.2	EBSD maps of Sample 364-77-A-132-R-1-22-24	273
H.3	EBSD maps of Sample 364-77-A-204-R-1-07-09	274
H.4	EBSD maps of Sample 364-77-A-219-R-1-22-24	275
H.5	EBSD maps of Sample 364-77-A-288-R-1-59-61	276

List of Tables

3.1	Shock classification scheme of quartz	27
5.1	West Clearwater Lake iSALE parameters	52
5.2	Summary of PDF statistics from West Clearwater Lake samples	58
5.3	Comparison of the best-fit acoustic fluidisation parameters across numerical impact studies.	68
6.1	Global model parameters for East Clearwater Lake simulations	77
6.2	Material model parameters of East Clearwater Lake simulations	78
6.3	Summary of PDF statistics in East Clearwater Lake samples	84
8.1	Global model parameters of Chicxulub simulation	106
8.2	Material model parameters of Chicxulub simulation	107
9.1	List of SEM imaged chicxulub thin sections	139
9.2	Acquisition parameters of EBSD data	140
9.3	PDF statistics of Chicxulub thin sections	145
9.4	Pore orientation distribution descriptions by sample	153
9.5	Range of target material densities used in gravity calculation	159
9.6	Density contrasts between fractured and undisturbed target rocks at several terrestrial impact structures	161
B.1	Full global model parameters for West Clearwater Lake simulations . . .	201
B.2	Full material model parameters of West Clearwater Lake simulations . .	202

B.3	Full global model parameters for East Clearwater Lake simulations	203
B.4	Full material model parameters of East Clearwater Lake simulations	204
B.5	Global model parameters of Chicxulub simulation	205
B.6	Material model parameters of Chicxulub simulation	206
C.1	Summary of thin section descriptions from Core 1-63 of West Clearwater Lake	208
C.2	PDF statistics of thin sections from Hole 1-63 from West Clearwater Lake	209
C.3	PDF statistics of thin sections from Hole 3-63 from West Clearwater Lake	210
C.4	Summary of thin section descriptions from Core 5-63 of West Clearwater Lake	211
C.5	PDF statistics of thin sections from Hole 5-63 from West Clearwater Lake	212
C.6	Sample location and PDF statistics of thin sections from field samples from West Clearwater Lake	213
C.7	Summary of thin section descriptions from East Clearwater Lake	214
C.8	PDF statistics of East Clearwater Lake thin sections	215
D.1	List of BSE imaged and analysed samples from East Clearwater Lake	216
H.1	List of samples for presented EBSD maps	271

1 Introduction

Large impact craters on rocky planetary bodies possess central peaks or a ring of peaks within the crater rim (Roddy, 1977). Impact structures with these morphologies are known as complex craters. In addition to central peaks or peak-rings, complex craters have substantially larger aspect ratios than the smaller, bowl-shaped, and so-called simple craters (Figure 1.1; Melosh, 1989). The transition from simple to complex craters occurs at a critical size threshold, which is inversely proportional to the gravitational acceleration on the cratered body (Pike, 1977). At, and beyond that critical size threshold, craters begin to display centrally uplifted peaks and/or rings and possess wide, terraced rim areas.

The dependence of the critical size threshold on gravity for the onset of complex crater formation indicates that the collapse of complex craters occurs due to weight overcoming the strength of rocks in the transient cavity. Static and dynamic models have indicated that a remarkable reduction of cohesion and internal friction is required for crater collapse (McKinnon, 1978; Melosh, 1977; O'Keefe and Ahrens, 1999; Wünnemann and Ivanov, 2003); the effective strength of impacted rocks must be less than ~ 3 MPa and there must be little or no internal friction. These properties are inconsistent with laboratory measurements of the properties of rocks and even those of damaged rocks. Therefore, there must be an additional mechanism or mechanisms that transiently and significantly reduce rock strength such that complex crater collapse is facilitated. Several mechanisms have been suggested to contribute to this significant and transient weakening; fracturing and rock damage (e.g. Collins et al., 2004; Melosh et al., 1992), bulk thermal softening (O'Keefe and Ahrens, 1999), fault weakening (Senft and Stewart, 2009) by shear-induced thermal softening (Spray, 1997) and other processes, and acoustic fluidisation (Melosh, 1979).

Resolving which, if any, of these mechanisms act during complex crater formation requires observational and/or experimental constraints. These constraints include not only direct measurements and observations of the potential products of those weakening mechanisms, but also indirect, geological, constraints that describe the bulk behaviour of rocks during crater collapse, i.e. kinematics.

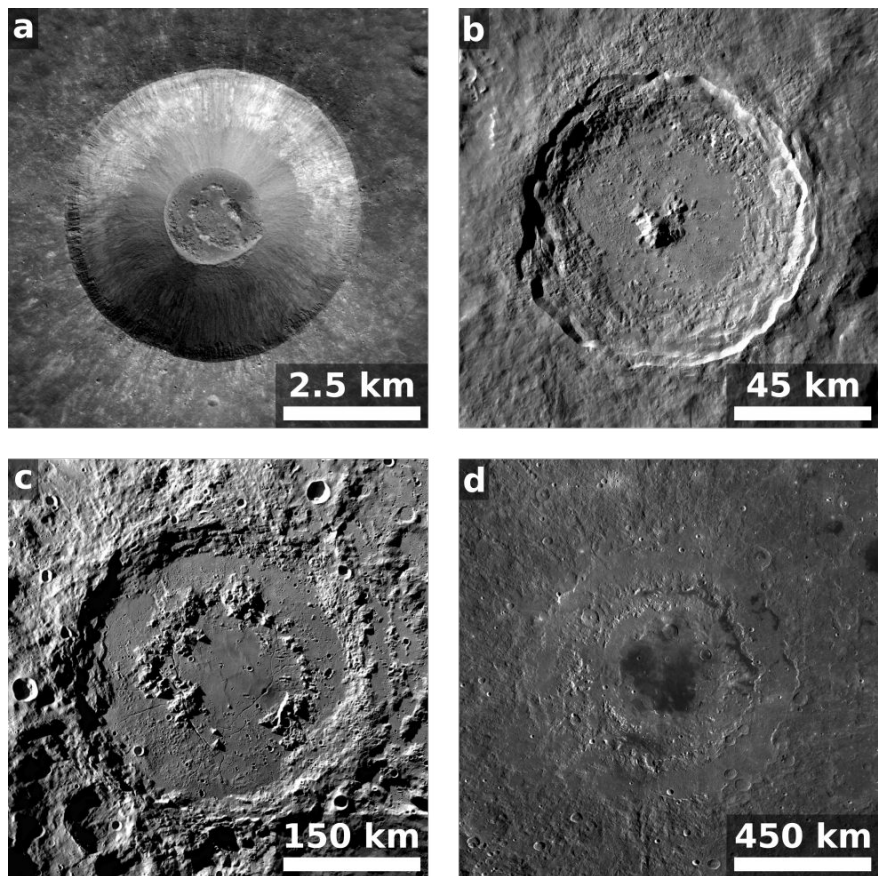


Figure 1.1: Progression of Lunar crater morphologies. a) the 5 km-diameter simple crater, Lichtenberg-B, b) the 86 km-diameter central-peak crater, Tycho, c) the 316 km-diameter peak-ring crater, Schrödinger, and d) the 930 km-diameter multi-ring crater, Orientale. All images obtained by the Lunar Reconnaissance Orbiter (NASA).

1.1 Objectives

In this thesis, I aim to constrain the kinematics of, and the mechanism that enables, complex crater collapse. This will be achieved by:

1. Using shock metamorphism to constrain the kinematic parameters of complex crater collapse;
2. Describing the mechanisms by which deformation is accommodated by rocks during collapse;
3. Generating data from numerical impact models that can be used for direct comparison with observations; in particular, quantitatively describing the history of deformation experienced by rocks during collapse;
4. Using geophysical data to constrain crater structure;
5. Linking the micro-structure of impactites with the geophysical character of craters and numerical simulations of cratering.

1.2 Thesis Structure

This thesis is subdivided into 4 parts.

Part I provides an introduction to the material that will follow in the subsequent parts and chapters of the thesis. It is subdivided into two chapters. Chapter 2 reviews the relevant previous work in the field of Impact Cratering to: (a) outline the relevant principles of impact cratering; (b) describe potential crater weakening mechanisms; and (c) provide a geological summary of impact craters. Chapter 3 describes the general methods used within this thesis, including: (a) the observational techniques used to generate data for comparison with numerical simulations; and (b) an overview of numerical impact modelling and the specific details of the iSALE shock physics code. Subsequent chapters will contain aspects of methodology specific to that chapter.

Part II contains results pertaining to the Clearwater Lake Impact structures, and is subdivided into three chapters. Chapter 4 provides an introduction to previous work on the Clearwater Lake impact structures. Chapter 5 focusses upon the West Clearwater Lake impact structure, where the distribution of shock metamorphism is used as a constraint on the parameters of weakening in numerical impact simulations. The results in this chapter have been published/presented in Rae et al. (2015a,b, 2017a). Chapter 6 focusses on the East Clearwater Lake structure, and on the deformation ex-

perienced by rocks within structural uplifts. The results of this have chapter have, in part, been presented in Rae et al. (2017c).

Part III contains results pertaining to the Chicxulub Impact Structure, and is subdivided into three chapters. Chapter 7 provides an introduction to previous work on the Chicxulub Impact Structure. In Chapter 8, I develop a new technique that allows for numerical impact simulations to make predictions of the deformation path of material. The results of this analysis for the Chicxulub peak-ring material is then compared to observations from IODP-ICDP Expedition 364. The results in this chapter have been presented in Rae et al. (2017d,e, 2018). In Chapter 9, observations of micro-fracturing and shock metamorphism, petrophysical data from Expedition 364, and previous gravity surveys are linked and compared to the results of numerical impact simulations. The results in this chapter have been presented by Rae et al. (2017b) and Rae et al. (2017d,e, 2018).

Part IV contains Chapter 10, which serves to summarise the previous chapters and to conclude the thesis, including some perspectives on the current state of play in this area of research.

This thesis contains eight appendices; Appendix A provides a detailed guide to measuring the orientation of Planar Deformation Features (PDFs) in quartz using a universal stage. Appendix B provides a full list of parameters used within the numerical simulations in this thesis (Chapters 5, 6, 8, and 9). Appendix C provides the full data sets produced by universal-stage analysis (Chapters 5, 6, and 9). Additionally, summarised thin section descriptions are provided. Appendix D provides the full set of imaged backscattered electron images used in Chapters 6 and 9). Supplementary results of the image analysis methods used are also presented. Appendix E provides the results of Energy Dispersive Spectroscopy used for phase identification in Chapter 6. Appendix F provides a comparison of the newly-revised model of the Chicxulub impact event presented in Chapter 8 with an alternative model and a previously published model. Appendix G provides a comparison between the stress-strain path described in Chapter 8 using a single Lagrangian pseudo-cell, with the stress-strain paths of alternative pseudo-cells distributed across the peak-ring material. Appendix H provides additional EBSD maps, supplementary to Chapter 9.

Part I

Background and Methods

2 Background

2.1 The Impact Cratering Process

The formation of an impact crater is often split into three distinct stages: Contact and Compression, Excavation, and Modification. Each of these stages is described and discussed in the section below — more extensive discussion can be found in Melosh (1989). Following a description of the impact cratering process in general, a more detailed review of the current state of understanding of complex crater collapse is provided — more extensive discussion of this topic can be found in Melosh and Ivanov (1999) and Kenkemann et al. (2012). Finally, the geological and geophysical products of impact cratering will be introduced.

2.1.1 Contact and Compression

The first stage of a planetary impact involves the projectile striking the planetary surface (assuming a negligible effect of any atmosphere). The projectile then pushes target material out of its path, compressing and accelerating the material. Concurrently, the target's resistance to penetration causes the projectile to decelerate. These accelerations are mediated by stress waves, which originate at the point of impact and are transmitted into both the target and projectile. The transmission of pressure through a material is always achieved by the propagation of a stress wave. Stress waves in solids can take one of three forms, depending on the magnitude of the pressure that they are transmitting: elastic waves, plastic waves with elastic precursors, and shock waves (Melosh, 1989).

Elastic body waves are the most generally familiar type of stress wave, and they occur as two types: longitudinal or transverse (commonly known as P-waves and S-waves respectively). Their names describe the orientation the particle velocity relative to the orientation of the wave velocity. Deviatoric stress in an elastic wave increases with the strength of the initial disturbance. While rocks are capable of supporting extremely large hydrostatic compressive stresses without failure, rocks are limited in their ability to support shear stresses. Shear stresses will always be present within a material experiencing deviatoric stresses. The relationship between pressure and shear

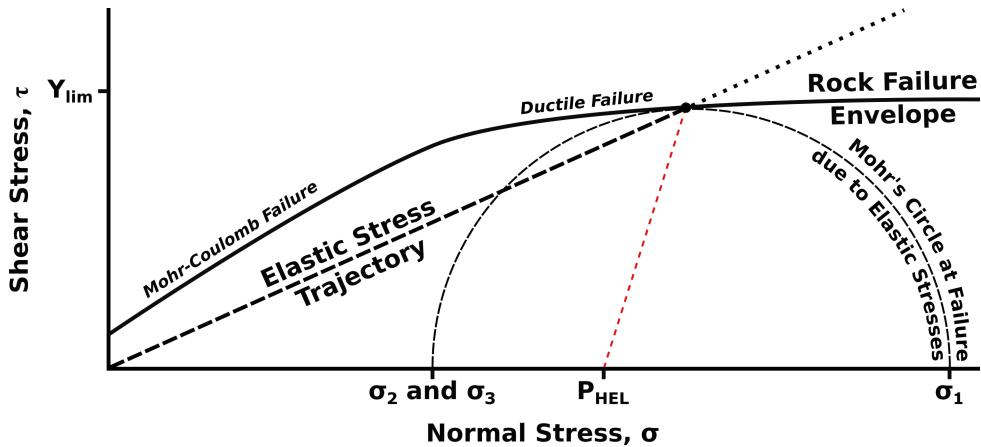


Figure 2.1: Failure of rock in a compressive wave. A rock failure envelope is shown where the material follows a coulombic failure criterion at low average normal stresses (i.e. pressures), and becomes independent of pressure at high pressure conditions. The shear stress in an elastic wave increases linearly with pressure, following the elastic stress trajectory. A Mohr's circle is shown at the condition where the elastic stresses cause failure, i.e. at the HEL. σ_1 corresponds to the longitudinal stress in the stress wave, and σ_2 and σ_3 correspond to the transverse stresses. The HEL is the pressure at which failure occurs, the average of σ_1 , σ_2 , and σ_3 . Modified from Melosh (1989).

stress in an elastic wave is known as the Elastic Stress Trajectory, the gradient of which is determined by the Poisson's ratio of the material. Consequently, an elastic wave can reach a pressure at which failure occurs due to the presence of shear stresses. At this pressure, which is known as the Hugoniot Elastic Limit (HEL), and beyond, the stress wave causes permanent deformation, and is therefore no longer an elastic wave but a plastic wave (Figure 2.1; Melosh, 1989).

Plastic waves, unlike elastic waves, have velocities that vary upon the pressures that they transmit. At low pressures (above the HEL), plastic waves are slower than elastic waves. In this regime, a plastic wave will always propagate with an elastic precursor wave. Beyond a critical pressure, the velocity of the plastic wave exceeds the elastic wavespeed, at this point the stress wave is known as a (strong) shock wave, and is characterised by an abrupt change in pressure at the wavefront (Melosh, 1989). For most rocks, the HEL is at ~ 3 GPa, and the transition from plastic waves with elastic precursors to strong shock waves is at ~ 40 GPa (Melosh, 1989), consequently, most solid-state state shock metamorphic effects occur in the plastic wave with elastic precursor regime.

Shock is released by the propagation of rarefaction waves from free surfaces into the shocked material. The velocity of a rarefaction wave occurs at the longitudinal wave speed of the material into which it propagates, as the rarefaction wave always

propagates into material in a state of shock, the rarefaction wave speed is faster than the shock velocity. Rarefaction waves are dispersive as their velocity depends on the pressure in the material into which they are propagating. Consequently, the tail of a rarefaction wave travels lags behind the head, leading to a characteristic gradual decline in pressure at the tail of a shock wave. Shock waves conserve mass, energy, and momentum. By contrast, rarefaction waves conserve all of these, in addition to entropy. Thus, shock is thermodynamically irreversible while rarefaction is reversible and adiabatic. This difference between shock and rarefaction processes result in shocked and unloaded material receiving a net energy gain; which is commonly manifested as an increased kinetic energy, entropy, and temperature, relative to the pre-shocked state (Melosh, 1989). The shapes of the three types of stress waves in solids is shown in Figure 2.2.

The conditions of deviatoric stresses during shock and decompression are non-trivial. For simplicity, we will consider the state of stress during planar shock and decompression (Figure 2.3). Prior to shock compression, geological materials typically experience lithostatic stress conditions. Where the maximum principal compression is vertical due to the weight of overlying rocks, and the other two principal stresses are horizontal and confine the material.

During shock, a large longitudinal stress is applied to the material. This stress is perpendicular to the shock wave front, and two transverse stresses are applied parallel to the shock wave front. The transverse stresses applied by the shock wave are identical and are dependent on the gradient of the elastic stress trajectory, which is itself dependent on the Poisson's ratio of the material. The effect of combining the transverse stresses of the shock wave with the lithostatic stresses may result in slight differences between σ_2 and σ_3 , the intermediate and minimum principal stresses. However, compared to the difference between those stresses and σ_1 , the maximum principal stress, σ_2 and σ_3 can be considered to be equal.

Rarefaction adds another component to the stress state that the shocked material experiences. Rarefaction has the opposite stress state to the shock wave, firstly, it is tensile in all directions, and secondly, it is most tensile in the longitudinal direction, and least tensile in the transverse directions. Consequently, in the case of planar shock and decompression, the minimum principal stress of the rarefaction acts in the same direction as the maximum principal stress of the shock wave. The resultant stress of the shock compression and the rarefaction lead to a final stress condition within the rarefaction wave that remains fully compressional.

Finally, the post-shock condition of the material is important to consider because the stress state does not return to its initial lithostatic condition. The material is now moving in the same direction as the shock and rarefaction waves; consequently, the orientation of maximum principal compressive stress after shock remains aligned

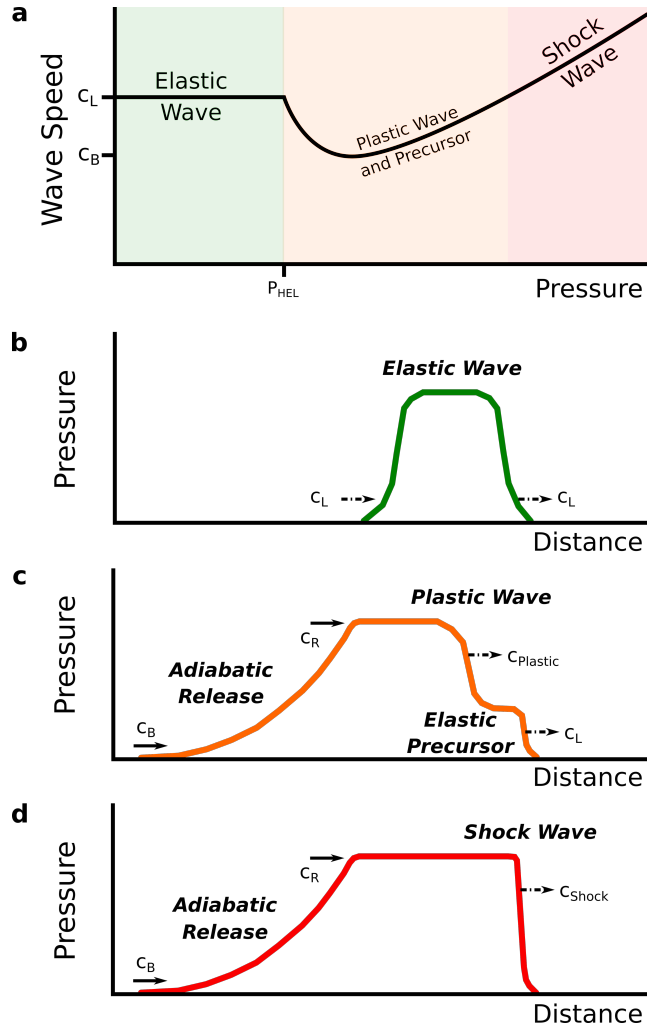


Figure 2.2: Types of stress wave. a) The propagation velocities of stress waves as a function of the pressure in the wave. Longitudinal elastic body waves travel at a constant velocity, C_L , otherwise known as the P-wave velocity. Stronger waves break into an elastic wave and a plastic wave that travels at a lower velocity, $C_{Plastic}$, which may be as low as the bulk sound speed C_B . At even higher pressures, the velocity of the shock wave C_{Shock} exceeds C_L and thus, there is no precursor. b), c), and d) show the three distinct forms of stress waves: elastic, plastic with an elastic precursor, and shock respectively. Rarefaction waves are dispersive, with minimum velocities of C_B , and maximum velocities C_R , which are always larger than $C_{Plastic}$ or C_{Shock} . Modified from Melosh (1989).

with the shock and rarefaction waves. During cratering, it is this remnant velocity that causes the growth of a transient cavity. The conditions of stress described here are diagrammatically shown in Figure 2.3. Consideration of the orientation of stresses during cratering, where the shock wave is roughly hemispherical, is considerably more complex; this is because rarefaction does not propagate parallel to the shock front and because of the effect of the expansion of the shock front at increasing radial distances.

The contact and compression stage ends after the projectile has unloaded from high pressure. The principal result of this stage is the transfer of most of the projectile's kinetic energy to the target. The contact and compression stage is typically over within a second, even for the largest of planetary impacts (Melosh, 1989).

2.1.2 Excavation

The excavation stage begins immediately after the contact and compression stage ends. During this stage, the shock wave propagates into the target, attenuating as it is transmitted due to the increased area of the shock front and eventually, due to the rarefaction wave catching up with the shock front. The combined effect of the shock and rarefaction waves is to accelerate the material such that a crater is opened by the excavation and ejection of material, as well as the displacement of material deeper into the target. The excavation stage typically lasts many times the length of the contact and compression stage, requiring seconds or minutes to reach completion, depending on the crater size (Melosh, 1989).

2.1.3 Modification

The modification stage begins after the crater has been fully excavated. The result of the excavation stage is a bowl-shaped “transient crater” which then, usually, collapses under gravity. The extent to which a crater undergoes modification is strongly dependent on the size of the transient crater. In small craters, debris flows slide down the interior walls of the transient cavity. In large craters, rim areas are terraced due to the slumping of large blocks at the rim while rocks are uplifted near to the crater centre, resulting in central peaks and/or peak-rings. These large craters are the focus of this thesis and will be described in greater detail in Section 2.2. This stage of cratering may last more than an order of magnitude longer than the excavation stage (Melosh, 1989).

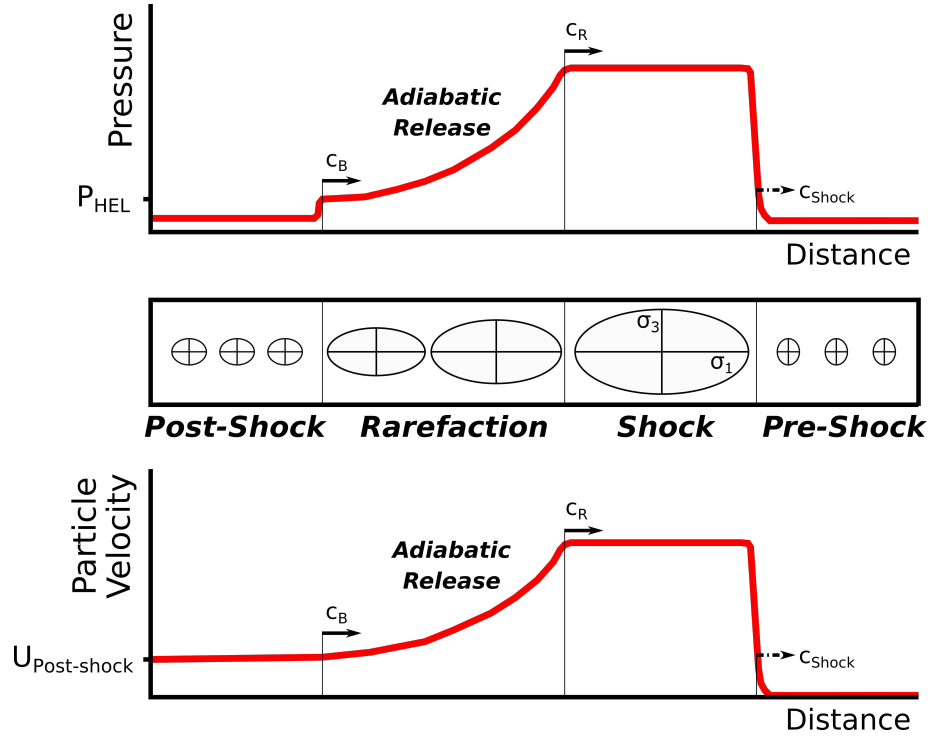


Figure 2.3: Pressure, stress, and particle velocity cross section of a shock wave. In this case, the shock wave is planar, and is followed by a parallel rarefaction wave. The stress condition is represented by Lamé stress ellipsoids. In the pre-shock condition, material is stationary and under lithostatic pressures, consequently σ_1 is oriented vertically. Upon shock, the material experiences a discontinuous increase in pressure, stress, and velocity. As the HEL is exceeded, shear stresses are at failure and near the ductile strength limit, Y_{lim} (see Figure 2.1). As the rarefaction wave arrives, pressure, deviatoric stress, and material velocity begin to decrease. At this point, the state of stress can be conceptually described as the sum of the shocked stress-ellipsoid, with the stress-ellipsoid of a rarefaction wave, which has entirely tensional principal stresses and is most tensional in the wave propagation direction. The net effect of this summation is to reduce the values of σ_1 and σ_3 , and, because the rarefaction is parallel to the shock wave, to maintain the orientation of the principal stress axes. Despite the change in pressure and principal stresses, the critically resolved shear stress remains near the same value, at failure and near Y_{lim} (see Figure 2.1). Upon the pressure decreasing beneath the HEL, the material enters a post-shock state, where the material retains some fraction of the material velocity that it gained during shock. This velocity exerts an effect on the state of stress, such that σ_1 remains in the shock direction.

2.2 Complex Crater Collapse

Large impact craters have complex morphologies, containing central peaks or peak-rings and wide terrace zones at their rim. By contrast, small impact craters have bowl-shaped, and so-called “simple” morphologies (Figure 1.1). Complex crater morphologies form during the collapse of a transient, bowl-shaped cavity. The diameter at which craters transition from simple to complex morphologies occurs over a narrow range, and is specific to each planetary body. On the Moon, complex craters can be observed at about 15 km diameter. On Mercury and Mars the transition occurs at about 7 km diameter, and on Earth, the transition occurs at about 2–4 km diameter, depending on the target material. It can therefore be seen that the simple-to-complex transition diameter scales inversely with the acceleration due to gravity on the given planetary body (Figure 2.4; Pike, 1980, 1988).

The dependence of the simple-to-complex transition on gravitational acceleration suggests that craters collapse due to weight, the force generated by the effect of gravity on mass, overcoming the strength of rocks i.e. the ability of the transient cavity to maintain its shape under stress. Static analysis of the stability of cavities has shown that for substantial rim collapse or floor uplift to occur, the actual effective strength must be less than 3 MPa, and there must be little or no internal friction (McKinnon, 1978; Melosh, 1977). Additionally dynamic models of crater formation require the same low yield strength and internal friction (O’Keefe and Ahrens, 1999; Wünnemann and Ivanov, 2003). These properties are inconsistent with laboratory measurements of the strength of rock (Kenkmann et al., 2012), thus some process must occur that reduces the effective strength of rocks during cratering. A variety of mechanisms could potentially cause the weakening of rocks within craters: damage and fracturing (see Kenkmann et al., 2012), bulk thermal softening (O’Keefe and Ahrens, 1999), fault lubrication by shear-induced melting (Spray, 1997) or other processes (Senft and Stewart, 2009), Acoustic Fluidisation (Melosh and Ivanov, 1999; Melosh, 1979), or some combination of these effects.

Damage and rock fracturing cannot be solely responsible for the required weakening. Figure 2.5 shows the damaged and intact strength profiles of a typical rock (see Section 3.2.2.2). It can be seen that while damage can reduce the shear strength of a rock to significantly less than several MPa, damage is only capable of causing sufficient weakening at normal stresses (i.e. pressures) less than approximately 10 MPa, equivalent to only 300 m of lithostatic overburden. The vast majority of rocks at failure during complex crater collapse are under normal stresses considerably greater than 10 MPa. In other words, the coefficient of internal friction of damaged rocks is too high, even for damaged and fractured rocks.

It has been proposed that the deposition of energy in the target due to the passage of the shock wave may cause the thermal softening of rocks (O’Keefe and

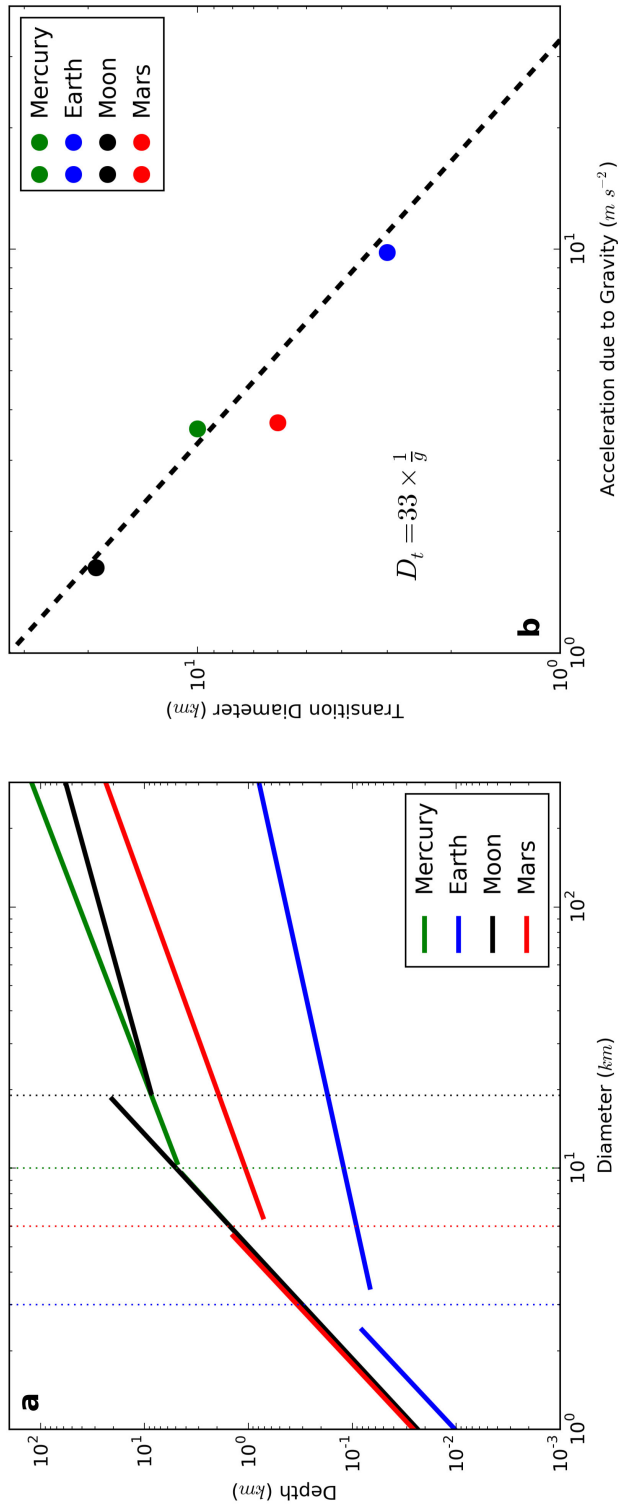


Figure 2.4: The dependence of gravity on the simple to complex transition. a) The best-fit depth-diameter trends of craters on Mercury, Earth, Moon, and Mars. The simple-complex transition diameters are indicated by the dotted lines. b) Transition diameter as a function of acceleration due to gravity. Based on Pike (1980, 1988).

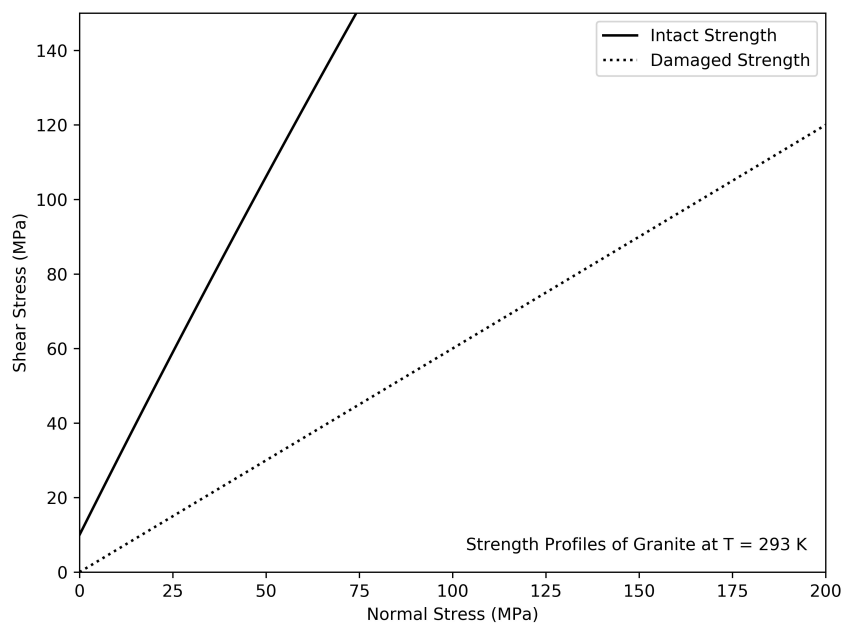


Figure 2.5: Intact and damaged strength envelopes of rocks as a function of pressure. See section 3.2.2.2 for the mathematical definitions of these failure criteria.

Ahrens, 1999). The effect of temperature on the strength of a typical rock can be seen in Figure 2.6a (see Section 3.2.2.2). Here, the strength of a rock under a pressure of 100 MPa is shown, and it can be seen that the strength reduction required for crater collapse, ~ 3 MPa can only be achieved when the rock is within 100 K of the melting temperature, ~ 1673 K. A final post-shock temperature > 1500 K is only possible for rocks that have experienced shock pressures in excess of 45 GPa (Figure 2.6b), potentially less if the rock has an elevated initial temperature. Nevertheless, on this basis, it is unlikely that bulk thermal softening can cause the weakening of a sufficient volume of rock to facilitate crater collapse. The exception to this rule would be for the very largest impact basins in the solar system, where the geothermal gradient and the relative increase in high-shock volume with crater size play important roles (Grieve and Cintala, 1992).

The hypothesis that faults of low strength may facilitate crater collapse (see Senft and Stewart, 2009) does not require any bulk-scale weakening. Instead the hypothesis would suggest that the impacted rock mass is only as strong as its weakest part. As long as the faults between rock blocks have a yield strength less than a few MPa and little to no coefficient of internal friction, then the entire rock mass, on the macroscopic scale, will behave with similar properties. Numerical impact simulations using this hypothesis have had some success (Senft and Stewart, 2009); however, the cause of faults possessing such low strengths is unknown. The most likely cause of such weak faults is the generation of frictional melts on faults (Spray, 1997); nevertheless, impact-pseudotachylites, which may be the product of frictional melting, are not generally abundant in complex impact structures, except for in the deeply eroded Vredefort and Sudbury impact structures (Reimold and Gibson, 2005). Other, more exotic, mechanisms for fault weakening have also been proposed (see Senft and Stewart, 2009).

Perhaps the most successful mechanism, in terms of a fully developed model, proposed to facilitate complex crater collapse is acoustic fluidisation (Melosh, 1979). In this model, short-wavelength elastic waves, produced by either the passage of the shock wave or subsequent deformation, cause a release of overburden pressure in the deforming material. Rocks, and other brittle materials, behave as a Coulomb material; that is, the yield strength of the material is directly proportional to the overburden pressure. The constant of proportionality between these two properties is the coefficient of internal friction, μ . Consequently, a release of overburden pressure due to vibrations in the material would be expected to cause reduction in the yield strength of the material (Melosh and Ivanov, 1999). The acoustic fluidisation model is commonly used in numerical simulations of complex crater collapse and has had considerable success in replicating the size-morphology progression of terrestrial and lunar craters (Baker et al., 2016; Collins, 2014), as well as modelling the specific features of individual craters (e.g. Collins et al., 2002, 2008b; Goldin et al., 2006; Vasconcelos et al., 2012; Wünnemann et al., 2005). Despite these successes, a considerable limitation of impact simulations that employ acoustic fluidisation is non-uniqueness. In produc-

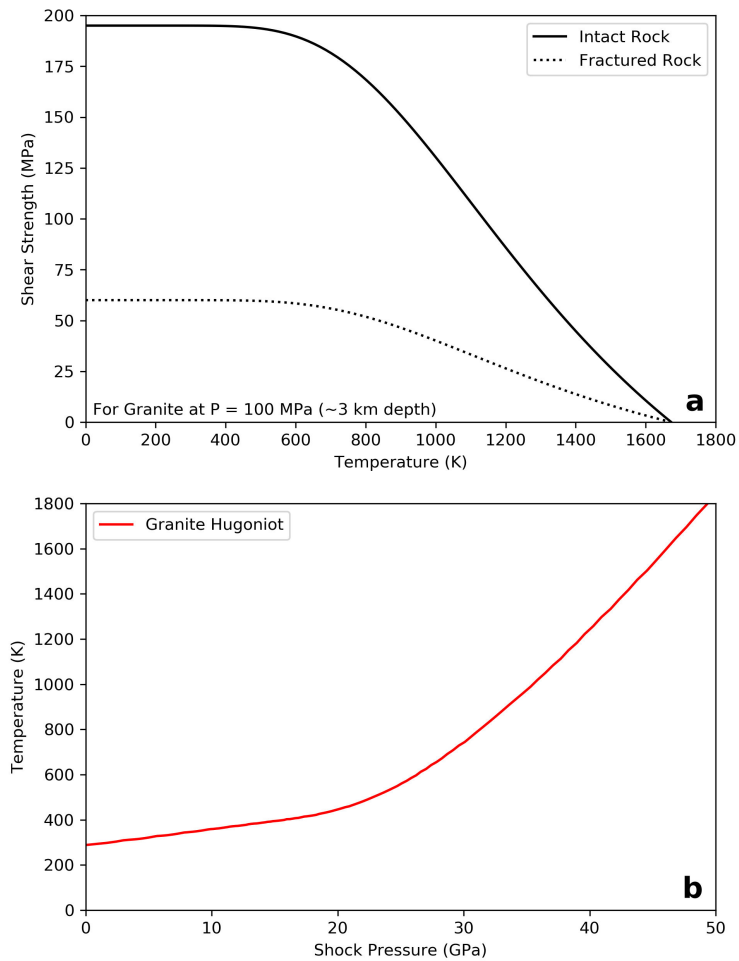


Figure 2.6: Thermal softening and thermal effect of shock. a) The strength of intact and damaged rock, granite, as a function of temperature. The material has no strength at its melting point. b) The relationship for post-shock temperature as a function of shock pressure, assuming the rock was initially at standard conditions.

ing final crater sizes and morphologies, there are trade-offs between impactor size and acoustic fluidisation parameters and, more importantly, there are trade-offs between the acoustic fluidisation parameters themselves (Wünnemann and Ivanov, 2003). For example, Wünnemann and Ivanov (2003) showed that the same crater size-morphology progression can be produced with short-lived, low-viscosity fluidisation or long-lived, high-viscosity fluidisation. Reducing the non-uniqueness of numerical impact simulations requires multiple quantitative observational data sets. A further challenge of the acoustic fluidisation model is the relationship between observable target properties, such as the size of discrete rock blocks, with the parameters of the model (e.g., Ivanov and Artemieva, 2002). The use of an acoustic fluidisation model is supported by recent observational evidence at Chicxulub by Riller et al. (in press), particularly during the earliest phases of crater collapse. Fault weakening due to the lubrication of faults may be an important process during the late stages of collapse. Nevertheless, it is clear that the acoustic fluidisation model accounts for the rheological behaviour that leads to the formation of peak-rings.

2.3 The Geology and Geophysics of Complex Craters

The process of impact cratering causes distinct and irreversible changes to the nature of rocks. The products of impact cratering can provide invaluable constraints on the process that occurs. Impact cratering causes lithological and petrophysical changes to target rocks, those changes are largely a result of shock metamorphism, initial location relative to the excavation flow, and/or the deformation path followed during crater collapse. In this section, the nature and terminology of impactites will be described within the context of crater structure and petrophysics.

2.3.1 Impactites

2.3.1.1 Nomenclature

Before describing the nature of impactites, it is necessary to briefly define the terminology that will be used throughout this thesis to classify impactites. The terminology used in this thesis takes after the recommendations to the IUGS on the nomenclature and classification of impactites by Stöffler and Grieve (2007), but is modified in consideration of proposed updated classification schemes (e.g. Stöffler et al., 2018) and outstanding disputes in the impact cratering community (Figure 2.7). In addition, the classification of fault rocks used in this thesis takes after Woodcock and Mort (2008) and Brodie et al. (2007) (Figure 2.8).

Impactites	
Location	Texture
Proximal	
	Target Rocks* <i>Shock</i> <i>Unshocked</i>
<i>Para-autochthonous</i>	Fault Rocks** Breccia <i>Lithic - Monomict</i> <i>Lithic - Polymict</i> <i>Melt-bearing / Suevitic***</i>
<i>Allochthonous</i> <i>(Occurring as crater fill, ejecta, or dikes within para-autochthon)</i>	Melt Rock <i>Clast-rich (>25%)</i> <i>Clast-poor (0-25%)</i> <i>Clast-free (0%)</i>
Distal	
	Spherule Tektite Microcrystite Microtektite

*For greater detail, standard rock classification terminology can be used to replace this term, e.g. "Shocked Target Rock" may become "Shocked Granite".

**Para-autochthonous fault rocks may be more specifically classified using the fault rock classification of Woodcock and Mort (2008).

***A polymict breccia with a lithic matrix containing rock and mineral clasts in all stages of shock metamorphism (including Melt Rock). Melt-bearing breccias may alternatively be termed Suevitic breccias or Suevite.

Figure 2.7: Impactite classification based on Stöffler and Grieve (2007). Definitions of terms, where not otherwise stated, may be found therein.

Fault Rocks			
		Non-foliated	Foliated
>30% large clasts (>2mm)			Fault Breccia
<30% large clasts (>2mm)	<i>Incohesive</i>		Fault Gouge
	Cohesive	0-50% matrix (<0.1mm)	Proto-cataclasite
		50-90% matrix (<0.1mm)	Cataclasite
	Cohesive	90-100% matrix (<0.1mm)	Ultra-cataclasite
		Glass or devitrified glass	Pseudotachylite*
		Pronounced grain growth	Blasto-mylonite**

*Ultrafine-grained vitreous-looking material, usually black and flinty in appearance, occurring as thin planar veins, injection veins or as a matrix to pseudoconglomerates or breccias (Brodie et al. 2007). Note: this term is not specific to any particular process of producing melt, such terminology can be achieved by adding a descriptor term, e.g. *Frictionally-generated pseudotachylite*.

**Mylonites are rare in impact structures. Mylonites typically form due to crystal-plastic deformation which occurs at low strain-rates. Impact cratering by its very nature is a high strain-rate process. Nevertheless, foliated fault rocks, produced by brittle processes, may occur in impact structures. Under this classification, these could be termed a "mylonite". An alternative term for this rock type in an impact structure would be a "foliated cataclasite".

Figure 2.8: Fault rock classification based on Woodcock and Mort (2008). Definitions of terms, where not otherwise stated, may be found therein.

2.3.1.2 Shock Metamorphism

The shock pressure that an impactite experiences strongly influences its petrological properties. Rocks that experience very high shock pressures ($> \sim 100$ GPa) vaporise upon rarefaction (Melosh, 1989). These vaporised rocks may then condense and solidify. The products of the condensation and solidification of shock-vaporised rock includes impact spherules and microcrystites (Glass and Simonson, 2012). These products are typically deposited distally from their source crater due to the extreme energy they acquire during shock.

Rocks that experience more moderate shock pressures (~ 50 – 100 GPa) will melt upon rarefaction. Those rocks that have experienced high shock pressures, close to the vapour transition, may begin to boil after pressure release, as suggested for tektites and microtektites (Koeberl, 1994, and refs therein). Nevertheless, the majority of rocks melted by shock in an impact event do not boil. These melted products can be readily seen in melt rocks or as clasts within melt-bearing breccias. Impact melts are unlike other naturally molten rocks because they are initially at extremely high temperatures, not limited by the liquidus temperature of the melt (Melosh, 1989). Impact melt rocks are most commonly found in impact melt sheets; coherent, laterally extensive bodies of solidified impact melt found near to the free surface of an impact crater. Impact melt sheets, due to cooling history and clast assimilation, contain internal stratigraphy. The grain size of an impact melt sheet coarsens upwards from the base, and downwards from the top; additionally, the base of an impact melt sheet is commonly rich in clasts of target rock material, thus clast concentration is considered an important descriptor of an impact melt rock. Impact melt rocks can contain geochemical traces of meteoritic material within them, and are often used to date impact structures (Jourdan et al., 2012; Koeberl et al., 2012).

Rocks that experience yet lower shock pressures ($< \sim 50$ GPa) remain in the solid state (Melosh, 1989). Rocks that experience average pressures in this range may be found in the form of breccias or para-autochthonous target rocks. Impact breccias have a matrix composed exclusively of unmelted material, and they are typically sub-classified on the basis of their clast populations. Melt-bearing (otherwise known as suevitic) breccias contain clasts of impact melt rock, in addition to unmelted, shocked and unshocked, clasts. Melt-bearing breccias may be produced by a number of processes:

1. During the excavation stage, where excavation flow lines cross-cut shock pressure contours in the target, mixing variably shocked material together (Pohl et al., 1977; Stöffler, 1977).
2. During modification, as a “ground surge”, where impact melt becomes entrained within breccia as the breccia and/or melt rocks are emplaced (Osinski, 2004; Pohl et al., 1977; Stöffler, 1977).
3. By melt-fuel coolent interaction (MFCI) after impact, where water and impact melt/ hot rock react explosively, resulting in the deposition of a breccia (Artemieva et al., 2013; Grieve et al., 2010; Stöffler et al., 2013).
4. Intruded as dikes into the para-autochthon from deposits of any of the three previous processes.

Monomict and polymict lithic breccias contain only unmelted material. They can be produced by the excavation and/or displacement of rocks during crater

excavation, or by rock slumping during crater modification (Kenkmann et al., 2014). Monomict lithic impact breccias may be classified as a fault breccia or vice versa, depending on field relationships.

Para-autochthonous shocked target rocks are the most volumetrically abundant impactites within a crater. These rocks are typically macroscopically indistinguishable from unshocked rocks, although they are commonly heavily fractured and deformed, and commonly contain fault rocks within them. Shocked para-autochthonous rocks may contain shatter cones (Dietz, 1959; French and Koeberl, 2010), the only unique macroscopic indicator of shock metamorphism. Determining the shocked nature of these rocks typically depends upon microscopic observation of shock metamorphism to individual minerals. Shock deformation has been identified in many minerals; however, only a few mineral systems produce features uniquely indicative of shock metamorphism. Furthermore, only a few minerals have well-calibrated shock metamorphic effects, in addition to a range of shock metamorphic effects over a wide pressure range (see French and Koeberl, 2010).

Perhaps the most well-understood mineral system under shock metamorphism is that of quartz (French and Koeberl, 2010). Quartz is particularly useful in terrestrial crater studies; it is both stable and abundant in terrestrial rocks, and it also displays a variety of shock metamorphic effects dependent upon the magnitude of the peak pressure (Grieve et al., 1996; Stöffler and Langenhorst, 1994). At low shock pressures (2–10 GPa), quartz develops planar fractures (PFs), open fractures similar to cleavage planes. Additionally, some PFs may possess feather feature (FF) lamellae. Another type of open fracture whose orientation can be used to constrain the orientation of maximum principal compressive stress during shock. At greater shock pressures (5–35 GPa), quartz develops planar deformation features (PDFs). These are closed, glassy planes within a crystal, oriented on rational crystallographic planes, with a spacing between features of 2–10 μm . PDFs may anneal over time, leaving evidence of their presence in the form of planar arrangements of fluid inclusions — these are termed “decorated” PDFs. It has been experimentally shown that the orientation at which PDFs form is dependent upon the peak shock pressure experienced by the grain (Carter, 1965; Hörz, 1968; Huffman and Reimold, 1996; Müller and Defourneaux, 1968). By characterising the orientations of PDFs, the distribution of shock metamorphism can be determined at impact structures, for example; Charlevoix, Manicouagan, Slate Islands, and Siljan (Dressler et al., 1998; Grieve et al., 1976; Holm et al., 2011; Robertson, 1975; Robertson and Grieve, 1977). At even greater pressures (35–50 GPa), quartz undergoes a transformation to diaplectic glass, an isotropic material that pseudomorphs the original quartz grain, significantly, this transformation occurs in the solid-state, without melting. After experiencing shock pressures greater than ~ 50 GPa, quartz will begin to melt. The glassy product of this process is known as lechatelierite (French and Koeberl, 2010; Grieve et al., 1996).

The lithological structure of typical simple and complex craters is shown in Figure 2.9.

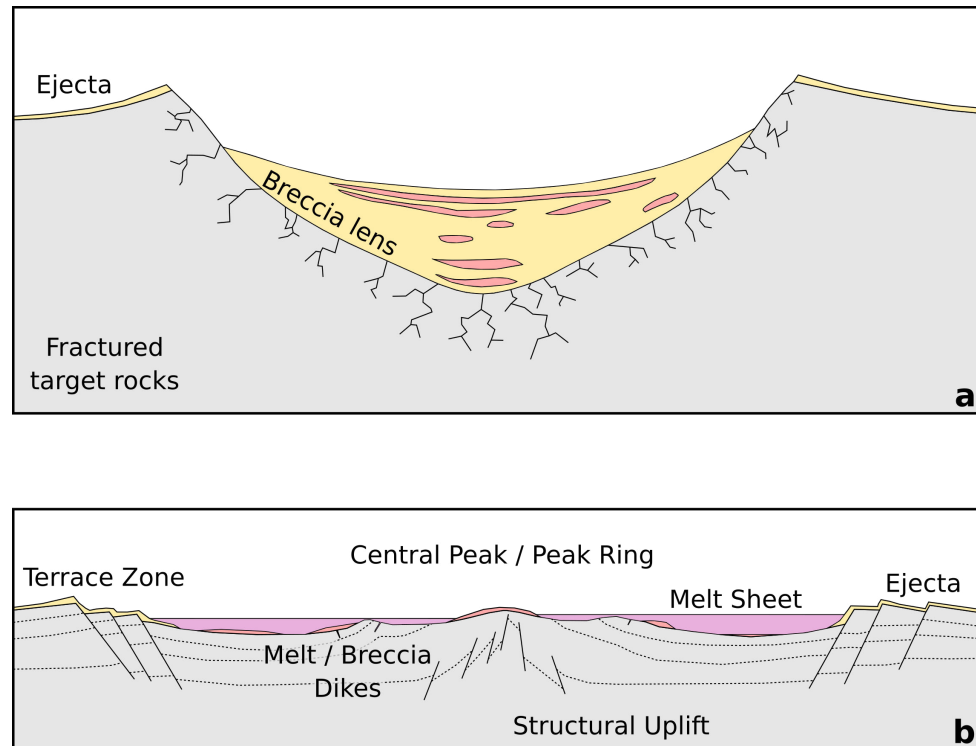


Figure 2.9: Schematic cross-sections of: a) a simple crater, and b) a complex crater. Modified from Grieve (1987).

2.3.1.3 Shock Barometry as a Structural Tool

One of the primary challenges in assessing transient weakening mechanisms is in the uncertainties regarding the kinematics of complex crater collapse. This is particularly challenging in crystalline target rocks, where there are no stratigraphic markers to identify the original position of material. However, the final distribution of shock metamorphism in complex craters provides a possible constraint on the kinematics of crater modification (Dence, 2004). At the point in time when the transient cavity is fully formed, shock isobars are arranged approximately concentrically around the transient cavity; from this point, the transient cavity undergoes modification to form the final crater. By analysing the distribution of shock metamorphism in three dimensions, constraints can be placed upon the kinematics of crater modification (e.g. Ivanov, 1994).

2.3.2 Physical Properties

The process of hyper-velocity impact causes irreversible changes to the physical properties of rocks (Melosh, 1989). These changes produce conspicuous geophysical anomalies within craters compared to surrounding rocks. The identification of craters on Earth and, increasingly, across the solar system (e.g. Zuber et al., 2013), is primarily achieved by remote geophysical surveying.

The most commonly observed geophysical signature of an impact structure is a circular region of negative residual gravity (Pilkington and Grieve, 1992). Negative residual gravity anomalies at craters are caused by the replacement of high density intact rocks in the pre-impact target with fractured para-autochthonous rocks, porous impact breccias, and/or the relative loss of mass due to excavation and basin infill (whether it is vacuum, atmosphere, water, or post-impact sedimentary rocks). Within complex craters, the main contributor to the gravity signature derives from fractured para-autochthonous target rocks beneath the floor of the crater (see Pilkington and Grieve, 1992). Additionally, complex craters, >40 km in diameter, may have relative gravity highs in their centre due to the uplift of high-density rocks during cratering. Low-density, fractured rocks can also be identified in impact structures using seismic velocities, which are typically correlated with density. Fractured basement rocks, central crater structures, and impact breccias typically possess low reflectivity, and low seismic velocities. Impact melt rocks and structural uplifts may possess high reflectivity, and high seismic velocities. Finally, many impact structures possess magnetic anomalies, a consequence of either the precipitation of magnetic minerals in impact melt rocks or due to hydrothermal activity (Morgan and Rebolledo-Vieyra, 2012).

The presence of low-density, porous rocks in impact structures has important implications for the transport of fluids within craters; affecting the viability and longevity of hydrothermal activity (e.g. Abramov and Kring, 2007), the distribution of potential hydrocarbon reservoirs (Grieve, 2005), and the habitability of impact structures for microbial life (Cockell, 2006).

3 Methods

To address the objectives of this thesis, both observational and numerical methods are required. In this section, the general methods used in this thesis will be described; specific methodological details of relevance to individual chapters can be found within the relevant chapter.

3.1 Observational Methods

3.1.1 Core Logging and Field Observations

Macro-scale observations on a scale comparable, though still generally finer, than the scale of an impact structure requires field observations or the recovery of drill cores. Field observations possess a significant advantage of scale, being limited only by available exposure and the time taken to travel between outcrops. Thus, field observations provide the lowest resolution, but greatest coverage data of an impact structure. On a somewhat smaller scale, drill cores provide the opportunity to take a one-dimensional section, with 100% exposure, of an impact structure. The advantage of a drill core is that it provides a nearly continuous section of rocks, generally including fault rocks and deformation fabrics that are only infrequently exposed in the field. In this thesis, a combination of core and field observations of lithological and structural variation will be used to provide constraints on the process of impact cratering. Additionally, samples for micro-scale analysis will derive from areas of interest defined on the basis of field or drill core analysis.

3.1.2 Petrography

Samples were prepared for petrographical analysis by the production of thin sections. These thin sections are $30\ \mu\text{m}$ in thickness, and mounted in a blue-dyed epoxy resin. The majority of sections prepared for this thesis were polished thin sections, appropriate for both optical and electron microscopy, the remaining prepared thin sections were covered sections. In Part II, many of the analysed thin sections derived from the Core and Sample Repository of the Geological Survey of Canada in

Ottawa, a branch of the Earth Sciences Sector of Natural Resources Canada. These thin sections are all covered, and have a colourless epoxy mounting medium.

3.1.2.1 Optical Microscopy

Thin sections analysed under the optical microscope were typically investigated first under a standard petrographic polarising light microscope. Modal mineralogies were estimated by eye, with comparison to a standard mineral percentage chart. Additional shock metamorphic and structural features were identified, described, and photographed under plane- and cross-polarised light.

Most of the thin sections were specifically chosen due to presence of quartz, which display distinctive features characteristic of the shock pressure that they have experienced. For the para-autochthonous rocks generally studied here, the most common shock metamorphic features of quartz are PDFs, PFs, and FFs. PDFs are particularly useful for shock barometry because the crystallographic orientation at which they form is determined by the pressure that they experience. Determining the crystallographic orientation of PDFs in quartz requires the use of a universal stage. Appendix A describes, in detail, the methodology of determining quartz PDF orientations using a universal stage. Here, a Zeiss 4-axis Universal stage was used following the techniques described by Engelhardt and Bertsch (1969) and Stöffler and Langenhorst (1994) and Ferrière et al. (2009). Analysis of PDF orientations requires the measurement of the orientation of the optic axis and the poles to all PDF planes in an individual quartz grain. These measurements were used to index the PDFs to specific crystallographic planes with the use of a stereographic projection template. Here, the program ANIE v1.1 (Huber et al., 2011) was used to index PDFs after cross-checking against plotting the PDFs manually using the new stereographic projection template (NSPT) of Ferrière et al. (2009).

During indexing, a 5° envelope was allowed to account for errors in measurement and for the slight variation of crystallographic orientation between domains of the crystal. There is an overlap between the 5° error envelopes of the $\{10\bar{1}3\}$ and $\{10\bar{1}4\}$ PDF orientations. In this thesis, if the pole to a PDF plane plotted within this region, it was considered to be in the $\{10\bar{1}3\}$ orientation.

In order to ensure reliable pressure estimates based on the PDF data, a sufficient number of quartz grains need to be measured (Ferrière et al., 2009). Here, where possible, 30 quartz grains per sample were measured. In samples with less than 30 quartz grains, all quartz grains were analysed. Quartz grains were included in the pressure estimates regardless of whether or not they contained PDFs.

Shock pressure estimates were made based on the indexed PDF orientations. Here, the method of Robertson and Grieve (1977) was used. Each quartz grain was assigned a shock pressure based on which PDF sets it contained; the shock cali-

bration scheme used here is based on the scheme suggested by Stöffler and Langenhorst (1994) and Grieve et al. (1996) and presented in Table 3.1. Since the start of the work presented in this thesis, a new shock classification scheme has been presented in Holm-Alwmark et al. (2018). I would recommend that any future shock barometry based on quartz PDFs use this new classification scheme; however, to ensure consistency between thesis chapters and the results published in Rae et al. (2017a), all shock barometry results in this thesis use the shock classification scheme in Table 3.1. The various shock classification schemes for quartz cause minimal variations to the results presented in this thesis. The shock pressure of the sample was then calculated by taking the arithmetic mean of the individually assigned shock pressures within the sample.

3.1.2.2 Electron Microscopy

Additional sample preparation was required prior to electron microscopy. Samples analysed using EBSD (electron backscatter diffraction) were given a final polish using $0.06\ \mu\text{m}$ colloidal silica in NaOH on a Buehler Vibromet II for four hours. A thin carbon coat was applied to all thin sections, preventing charge accumulation on the section during imaging.

Backscattered Electron Scanning Microscopy — The most commonly used electron microscopic method in this thesis is backscattered electron (BSE) imaging. BSE images acquired here used either a JEOL JXA-8530F field-emission electron microprobe at the Earth and Planetary Materials Analysis Laboratory, Western University, or a Zeiss Ultra Plus Field Emission Scanning Electron Microscope (SEM) at the Natural History Museum, London.

Backscattering occurs due the elastic scattering of electrons in a material. Elastic scattering is a process that alters the trajectory of incident electrons without a significant change in their kinetic energy. The degree to which electrons, of a specific energy, are elastically scattered is directly dependent upon the atomic number (Z) of the target. High- Z materials cause large amounts of elastic scattering due to the increased size and charge of atomic nuclei. Thus, a brighter BSE intensity corresponds to a greater average Z in the spot sample volume. Typically, a BSE image will be acquired where the sample is normal to the electron beam, and the BSE detector is located close to the electron gun. A BSE image is a map of BSE intensity over a selected region. The primary use of a BSE image is to distinguish different phases and textures within a sample.

Energy Dispersive Spectroscopy — Electron microscopy can be used to determine chemical composition. Energy-dispersive X-ray spectroscopy (EDS) is an analytical technique used for the chemical characterisation of a sample. EDS uses an electron

Observation	Shock pressure range (GPa)	Median shock pressure (GPa)
No observed PDFs, within shatter cone radius	2–5	3.5
(0001)	5–10	7.5
{10̄13}	10–20	15.0
{10̄12}, within shatter cone radius	20–35	27.5
Diaplectic quartz glass	> 35	—

Table 3.1: Shock classification scheme of quartz, based on Stöffler and Langenhorst (1994) and Grieve et al. (1996).

beam, typically in an electron microprobe or SEM, to excite ground state electrons within atoms of the sample to higher valence shells. As the electron drops back to the ground state, energy may be released in the form of an X-ray. The specific energy of the emitted X-ray depends on the energy difference between the electron valence states, and is characteristic of the excited element. Thus, the energies of emitted X-rays provide information necessary to identify the elements in the excited volume, while the number of X-rays provides information necessary to quantify the relative abundances of elements in the excited volume.

In this thesis, EDS was used to identify mineral phases, requiring only relatively short counting times of 2 s. Consequently, the detection limit of elements was ~ 1 wt%. The quantification of major elements is typically accurate to within relative errors of $\pm 2\%$, while minor elements, if detected, are likely to have larger uncertainties. Furthermore, quantification of elements by EDS may be inaccurate if the analysed mineral is hydrated or contains other light elements; accurate quantification of any element with an atomic number less than 10 requires specialised EDS analysis. Oxygen totals are calculated by stoichiometry.

Electron Backscatter Diffraction — Finally, electron microscopy can be used to determine crystallographic orientation. This can be achieved using EBSD (electron backscatter diffraction). EBSD is conducted using an SEM and an EBSD detector, which contains a phosphor screen and CCD camera. The primary difference between EBSD and BSE imaging is that EBSD measurements are made when the sample is inclined at a high angle (70°) to the electron source, and the detector is placed at around 90° to the direction of the electron beam. This high angle between the electron beam and the sample causes some of the backscattered electrons to be diffracted by the material's crystal lattice according to Bragg's law, producing an interference pattern that is measured by the EBSD detector. The obtained interference pattern of a crystalline material will be composed of individual lines, known as Kikuchi Bands, that are each specific to a single crystallographic plane. The arrangement of Kikuchi Bands is directly related to the spacing between crystallographic planes, and the symmetry of the crystal structure. If the crystallographic system geometries of the targeted phases are well described, it is possible to relate the bands present in the diffraction pattern to the underlying phase and its crystallographic orientation within the electron interaction volume. In most minerals, at least three intersecting Kikuchi bands must be present to describe a unique solution to the crystal orientation. An EBSD map therefore represents many diffraction patterns, where each pixel of the map corresponds to an individually measured diffraction pattern, which in most cases will be indexed with a crystallographic phase and orientation. EBSD requires that the user defines the minerals that may be present within the sample such that the diffraction pattern(s) can be analysed by a computational algorithm that identifies the analysed mineral based on the user-defined

selection of minerals present.

EBSD carried out in this thesis was achieved using combined EDS and EBSD mapping equipment with an Oxford Instruments AZTec system on a Tescan MIRA3 at Curtin University. EBSD data were processed using the Tango and Mambo modules of Oxford Instruments Channel 5.10 to produce thematic maps and pole figures, respectively.

EBSD data can be represented on a map in many ways. In this thesis, four types of EBSD map will be presented. Firstly, every EBSD point is assigned a band contrast value, which measures the contrast between the Kikuchi bands and the background. EBSD points with low band contrast values may not be indexable. EBSD maps are often underlain with band contrast maps to clarify areas with high quality data. Secondly, indexed EBSD data may be used to generate phase maps; when a diffraction pattern is indexed, it is assigned a phase as it is assigned an orientation. The remaining two types of EBSD map presented in this thesis provide measures and/or visualisations of the strain experienced by a sample. The first of these is a misorientation map. Misorientation is an orientation defined with another crystal orientation frame as reference instead of the sample reference frame; misorientation maps are often plotted as angular differences relative to a chosen orientation selected in the sample. Thus, a misorientation map shows the minimum rotation required to bring the pixel into alignment with the reference pixel. The second method of visualising strain within an EBSD map is a local disorientation map. Local disorientation is the mean angular difference between the orientation of one point (a pixel) and the eight nearest neighbours of that point (i.e. a 3×3 pixel grid). Thus, misorientation displays strain while local disorientation displays the gradient of strain. Local disorientation only provides a semi-quantitative measure of strain because it is resolution dependent: large point sizes will lead to larger absolute values of local disorientation.

3.2 Numerical Methods

While observational approaches to studying impact cratering are extremely useful, they are somewhat limited. Unfortunately for impact cratering researchers, but somewhat more fortunately for life on Earth, large impact events on Earth are extremely rare on a human timescale, therefore they cannot be directly observed. Cratering as a process can be directly observed experimentally: light-gas guns are able to produce impact craters up to the centimetre scale and larger scale explosions are able to provide analogue processes up to the kilometre scale. Nonetheless, even these experiments are too small to be directly relevant to the scale of cratering in this thesis. Therefore, to “observe” the formation of large impact craters, experiments must be carried out using a numerical model.

Impact processes are typically modelled using a “hydrocode”. These computer codes were historically used to model fluid flow. However, in the field of impact processes, these codes have now been developed such that material strength is considered, and thus most impact codes today are not, strictly speaking, “hydrocodes”. In this thesis, the iSALE shock physics code is used, which is described below.

3.2.1 The iSALE Shock Physics Code

iSALE (impact-SALE) is a multi-rheology, multi-material code based on the SALE (Simplified Arbitrary Lagrangian Eulerian) hydrocode (Amsden et al., 1980). The original SALE code was developed to model a single, strengthless material. Modifications to that code have since been implemented by a number of researchers since the early 1990s.

Early developments to the code were primarily made by H. J. Melosh and B. A. Ivanov. An elasto-plastic constitutive model, fragmentation algorithms, and support for some equations of state were among the first updates to be implemented for impact cratering research (Melosh et al., 1992). Concurrently, SALE’s solution algorithm was improved by the implementation of; interface-tracking in Eulerian mode, damage accumulation and strain-weakening within the constitutive model, and the Analytic EoS program (ANEOS, Thompson and Lauson, 1974) was implemented (Ivanov et al., 1997). The result of this work was the SALE-B code (Ivanov and Artemieva, 2002; Ivanov and Deutsch, 1999).

Separately to the SALE-B code, G. S. Collins modified the original SALE code of Melosh to include a wider range of rheological models (resulting in the SALES-2 code). This model was used to simulate the formation of peak-rings in large impact craters (Collins et al., 2002). At around the same time, K. Wünnemann and others made several advancements to the SALE-B code (Wünnemann and Ivanov, 2003; Wünnemann and Lange, 2002; Wünnemann et al., 2005), including rewriting large portions of the code, while extending the code to be able to model three materials. Additionally, the constitutive model of SALE-B was modified by Collins et al. (2004).

In 2004, the SALE-B and SALES-2 codes were combined to produce the iSALE shock physics code, and a porous-compaction model was included (Wünnemann et al., 2006). More recently; iSALE was rewritten in Fortran 90, a three-dimensional version of iSALE (iSALE3D) has become available, and tools for iSALE were developed by Dirk Elbeshausen. A dilatancy model, accounting for the creation of porosity in shearing materials, has recently been added to iSALE (Collins, 2014), and, most recently, T. Davison has developed the PySALEPlot tool, a Python-based tool to allow access to the data stored within iSALE datafiles.

The iSALE (and the related SALE-B) code has been used to model sev-

eral terrestrial impact structures: Chesapeake Bay (Collins and Wünnemann, 2005; Kenkemann et al., 2009); Ries (Collins et al., 2008a; Wünnemann et al., 2005); Sierra Madera (Goldin et al., 2006); Chicxulub (Collins et al., 2008b; Ivanov, 2005); Haughton and El'gygytgyn (Collins et al., 2008a); West Clearwater Lake (Rae et al., 2017a; see Chapter 5); and Siljan (Holm-Almark et al., 2017).

3.2.1.1 Hydrocode Modelling

The fundamentals of hydrocode modelling are described by Anderson (1987) and Pierazzo and Collins (2004). In summary, hydrocodes solve a set of five equations. The first three are differential equations describing the Newtonian laws of physics: conserving mass, momentum and energy. In a reference frame that follows the material (Lagrangian), respectively these are:

$$\frac{d\rho}{dt} + \rho \frac{\partial u_i}{\partial x_i} = 0 , \quad (3.1)$$

$$\frac{du_i}{dt} = f_i + \frac{1}{\rho} \frac{\partial \sigma_{ij}}{\partial x_j} , \quad (3.2)$$

$$\frac{dE}{dt} = -\frac{P}{\rho} \frac{\partial u_i}{\partial x_i} + \frac{1}{\rho} s_{ij} \dot{\varepsilon}'_{ij} , \quad (3.3)$$

where u_i is the velocity, f_i is the external body forces per unit mass, σ_{ij} is the stress tensor, composed of the pressure, P and the deviatoric stress tensor, s_{ij} . ρ is the density, E is the specific internal energy, t is time, and x is position in space. $\dot{\varepsilon}'_{ij}$ is the deviatoric strain rate. The i and j subscripts denote coordinate directions.

The fourth equation, the equation of state, accounts for the thermodynamic response of the material. In iSALE, the equation of state takes the form:

$$P = f(\rho, E) . \quad (3.4)$$

In this thesis, all equations of state are generated using ANEOS (see Section 3.2.2.1).

The fifth and final equation, the constitutive equation, describes the strength of the material, Y , i.e. the stress that resists deformation:

$$Y = f(P, D, T, \dots) , \quad (3.5)$$

where T is temperature, and D is damage, a value that describes the extent to which a material behaves with a damaged strength profile as compared to the intact strength profile (see Collins et al., 2004). Pressure, damage, and temperature are the variables primarily responsible for variations in the strength of a material, nevertheless, there may be an effect from some additional variables, e.g. strain rate, or from transient weakening effects.

3.2.1.2 Spatial Discretisation and Resolution

Equations 3.1-3.3 describe a material as a continuum. Computers, however, only possess a finite memory capacity, thus, in order to make a model computationally possible, the problem space must be sub-divided into a series of smaller volumes. iSALE sub-divides the problem space into a grid of computational cells. For each cell, scalar values and stress tensors are cell-centred, while non-scalar values (e.g. velocity) are node-centred. As long as a sufficient number of discrete cells are present in the simulation, the model should adequately represent important variations within the domain.

iSALE's computational mesh can be in either Cartesian or cylindrical coordinates. In this thesis, a cylindrical mesh system will be used exclusively. In this arrangement, the left-hand boundary forms an axis about which the mesh is rotated. Using this axial symmetry forces the angle of impact to be perpendicular to the target surface, but is computationally efficient. Adjacent to the rotation axis, a "high-resolution" zone exists. Within this zone, the computational cells are regularly sized and spaced, and are at their smallest. In order to ensure maximum accuracy, this region of the mesh should contain all areas of interest throughout the simulation. The high-resolution zone may be bounded on any side (except the symmetry axis) by an extension zone. Cells within the extension zones become progressively larger as they become further from the high-resolution zone. Extension cells are used to mitigate the effects of the boundaries of the mesh interfering with the solution in the area of interest, without using too many cells to significantly effect the computational performance of the simulation. A schematic representation of the iSALE mesh geometry is shown in Figure 3.1.

3.2.1.3 Lagrangian and Eulerian descriptions

There are two distinct methods to mathematically characterise fluid motion: Lagrangian and Eulerian. A Lagrangian reference frame is a way of looking at fluid motion where the point of observation tracks the individual parcel of the fluid. An Eulerian reference frame is spatially fixed, and where the fluid passes through a fixed observation point.

Equations 3.1-3.5 are written using a Lagrangian reference frame, i.e. they refer to a specific parcel of fluid and are a "material description". iSALE can solve these

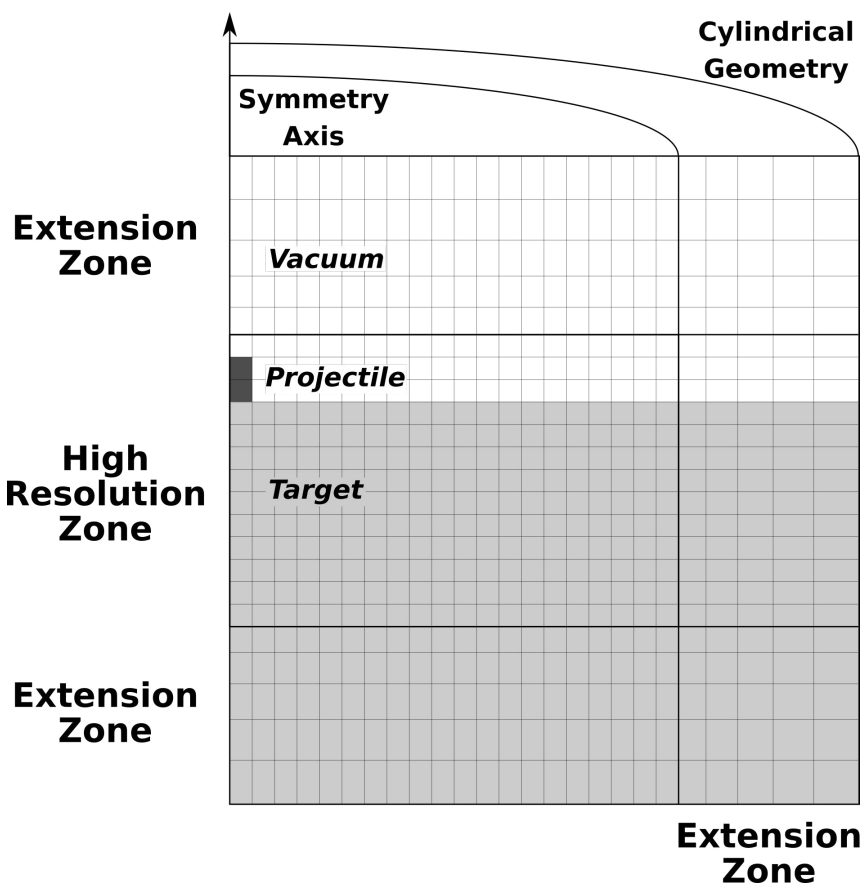


Figure 3.1: Schematic diagram of the iSALE mesh geometry. Bold lines indicate the extent of the high resolution zone. The target material is coloured light grey, the white space above is modelled as a vacuum, and the projectile is coloured in dark grey and measures as 1 cell per projectile radius.

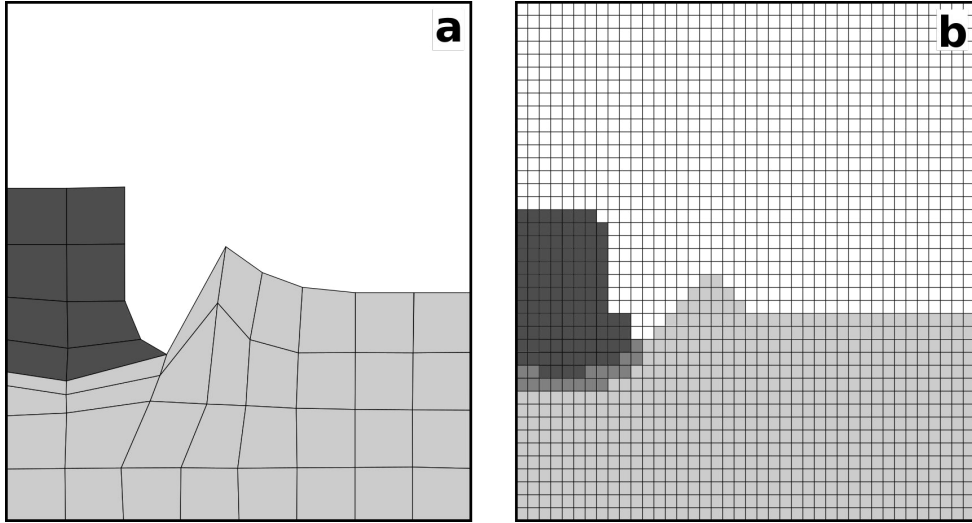


Figure 3.2: Comparison between Eulerian and Lagrangian calculations. In these schematic representations, a cylindrical impactor (dark grey) strikes downwards into a planar target (light grey). a) The Lagrangian description, where the computational mesh moves with the material. b) The Eulerian description, where the material flows through a fixed computational mesh. Mid-grey cells on the boundary between the impactor and target are mixed material cells.

equations, the equivalent Eulerian expressions of them, or a hybrid approach known as an Arbitrary Lagrangian Eulerian description (ALE). In the Lagrangian description, the mesh of cells is defined at the start of the calculation to define the geometry of the problem. Each cell contains a fixed mass and volume of material. As the simulation progresses, mass translates by deformation of the mesh. In the Eulerian description, the computational mesh is spatially and temporally fixed, and as the simulation progresses, material translates from cell to cell. Properties of the material must therefore be advected through the grid, and cells may contain a mixture of materials; such cells require special treatment to average the material properties (Figure 3.2).

While both frames of reference are computationally possible in iS^ALE, they each have distinct advantages and disadvantages. Lagrangian calculations tend to be faster than Eulerian calculations of the same resolution, due to the complexities of advection and mixture routines in Eulerian calculations. Additionally, Lagrangian calculations do not have to grid areas of empty space, which is required in an Eulerian calculation, and thus saves computational time. However, significant problems may occur in Lagrangian calculations when the mesh becomes highly deformed. Most hydrocodes, including iS^ALE, use the finite difference approximation (see next section) to discretise equations 3.1-3.5 in time and space; under larger and larger distortions of the Lagrangian mesh, the finite difference method causes discretised timesteps to become increasingly closer together, effectively freezing the simulation once a Lagrangian cell

becomes too distorted. Eulerian calculations do not suffer from this problem because the grid remains fixed, regardless of the deformation of the material. For this reason, impact simulations, which by their nature involve large deformations of material, are typically run with an Eulerian grid. All simulations in this thesis use an Eulerian grid.

3.2.1.4 Finite Difference Method

The differential equations 3.1-3.3, or their equivalent Eulerian equations, must be discretised in time and space in order to be computationally solved. iSALE uses the finite difference method to achieve this. This method replaces derivatives in the differential equations with relative differences (partial derivatives $\frac{\partial}{\partial}$, become $\frac{\Delta}{\Delta}$) which can be measured from the mesh. A detailed description of the finite difference equations used by iSALE may be found in Amsden et al. (1980) or the iSALE manual.

3.2.1.5 Artificial Viscosity

As described in Section 2.1, shock waves cause an instantaneous increase in pressure, velocity, and density. Truly instantaneous spatial and temporal jumps cannot be robustly modelled using a discretised space. This can be easily seen if one considers that the width of a shock front is substantially smaller than the size of any computational cell. Without any correction, numerically modelled shock pulses are followed by a train of spurious high-pressure oscillations. iSALE uses an artificial viscosity term to dampen these oscillations. This works by smoothing the jump at the shock front over several cells, which smooths any spurious pressure oscillations in the shocked material while maintaining a spatially narrow shock front.

3.2.1.6 Initial and Boundary Conditions

In all the cratering simulations presented in this thesis, the initial and boundary conditions of the calculation are qualitatively similar.

All simulations use a spherical impactor, of a size specific to the crater being modelled, travelling perpendicular to the target surface at a specified velocity, which is maintained across all simulations. In this thesis, which focusses exclusively on terrestrial impacts, the velocity of the impactor in all simulations is 15 km s^{-1} . This velocity can be justified because, while the average impactor velocity on Earth is 20.5 km s^{-1} , (Le Feuvre and Wieczorek, 2011), statistical probability indicates that vertical impacts are unlikely and that the most probable impact angle is 45° (Melosh, 1989). Using the two-dimensional iSALE code, therefore, requires that the velocity of 20.5 km s^{-1} is adjusted to account for how impactor obliquity may affect crater size. It has been shown that transient cavity size scales with the vertical component of the

impactor velocity (Chapman and McKinnon, 1986; Elbeshausen et al., 2009). Thus, highly oblique impacts produce small craters compared to direct impacts, provided that the impactor size and mass remain the same. On this basis, the velocity chosen in this thesis for all simulations, 15 km s^{-1} , is the vertical component of an impactor striking at 45° to the surface with a speed of 20.5 km s^{-1} . An additional advantage of using a lower impact velocity is that computational efficiency improves due to the reduced volume of vaporized rock. In this thesis, the target material is always planar (none of the simulated craters are large enough to be affected by planetary curvature), and stationary immediately prior to impact.

The behaviour of material at the edge of the mesh is determined by the boundary conditions for each edge. In the simulations in this thesis, the tops of the meshes are assigned outflow boundary conditions, such that material can be ejected outside of the mesh, and once material leaves the boundary it is deleted and does not re-enter the mesh. The left- and right-hand edges of the mesh are assigned free-slip boundary conditions, such that material may move parallel to the edge of the mesh, up and down, but never across the boundary. The bottom edge of the mesh is assigned a no-slip boundary condition such that material at the boundary cannot move in any direction. Both the free-slip and no-slip conditions at the right and bottom of the grid do cause reflections of shock/stress waves back into the mesh; however, provided the extension zones of the mesh are large enough, there is no significant effect on the final solution.

3.2.1.7 Lagrangian Tracer Particles

In an Eulerian description, material histories cannot be tracked directly. Material history is particularly useful because it allows properties such as location, pressure, temperature, distension, stress, and strain for a particular parcel of material to be tracked for every timestep of the simulation. To record this kind of information, iSALE uses Lagrangian tracer particles. These are marker particles, inserted into the computational grid at the start of the simulation, typically one per computational cell. As the simulation progresses, these tracer particles are moved with the material, according either to the local velocity field or the local material fluxes, without interacting with the material, and recording the position and thermodynamic history of the material package (e.g., Collins et al., 2008a; Davison et al., 2016; Pierazzo et al., 1997).

3.2.2 Material Models

Two of the five critical equations (3.4 and 3.5) solved by a numerical impact simulation relate to the properties of the material that is being modelled. Equation 3.4 is an expression of an equation of state while equation 3.5 is an expression of the

constitutive model.

3.2.2.1 Equations of State

An equation of state describes the thermodynamic state of a material under a given set of physical conditions. The equation may relate quantities such as entropy, temperature, pressure, internal energy, or density. Different materials possess different equations of state and the equation is a complex function of the molecular and atomic structure of the given substance. Consequently, rocks have extremely complex equations of state. As the thermodynamic responses of only a few materials are known well enough for numerical impact simulations; consequently, numerical impact modelling requires the selection of analogue materials, similar to the material being simulated. Melosh (1989) provides a useful summary of commonly used equations of state in numerical impact simulations. Here, the Analytic EoS program (ANEOS, Thompson and Lauson, 1974) was used. The ANEOS program is based around an analytic expression for the Helmholtz free energy $F(\rho, T)$. From the Helmholtz free energy; entropy (S), pressure (P), and the internal energy (E) can all be derived:

$$S = -\frac{\partial F}{\partial T} \Big|_{\rho}, \quad (3.6)$$

$$P = \rho^2 \frac{\partial F}{\partial \rho} \Big|_T, \quad (3.7)$$

$$E = F + TS. \quad (3.8)$$

iSALE uses density and specific internal energy as independent variables. If used directly, ANEOS generates density and temperature as independent variables. Thus, instead of calculating the specific internal energy from the analytical equation of state for each node, it is typically more computationally expedient to use ANEOS to generate a tabulated equation of state in terms of density and specific internal energy, which can then be directly used by iSALE. In this thesis, ANEOS was used to generate tabulated equations of state for the materials; granite, calcite, and dunite, based on parameters described in Pierazzo et al. (1997). These materials were chosen to respectively correspond to continental crustal rocks, limestone sedimentary rocks, and peridotitic mantle rocks.

3.2.2.2 Constitutive Models

The equation of state is most critical during the early stages of cratering, when material strength is negligible compared to the stresses in the shock wave. Later in

the impact process, when pressures have dropped, material strength becomes critically important. The constitutive model describes the response of a material to deviatoric stresses. The stress at which a material fails is a function of confining pressure, damage, temperature, and strain rate (equation 3.5). In this thesis, the effect of strain rate is neglected because, for the craters simulated in this thesis, strain rates never exceed 1 s^{-1} , the strain rate above which rocks tend to exhibit dynamic strength effects (e.g. Zwiessler et al., 2017).

Static Strength Model — The strength of an intact rock (Y_i) can be simply defined by a Lundborg strength envelope (Lundborg, 1968):

$$Y_i = Y_0 + \frac{\mu_i P}{1 + \mu_i P/(Y_m - Y_0)} , \quad (3.9)$$

where Y_0 is the cohesion of the material, μ_i is the intact coefficient of internal friction, and Y_m is the limiting strength at high pressure.

The strength of a fully damaged rock (Y_d) can be simply defined by a Drucker-Prager strength envelope (Drucker and Prager, 1952):

$$Y_d = \min(Y_{d0} + \mu_d P, Y_{dm}) , \quad (3.10)$$

where Y_{d0} is the cohesion of fully damaged material, μ_d is the damaged coefficient of internal friction, and Y_{dm} is the limiting strength at high pressure.

These two strength profiles can be combined together to provide a model of cold rock strength (Y_c) that depends on the amount of damage, D , that a rock possesses:

$$Y_c = \min(Y_d D + Y_i(1 - D), Y_i) , \quad (3.11)$$

where D can vary from 0 to 1, where 0 indicates an undamaged material and 1 indicates a fully damaged material. In the simulations presented in this thesis, the damage model of Ivanov et al. (2010) was used. In this model, damage is a function of plastic strain:

$$D = \min\left(\frac{\varepsilon_p}{\varepsilon_f}, 1\right) , \quad (3.12)$$

where ε_p is an invariant measure of the accumulated plastic strain and ε_f is the plastic strain at failure, which is defined as a function of pressure:

$$\varepsilon_f = \max(\varepsilon_{fb}, B(P - P_c)) , \quad (3.13)$$

where ε_{fb} is the minimum failure strain, B is a positive constant, and P_c is the pressure above which failure is compressional.

In addition to confining pressure and damage affecting shear strength, temperature plays an important role. As a material approaches its melting temperature, its shear strength rapidly decreases. This behaviour can be described by the simple relationship (after Ohnaka, 1995):

$$Y = Y_c \tanh \left(\xi \left(\frac{T_m}{T} - 1 \right) \right), \quad (3.14)$$

where Y is the yield strength of the material, Y_c is the cold yield strength, T is the temperature, ξ is a constant, and T_m is the melting temperature. The melting temperature of a material is known to vary as a function of pressure. iSALE uses the Simon approximation to define the melting temperature, T_m :

$$T_m = T_{m0} \left(\frac{P}{a} + 1 \right)^{1/c}, \quad (3.15)$$

where T_{m0} is the melting temperature at zero pressure, and a and c are constants that vary depending on the modelled material.

Transient Weakening — The static constitutive model described above is supplemented in iSALE by the block model of acoustic fluidisation, a transient weakening model, such that gravitational collapse of the transient cavity is facilitated (Melosh, 1989; Melosh and Ivanov, 1999). Acoustic fluidisation supposes that short-wavelength elastic waves, produced by either the passage of the shock wave or subsequent deformation, cause temporary fluctuations of overburden pressure in the deforming material such that, at some moments in time, shear failure occurs (see Section 2.2). The temporally-and spatially-averaged effect of these pressure oscillations is that the rock-mass behaves as a viscous fluid.

Before describing the block model of acoustic fluidisation, it is necessary to describe the full model of acoustic fluidisation (Collins and Melosh, 2003; Melosh, 1996, 1979). The yield strength of an acoustically fluidised material, Y_{vib} , is given by:

$$Y_{vib} = \eta_{eff} \dot{\varepsilon}, \quad (3.16)$$

where η_{eff} , the effective viscosity, is given by:

$$\eta_{eff} = \frac{\rho \lambda C_L}{2\psi} \frac{1 + erf(\chi)}{1 - erf(\chi)}, \quad (3.17)$$

where λ is the dominant wavelength of acoustic vibrations, ψ is the square of the ratio between the longitudinal- and shear-wave speeds. χ is defined as:

$$\chi = \frac{s_c}{\sigma} , \quad (3.18)$$

where s_c is the critical vibrational pressure for failure to occur, and σ is the variance of the vibrational pressure, P_{vib} . Assuming that the pressure oscillations in the material behave as gaussian noise:

$$\sigma = C_L \rho v_{vib} , \quad (3.19)$$

where v_{vib} is the vibrational velocity. The vibrational velocity is related to P_{vib} , and the vibrational energy density, E_{vib} by the equations:

$$P_{vib} = \rho C_B v_{vib} , \quad (3.20)$$

$$E_{vib} = \frac{1}{2} v_{vib}^2 . \quad (3.21)$$

The temporal evolution of E_{vib} is crucial to the process of acoustic fluidisation. It is described by the non-linear, ordinary differential equation:

$$\frac{dE_{vib}}{dt} = \frac{\xi}{4} \nabla^2 E_{vib} - \frac{C_L}{\lambda Q} E_{vib} + e \tau_{ij} \dot{\varepsilon}_{ij} , \quad (3.22)$$

where ξ is the scattering diffusivity, Q is the quality factor of acoustic dissipation, e is a parameter that defines the efficiency of acoustic regeneration, and τ_{ij} is the shear stress.

The first term on the right-hand side of equation 3.22 describes the scattering of acoustic energy. The second term describes the attenuation of acoustic energy by conversion to heat. The final term acts to generate acoustic energy in regions with large stresses and strain rates, which will occur during shock and from the deformation of rocks during excavation and modification. The primary input parameters of the full model of acoustic fluidisation are: ξ , λ , Q , and e . None of these parameters are easily known without direct observation of the fluidised material.

The block model of acoustic fluidisation (Ivanov and Kostuchenko, 1997) is a simplification of the full model of acoustic fluidisation (Melosh, 1979). The block model is an attempt to reconcile direct, and measureable, geological observations of the structural uplifts of complex craters to the parameters of numerical models, motivated by observations of the Puchezh-Katunki deep drill core (Ivanov et al., 1996), where discrete rock blocks were observed to be separated by inter-block breccias. The yield

strength of material in the block model, Y_{eff} , possesses an additional term to the full model of acoustic fluidisation (equation 3.16):

$$Y_{eff} = \mu(P - P_{vib}) + \eta\dot{\varepsilon}, \quad (3.23)$$

where η , the effective viscosity, is a direct input parameter, rather than a function of the acoustic energy field. The block model makes an additional simplification to the acoustic energy evolution (equation 3.22), whereby the first and last terms are ignored:

$$\frac{dE_{vib}}{dt} = -T_{dec} E_{vib}, \quad (3.24)$$

where T_{dec} is the decay time of acoustic oscillations, which is likely to be a function of the size of the blocks (wavelength of acoustic waves) and the quality factor of acoustic waves. T_{dec} is another direct input parameter.

The simplifications made by the block model of acoustic fluidisation mean that the acoustic energy field that facilitates transient weakening must be initialised. In iSALE, the initialisation of the acoustic energy field is manually restricted to the earliest stages of cratering; from the initialisation of the model until after the passage of the shock wave but before the end of the excavation stage. During this interval of time, material is assigned a vibrational velocity as a defined fraction of the velocity of the material, this vibrational velocity is limited to a specified upper value.

Thus, the block-oscillation model produces a rheology with a time-dependent yield strength and a constant effective viscosity, η ; i.e., a time-varying Bingham fluid rheology. As time evolves, the strength of the fluidised material increases as vibrational energy decays exponentially, with decay time constant T_{dec} . Several impact modelling studies (Baker et al., 2016; Collins, 2014; Wünnemann and Ivanov, 2003) have shown that the size-morphology progression of craters on Earth and the Moon is well reproduced by assuming a linear proportionality between impactor size and both η and T_{dec} . Following the definitions of Wünnemann and Ivanov (2003), we adopt:

$$\eta = \gamma_\eta C_B r \rho, \quad (3.25)$$

$$T_{dec} = \gamma_T \frac{r}{c_s}, \quad (3.26)$$

where C_B is the bulk sound speed, r is the impactor radius, and ρ is the material density. γ_η and γ_T are dimensionless scaling constants.

Effective viscosity and decay time can be converted to block size, h , and quality factor for acoustic attenuation, Q , under several assumptions. In one approxi-

mation, harmonic motion of blocks is assumed, where the oscillation period is controlled by the compressibility and thickness of the interblock matrix relative to the blocks and is proportional to block size (Ivanov and Artemieva, 2002). In this case, both effective viscosity and decay time are proportional to block size h and the quality factor Q is proportional to the ratio η/T_{dec} . The validity of this scaling requires the time taken for sound to cross a block to be shorter than the period of the block oscillation; that is, compared to the blocks, the breccia must be significantly thick ($\sim 10\%$ of the block size) and compressible ($\sim 2 \times$ that of the block).

3.2.2.3 Porosity and Dilatancy

Dilatancy is the volume change observed in granular and rocky materials when they are subjected to shear deformations. The dilatancy model in iSALE is described by Collins (2014). In iSALE, the equation used to calculate the rate of porosity change in cells undergoing shear deformation is:

$$\frac{d\alpha}{dt} = \frac{d\alpha}{d\epsilon_v} \times \frac{d\epsilon_v}{d\gamma_p} \times \frac{d\gamma_p}{dt}, \quad (3.27)$$

where α is the distension, which is defined as the ratio of the grain density to the bulk density $\frac{\rho_s}{\rho}$ (and can be defined as a function of porosity, $\frac{1}{1-\phi}$), ϵ_v is the natural volumetric strain, which is defined as the natural logarithm of the ratio between the initial volume and final volume, $\ln(V_0/V)$, γ_p is the plastic shear strain, and t is time.

The first term of Equation 3.27 relates the dilation to a change in distension, it can be defined by considering the idealised case of a dilatant material that experiences shear deformation at isobaric conditions; i.e. where the grain density, ρ_s , remains constant. From the definitions of distension and volume strain, it follows that $\frac{d\alpha}{d\epsilon_v} = \rho_s/\rho = \alpha$. The final term of Equation 3.27 is the plastic shear strain rate, this value is determined based on velocity gradients in the cell. The second, and most important term in Equation 3.27 is known as the dilatancy coefficient, β , which describes the material's tendency to gain volume upon plastic shear strain; and is a function of pressure, temperature, and the pre-existing distension of the material:

$$\beta = \beta_{max} \left(\frac{\alpha_c - \alpha}{\alpha_c - \alpha_{min}} \right) \left(1 - \frac{\log(p/10^5)}{\log(p_{lim}/10^5)} \tanh \left(\xi \left(\frac{T}{T_m} - 1 \right) \right) \right), \quad (3.28)$$

β_{max} is a material specific value, where large values indicate a strong tendency to dilate upon shear deformation. For impact cratering simulations, and large-scale numerical simulations of rock masses, Collins (2014) suggests that β_{max} values range between 0.045–0.18, where $\beta_{max} = 0.045$ provides the best fit to the gravity and porosity data of

simple craters and small complex craters. Here, that value is used to test its applicability to larger complex craters.

Predicting the Gravity Signature of Modelled Craters — Dilatancy of rocks plays an important factor in determining the gravity signature of a crater. Here, Bouguer gravity profiles of simulated craters will be presented. Calculating the predicted gravity signature of a crater requires 4 major considerations:

1. The mass deficit due to dilatancy.
2. The removal of material due to erosion.
3. The mass deficit due to sediment or water infill.
4. The application of a Bouguer correction.

The mass deficit due to dilatancy is calculated by determining a density difference between the dilated final material and the original undeformed material. The effect of erosion is accounted for in the gravity calculation by peneplaning the target to a certain depth; this removes all the mass above the peneplane from the gravity calculation. The remaining topography can then be infilled, to a specified depth, by a material of a given density, this material contributes to the calculated gravity signature by determining the density difference between the infill material and the Bouguer density. Finally, a Bouguer correction must be applied to account for any remaining topography; removing the affect of any material above the specified planar surface by removing the expected signature of that amount of material with the specified Bouguer density, and adding the affect of any lack of material beneath the specified planar surface by adding the expected signature of that amount of material with the specified Bouguer density. Additionally, the altitude at which the Bouguer profile is obtained affects the wavelength of the signal; greater altitude leads to a longer wavelength gravity profile. High density impact melt rocks are accounted for in this calculation because materials approaching or above their melting temperature have suppressed dilatancy. However, due to the simplifications of the model, vertical changes in crustal composition, and therefore density, are not accounted for.

Part II

The Clearwater Lake Impact Structures

4 Introduction to the Clearwater Lake Impact Structures

Located in northern Quebec, Canada (Figure 4.1), Clearwater Lake is composed of two broadly circular lobes; each lobe is a distinct impact structure. The structures were first suggested as a pair of impact craters by Beals et al. (1956). Subsequent work through the 1960s debated an impact or volcanic origin for the structures (Bostock, 1969; Dence, 1964, 1965; Dence et al., 1965; Kranck and Sinclair, 1963), and during this time two drill cores from East Clearwater Lake and five drill cores from West Clearwater Lake were recovered by the Dominion Observatory, Ottawa (subsequently incorporated into the Department of Energy, Mines and Resources, later into the Geological Survey of Canada (GSC), and now part of Natural Resources Canada). Concurrently, PDFs were beginning to be recognised as unique shock metamorphism indicators and were observed in breccias at West Clearwater Lake (Engelhardt et al., 1968), proving an impact origin of the structure. Further fieldwork and petrologic studies (Hische, 1994; Phinney et al., 1978; Simonds et al., 1978) confirmed an impact origin of both structures. The geology and history of study of the Clearwater Lake impact structures are comprehensively reviewed by Grieve (2006).

The larger structure, West Clearwater Lake, has an apparent diameter of 32 km, while the smaller structure, East Clearwater Lake, has an apparent diameter of 24 km (Grieve, 2006). West Clearwater Lake has a conspicuous island ring 6–11 km from the centre of the structure, as well as several small islands, no larger than 100 m in length, located in the centre of the structure. West Clearwater Lake has a shallow bathymetry, rarely exceeding 100 m in depth. West Clearwater Lake has generally been considered to be a peak-ring impact structure (Grieve, 2006).

All five of the drill cores from the West Clearwater Lake impact structure were recovered from within the island ring. Core 1-63 was recovered close to the crater centre while cores 5-63, 4a-63, and 4-63 were located close to the island ring and somewhat east of the crater centre. Core 3-63 was recovered at a location directly between Hole 1-63 and Holes 5-63, 4a-63, and 4-63. Holes 4a-63 and 4-63 were drilled in approximately the same location after Hole 4a-63 was aborted due to drilling problems. Hole 1-63 began recovering core at 20 m (62 ft) below lake level and reached a depth of 397.3 m (1307 ft) below lake level, recovering a sequence of deformed para-autochthonous gran-

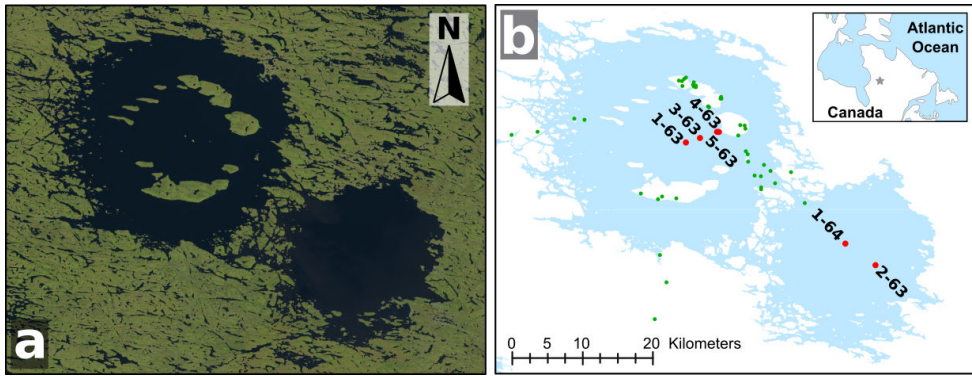


Figure 4.1: Map of Clearwater Lake, and the locations of drill cores and field samples, a) Satellite image of Clearwater Lake taken by Landsat (Image Source: Landsat Operational Land Imager/ USGS). b) Outline map of Clearwater Lake. Red circles indicate the location of recovered drill cores, small green circles indicate the location of the field samples used in this thesis (Data source: CDED, GeoBase Canada). Modified from Rae et al. (2017a).

ites, gneisses, and amphibolites. Hole 3-63 began recovering core at 7 m (25 ft) below lake level and reached a depth of 394.3 m (1297 ft) below lake level, similarly recovering a sequence of deformed para-autochthonous granites, gneisses, and amphibolites. Core 4-63 began recovering core at 42 m (137 ft) below lake level and reached a depth of 119.2 m (392 ft) below lake level, recovering a sequence of impact melt rocks containing large blocks of crystalline basement down to 61 m (200 ft) depth before transitioning to crystalline basement rocks composed of granites, gneisses, and amphibolites. Core 4a-63 began recovering core at 43 m (140 ft) below lake level and reached a depth of 64.4 m (212 ft) below lake level, recovering a sequence of impact melt rocks containing blocks of crystalline basement. Core 5-63 began recovering core at 29 m (94.5 ft) below lake level and reached a depth of 219.5 m (722 ft) below lake level, recovering a sequence of deformed para-autochthonous granites, gneisses, and amphibolites, with a small amount of impact melt rock within the top 10 m of the core top (Dence et al., 1965; Hische, 1994).

By contrast, East Clearwater Lake contains no islands close to its centre, and the lake is considerably deeper than its younger counterpart, occasionally exceeding 160 m in depth (Grieve, 2006). East Clearwater Lake is generally considered to be a central peak crater; this assessment is principally based on the two drill cores recovered from the structure.

Hole 1-64 is centrally located (Figure 4.1), reached a depth of 1006.8 m (3312 ft) below lake level, and, after penetrating 120 m of water and 12 m of glacial drift, recovered 2 m of post-impact sedimentary rocks on top of a sequence of shocked target rocks that continue, uninterrupted, to the bottom of the hole. Despite the extra-ordinary

length of Hole 1-64, only basic lithological descriptions have been published within scientific literature (Dence, 1965) and a more detailed logging and petrographic description within the PhD thesis of Hische (1994). Reported evidence of shock metamorphism within Hole 1-64 consists of partially diaplectic quartz, PDFs in quartz, mechanical twins in pyroxenes, kink banding in biotite, mosaicism, and fracturing of minerals (Hische, 1994). By contrast, Hole 2-63 is more radially distant than Hole 1-64 (Figure 4.1), and reached a total length of 300 m (900 ft). The hole deviated significantly from a vertical orientation during drilling, resulting in an angle of 30° from vertical by the bottom of the hole. Consequently the final length of recovered core is somewhat longer than the final depth reached, which is uncertain. Hole 2-63 recovered a thicker (112 m) sequence of post-impact sedimentary rocks and subsequently recovered clast-bearing impact melt rocks to the bottom of the hole (Dence, 1965; Grieve, 2006). The impact melt rocks in Hole 2-63 have been shown to contain a considerable quantity of chondritic meteorite component. By contrast, West Clearwater Lake impact melt rocks have no discernible traces of a meteoritic component (Grieve, 1978; Palme et al., 1978). Additional support for a central uplift within the East Clearwater structure derives from its gravity signature, which, whilst circular, bowl-shaped, and without a central high, is less negative (~ -9 mGal), than would be expected from an extrapolation from simple craters (Dence et al., 1965; Plante et al., 1990).

Dence et al. (1965) suggested that the East and West Clearwater Lake structures formed by the impact of a binary asteroid: this hypothesis was initially supported by Rb-Sr dating (Reimold et al., 1981), suggesting an impact 285–300 Ma ago. However, high-precision $^{40}\text{Ar}/^{39}\text{Ar}$ dating (Schmieder et al., 2015), supported by (U-Th)/He dating (Biren et al., 2016), has indicated that East Clearwater Lake is 460–470 Ma old (Ordovician) and that West Clearwater Lake is 286.2 ± 2.2 Ma old (Permian).

The target rocks of the Clearwater Lake impact structures were amphibolite-to granulite-facies metamorphosed granites, granodiorites, tonalites, and felsic gneisses, with local mafic amphibolites belonging to the 2.6–2.8 Ga Archean Bienville sub-province of the Superior Province of the Canadian Shield. A thin, possibly non-continuous, veneer of Ordovician limestone, subsequently eroded away from the local area, overlay the basement rocks at the time of the West Clearwater Lake impact. The presence of this unit in the target of the East Clearwater Lake structure is presumed, but has not been directly observed (Grieve, 2006). There are no specific estimates of the amount of erosion that Clearwater Lake has experienced since the time of either impact.

Impactites within the Clearwater Lake impact structures include: shocked crystalline basement, lithic breccias (Dence, 1964; Engelhardt et al., 1968), impact-melt bearing breccias, and the lower part of two coherent impact-melt sheets (Hische, 1994; Phinney et al., 1978; Rosa, 2004, 2011; Simonds et al., 1978). Estimates of the original melt volume at West Clearwater Lake range from 68–100 km³ (Grieve et al., 1976;

Phinney and Simonds, 1977); there are no estimates of the impact melt volume at East Clearwater.

5 Constraining the Parameters of Transient Weakening during Crater Collapse using Observations of Shock Metamorphism and Deformation: The West Clearwater Lake Impact Structure

5.1 Introduction

Constraining exactly which mechanism facilitates the transient weakening of rocks during crater collapse is extremely challenging. It is somewhat simpler to constrain the kinematic result that the mechanism produces, i.e. the rheological behaviour of rocks during modification. Methods to achieve this may include structural, stratigraphic, petrographic, petrological, geochemical, and/or geochronological observations. In this chapter, I will demonstrate how petrographically-constrained shock metamorphism, primarily, can be used as a quantitative constraint of the rheology of rocks during collapse. Conceptually, this method of constraining collapse has been used before (Dence et al., 1977; Dence, 2004; Robertson, 1975; Robertson and Grieve, 1977). Here though, more realistic numerical models, as opposed to conceptual and/or geometric models, will be used. Constraining the rheology of collapse can be used to assess the applicability of transient weakening mechanisms.

In this chapter, the West Clearwater Lake impact structure, Canada, will be used as an example of this method, where the results of numerical models are compared with geological observations; in particular, shock barometry, core logging, and field observations, with the aim of constraining the model parameters describing acoustic fluidisation and, hence, the kinematics and dynamics of complex crater formation.

5.2 Methods

5.2.1 Samples

Sixty samples of exposed bedrock were recovered from the West Clearwater Lake structure during a field campaign in the summer of 2014 (Table C.6). For this study, only basement rocks were sampled. The sampled lithologies represent granites,

granodiorites and tonalites, and occasional mafic amphibolites. In hand-specimen, the felsic samples are medium to very coarse-grained, are grey to reddish-grey in colour, and can be quite friable. Samples were recovered from localities interpreted to be para-autochthonous spread across the structure, although in some areas it was challenging to determine whether the outcropping basement material was part of an allochthonous megablock within the impact-melt sheet or part of the para-autochthon. The occurrence of shatter cones was noted around the structure.

In addition, five recovered drill cores from West Clearwater Lake were logged. These drill cores were recovered in the winter of 1963 by the Dominion Observatory and are now housed at the Natural Resources Canada core facility in Ottawa. The locations of the cores are indicated on Figure 4.1. Samples were used from cores 1-63, 3-63, and 5-63 for shock analysis; cores 4-63 and 4a-63 did not drill deep enough to sample a significant amount of para-autochthonous lithologies.

5.2.2 Shock Barometry

In total, 149 thin sections of para-autochthonous lithologies were petrographically analysed. Of these, 60 thin sections derived from the field samples and 89 thin sections derived from the drill cores. 47 field thin sections and 70 drill core thin sections contained quartz and were studied with respect to characterising PDFs in quartz. The thin sections were first characterised based on mineral assemblage and searched for shock metamorphic features with an optical microscope. Subsequently, the thin sections containing shocked quartz were investigated using a universal stage to obtain PDF orientations, and consequently estimate the peak shock pressures experienced by the samples.

5.2.3 Numerical Modelling

Models of the West Clearwater Lake impact event were carried out using the iSALE shock physics code with the aim of investigating the effect of acoustic fluidisation parameters on shock pressure distribution. Consequently, all impact model parameters, other than acoustic fluidisation parameters, were kept constant between different simulations. The target consists of crystalline granitic basement; assuming that the sedimentary cover at the time of impact was negligible. As there is no indication of the impactor composition at West Clearwater Lake, a granitic impactor was used for computational efficiency and because the density of granite is representative of stony meteorites. The impactor velocity in all simulations was fixed at 15 km s^{-1} (see Chapter 3). A nominal impactor diameter of 3 km was chosen, such that a structure of approximately the correct proportions was formed, and that models with different acoustic fluidisation parameters were directly comparable. The impactor parameters and acous-

tic fluidisation parameters trade-off against each other to produce a crater of a specific size, creating uncertainty in the final acoustic fluidisation parameters. Furthermore, the symmetry of the shock pressure distribution would be affected by a non-vertical impact. Nonetheless, for a reasonable range of impactor parameters, at fixed acoustic fluidisation parameters, the process of crater collapse is qualitatively identical, although the final crater size varies. The important parameters for the models are included in Table 5.1, and a full list of parameters may be found in Appendix B.

Here, the thermodynamic behaviour of the materials in the simulation are modelled using granite parameters described in Pierazzo et al. (1997) for the ANEOS program.

The strength parameters used for the granitic crystalline basement in these simulations were based on those used in previous models (e.g., Wünnemann et al., 2005). The parameters of the constitutive model between all simulations were fixed, as varying these parameters would change the distribution and magnitude of damage. As acoustic fluidisation only occurs where material is damaged, this would affect where acoustic fluidisation is able to reduce strength. As such, there is a small trade-off between these parameters and acoustic fluidisation parameters, γ_η and γ_T , which were varied between simulations.

5.3 Results

5.3.1 Observations

5.3.1.1 Macroscopic

Fieldwork in summer 2014 demonstrated that the stratigraphy preserved at West Clearwater Lake consists of (a) fractured basement, (b) monomict lithic breccia, (c) impact-melt-bearing lithic breccia, (d) clast-rich fine-grained impact-melt rock, (e) clast-poor fine-grained impact-melt rock, and (f) clast-poor medium-grained impact-melt rock (Osinski et al., 2015), similar to the identified stratigraphies of Bostock (1969) and Simonds et al. (1978). Structural mapping of these lithologies indicates that the para-autochthonous-allochthonous contact, between the fractured basement and overlying units, is located at, or near, the lake surface around the ring structure. Most of the verifiably para-autochthonous basement material is located on shoreline exposures, while occasional outcrops inland either reflect a rugged basement topography or are actually allochthonous mega-blocks. The island ring has ~ 100 m of topography (relative to the lake surface) and, at the present level of exposure, is composed largely of impact-melt rocks and some impact breccias.

The small islands located in the centre of the structure (Figure 4.1b) are

Table 5.1: West Clearwater Lake *iSALE* parameters — a full list of parameters may be found in Appendix B.

Symbol	Definition (unit)	Value
L	Impactor diameter (km)	3.0
v_i	Impact velocity (km s ⁻¹)	15.0
ρ_i	Impactor density (kg m ⁻³)	2630
ρ_t	Target density (kg m ⁻³)	2630
ν	Poisson's ratio	0.3
Y_0	Cohesion (MPa)	10
Y_M	Von Mises plastic limit (MPa)	2500
μ_i	Coefficient of internal friction	2
Y_{d0}	Cohesion of damaged material (MPa)	0.01
μ_{di}	Coefficient of internal friction of damaged material	0.6
T_m	Melting temperature (K)	1673
ξ	Thermal softening parameter	1.2
ε_{fb}	Minimum failure strain for low pressure states	1×10^{-4}
B	Constant of proportionality between failure strain and pressure	1×10^{11}
P_c	Pressure above which failure is compressional (Pa)	3×10^8
C_{vib}	Vibrational particle velocity as a fraction of particle velocity	0.1
$V_{ib,max}$	Maximum vibrational particle velocity (m s ⁻¹)	200
t_{off}	Time after which no new acoustic vibrations are generated (s)	16.0

composed of para-autochthonous, fractured basement. The fractured basement commonly has poorly developed shatter cones (Figure 5.1), from the centre of the structure and beyond the extent of the island ring to \sim 11 km radial distance. On the central islands, the contact with allochthonous lithologies is located somewhere above the present day exposure; that is, all allochthonous lithologies were eroded from the centre of the structure. Furthermore, no impact ejecta was found toward the rim of the structure.

The drill cores confirm that, at the island ring, the para-autochthonous contact is located near to the lake surface (39.7 m below lake surface in core 5-63 and 64.1 m below lake surface in core 4-63), while cores 1-63 and 3-63 show only para-autochthonous rocks. The basement rocks show clear evidence of deformation, in the form of breccias, melt veins, and cataclasites (Figures 5.1 and 5.2). Deformation is, in general, most pervasive in the central drill cores and toward the top of the cores. Individual deformation bands are narrow; melt veins are particularly common, <1 cm wide and, in most cases, have no discernible displacement. Cataclasites are <10 cm wide and vary significantly in maturity, from protocataclasites to ultracataclasites that occasionally contain within them pseudotachylites. Breccias are rare in the drill core, are <50 cm wide, and commonly have melt matrixes. Breccias and melt veins were observed in the field (Wilks and Osinski, 2015) (Figure 5.1); however, exposure of the fractured basement was too limited to map individual blocks. Nonetheless, estimates of block size and matrix thickness can be made based on the drill core logs (Figure 5.2).

Block sizes in the drill cores were estimated by measuring the distance between each separate discontinuity, with the discontinuity being either a cataclasite, melt vein, or breccia. A significant number of discontinuities, particularly the melt veins, have likely seen no displacement, indicating that block sizes would be underestimated. Conversely, deformation zones are under-sampled. There are significant sections of core that have poor or no core recovery; it is likely that the cause of these missing sections of rock is that they contain a greater concentration of deformation zones, which would lead to block size overestimation. Thus, only crude estimates of the block size were possible. Across all the cores, the average block size is 12 m with the largest block \sim 43 m and the smallest block <1 m. The average block size in core 1-63 is \sim 10 m compared to \sim 14 m in cores 3-63 and 5-63.

5.3.1.2 Petrographic Description

The felsic basement rocks contained abundant shock metamorphic features in quartz, particularly PDFs, alongside planar fractures (PFs), and feather features (FFs). Furthermore, kink banding in biotite and occasional PDFs in plagioclase feldspars were observed (Figure 5.3). A complete table of PDF statistics can be found in Appendix C, and is summarised in Table 5.2. Between 0 and 5 PDF sets were observed

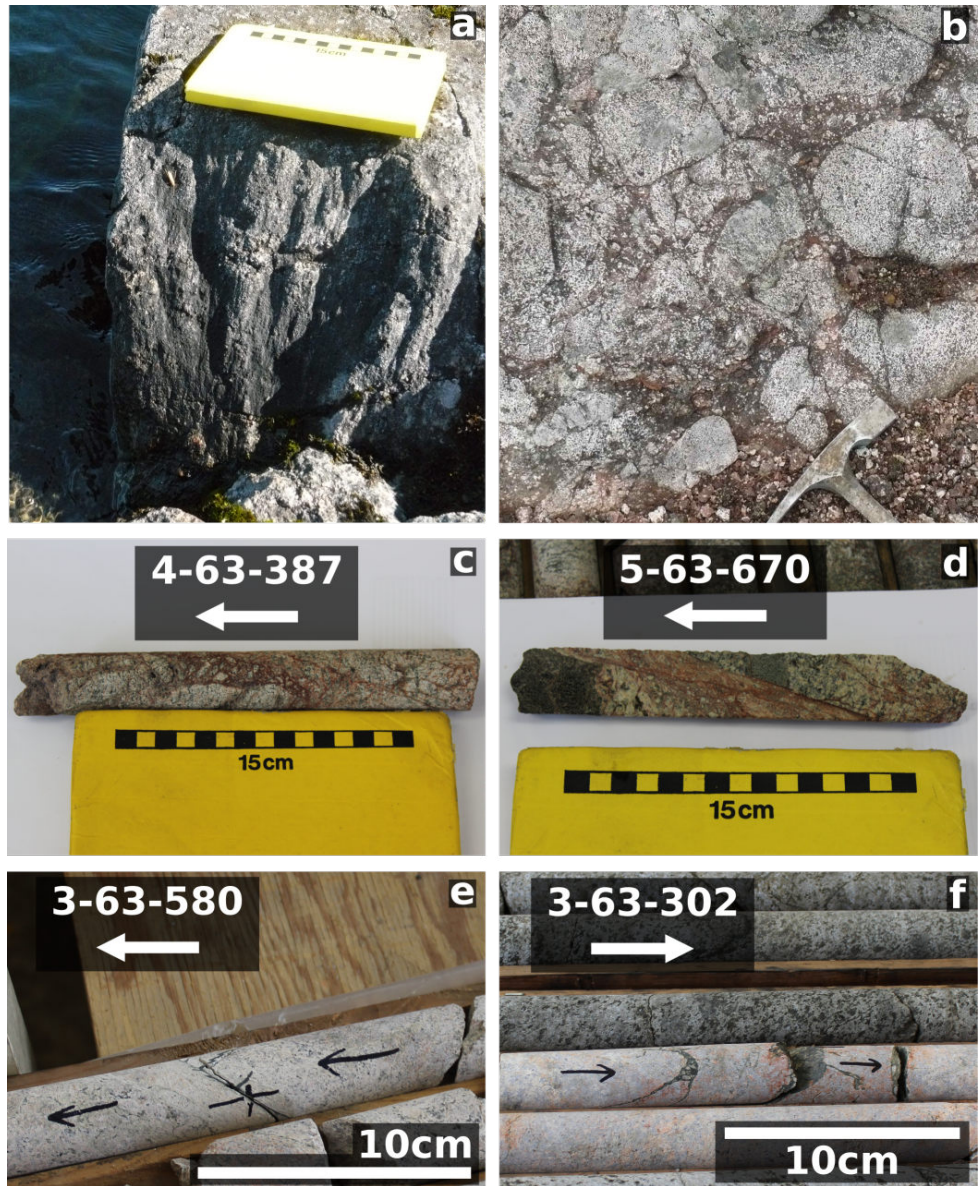


Figure 5.1: Macroscopic products of impact deformation at West Clearwater Lake. a) Shatter cone. b) Breccia dike with melt matrix emplaced into intact crystalline basement. c) Pseudotachylitic impact breccia. d) Cataclastic displacement zone. e) Cataclasite and associated pseudotachylite. f) Solidified impact-melt veins. Arrow indicates the up direction of the drill core, sample names indicate the core followed by the depth in feet from the lake surface.

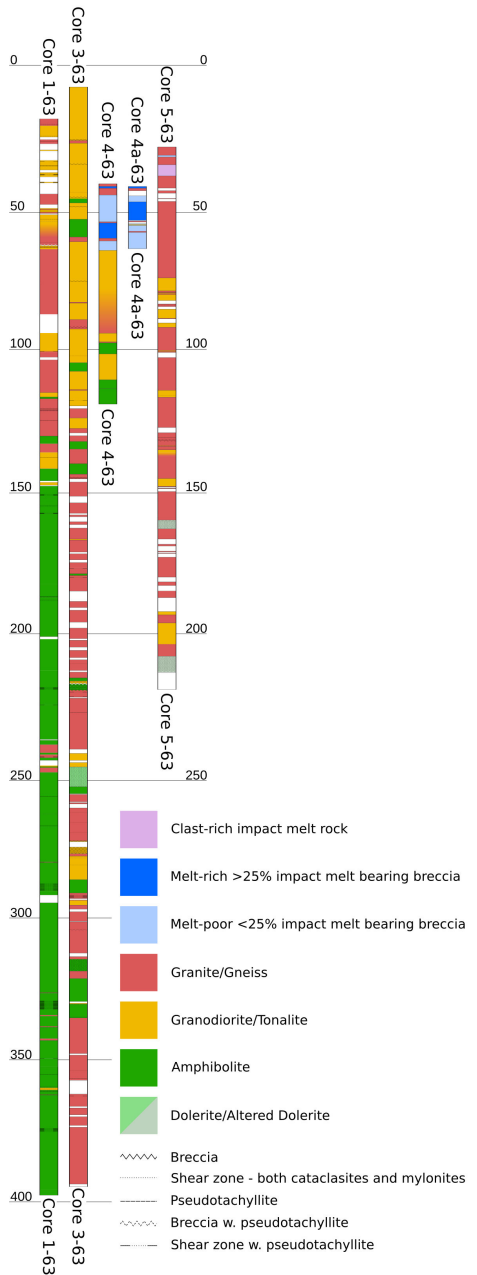


Figure 5.2: Logs of Holes 1-63, 3-63, 4-63, 4a-63, and 5-63 from West Clearwater Lake, describing both lithological and structural features. Depth is indicated in meters below lake surface.

per quartz grain with the average number of PDFs per grain in a sample ranging from 0 to 2.17 (Table 5.2). The PDF sets are generally decorated although some samples show undecorated PDFs. As samples become less shocked, PDFs are less well developed; in particular, poorly shocked samples rarely have PDFs across the entire width of the grain.

In overall abundance, (0001) orientations account for 36.5% of the total measured planes, $\{10\bar{1}4\}$ account for 11.5%, $\{10\bar{1}3\}$ account for 27.1%, $\{10\bar{1}2\}$ account for 4.6%, and the remaining orientations account for the remaining 9.0% (Table 5.2). Approximately 11% of measured planes could not be indexed. This either reflects human error in the original measurements or that there are possible PDF planes not included in the New Stereographic Projection Template (NSPT) (Ferrière et al., 2009).

PFs in quartz occur infrequently as open, and widely (0.1–1 mm) spaced fractures. These PFs were generally, but not exclusively, observed parallel to the (0001) plane. Feather feature lamellae were occasionally observed against planar fractures.

Other impact-related features observed in the samples include melt veins and cataclasites. In many cases, except for ultracataclasites, shocked quartz grains can be identified within the cataclastic zone. Here, PDFs were measured and oriented, although care was taken to avoid remeasuring a PDF orientation in a grain fragment that had already been measured in a different fragment. Shocked quartz was not observed in the melt veins.

Most of the mafic lithologies analysed showed no definitive shock metamorphic effects. Only one section, from the centre of structure, contained a partially diaplectic plagioclase feldspar glass (Figure 5.3e).

5.3.1.3 Shock Barometry

Pressure estimates based on the measured PDF data are shown in Figures 5.4 and 5.5. In general, shock decreases as a function of distance from the centre. Among the surface samples, shock pressures are relatively constant (~ 17.5 GPa) across the centre of the structure until ~ 8 km radial distance, where the number of PDFs drops almost immediately to zero; no PDFs were observed in any samples beyond ~ 8.5 km radial distance. Field observations suggest that the radial extent of shatter cones is 11 km.

These results are consistent with shock pressures estimated from the drill cores where, at the top of each drill core, shock pressure estimates based on the shock metamorphism of quartz are ~ 17.5 GPa. In all drill cores, there is a general trend toward shock pressures decreasing with depth. This is most apparent in core 5-63, located at the greatest radial distance, where no PDFs are observed toward the bottom

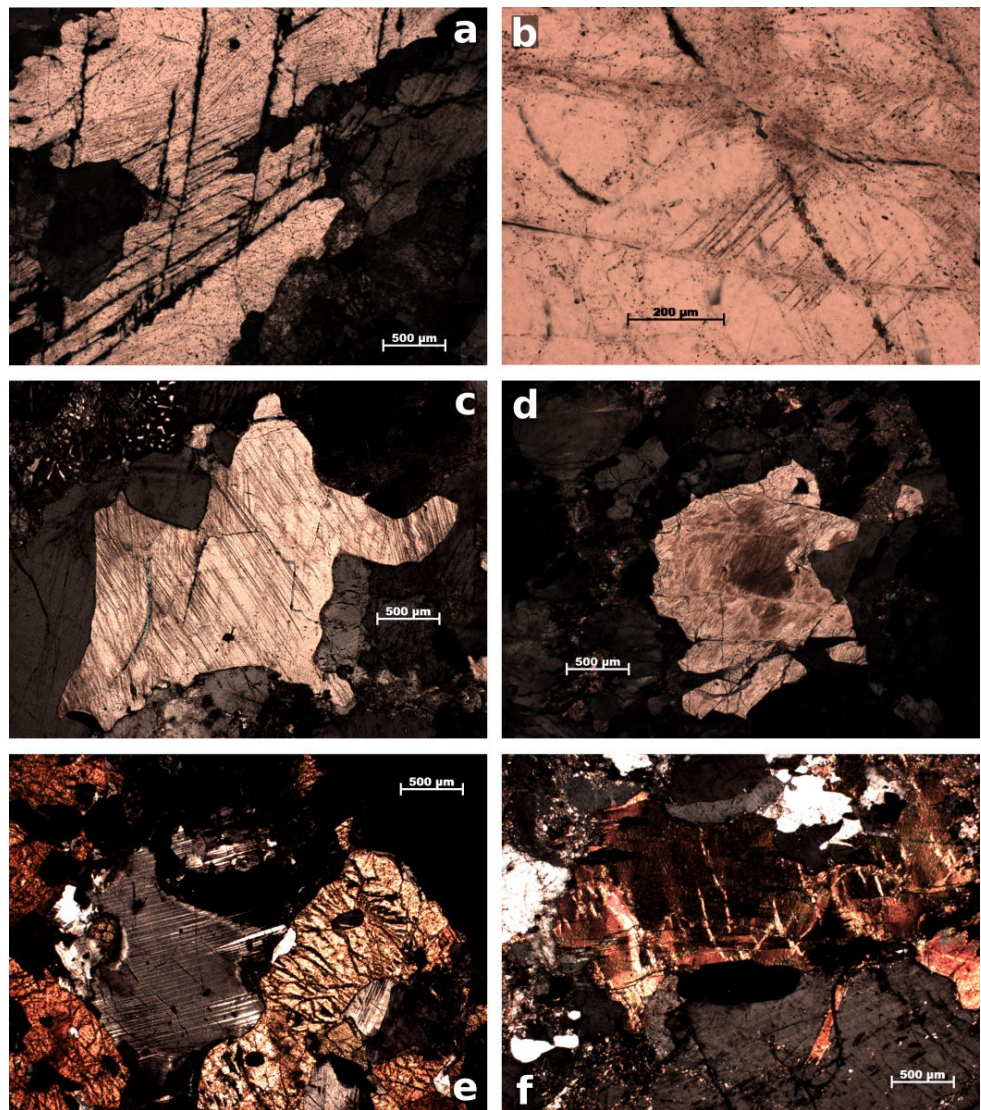


Figure 5.3: Microphotographs under cross-polarised light of shock indicators from West Clearwater Lake a) Two PF sets in quartz (with three PDF sets). b) Feather Features (FFs) in quartz. c) Three sets of PDFs in quartz. d) Toasted quartz with at least two PDF sets. e) Partially diaplectic feldspar glass in mafic basement. f) Kink-banded biotite.

Table 5.2: Summary of PDF statistics from West Clearwater Lake samples.

No. of grains (n)	No. of shocked grains (n*)	No. of measured sets (N)	No. of measured setsa (N*)	Average No. of PDF sets per shocked grain (N*/n*)											
3405	1939	3388	3005	1.55											
				Indexed PDF crystallographic orientations (absolute frequency percent ^a)											
(0001)	{1014}	{1013}	{1012}	{1011}	{1010}	{1122}	{1121}	{2131}	{5161}	{1120}	{2241}	{3141}	{4041}	{5160}	
36.5	11.5	23.1 + 4.0	4.6	1.5	0.2	1.6	0.7	1.0	1.1	0.2	0.7	0.9	0.4	0.4	11.3

^a This is given by the total number of observed PDFs in the specific orientation divided by the total number of measured sets (N), indexed and unindexed.

b This orientation includes all PDFs that were indexed in the overlapping error envelopes of the 1014 orientation and 1013 orientation. The number of PDFs within the envelope is indicated by the additional term.

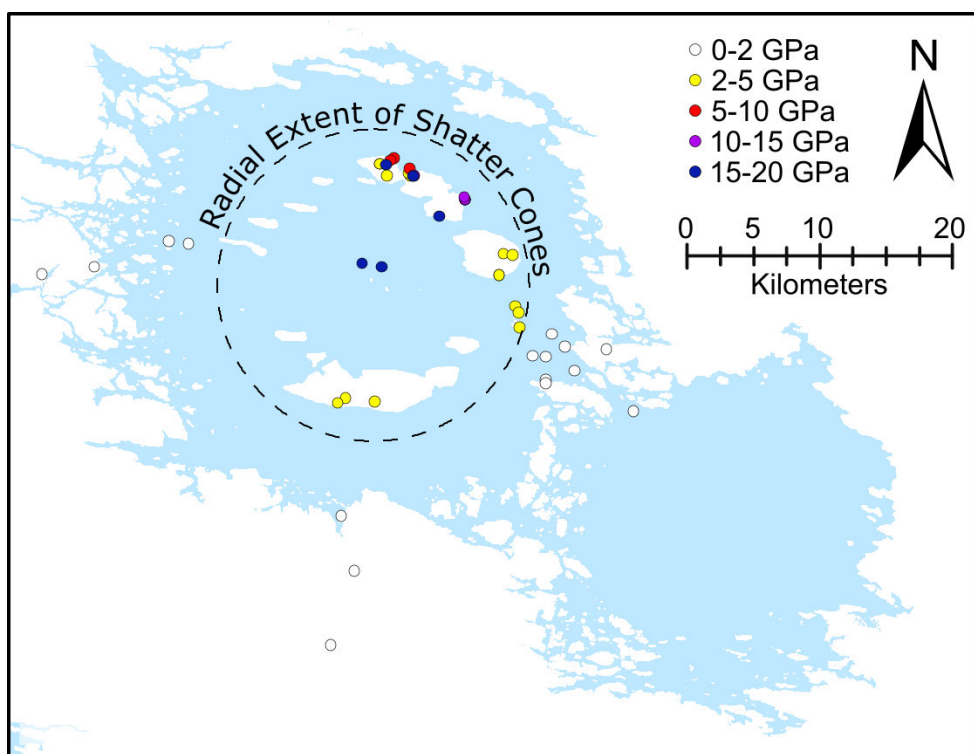


Figure 5.4: Location of quartz-bearing surface samples coloured by estimated shock pressure.

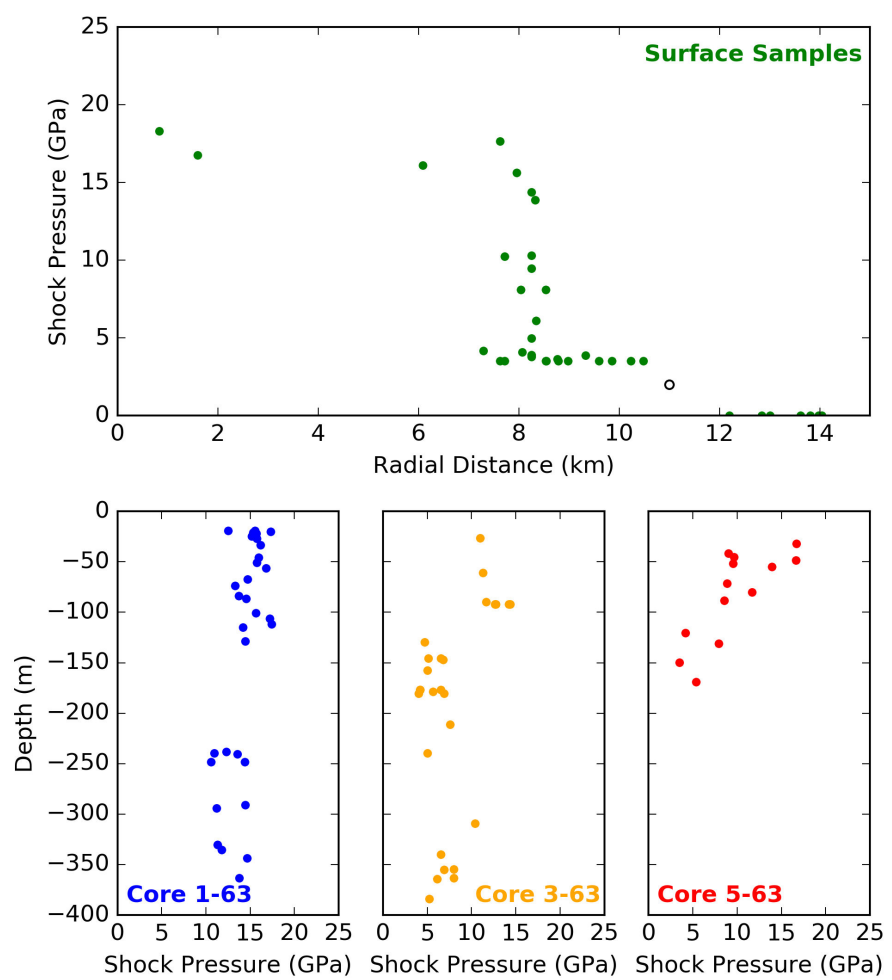


Figure 5.5: Shock distribution at West Clearwater Lake by depth and radial distance in the three drill cores and surface samples.

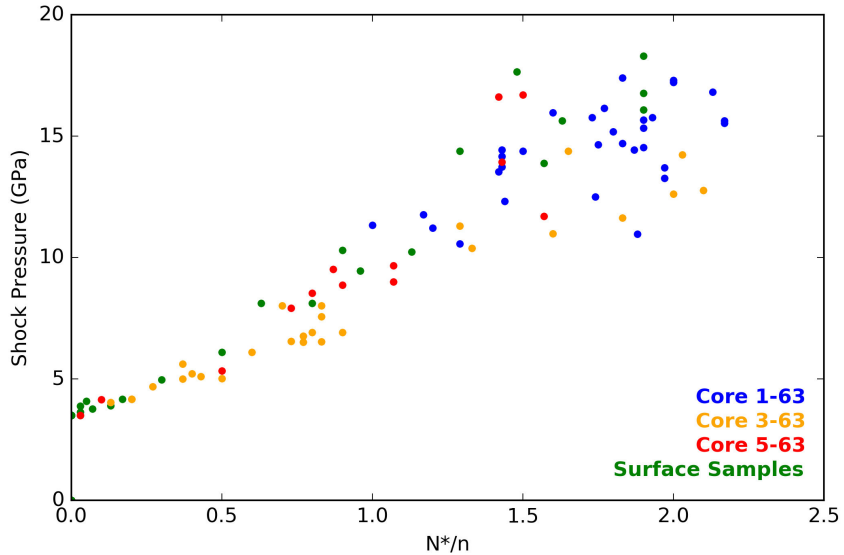


Figure 5.6: Correlation between the number of PDF sets per grain (N^*/n) and the estimated peak shock pressure in samples from West Clearwater Lake.

of the core at >150 m depth. Shock pressure attenuates at the lowest rate in the most central core, 1-63, while shock attenuates at an intermediate rate in core 3-63. The mean standard deviation for all of the pressure estimates is 4.0 GPa (Appendix C).

There is a good correlation between shock pressure and the average number of PDFs per grain (Figure 5.6), confirming that the number of PDFs per grain could be used as a proxy for peak shock pressure (Ferrière et al., 2008).

5.3.2 Numerical Modelling

With all other parameters held constant between models, different effective viscosities, η , and decay times, T_{dec} , were used to model the West Clearwater Lake impact event. After preliminary modelling using values of η from 1×10^8 Pa s to 1×10^{10} Pa s, and values of T_{dec} from 7 to 600 s, it was found that the morphology of the crater could only be matched when $30 \text{ s} < T_{dec} < 120 \text{ s}$. That is, when the decay time is sufficient to allow the material to be weakened long enough to facilitate collapse but is not fluidised to the extent that the structure becomes completely flat. Furthermore, effective viscosities are restricted to 6.25×10^7 Pa s $< \eta < 1 \times 10^9$ Pa s.

Figure 5.7 shows the result of varying η between 1.25×10^8 Pa s and 1×10^9 Pa s, and T_{dec} between 30 and 90 s. Recall that, under the assumption of harmonic block oscillation with a period proportional to the block size, the characteristic block

size, h , is directly proportional to η and the quality factor, Q , is proportional to η/T_{dec} .

The varying of block model parameters leads to systematic variation of crater morphology and structure. The final crater diameter varies from 34 km where $\eta = 1 \times 10^9$ Pa s and $T_{dec} = 30$ s, to 50 km, where $\eta = 1.25 \times 10^8$ Pa s and $T_{dec} = 90$ s. The amount of structural uplift varies from 3 km, where $\eta = 1 \times 10^9$ Pa s and $T_{dec} = 30$ s, to 7 km, where $\eta = 1.25 \times 10^8$ Pa s and $T_{dec} = 90$ s. Structural uplift and final crater diameter increases with decreasing viscosity and increasing decay time.

Simulated drill cores and horizontal slices are constructed through the models (see Figures 5.8 and 5.9) to allow comparison with the measured peak shock pressures. The present-day level of erosion and the contact between the allochthon and para-autochthon have been selected on the basis of the topography of the crater, the position of impact-melt rocks, and the variability of shock pressure in the simulated cores. From this, the peak shock pressures in the numerical models can be directly compared to the measured peak shock data (Figure 5.10).

5.4 Discussion

Overall, the numerical simulations show significant variation in final crater morphology and shock distribution, when the block-model parameters, effective viscosity (η), and decay time (T_{dec}), are varied. There are several models within a tightly constrained viscosity and decay time range that share similarities with the observed shock distribution. Specifically, those models in Figures 5.7–5.9 where $\eta = 5 \times 10^8$ Pa s and $T_{dec} = 30$ s or 60 s, or where $\eta = 2.5 \times 10^8$ Pa s and $T_{dec} = 60$ s. These models show rapid rates of shock attenuation at greater radial distances, and, in general, show the highest magnitudes of shock pressure in the centre of the structure. The model that best fits the shock data (Figure 5.10), for which $\eta = 5 \times 10^8$ Pa s and $T_{dec} = 30$ s, displays a reasonable fit to the observed morphometry of the structure with a structural uplift of ~ 4 km. Furthermore, these values are broadly consistent with the viscosities and decay times in previous numerical modelling studies (e.g., (Collins et al., 2008a; Collins et al., 2002; Goldin et al., 2006; Wünnemann et al., 2005)).

The best-fit viscosity and decay times are achieved using the non-dimensional parameters, $\gamma_\eta = 0.025$ and $\gamma_T = 100$; these values are consistent within the range of parameter values used in previous studies (Table 5.3). The range of γ_T values used in previous studies varies within a factor of three (115–300); the best-fit value of γ_T lies at the low-end of this range. However, while the best-fit value of γ_η is near the centre of the range used in previous studies (0.008–0.2), that range encompasses two orders of magnitude. Simulations consistent with the observations would not be possible using the extreme values of γ_η in that range; thus, γ_η is restricted to $0.01 < \gamma_\eta < 0.1$, corresponding approximately to viscosities between 1×10^8 Pa s and 1×10^9 Pa s for the West

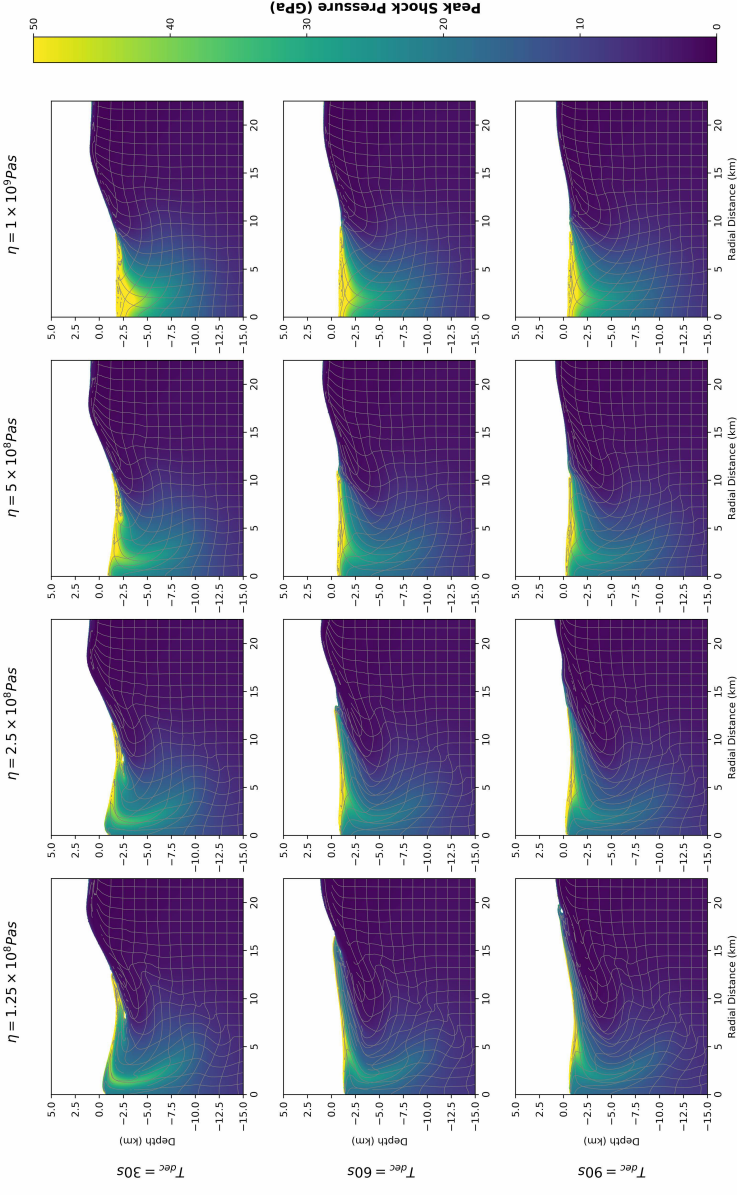


Figure 5.7: The effect of varying acoustic fluidisation parameters on the morphology and shock distribution of the final crater. Models are arranged with effective viscosity, η , increasing from left to right and with decay time, T_{dec} , increasing from top to bottom. Material is coloured by peak shock pressure. The grey grid, with originally uniform spacing and orthogonal lines, shows the sub-crater deformation.

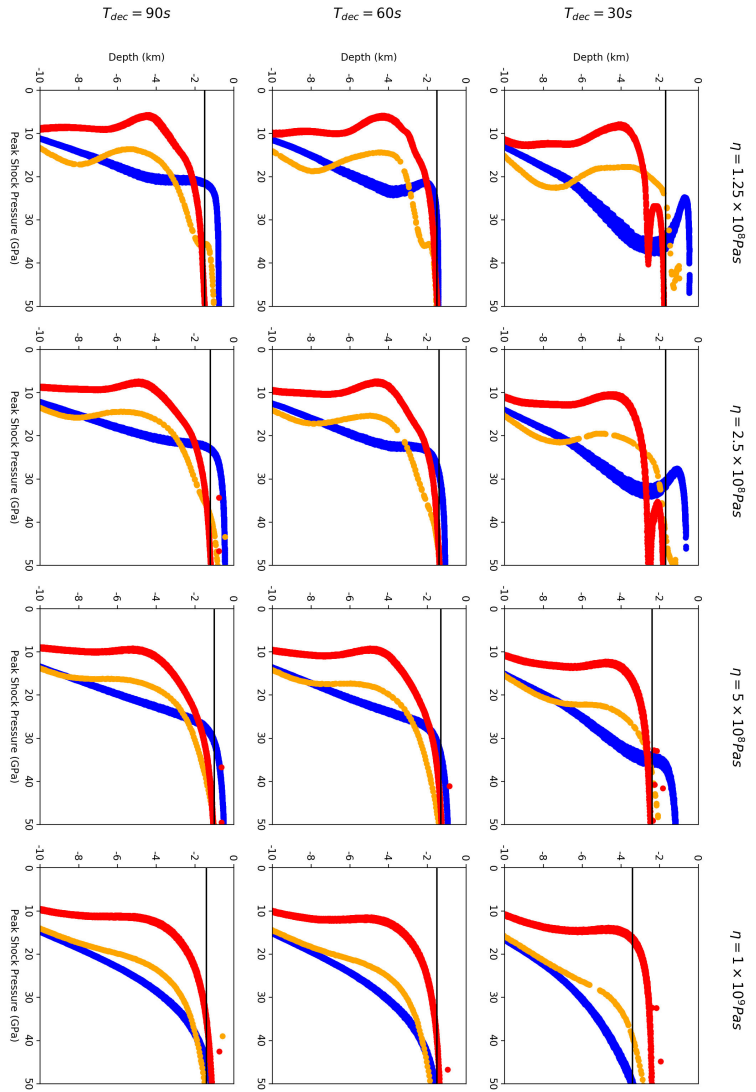


Figure 5.8: Shock pressures in simulated drill cores through the numerical simulations at varying acoustic fluidisation parameters. Blue, orange, and red points correspond in position to cores 1-63, 3-63, and 5-63, respectively. The interpreted position of the para-autochthonous contact in the model is indicated by the horizontal black line (see Figure 5.7).

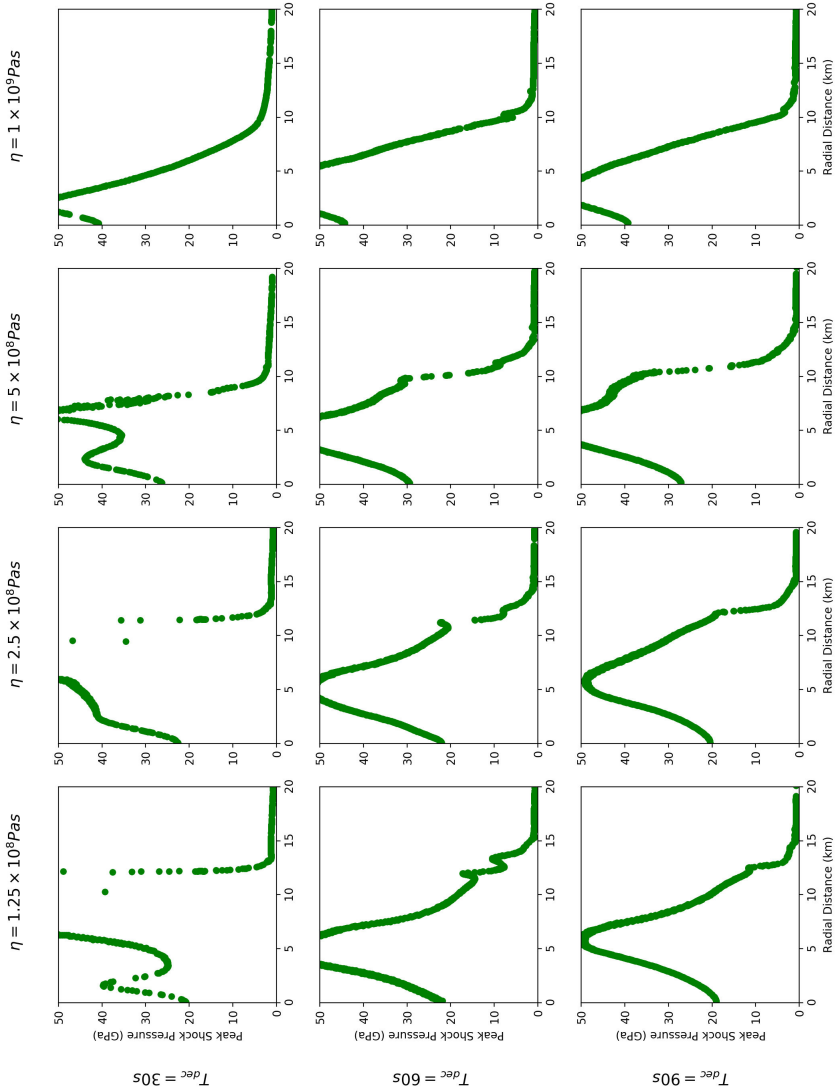


Figure 5.9: Shock pressures in simulated slices through the numerical simulations corresponding to the interpreted depth at the para-autochthonous contact for each model (see Figure 5.7).

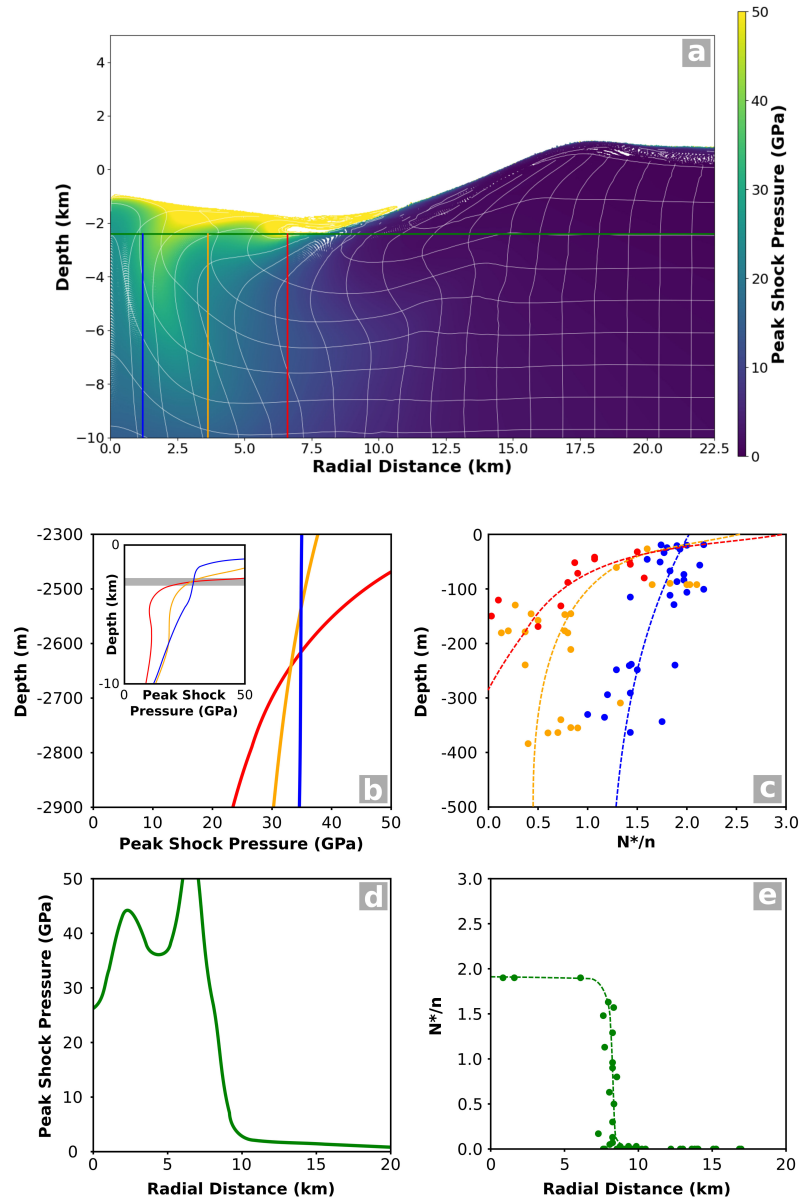


Figure 5.10: a) Best fit numerical model ($\eta = 5 \times 10^8 \text{ Pa s}$ and $T_{dec} = 30 \text{ s}$) coloured by peak shock pressure. Coloured vertical lines at 1 km (blue), 4 km (orange), and 6 km (red) radial distances correspond to simulated drill cores in (b), where peak shock pressure variation is shown with depth. This can be compared to (c), the observed shock attenuation pattern, shown by the average number of PDF sets per grain in a sample. Dashed lines indicate the overall trends of the data. d) A simulated horizontal slice is shown, corresponding to the horizontal line (green) at 2.4 km depth in (a). This can be compared to (e) the shock attenuation pattern in the field samples.

Clearwater Lake structure.

Due to the trade-offs between impactor size and acoustic fluidisation parameters in producing morphometrically similar craters, an absolute match between the recorded and modelled shock data is not expected in the simulations. Nonetheless, the qualitative trends in shock attenuation would be expected to match; as a reflection of the mechanism of crater collapse. In the drill cores, observations suggest that shock attenuates at a very low rate in the centre of the structure while at 6 km radial distance, shock attenuates rapidly with depth, while shock pressures at the top of the cores and in the field samples suggest relatively high and constant shock pressures until ~ 8.5 km radial distance, beyond which, shock attenuates rapidly to zero (Figure 5.5). The general patterns of shock attenuation in the drill cores are matched by the best-fit model, and the simulation also produces a rapid attenuation of shock pressure at radial distances beyond ~ 7.5 km (Figure 5.10).

If, contrary to recent geochronological dating, the West Clearwater Lake structure is part of a binary doublet, the acoustic energy from one impact may have influenced the collapse of the other crater and vice versa. The effect of interfering acoustic energy between two impacts could lead the analysis to slightly overestimate acoustic fluidisation parameters; nonetheless, the kinematics of crater collapse would be no different. Furthermore, the shock attenuation pattern observed at West Clearwater Lake is unlikely to be affected by the East Clearwater Lake impact.

5.4.1 Shock Barometry

There is an offset between the estimated and modelled peak shock pressures of $\sim 10\text{--}20$ GPa and there is considerable difference between the absolute attenuation rates in the observations compared to the numerical simulations. This can be explained in two ways; (1) the numerical simulations may overestimate shock pressures and underestimate attenuation rates in natural rocks, or (2) shock pressure estimates based on PDF orientations in quartz may be inaccurate. The inaccuracy of the shock pressure estimates is likely to be due to a discrepancy between the shock pressures at which specific PDFs develop in quartz in naturally shocked rocks versus quartz in shock recovery experiments.

In this study, the estimated maximum shock pressures of ~ 17.5 GPa are largely due to the lack of diaplectic quartz, or devitrified diaplectic quartz glass, in any of the samples analysed and only one occurrence of partially diaplectic feldspar glass. In the Robertson and Grieve (1977) method used here, the presence of diaplectic quartz allows for shock pressure estimates to be >27.5 GPa (Table 3.1). However, there is a noticeable dearth of diaplectic quartz glasses in para-autochthonous rocks across most impact structures where shock attenuation has been documented; Charlevoix (Robert-

Table 5.3: Comparison of the best-fit acoustic fluidisation parameters across numerical impact studies.

Structure	γ_η	γ_T	Reference
West Clearwater Lake	0.025	100	This study
Lunar Peak-Ring Basins	0.015	300	Baker et al. (2016)
Chesapeake Bay	0.01	120	Collins and Wünnemann (2005)
El'gygytgyn, Ries, Haughton	0.1	200	Collins et al. (2008a)
Chicxulub	0.008	115	Collins et al. (2008b)
Puchezh-Katunki	0.008	115	Collins (2014)
Sierra Madera	0.003	300	Goldin et al. (2006)
Puchezh-Katunkia ^a	0.012	225	Ivanov and Artemieva (2002)
Sierra da Cangalha	0.05	150	Vasconcelos et al. (2012)
Ries	0.2	300	Wünnemann et al. (2005)
Terrestrial and Lunar Craters	0.1	150	Wünnemann and Ivanov (2003)

^a Assuming an impactor diameter of 3 km (Ivanov, 1994).

son and Grieve, 1977), Slate Islands (Dressler et al., 1998; Robertson and Grieve, 1977), Siljan (Holm et al., 2011), and at West Clearwater Lake, while diaplectic quartz and feldspar glasses can be found at the Manicouagan (Dressler, 1990) and Mistastin (Currie, 1971) structures. While this pattern may be a reflection of the deeper levels of erosion at the Charlevoix, Slate Islands, and Siljan structures, West Clearwater Lake is a comparatively well preserved structure with at least half the stratigraphy of the impact-melt sheet preserved. There should be a significant volume of rock shocked between 35 GPa, commonly stated (Stöffler and Langenhorst, 1994 and refs. therein) as the shock pressure for the transformation of quartz to diaplectic glass, and 50–60 GPa, where shock melting begins. The models suggest that this volume should be $\sim 82 \text{ km}^3$, which, if distributed evenly across the area up to the furthest extent of observed PDFs ($\sim 8.5 \text{ km}$ radial distance), would be $\sim 360 \text{ m}$ thick. This material, which would have to be accounted for by the allochthonous breccias, only has an observed stratigraphic thickness from 0– $\sim 40 \text{ m}$ (Osinski et al., 2015).

There is a significant discrepancy between the estimated and modelled peak shock pressures. However, the estimated peak shock pressures at West Clearwater Lake correlate well with the average number of PDFs per grain in each sample, considered to be a proxy of peak shock pressure (Ferrière et al., 2008). Hence, the shock-pressure estimates reliably and precisely reflect a real variation in peak shock pressure; however, the absolute value of estimated peak shock pressure may be in error.

5.4.2 Original Crater Morphology

The models consistent with the shock barometry results have final crater diameters from 35–40 km where the best-fit numerical model has a final crater diameter of 35 km. Consequently, considering the uncertainties of the method, the final crater diameter of the West Clearwater Lake impact structure was 35–40 km, which is slightly larger than the often stated 32 km apparent crater diameter based on the position of the lake shore (Dence, 1964; Grieve, 2006). The transient crater diameter in the simulations is $\sim 16 \text{ km}$. These estimates based on the best-fit numerical model is also consistent with scaling-law calculations that relate the radial extent of PDFs (8.5 km) or shatter cones (11 km) to the transient cavity diameter (Dence, 1972; Osinski and Ferrière, 2016; Robertson and Grieve, 1977; Stöffler et al., 1988), and then transient cavity diameter to final crater diameter (Grieve et al., 1981; Schenk and McKinnon, 1985). Estimates based on these scaling laws produce transient crater diameters of $\geq 11\text{--}13 \text{ km}$ and final crater diameters that range from 32 to 56 km.

In the best-fit numerical simulation, $\sim 8 \text{ km}$ radial distance marks the edge of the central uplift. Beyond this, modelled shock pressure rapidly attenuates. This is a consequence of the outward movement of the central uplift over the collapsing transient

cavity floor, such that highly shocked material from the centre of the structure slides outward over the relatively unshocked, downwardly collapsing, transient cavity floor. The observed shock attenuation pattern at West Clearwater Lake follows this pattern where shock attenuates rapidly at ~ 8.5 km radial distance.

In comparison to other impact structures, the lack of attenuation of shock pressure across the central uplift is unusual (Dressler et al., 1998; Holm et al., 2011; Robertson, 1975; Robertson and Grieve, 1977). This may be an effect of erosion at these other structures. In the models, deeper horizontal slices show a more gentle and continuous shock attenuation with radial distance. West Clearwater Lake is one of the least eroded structures that has been analysed for shock attenuation; whereas, Siljan, Charlevoix, or Slate islands, with their gentler attenuation of shock pressure, are more heavily eroded structures. Erosion estimates from the three close-fit numerical models, made by comparison between estimated and predicted shock pressures, show that 1.3–2.4 km of erosion has occurred at West Clearwater Lake, relative to the preimpact topography, since the time of impact.

The shock attenuation pattern is consistent with models that show significant central-uplift collapse; however, while there is a prominent topographic peak-ring at modern day exposure, the island ring seen today might not be the remnant of a topographic peak-ring in the original structure. The topography of the island ring is almost entirely formed from impact-melt rock and, therefore, would have been unable, in its molten form, to support topography on the original crater. Furthermore, while some of the close-fit models do produce a subtle topographic ring or a ring shaped feature within the impact-melt sheet, the dominant topographic feature within the final crater diameter remains the central uplift, particularly so within the best-fit model. Consequently, in its pristine condition, the West Clearwater Lake structure would have been a transitional central-peak to peak-ring crater, somewhat akin to “proto-basins” on Mercury and the Moon (Baker et al., 2011a,b; Pike, 1988). The erosional resistant topographic ring structure seen today is likely to be related to concentric structure caused by the crater modification process.

Furthermore, the model provides an estimate of the impact-melt volume produced during the West Clearwater Lake impact; a total of ~ 90 km³ of melt (shocked to >60 GPa) is produced of which ~ 62 km³ remains within the crater to form the impact-melt sheet. This value is broadly consistent with previous impact-melt sheet volume estimates between 68–100 km³ (Grieve et al., 1976; Phinney and Simonds, 1977).

5.4.3 The Block Model Implementation of Acoustic Fluidisation

The numerical models of the West Clearwater impact event are broadly consistent with morphometric observations and shock metamorphism at West Clearwa-

ter Lake. A best-fit model was achieved with parameters, $\eta = 5 \times 10^8$ Pa s and $T_{dec} = 30$ s, although an almost equivalent fit can be achieved by doubling the decay time, and halving the viscosity. These parameters can be related to observable quantities, the block size, h , and quality factor, Q (Ivanov and Artemieva, 2002):

$$\eta = \frac{2\pi\rho h^2}{T}, \quad (5.1)$$

$$T_{dec} = QT, \quad (5.2)$$

where T is the time period of the block oscillations. Assuming the damped harmonic oscillation of blocks in compressible interblock breccia:

$$T = \frac{2\pi h}{c_s} \sqrt{\frac{\rho_b}{\rho_b h}}, \quad (5.3)$$

where ρ_b and h_b are the density and thickness of the interblock breccia, respectively. Previous studies have used the relations, $\rho_b = \rho/2$ and $h_b = 0.1 \times h$, to allow estimation of block size (Ivanov and Artemieva, 2002). Fundamentally, this definition of block-oscillation period requires a significant quantity of highly compressible (i.e., low density) interblock breccia to be valid (Melosh and Ivanov, 1999), which is not observed in the Clearwater Lake cores.

The block size, h , and quality factor, Q , can be calculated for the presented models using the relations $\rho_b = \rho/2$ and $h_b = 0.1 \times h$. For the best-fit model, where $\eta = 5 \times 10^8$ Pa s and $T_{dec} = 60$ s, $h = 17$ m and $Q = 3140$; other reasonable models (Figures 5.7–5.9) indicate that Q could be as high as 6280. These parameters should correspond to observable characteristics in the rock record. For example, the block size (h) should correspond to the observed distance between discontinuities in the drill cores. Logging of the drill cores at West Clearwater Lake suggests that the size of individual “blocks”, while variable and between <1 and ~ 43 m, was ~ 12 m on average. The drill cores only sample the upper, highly deformed portion of the para-autochthon, hence, measurements here would be expected to underestimate the “characteristic block size” parameter, h . Therefore, a value of $h = 17$ m is a reasonable value for the “characteristic block size”. However, the quality factor, Q , representing the attenuation factor of acoustic energy, is considered to be somewhat analogous to the seismic quality factor of rocks (Melosh, 1996); the acoustic waves of the acoustic fluidisation model merely being short-wavelength seismic waves. While attenuation rates of seismic waves are frequency dependent, there is an expectation that the acoustic field should decay with a broadly similar quality factor to that of seismic waves. In crystalline rocks within a few kilometres of the surface, this value is generally between 50 and 600 (Bradley and

Fort, 1966; Waters, 1981). The quality factor used in the best-fit simulation is an order of magnitude greater, implying that the deforming rocks during crater modification are fluidised for longer than expected. This might imply that significant regeneration of acoustic energy occurs during crater growth and collapse. Efficient regeneration of acoustic energy, which is not accounted for in the present simulations, would sustain fluidisation for long enough to explain the long decay time implied by the models, while allowing small quality factors (<1000) to attenuate the acoustic field more rapidly.

On the other hand, observations from the West Clearwater Lake drill cores raise questions over the validity of the conceptual model of a stiff block oscillating in compressible breccia and, hence, the simple scaling between T_{dec} , η , h , T , and Q . The drill core logging suggests that $\rho/\rho_b = 2$ and $h_b/h = 0.1$ are not reasonable assumptions at West Clearwater Lake. Instead, it has been found that $h_b/h \leq 0.01$, and while direct measurements of the densities of discontinuities and rock blocks were not made, a more realistic constraint is $\rho/\rho_b \leq 1.1$. Using these more realistic values, together with the best-fit model parameters, only increases Q to a value to ~ 30000 , while reducing the block size, h , to 4 m. Similar issues with the block model have been raised at other impact structures, for example, Haughton (Osinski et al., 2005). Importantly, the observation of interblock breccia thicknesses less than 1% of the block size brings into question the applicability of a model based on damped harmonic oscillation of independently oscillating blocks in breccia.

The combination of the unrealistic value of the quality factor parameter and the inconsistencies between observations and the justification of the block model leads us to the conclusion that the block model, while capable of producing a rheology of deforming material to explain the morphology of complex craters, cannot be used to directly constrain physical parameters, such as block size. Despite some uncertainty in the absolute values of the acoustic fluidisation parameters, largely due to trade-offs with impactor parameters, it is clear that the assumption of a uniform block size with distance from the crater centre in the current block model implementation is an oversimplification (e.g., Kenkmann et al., 2006). A treatment of the full acoustic fluidisation model, as described by Melosh (1979), which makes no assumption about the presence of significant interblock breccias and which prolongs weakening in strongly deforming regions, may provide better justification for the collapse of large impact structures. These factors may qualitatively change the kinematics of crater collapse in numerical simulations to better reflect the process of central uplift formation.

5.5 Summary

Shock pressure estimates from observations of PDFs in quartz-bearing lithologies at West Clearwater Lake show that peak shock pressures are fairly constant across the central uplift, with a maximum value in the centre of the structure of

at least 17.5 GPa. Shock pressure attenuates more rapidly with depth at greater radial distances.

This shock distribution pattern can be explained by the outward collapse of a highly shocked central-uplift over a downwardly and inwardly collapsing, weakly shocked crater rim. The kinematics of numerical impact simulations using the block model of acoustic fluidisation are capable of qualitatively matching this shock distribution, while remaining consistent with the geologically observable morphology of the crater.

The conceptual idea behind the justification of the block model of acoustic fluidisation lacks observational support at West Clearwater Lake. The assumption that the deforming “interblock breccia” is significantly compressible and present in “large” volumes is not supported by observations of deformation zones in the drill cores. In addition, while the block model succeeds in reproducing the kinematics of complex crater collapse, it does not appear to be possible to relate the parameters to observable quantities. One possible explanation for this disconnect is that regeneration of acoustic vibrations during the cratering process, which is not accounted for in the present implementation of the block model, is important in prolonging acoustic fluidisation, allowing complete crater collapse.

The original final crater (rim) diameter of the West Clearwater Lake impact structure is estimated to be 35–40 km. Subsequent differential erosion of the structure has led to up to \sim 2 km of denudation (relative to the pre-impact topography), removing all impact ejecta and at least half the thickness of the impact-melt sheet. The impact-melt volume estimated by the numerical simulations is \sim 90 km³, of this, \sim 62 km³ remains within the crater cavity to form an impact-melt sheet. These estimates are consistent with previous estimates of the original impact-melt volume at West Clearwater Lake. The original morphology of the structure was a transitional central-peak–peak-ring crater.

6 Characterisation of Deformation during Complex Crater Formation: The East Clearwater Lake Impact Structure

6.1 Introduction

In the previous chapter, it was shown how the viscosity and decay time of transient weakening during complex crater formation can be constrained by combining observations of shock metamorphism with numerical impact simulations, and that the block model implementation of acoustic fluidisation is capable of producing the necessary rheology. Nevertheless, the structures that accommodate the extreme deformations that occur during collapse are uncertain.

This chapter will focus upon deformation within the central uplift of the East Clearwater Lake impact structure. A remarkably long drill core from the structure was recovered in the mid-1960s, providing an excellent opportunity to investigate the process of central peak formation. Specifically:

1. A lithological, structural, and petrographical description of para-authochthonous target rocks within the East Clearwater Lake impact structure are presented;
2. Observations from the East Clearwater Lake structure are compared and contrasted with the more well-studied West Clearwater Lake structure;
3. A well-constrained numerical model of the East Clearwater Lake impact event is presented.

6.2 Methods

6.2.1 Core Logging

Cores from Hole 1-64 were logged with the aim of lithologically and structurally mapping the central uplift of the East Clearwater Lake impact structure. Lithological logging was achieved with a spatial resolution of 15 cm (0.5 ft) while structural

features were logged wherever they occurred. The observed deformation was subdivided into five distinct styles: 1) cataclasites, 2) cataclasites containing melt veins 3) breccias with lithic matrix, 4) breccias with melt matrix, and 5) melt veins. If a particular deformation structure exceeded the minimum spatial resolution (15 cm), its width was measured, otherwise, its occurrence depth was measured.

6.2.2 Optical Microscopy

58 thin sections of samples from Hole 1-64 were investigated with an optical microscope and their mineralogies identified, described, and quantified. Mineral abundance was achieved by visual approximation. Locations of thin sections were decided partly by the available selection of thin sections held within the GSC collection, and additional thin sections were prepared from selected areas based on core logging. Following initial description, peak shock pressure estimates of the samples were made by the measurement and analysis of PDFs in quartz using a universal stage.

6.2.3 Electron Microscopy

Following optical analysis, an additional 14 thin sections were prepared for BSE imaging and EDS. The primary aims of using electron microscopy were: 1) to texturally analyse deformation features, and 2) to determine a relative timing of deformation features. Imaging was carried out using a JEOL JXA-8530F field-emission electron microprobe at the Earth and Planetary Materials Analysis Laboratory, Western University, Canada. An accelerating voltage of 15 kV was used with a working distance of approximately 10 mm for all analysis in this chapter. Primarily, BSE images were acquired along transects such that high-resolution image stitches across deformation features could be produced. EDS spectra were acquired to aid mineral identification.

Images were processed and analysed using the ImageJ software package. First, individual images were stitched and cropped to produce transects. Following this, image noise was reduced using a gaussian blur function with a 1σ value of 3 pixels. Images were then thresholded to separate pores from grains. Here, the ImageJ Default thresholding algorithm was generally used to determine the threshold value between pores and grains. However, in some instances where this algorithm performed poorly at distinguishing pores from grains, the RenyiEntropy, Shanbhag, or Li thresholding algorithms were used. From thresholding, two images were produced; one, where pores were selected, and a second, where grains were selected. Both images underwent binary image refinement after thresholding. Grain images underwent a closing algorithm, a dilation followed by an erosion, such that small pores within grains were eliminated, and sub-grains were connected. Pore images underwent an opening algorithm, an erosion followed by a dilation, such that individual pores would separate. Neither operation

significantly affects the total selection area. Finally, for the production of radial transects, a watershed algorithm was applied to the two images, such that individual grains and pores separated. Ultimately, the watershed algorithm over-separates large grains and pores, resulting in smaller average grain sizes than the true average grain size of the sample. Nevertheless, this is preferred to the significant overestimation of grain size that occurs without the watershed algorithm.

6.2.4 Numerical Modelling

Simulations of the formation of the East Clearwater Lake impact structure were performed using the iSALE shock physics code. Here, we simulate the East Clearwater Lake impact event using many of the parameters chosen within Rae et al. (2017a) and Chapter 5.

The target rocks were simulated in our numerical simulation by the use of a single granite layer; this assumes that the sedimentary cover at the time of impact was negligible and that the behaviour of the mantle is insignificant. The chondritic body that impacted at East Clearwater Lake was simulated by a granite sphere. This was chosen for several reasons: 1) the density of granite is comparable to the density of stony meteorites, 2) it is more computationally efficient to reduce the number of materials used, and 3) it ensures consistency between the impact model presented here, and the impact model presented in Rae et al. (2017a) and Chapter 5. The impactor diameter and velocity used in this simulation is 1.5 km and 15 km s^{-1} . Following the crater scaling relations of Holsapple and Schmidt (1979) and Schenk and McKinnon (1985), this would be expected to result in a crater with a rim-to-rim diameter of 18.6 km. Here, the thermodynamic behaviour of the materials in the simulation are modelled using granite parameters described in Pierazzo et al. (1997) for the ANEOS program. The parameters of the constitutive model used in the simulations presented in this chapter are identical to those chosen in Chapter 5. Additionally, the dilatancy model of Collins (2014), was used such that the porosity and gravity signature of the final crater could be modelled.

A list of the parameters used in our simulation is shown in Table 8.1 (Global Parameters) and Table 8.2 (Material Parameters), and a full list of parameters may be found in Appendix B.

Table 6.1: Global model parameters for East Clearwater Lake simulations. A full list of parameters may be found in Appendix B.

Parameter	Symbol (units)	Value
Cell resolution	(m)	100
Cells per impactor radius		70
Horizontal cells in high resolution zone		1000
Horizontal cells in outer extension zone		200
Vertical cells in high resolution zone		800
Vertical cells in upper extension zone		0
Vertical cells in lower extension zone		200
Impactor velocity	v_i (km s ⁻¹)	15
Impactor density	ρ_i (kg m ⁻³)	2630
Acceleration due to gravity	g (m s ⁻²)	9.81
Surface temperature	T_{surf} (K)	273
Surface temperature gradient	T_{grad} (K m ⁻¹)	0.0051
Lithospheric thickness	d_{lith} (km)	200

6.3 Results

6.3.1 Core Logging

Logging of core 1-64 indicates that the dominant lithologies within the East Clearwater Lake central uplift are granitic composition rocks with occasional gneissic foliation. In addition to the granitic rocks, mafic amphibolites are occasionally found with sharp contacts to the surrounding granitic rocks, indicating the origin of these lithologies as doleritic dikes.

Deformation throughout the core was extremely common, with 319 distinct occurrences of individual deformation features. 199 occurrences of cataclasites were found, of which 53 were associated with melt veins. 13 of these cataclasites occurred at contacts between lithologies, 8.6% of the total number of recorded contacts. 31 occurrences of breccias were found, of which 15 had a matrix of melt rock. Finally, 89 occurrences of melt veins without any other deformation were found.

Overall, the distribution of deformation is most concentrated at the top of the core, and decreases towards the core bottom. Within this general trend of decreasing deformation intensity with increased depth, there are several regions that are more greatly deformed than the rocks directly overlying them e.g. 280–340 mbfs (metres below lake surface), 580–620 mbfs, 640–700 mbfs, 860–900 mbfs, and 960–1000 mbfs. The distribution of these 319 deformation features is shown on Figure 6.1. The distribution

Table 6.2: Material model parameters for East Clearwater Lake simulations. A full list of parameters may be found in Appendix B.

Parameter	Symbol (units)	Crust (Granite)
Reference Density	ρ (kg m ⁻³)	2630
Poisson's ratio	ν	0.30
Intact cohesive strength	Y_0 (MPa)	10
Intact friction coefficient	μ_i	2.0
Intact and damaged strength limit	Y_m (MPa)	2500
Damaged cohesive strength	Y_{d0} (MPa)	0.01
Damaged friction coefficient	μ_{di}	0.6
Minimum failure strain for low pressure states	$\varepsilon_f b$	1×10^{-4}
Constant of proportionality between failure strain and pressure	B	1×10^{-11}
Pressure above which failure is compressional (Pa)	P_c (MPa)	300
Melt Temperature	T_m (K)	1673
Thermal softening coefficient	ξ	1.2
Constant in Simon Approximation	p_{bp}	1.52×10^9
Exponent in Simon Approximation	y_{t0}	4.05
Acoustic Fluidisation viscosity constant	γ_η	0.025
Acoustic Fluidisation decay time constant	γ_T	125
Vibrational particle velocity as a fraction of particle velocity	C_{vib}	0.1
Maximum vibrational particle velocity	$V_{vib,max}$ (m s ⁻¹)	200
Time after which no new acoustic vibrations are generated	t_{off} (s)	16
Maximum dilatancy coefficient	β_{max}	0.09
Critical distension	α_c	1.2
Critical friction coefficient	μ_c	0.4
Initial distension	α_0	1.0

of deformation, sub-divided by deformation type indicates that melt veins, cataclasites with melt veins, and breccias with melt matrices are most common above 350 mbars, and become comparatively, though not completely, negligible beneath this depth. Cataclasites, on the other hand, are a common deformation feature at all depths.

6.3.2 Optical Microscopy

Investigation of the suite of 58 thin sections from core 1-64 by optical microscopy shows that the granitic rocks of core 1-63 typically possess a modal mineralogy of: 35% Quartz, 35% Alkali Feldspar, 20% Plagioclase, 5% Biotite, and 5% secondary minerals (calcite and/or chlorite). Quartz abundance varies from 5–60%, alkali feldspar abundance varies from 10–65%, and plagioclase abundance varies from 5–50% across all samples. The relative abundances of these minerals place the majority of thin sections within the Granite classification field (Figure 6.2).

Within the felsic target rocks, nearly all quartz grains contain decorated planar deformation features (PDFs), often with more than one set (Figure 6.3a,c,d,e,f), and many quartz grains contain planar fractures (PFs) (Figure 6.3c,d). Alkali feldspar grains commonly possess a perthitic texture. Plagioclase grains are occasionally myrmekitic. Finally, biotite grains are occasionally kinked (Figure 6.3b).

Texturally, the felsic target rocks are characterised by abundant brecciation and cataclasis (Figure 6.3d,e,f). Comparatively undeformed sections indicate that the original maximum grain size within the target rocks was generally 3 mm in length, with occasional areas with grains up to 10 mm in length (Figure 6.3c). Cataclasites typically possess planar contacts with the surrounding target rocks, particularly so for the finer-grained and more mature cataclasites. Many of the sectioned cataclasites contain optically opaque bands within them (Figure 6.3e,f), identified during logging as melt veins. These bands have irregular contacts, which are typically sharp but occasionally diffuse, with the cataclasites that contain them. These opaque bands contain within them clasts of fragmented grains from the granitic target rocks, of a comparable size to the fragment size within the surrounding cataclasite.

Tabulated descriptions of the thin sections in this Chapter can be found within Appendix C.

6.3.2.1 Shock Barometry

The crystallographic orientations of PDFs in the 58 quartz-bearing samples identified by optical description were obtained by universal-stage analysis. Table 6.3 contains a summary of the PDF statistics in all thin sections while statistics organised by sample can be found in Appendix C.

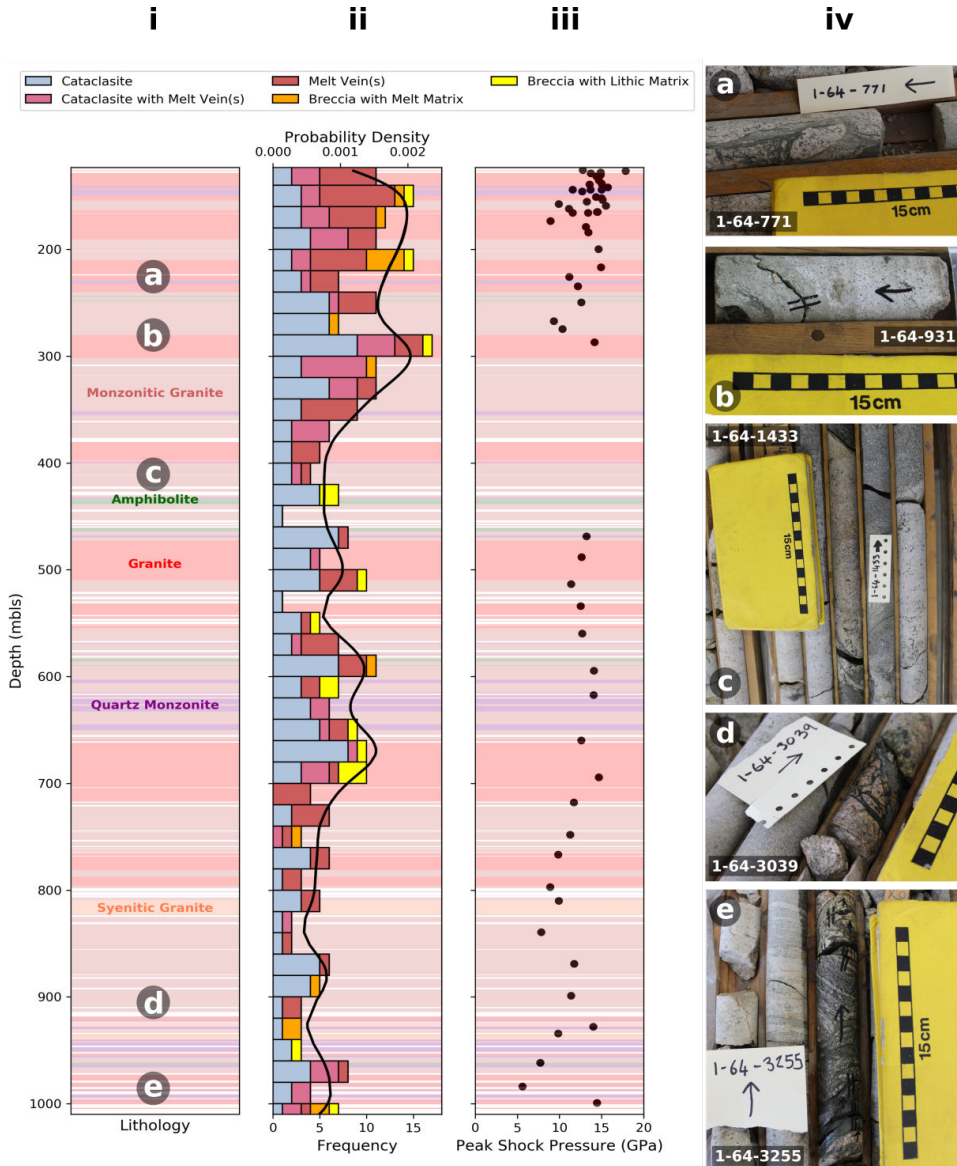


Figure 6.1: Log of core 1-64 from East Clearwater Lake. i) Lithological column. ii) Histogram of deformation frequency, sub-divided by deformation type, probability density function of all deformation features as calculated by kernel density estimation is also plotted. iii) Estimated peak shock pressures from universal-stage analysis of quartz. iv) Images of core samples at depths corresponding to indicators on the lithological column: a) breccia with a matrix of impact melt rock, b) Cataclasite containing wispy impact melt veins, c) cataclasites occurring on lithological boundary between amphibolite and granitoid, d) breccia with a matrix of impact melt rock, and e) cataclasites on lithological boundaries, one of which becomes ultra fine-grained against the contact.

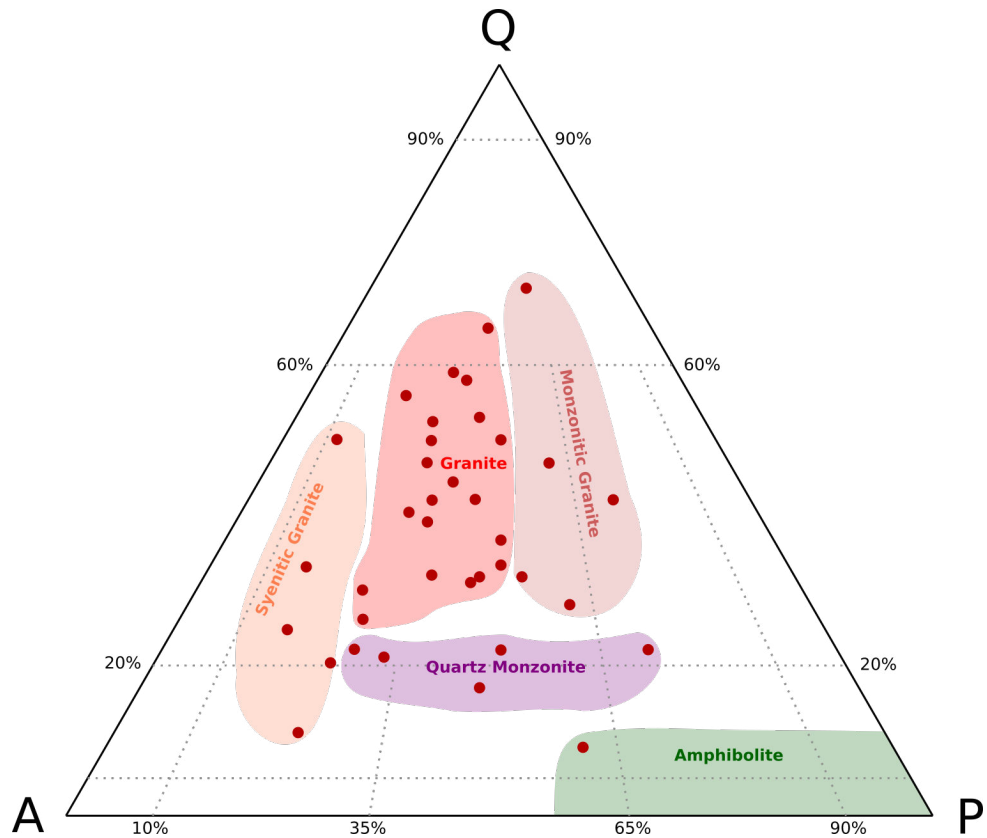


Figure 6.2: Categorisation of the mineralogical composition of thin sections from Hole 1-64 on ternary QAP diagram. Q – Quartz, A – Alkali Feldspar, P – Plagioclase Feldspar. The logging units and their mineralogical composition are indicated by coloured fields. Notably the logging units do not perfectly correspond to the fields of the QAP diagram; e.g., the logging unit, monzonitic granite, includes both plagioclase-rich granites and granodiorites.

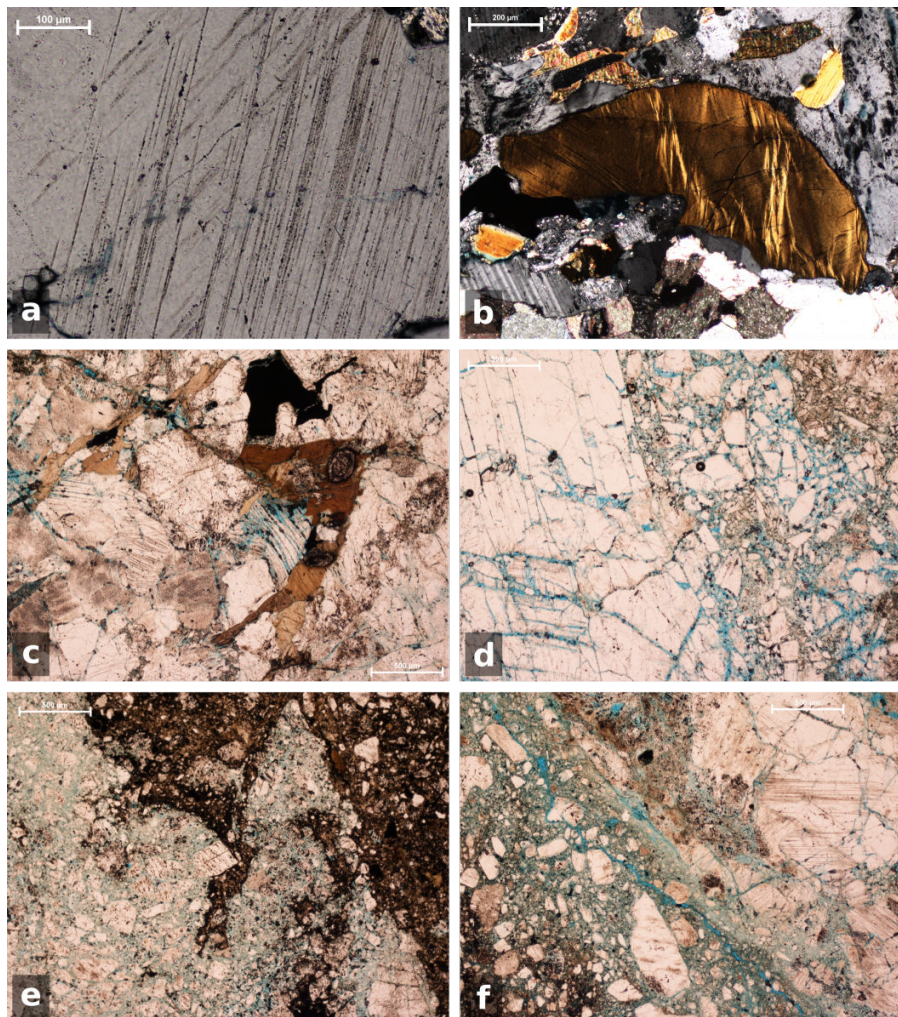


Figure 6.3: Deformation structures observed by optical microscopy. a) PDFs in quartz in cross-polarised light (XPL). b) Kink-banding in biotite under XPL. c) Comparatively undeformed granite with PDFs in quartz, highly open PFs in quartz, and other mineral phases, Alkali Feldspar, Plagioclase, Biotite, Titanite, and opaque minerals under plane-polarised light (PPL). d) Planar contact between cataclasite and host granitoid under PPL. e) Irregular and sharp contact between cataclasite and opaque-rich vein, described in core logging as a melt vein under PPL. f) Sharp contact between host granitoid and cataclasite and diffuse contact between cataclasite and opaque-rich vein under PPL.

Between 0 and 4 PDF sets were observed per quartz grain with an average number of PDFs per grain in a sample ranging from 0.59 to 2.17. All observed PDFs were decorated. Across all of the thin sections (0001) and {10̄13} PDF orientations were most common, accounting for 38.8% and 31.2% of the total number of measured sets respectively. Additional common PDF sets include {10̄14}, {10̄12}, {10̄11} orientations which account for 12.5%, 5.8%, and 4.2% of the total number of measured sets respectively. 9.5% of the measured sets could not be indexed. This either reflects human error in the original measurements or that there are possible PDF planes not included in the New Stereographic Projection Template (NSPT) (Ferrière et al., 2009).

The estimated shock pressures of each sample are shown on Figure 6.1. In general, peak shock pressures decrease with increased depth within the central uplift; from values of \sim 15 GPa at the top of the core, down to \sim 7.5 GPa at the bottom of the core. These pressure estimates are derived by calculating the mean of individually assigned pressures to each crystal, the standard deviation of this average varies between 2.12 GPa and 8.45 GPa, with a mean standard deviation of 5.63 GPa. These standard deviations do not represent errors, but provide a measure of the distribution of shock pressure within a sample.

6.3.3 Electron Microscopy

BSE imaging of the thin sections shows at least three phases of deformation to the para-autochthonous rocks:

1. Shock deformation;
2. Cataclasis;
3. Melt/ hydrothermal fluid infiltration.

Shock deformation is evident in the thin sections by the presence of PFs, often seen in quartz, but also in alkali feldspar and plagioclase (Figure 6.6a,b). More-generally, pervasive, grain-scale fracturing is common across all minerals (Figure 6.6b). Additional deformation associated with shock metamorphism, not readily observable using BSE images, include PDFs in quartz.

Subsequently to shock deformation, the para-autochthonous rocks of Hole 1-64 were affected by a significant deformation event or series of deformation events characterised by cataclasis along discrete planes within the para-autochthon (Figure 6.6a,b). Evidence of the relative timing of this cataclastic “event” compared to shock deformation derives from: a) the occurrence of clasts within the cataclasites that contain poorly developed PFs (Figure 6.7i), b) the activation of planar fractures as slip surfaces

No. of grains (n)	No. of shocked grains (n*)	No. of measured sets (N)	No. of indexed sets (N*)	Average No. of PDF sets per shocked grain (N*/n*)										
1671	1545	2839	2570	1.54										
Indexed PDF crystallographic orientations (absolute frequency percent ^a)														
(0001)	{10̄4}	{10̄3}	{012}	{10̄1}	{010}	{1122}	{1121}	{213̄1}	{510̄1}	{1120}	{2211}	{3141}	{40̄11}	{510̄0}
38.8	12.5	25.4 + 5.8	4.2	0.4	0.3	0.6	0.6	0.4	0.1	0.3	0.3	0.1	0.0	9.5

^a This is given by the total number of observed PDFs in the specific orientation divided by the total number of measured sets (N), indexed and unindexed.

Table 6.3: Summary of PDF statistics in East Clearwater Lake samples. Statistics organised by sample can be found in Appendix C.

near to cataclasites (Figure 6.7ii,iii), c) the partial disaggregation of pervasively shock-fractured grains into cataclasites (Figure 6.7ii,iii).

The cataclasites can broadly be characterised by:-

1. Porosities of $\sim 20\%$ which, locally, can exceed 30% . In comparison to the “intact” granitic rocks which have porosities of $\sim 5\%$ (e.g. Figure 6.4; Appendix D);
2. Log-normal grain size distributions with average (geometric mean) grain sizes of $0.86\text{--}3.51\ \mu\text{m}$ (e.g. Figure 6.5; Appendix D);
3. Power-law distributions of pores, where 50% of the total porosity is typically contributed by pores between $2\ \mu\text{m}$ and $50\ \mu\text{m}$ (e.g. Figure 6.5; Appendix D).

Deformation after the cataclastic event(s) can be seen within the BSE images. Comparatively clast-poor and low porosity veins of high BSE-intensity material are often found within cataclasite zones. Under the optical microscope, these veins appear as optically opaque bands, and were described during logging as melt veins.

These veins are texturally complex. The contacts between the veins and the host cataclasite can be sub-planar and sharp (Figure 6.6f), sub-planar and partially diffuse (Figure 6.7iv), or irregular and completely diffuse (Figure 6.7v). The sub-planar, partially diffuse contacts occur where the matrix material of the veins fills the interstitial spaces within the host cataclasite (Figure 6.7vi). The veins with completely diffuse and irregular contacts occur where the vein matrix material fills the interstitial spaces of the cataclasite, without any change in clasts from the host cataclasite through the vein (6.7v).

Within the veins, clast concentration can be highly variable, both within and between veins. The veins with completely diffuse contacts possess the same clast populations, in terms of size, shape, and composition, as the fragmented grains within the host cataclasite, where only the original porosity has been replaced by matrix material. Other veins contain substantially smaller clast concentrations, and a greater proportion of matrix material. Nevertheless, the clasts themselves are similar in size, shape, and composition to the fragmented grains in the host cataclasite. Some veins contain regions that are completely clast-free, consisting entirely of the matrix material, and round, micron-scale pores, which may be vesicles (Figure E.5). These regions have sharp contacts to clast-bearing regions but the matrix material continues across the contact (Figure 6.6e). The matrix material across all veins is texturally and chemically similar, consisting almost exclusively of a micron-sized, platy mineral (Figure E.6) with EDS spectra indicative of a chlorite group mineral (Fe, Al, Mg, (Na, Ca), Si, O; Figures E.4, E.5, and E.6) and an occasional high-BSE intensity, rounded, sulfur-bearing mineral (Figure E.5; see Appendix E for additional EDS results).

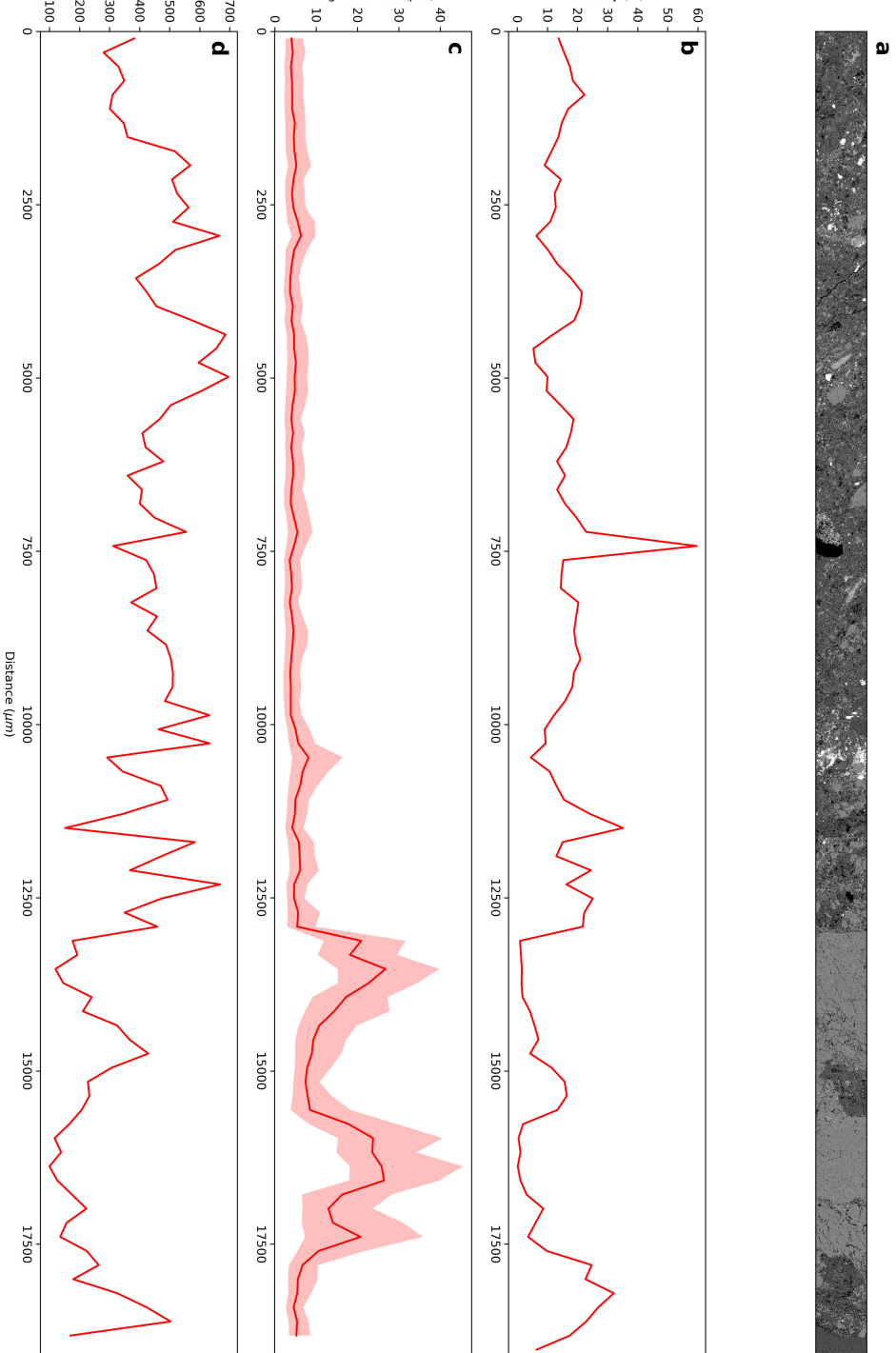


Figure 6.4: Quantitative analysis of a) a transect through a cataclasite in Sample 1-64-2206. b) Local porosity with distance. c) Local grain size with distance. d) Local grain density with distance.

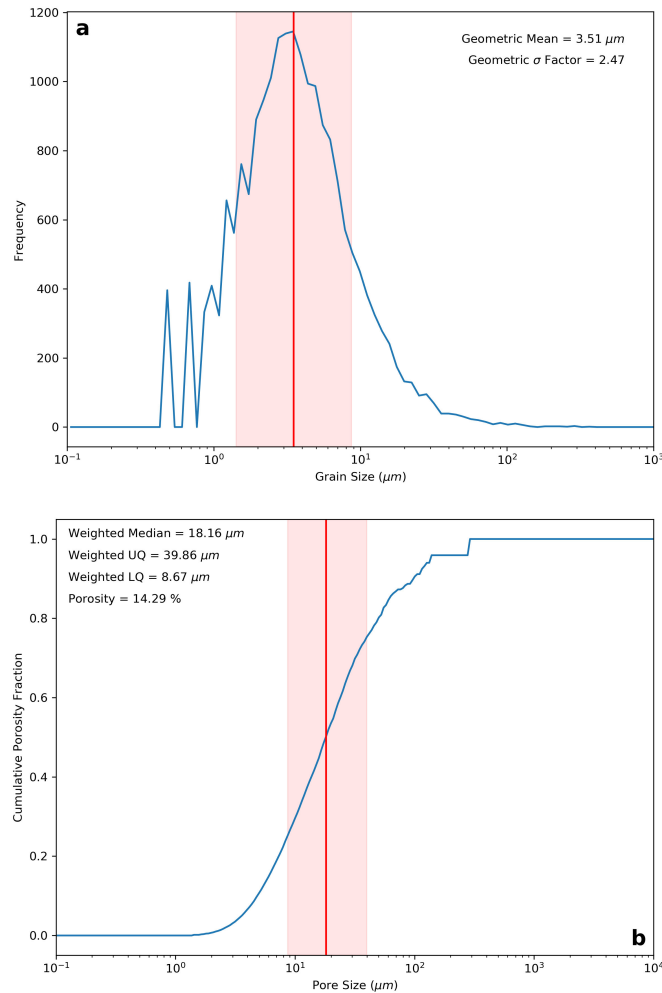


Figure 6.5: Grain- and pore-size distributions of cataclasite in Sample 1-64-2206. a) Grain size-frequency distribution in Sample 1-64-2206, the red line indicates the geometric mean of the distribution while the red area indicates the pore sizes within one geometric standard deviation of the geometric mean. b) Cumulative pore size-fraction distribution in Sample 1-64-2206, the red line indicates the weighted median of the distribution, i.e. the pore size with the median pore-area contribution, the red area indicates the inter-quartile range.

Two potential interpretations of these veins are apparent on the basis of the observations presented:

1. Solidified veins of molten material;
2. Hydrothermal dissolution and precipitation along porous channels.

The presence of completely clast-free vein material favours the interpretation of melt veins, supported by the presence of vesicles in addition to the lack of likelihood that hydrothermal processes could dissolve 100% of the cataclasite mineral fragments within a channel. Nevertheless, the completely diffuse and partially diffuse contacts of some of the veins suggest hydrothermal fluid infiltration and precipitation, it being unlikely that a melt could have a low enough viscosity and/or enough energy during emplacement to infiltrate such small pores. Furthermore, there is significant evidence of post-impact hydrothermal processes elsewhere in the core samples, where precipitated Ca-Al-bearing zeolite group minerals and celestine (SrSO_4) can be found (Figures E.10 and E.11). The Fe-rich chemical composition of the vein material does not necessarily indicate one or other process; however, it does eliminate the possibility of a locally generated melt; i.e., frictionally-generated pseudotachylite, as the host rocks have significantly lower Fe concentrations. Thus if it is a melt, then it is an infiltrated melt from another source region. The origin of these veins is therefore uncertain. Nevertheless, the presence of matrix material as an interstitial phase within the cataclasite host of the veins indicates that the emplacement of the vein material must have occurred after the cataclastic event(s).

6.3.4 Numerical Simulations

Selected timesteps of the simulation of the East Clearwater event are shown in Figure 6.8. The presented simulation results in a central peak crater with a rim-to-rim diameter of approximately 20 km, a depth at the crater centre of 0.72 km and within the annular trough of 1.4 km, and a maximum structural uplift of 2.1 km.

The predicted peak shock conditions within Hole 1-64 are shown on Figure 6.9. The simulated core is located at 1 km radial distance from the crater centre. Additionally, consideration needs to be paid to the amount of erosion since impact before direct comparison with observations.

By the use of the dilatancy model of Collins (2014), the results of the simulation can be used to provide a prediction of the local Bouguer Gravity signature associated with the crater. Calculation of this Bouguer Gravity anomaly assumes, based on Plante et al. (1990), a density of the initial granitic target of 2630 kg m^{-3} . Additionally, the amount of erosion since the time of impact must be considered. Rae et al. (2017a) (see Chapter 5) suggest that the amount of erosion since the time of the

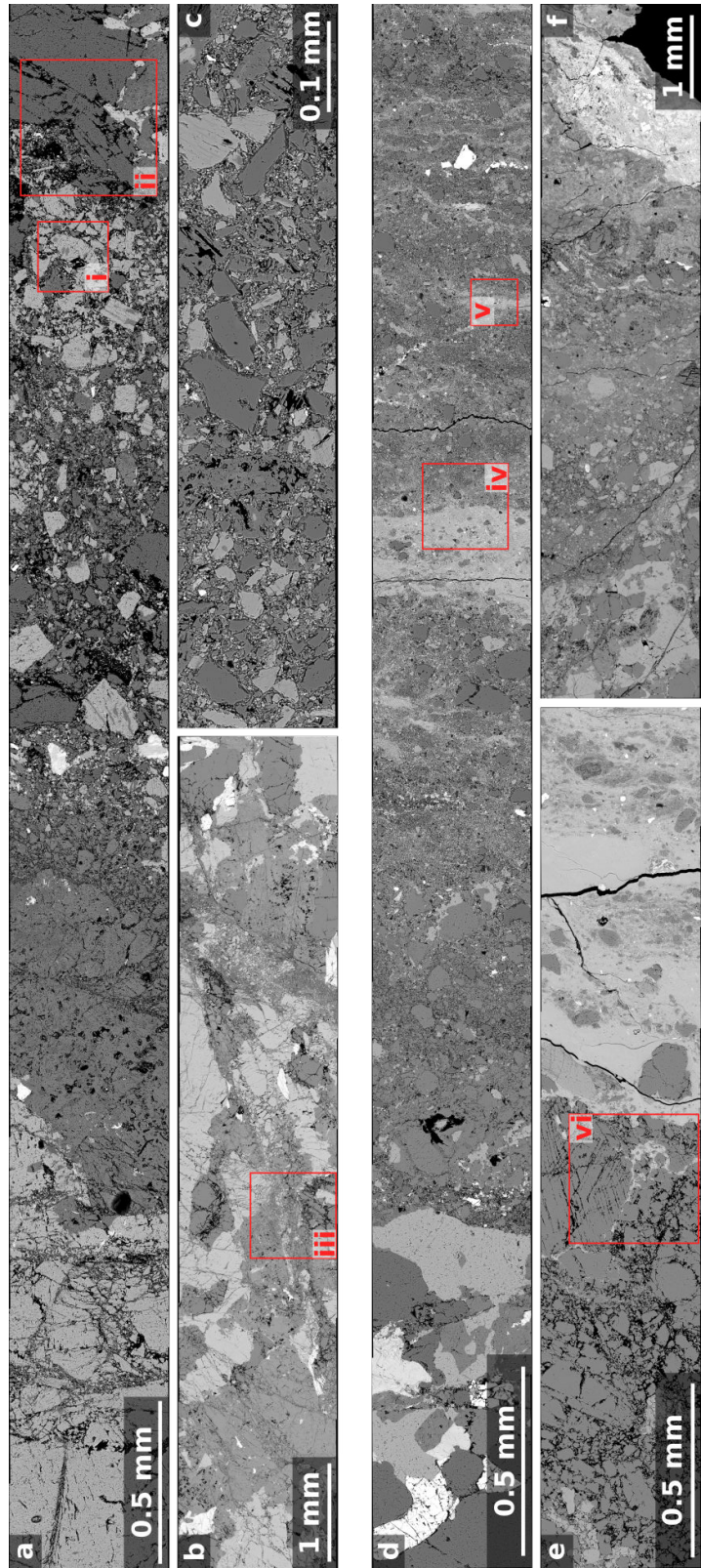


Figure 6: Stitched BSE SEM images of deformation features within the granitic rocks of Hole 1-64. a) Transect through cataclasite hosted within fractured granitic basement rocks (1617 ft). b) Proto-cataclasite within fractured granitic host rock (1090 ft). c) High-magnification image of cataclasite (2140 ft). d) Transect from fractured granitic host rock into cataclasite that contains veins of low-porosity, clast-poor material with both diffuse and sharp contacts (2763 ft). e) High magnification contact between cataclasite and clast-poor, and occasionally clast-free, vein material, which has filled some of the interstitial spaces within the cataclasite (544 ft). f) Transect from fractured granitic host rock, through cataclasite, and into vein material (544 ft). Red squares indicate the location of close-up photos in Figure 6.7

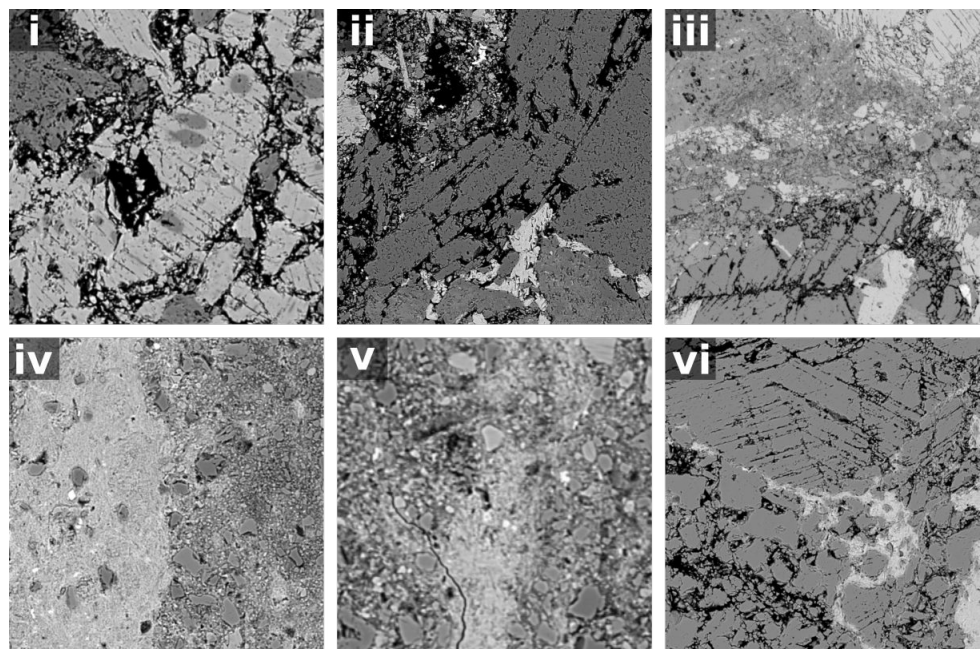


Figure 6.7: Close-ups of features within BSE SEM stitches in Figure 6.6: i) Alkali feldspar clast within cataclasite containing PFs. ii) Partial disaggregation of quartz grain into cataclasite. iii) Sinistral displacement along PF within quartz adjacent to cataclasite. iv) Semi-diffuse contact between clast-poor vein and cataclasite, the contact is generally planar; however, vein matrix material infiltrates the interstitial spaces of the host cataclasite. v) Wispy vein with completely diffuse boundaries, filling interstitial spaces within cataclasite. vi) Vein material partially infilling a cataclasite adjacent to a vein of clast-poor and clast-free material.

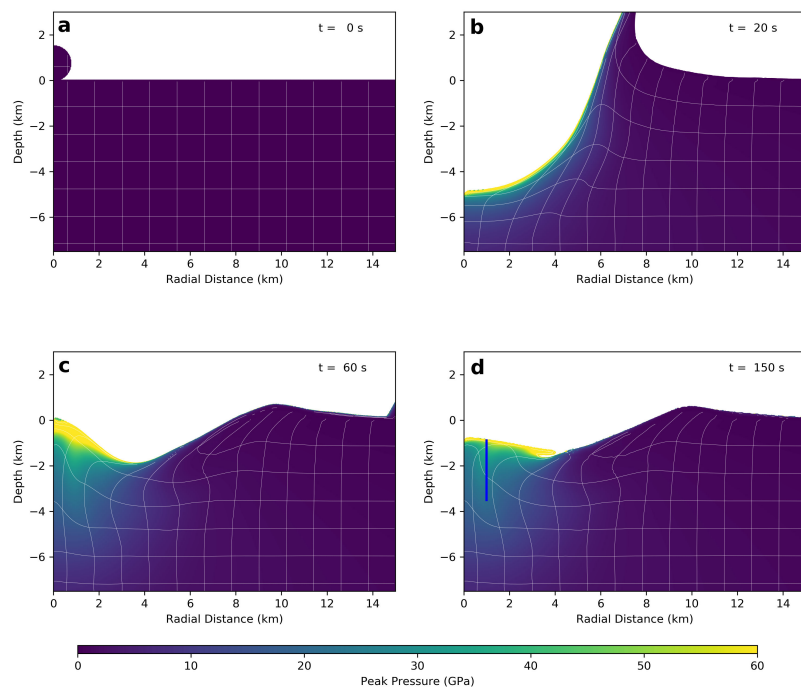


Figure 6.8: Selected timesteps of the numerical model of the East Clearwater Lake impact. Material is coloured by its peak recorded shock pressure, and a grid of tracer particles is shown in white within the target to highlight sub-crater deformation. a) The initialised model. b) The transient crater. c) Maximum central uplift. d) The final timestep, additionally, in this frame, the location of the simulated Hole 1-64 is indicated by the blue vertical line.

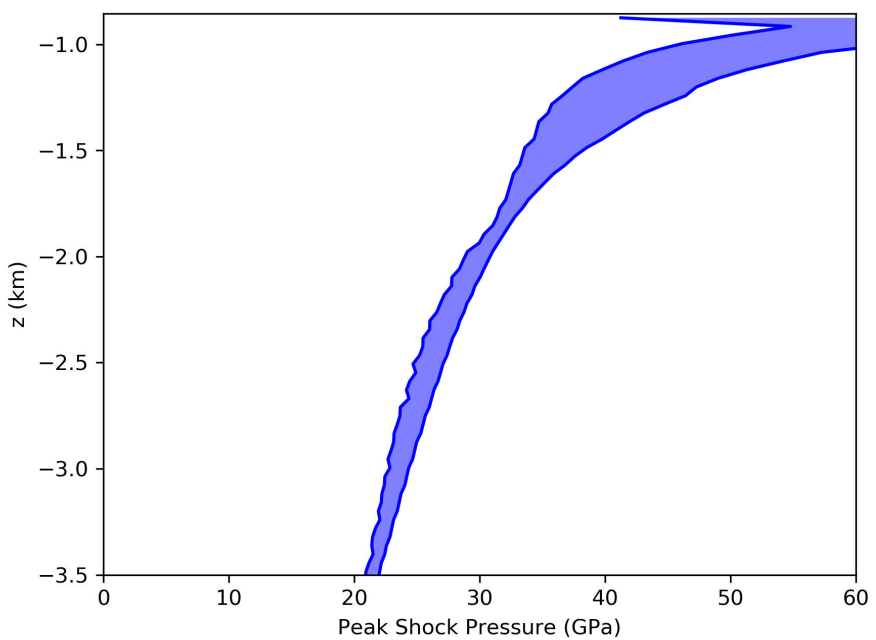


Figure 6.9: Predicted peak shock pressures in Hole 1-64 from the numerical simulations in Figure 6.8. The profile is obtained at 1 ± 0.25 km radial distance from the crater centre, shown on Figure 6.8, where the filled area represents the range of shock pressures found within the radial distance range at the corresponding depth.

West Clearwater Lake impact event is between 1.3–2.4 km. Considering that Hole 2-63, which penetrated the annular trough of the East Clearwater Lake structure recovered approximately 112 m of post-impact sedimentary rocks, followed by a 42 m long sequence of impact melt rocks means that the level of erosion within the annular trough cannot exceed the maximum depth of impact melt rocks within the simulation, which is 1.75 km beneath the pre-impact surface. Consequently, our calculation of the Bouguer gravity anomaly associated with the East Clearwater Lake impact structure assumes erosion since the time of impact from 1.30–1.75 km beneath the pre-impact surface. The maximum post-impact sediment thickness within the lake must occur within the annular trough. Therefore, no more than a \sim 100 m thickness of post-impact sediments occur within the basin, and the post-impact sediments only make a small contribution to the Bouguer gravity anomaly. Nevertheless, in our calculation the post-impact sediments possess a density of 2350 kg m^{-3} (Plante et al., 1990). The dominant cause of the anomalous Bouguer Gravity signal associated with the East Clearwater Lake structure is the introduction of porosity due to fracturing of the target rocks, this process is accounted for in our simulation by the use of a shear-induced dilatancy model. Our calculation assumes that any porosity introduced by dilatancy is fully water saturated. The simulated porosity of the final crater and calculated gravity profile, compared to the observed gravity signature, are shown on Figure 6.10.

6.4 Discussion

6.4.1 Deformation during Central Peak Formation

Observed PDF orientations in Hole 1-64 indicate that shock pressures reached up to 18 GPa for the most highly shocked rocks near the top of the hole, down to a little over 5 GPa for the least shocked rocks at the hole bottom. Additional evidence of shock metamorphism includes FFs in quartz, kinked biotite, and abundant PFs in quartz. In addition, most grains within samples from Hole 1-64 are fractured to some degree. The PFs typically predate PDFs, this is apparent based on the observation that PDFs truncate against PFs. Nevertheless, the majority of fracturing in these rocks occurs after the formation of PDFs. PDFs generally continue across both sides of fractures, sometimes with small displacements. Additionally, it is clear that shock metamorphism and fracturing is followed by the formation of cataclasites (Figure 6.7i,ii,iii), which are observable on the core-scale.

The frequency of the occurrence of macroscopic deformation features within Hole 1-64 follows a similar trend to the attenuation of shock pressure with increasing distance. Within this trend, impact-related deformation features associated with melt veins, cataclasites with melt veins, and breccias with melt matrix, only occur significantly above 400 mbars. Additionally, the “melt veins” have a significantly different

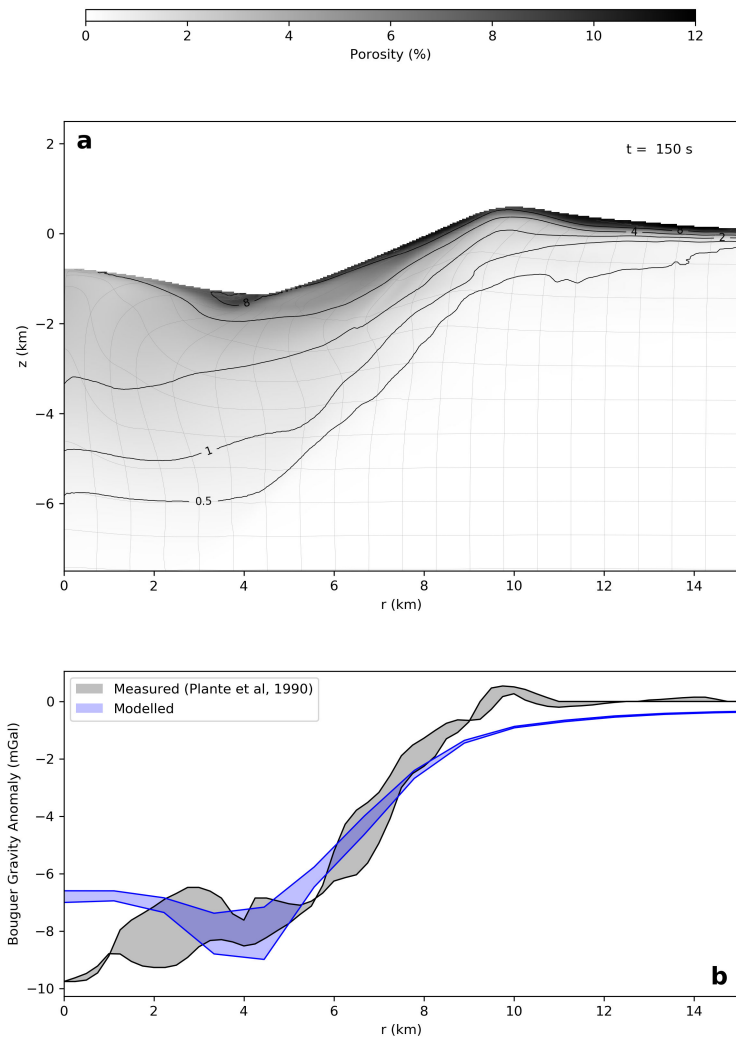


Figure 6.10: Results of the dilatancy model in the East Clearwater Lake simulation. a) Modelled porosity distribution within the final crater, porosity is contoured at 0.5, 1, 2, 4, and 8%. b) Observed radial gravity profiles (grey), are compared with the prediction of the gravity profile derived by calculation from the model results (blue). A field of profiles is plotted, reflecting the propagation of uncertainty in the gravity model parameters.

chemistry to their host rocks. Together, this suggests that the melt within Hole 1-64 infiltrated from the impact melt sheet of the East Clearwater Lake structure, either during crater modification or after significant crater motions ceased. This observation conversely suggests that frictionally generated melts were not significant in the formation of the central uplift at East Clearwater Lake. Additionally, this implies that the top of Hole 1-64 was originally close to the uneroded surface of the central peak within the East Clearwater Lake structure.

By far the most common deformation features in Hole 1-64 are cataclasites, mostly without any melt associated with them. Over the entire core, these features occur with an average spacing of 4–5 m. The extraordinary length of Hole 1-64, compared to the size of the crater itself, excludes the possibility that Hole 1-64 drilled through only one allochthonous block. Therefore, the observed deformation features in Hole 1-64 must be the primary mechanisms by which deformation is accommodated across the central uplift. Thus, on the macroscopic scale, it is clear that deformation during the formation of a central uplift is primarily accommodated by cataclasites; i.e., “dry” faults without significant volumes of breccia.

Ultimately, the deformation experienced by the rocks of Hole 1-64 from the East Clearwater Lake structure is similar to the deformation experienced by rocks from West Clearwater Lake (Chapter 5). The maximum shock pressures experienced by the recovered para-autochthonous rocks from West Clearwater Lake are slightly higher than those experienced by the para-autochthonous rocks from East Clearwater Lake. Additionally, the most common macroscopic deformation structures in both East and West Clearwater Lake, within drill cores, are cataclasites. Furthermore, the spacing between deformation structures is of a similar order of magnitude between Hole 1-64, from the centre of the East Clearwater Lake structure, and Hole 1-63, from the centre of the West Clearwater Lake structure, where block sizes were estimated to be \sim 10 m (Chapter 5). Here, the average spacing between all deformation features is \sim 3 m, while the average spacing between cataclasites, which accommodate most of the deformation, is \sim 4.5 m. The smaller observed spacing between deformation in Hole 1-64 may be a consequence of the smaller crater size compared to West Clearwater Lake, or a result of more careful logging.

6.4.2 Numerical Modelling

East Clearwater Lake has an apparent diameter, based on morphology, of 24 km; the simulation presented in this Chapter has a rim-to-rim diameter of 20 km. Nevertheless, the local Bouguer gravity anomaly of the structure only possesses a diameter of 20 km, similar to the diameter of the gravity anomaly of the crater modelled in this chapter (Figure 6.10). The magnitude of the predicted gravity anomaly also closely matches the present-day gravity anomaly at the structure, except that the

modelled crater would predict a slight central gravity high. Additionally, the modelled crater possesses structural characteristics similar to the observed characteristics of the crater: a central uplift of para-autochthonous material and an impact melt sheet at \sim 4 km radial distance from the crater centre (defined by the centre of the gravity anomaly), where Hole 2-63 was drilled.

Comparing the shock attenuation patterns in Hole 1-64, from the centre of East Clearwater Lake, and Hole 1-63, from the centre of West Clearwater Lake indicates similar rates of shock attenuation and slightly lower shock pressures in Hole 1-64. These results are reproduced by the numerical simulation of the East Clearwater Lake structure compared to the West Clearwater Lake simulation presented in Rae et al. (2017a) (Figure 6.11). Nevertheless, as seen in Chapter 5, the absolute values of predicted shock pressures are significant (\sim 10–15 GPa) overestimates of observationally-derived peak shock pressures. Additionally, numerical simulations underestimate the measured shock attenuation rates. The consistency of this offset in two impact structures suggests that there is a systematic error associated either with numerical impact simulations or the method of observationally constraining peak shock conditions.

On the whole, it can therefore be seen that the presented model of East Clearwater Lake is well-constrained. One implication of this model, when combined with both gravity and shock data, is that East Clearwater Lake has experienced \sim 1.5 km erosion, relative to the pre-impact surface, since the time of impact. As the West Clearwater Lake impact event occurred after the formation of the East Clearwater Lake structure (Schmieder et al., 2015), this limits the maximum extent of erosion at West Clearwater Lake to no more than 1.5 km. In Chapter 5, it was shown that the West Clearwater Lake impact structure had experienced no less than 1.3 km of erosion. Therefore, this work suggests that there was very little erosion of the Canadian Shield in the regional vicinity of Clearwater Lake between mid-Ordovician and Permian times.

6.5 Conclusions

Observations and simulations of the East Clearwater Lake impact structure show that the granitic rocks within the central uplift of the East Clearwater Lake impact structure have experienced extremely large deformations during cratering. Furthermore, a sequence of deformation styles occur during cratering: Initially, shock metamorphism at pressures from 15 GPa, at the core top, to near 5 GPa at the core bottom. Following shock metamorphism, grain-scale deformation, potentially associated with crater excavation, continued to occur by fracturing. After this, modification related deformation was accommodated on cataclasites, spaced on the meter scale. Finally, impact melts infiltrated the central peak from the overlying impact melt sheet, either during late-stage modification or after cratering, and hydrothermal activity occurred.

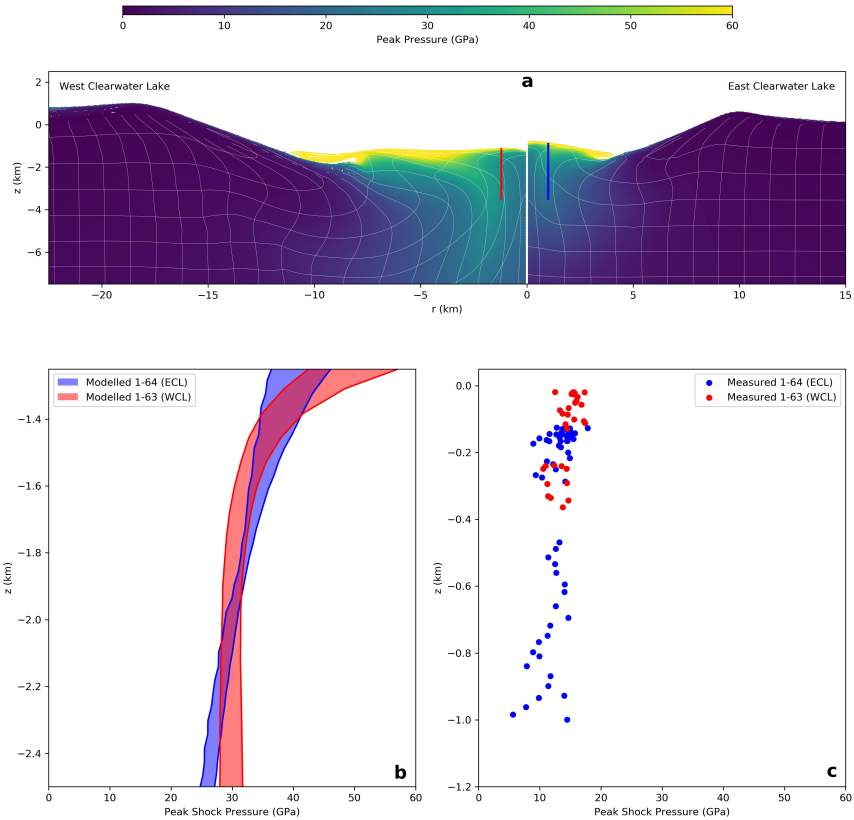


Figure 6.11: Comparison between East and West Clearwater Lake simulations. a) Comparison between crater morphology, deformation, and peak shock pressures in the East Clearwater Lake model presented here and the model of West Clearwater Lake presented in Rae et al. (2017a) (see Chapter 5). Blue and red lines indicate the locations of Holes 1-64 and 1-63 in the East and West Clearwater Lake structures respectively. Beneath, a comparison between modelled (b) and observed (c) shock attenuation patterns at East Clearwater Lake (Hole 1-64) and West Clearwater Lake (Hole 1-63).

The deformation structures that occur in the central uplift of East Clearwater Lake are similar to the structures that can be seen at West Clearwater Lake. Additionally, the shock attenuation rates within the two central uplifts are similar, while East Clearwater Lake has experienced slightly lower shock pressures. This is likely to reflect the smaller size of the impact structure, or, potentially, a greater level of erosion.

A well-constrained numerical model of the East Clearwater Lake impact event has been presented. Constraints of the model include: the approximate crater size based on the gravity signature of the crater, the distribution of shock metamorphism, and present-day morphology of the crater. The presented modelling demonstrates the effectiveness of using the gravity anomaly of a crater to constrain numerical simulations of eroded impact structures. Additionally, this study provides a second example of modelled shock distributions systematically over-estimating observed shock measurements. Modelling of the East Clearwater Lake impact event further constrains the amount of erosion since the time of impact to be ~ 1.5 km, which itself, limits the amount of erosion since the time of the West Clearwater Lake impact event to be < 1.5 km. Hence, erosion in the period between the two impacts was minimal.

Part III

The Chicxulub Impact Structure

7 Introduction to the Chicxulub Impact Structure

The Chicxulub Crater, located in the Yucatán peninsula of Mexico, is a ~ 180 km diameter impact structure. The identification of the Chicxulub structure (Hildebrand et al., 1991; Penfield and Camargo, 1981) was made on the basis of large-scale geophysical signatures: a large negative Bouguer gravity anomaly and magnetic anomalies. The crater is buried, and the only surface expression of its presence is a 180 km diameter ring of cenotes, sinkholes in the Cenozoic limestones that overlie the crater.

Following the discovery of the crater, several attempts were made to constrain the size and structure of the Chicxulub based on forward modelling of potential field data (Espindola et al., 1995; Hildebrand et al., 1995; Hildebrand et al., 1991; Sharpton et al., 1993, 1996). The variation between these models, in terms of structure and the density contrasts between lithologies are large as a consequence of the non-uniqueness of gravity and magnetic modelling, for example, the estimated density contrasts between fractured basement rocks and intact crustal rocks vary between 0 kg m^{-3} and 490 kg m^{-3} , assuming a minimum density of deep crustal rocks to be 2600 kg m^{-3} , this corresponds to porosities from 0%, up to 19%.

Seismic reflection and refraction surveys were carried out at the site in order to resolve the crater and sub-crater structure (Gulick et al., 2008; Morgan et al., 1997). The results of those surveys (Gulick et al., 2013 and refs therein) indicated that the Chicxulub crater possesses:

1. A topographic (inner) rim, ~ 150 km in diameter, hereafter termed the “crater rim”;
2. Non-continuous ring-faults, external to the crater rim; one, the “outer” ring ~ 200 km in diameter, and a second, “exterior” ring ~ 250 km in diameter;
3. An 80–90 km diameter peak-ring which rises up to 400 m above the crater floor;
4. A strong reflector beneath the peak-ring which dips towards the crater centre;
5. A low-velocity zone, $\sim 4\text{ km s}^{-1}$, associated with the peak-ring, which continues downwards and inwards, towards the crater centre, parallel to the dipping reflector;

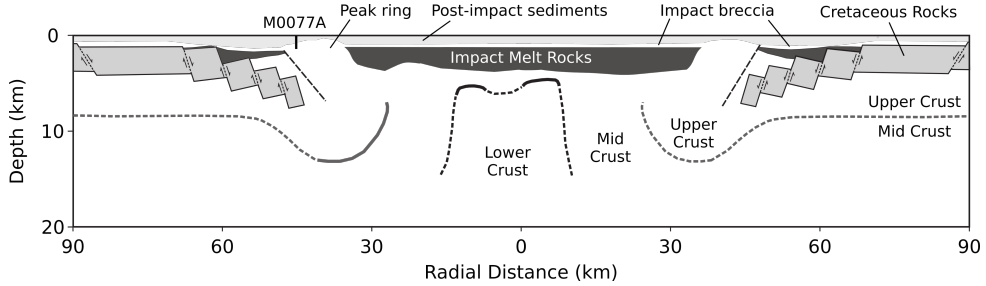


Figure 7.1: Geophysically constrained cross section of upper 20 km of the Chicxulub impact structure. The IODP-ICDP drill site, M0077A, is indicated. Modified from Vermeesch and Morgan (2008).

6. A ring-shaped gravity minimum within the crater at ~ 35 km radial distance, slightly within the peak-ring, associated with the peak-ring structure;
7. A terrace zone that extends inwards from the crater rim, towards and beneath the peak-ring, separated by the dipping reflector;
8. 1.5–2 km of mantle uplift beneath the crater centre.

These results of the geophysical surveys of the Chicxulub Crater motivated the initial numerical simulations of peak-ring formation by dynamic collapse (Collins et al., 2002), and provide important constraints on any model of peak-ring formation. The combination of geophysical constraints with numerical impact models suggest that the peak-ring belongs to the para-autochthonous rocks within the crater, albeit, possessing unusually low densities and seismic velocities. The structure has been drilled on several occasions, many of which were before the identification of the structure as a crater. Figure 7.1 shows a cross-section of the crater on the basis of all geophysical surveys and drillings until the time of the recent IODP-ICDP drilling, Expedition 364.

Prior to impact, the area around Chicxulub was a shallow carbonate platform with water depths of up to a few hundred metres. However, water depths to the north-east would have been 2–2.5 km (Collins et al., 2008b; Gulick et al., 2008). In the shallower parts of the Cretaceous basin, sedimentary rock thicknesses overlying the crystalline basement were approximately 3 km, while the deeper part of the basin to the north-east would have had sedimentary thicknesses up to 4.5 km. Since the time of impact, the basin has been entirely filled by Cenozoic sedimentary rocks.

A comprehensive description of the geophysical characteristics can be found in Gulick et al. (2013).

In 2016, IODP-ICDP Expedition 364 drilled into the peak-ring of the Chicxulub structure (Figure 7.2). One of the primary aims of the expedition was to investigate the mechanism of peak-ring formation (Morgan et al., 2017). The expedi-

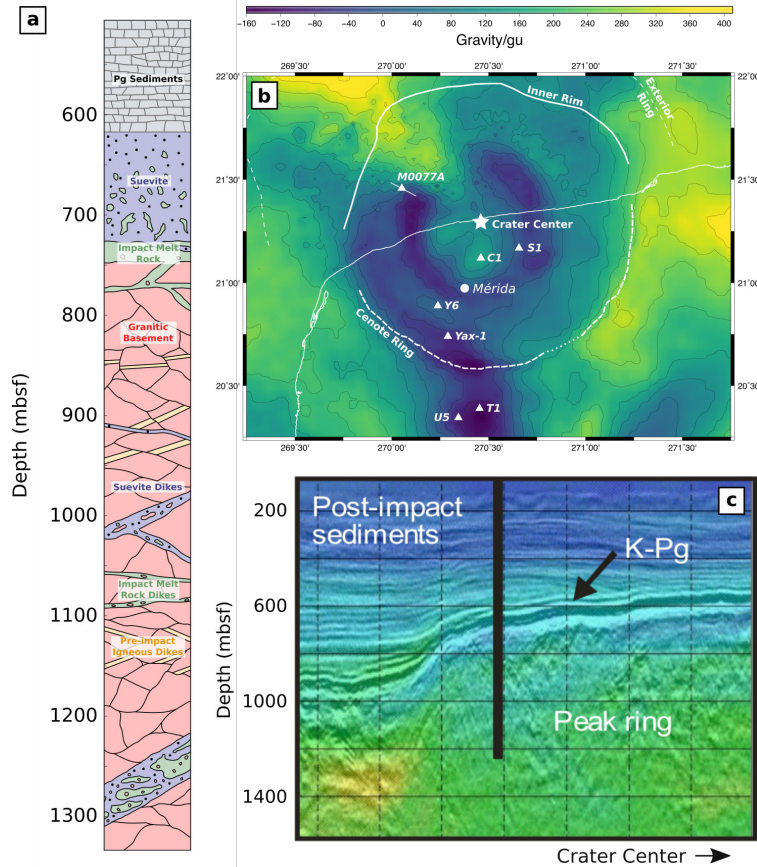


Figure 7.2: a) Schematic stratigraphic log of Hole M0077A. The location of M0077A is indicated on subfigures b) a Bouguer gravity anomaly map of the crater, and c) a radial seismic profile of the peak-ring through the site location. Modified from Gulick et al. (2013) and Morgan et al. (2016).

tion recovered core between 505.42 and 1363.05 mbsf (metres below sea floor) including: from 505.42 - 617.82 mbsf, a sequence of carbonate-rich Palaeogene sedimentary rocks, from 617.82 - 750.25 mbsf, a sequence of allochthonous impactites, predominantly fining-upward suevitic breccias (a polymict breccia containing clasts of impact melt rock/glass) with impact melt rock at its base, and from 750.25 - 1363.05 mbsf, a sequence of uplifted granitic target rocks, with occasional dikes of pre-impact igneous rocks (porphyritic and non-porphyritic dolerites, porphyritic dacite, and a homogeneous fine-grained felsite) and impact-related breccias and melt rocks. A schematic lithological column and location map is shown in Figure 7.2.

Initial analysis of the recovered core provided several constraints on the provenance of peak-ring material and the deformation that those rocks must have experienced during cratering. The occurrence of crystalline rocks at depths of only 750 mbsf

suggests that the crystalline rocks have been uplifted by at least 2.25 km, such that rocks derived from beneath the 3 km-thick Mesozoic sedimentary sequence reach their final location in the peak-ring. Additionally, the presence of abundant quartz PDFs and no diaplectic quartz glasses within the granitic target rocks indicate that the recovered para-autochthon, the shocked target rocks, experienced shock pressures from 10–35 GPa (Morgan et al., 2016). Additionally physical property measurements (Christeson et al., 2018; Morgan et al., 2017) has indicated that the shocked target rocks within the Chicxulub peak-ring has porosities of approximately 10%, a likely contributor to the gravity minimum associated with the peak-ring. Finally, constraints have also been applied to the structural history of the peak-ring rocks by Riller et al. (in press) (see Morgan et al., 2017). Initially, target rocks were pervasive fractured followed, sequentially by the formation of cataclasite zones, ultra-cataclasite zones, shear faults, the emplacement of impact breccias and impact melts into dilatant fractures, and finally, the formation of ductile band structures.

8 Stress and Strain during Complex Crater Formation: Linking Models with Observations

8.1 Introduction

With the recent recovery of a drill-core from the peak-ring of the Chicxulub crater by the International Ocean Discovery Program (IODP) and International Continental Scientific Drilling Program (ICDP), the imperative has arisen for the Dynamic Collapse Model to make quantitative predictions of the deformation path followed by peak-ring material during crater collapse. Here, analysis of the stress-strain path followed by material in the Dynamic Collapse Model of peak-ring formation is presented; quantitatively predicting the stress and strain histories of peak-ring rocks during cratering; constraining the timing, magnitude, and orientation of deformation. This aim will be addressed by the novel implementation of stress and strain tensorial analysis to the results of numerical impact simulations, and the subsequent comparison with observed deformation from the Chicxulub peak-ring.

8.2 Stress and Strain during Shock and Deformation

The formation of the Chicxulub impact structure was simulated using the iSALE shock physics code. iSALE and its precursor codes, SALES-2 (Collins et al., 2002) and SALE-B (Ivanov, 2005) have been used to simulate the formation of the Chicxulub impact structure in previous studies (Collins et al., 2002, 2008b; Ivanov, 2005; Morgan et al., 2016). Here, we present an updated model, including use of a dilatancy model (Collins, 2014), increased resolution, and updating previously used parameters in light of recent advances.

Computational improvements over recent years have permitted us to substantially increase the resolution of the Chicxulub model presented here. We use a resolution of 60 cells per impactor radius, which, with an impactor radius of 6 km, results in a cell resolution of 100 m. iSALE simulations possess a high-resolution zone, with a regular grid spacing, and extension zones at the edges of the high-resolution zone. The purpose of the extension zones is to minimise the effects of reflections from

the boundaries of the mesh. Here, a high-resolution zone, 800 cells \times 1000 cells (i.e. 80 km \times 100 km) was used, ensuring that the entire crater structure (80 km radius) was included within it.

Impactor parameters in previous simulations of the Chicxulub impact event (e.g. Collins et al., 2008b) have used impactor densities, diameters, and velocities of 2630 kg m $^{-3}$, 14 km, and 12.0 km s $^{-1}$, respectively. In this study, we have made modified those parameters; where the impactor density, diameter, and velocity are 2630 kg m $^{-3}$, 12 km, and 15.0 km s $^{-1}$, respectively. The impactor velocity has been increased in the simulation presented here because of the upward revision of the average asteroidal impactor since previous models were published (Le Feuvre and Wieczorek, 2011). 15.0 km s $^{-1}$ was selected as the vertical component of the average impact velocity on Earth, 20.5 km s $^{-1}$. As a consequence of the increase in impactor velocity in this simulation, the impactor diameter has been decreased, to 12 km, from the value used in previous simulations (e.g. Collins et al., 2008b), 14 km, such that the impact energy (and, approximately, the transient cavity diameter) of the presented simulation is consistent with previous models. Nevertheless, we note that there are considerable uncertainties in the choice of impactor diameter. Primarily, this is a consequence of a trade-off between impactor parameters/ transient cavity size and acoustic fluidisation parameters in determining the final crater dimensions. A comparison between the model presented here, previous models, and alternative models is presented within Appendix F. Ultimately, the stress-strain measurements presented here are qualitatively identical to the results of those alternative models.

A three-layer target was chosen to replicate the conditions of the Yucatán platform at the time of impact. A 3 km layer of sedimentary rocks overlies a 30 km layer of crystalline crustal rocks which overlies crystalline mantle rocks. The thermodynamic behaviour of the materials in the model are described by analytical equations of state (ANEOS; Thompson and Lauson, 1974), using parameters described in Pierazzo et al. (1997).

Strength parameters used for the three materials were based on those used in previous models (e.g., Collins et al., 2008b). The constitutive model is supplemented by the block model of acoustic fluidisation, a transient weakening model, such that gravitational collapse of the transient cavity is facilitated (Melosh, 1989; Melosh and Ivanov, 1999). In this simulation, the dilatancy model of Collins (2014) was used.

A list of the parameters used in our simulation is shown in Table 8.1 (Global Parameters) and Table 8.2 (Material Parameters). A full list of parameters may be found in Appendix B.

The analysis of Lagrangian tracer particles permits the tracking of the stress-strain-time path of material during crater collapse. Here, tracers are advected through the grid based on the velocities of the Eulerian grid nodes. The methodology

Table 8.1: Global Model Parameters for Chicxulub simulations. A full list of parameters may be found in Appendix B.

Parameter	Symbol (units)	Value
Cell resolution	(m)	100
Cells per impactor radius		60
Horizontal cells in high resolution zone		1000
Horizontal cells in outer extension zone		200
Vertical cells in high resolution zone		800
Vertical cells in upper extension zone		0
Vertical cells in lower extension zone		200
Impactor velocity	v_i (km s ⁻¹)	15
Impactor density	ρ_i (kg m ⁻³)	2630
Acceleration due to gravity	g (m s ⁻²)	9.81
Surface temperature	T_{surf} (K)	288
Surface temperature gradient	T_{grad} (K m ⁻¹)	0.01
Lithospheric thickness	d_{lith} (km)	100

employed here to quantify stress and strain is an application of the descriptions by Allmendinger et al. (2012), Fossen (2016), Fossen and Tikoff (1993), and Tikoff and Fossen (1995).

8.2.1 Strain Quantification

Rocks undergo deformation during impact cratering. Deformation is the transformation from an initial to a final geometry by means of rigid body translation, rigid body rotation, and/or strain, which can be a distortion or a volume change. Translations and rotations are known as rigid body deformations, while distortions and volume changes are known as non-rigid body deformations (Fossen, 2016). These deformations are variably complex to quantify by observation. Commonly, non-rigid body deformations are the easiest to observationally quantify. Consequently, providing quantitative predictions of deformation, separating translations, rotations, and strains, is of paramount importance to numerical impact simulations.

Here, we quantify deformation during impact simulations by considering a 3D-Lagrangian pseudo-cell i.e. a “logical cube” of neighbouring Lagrangian tracer particles. The three dimensions of the simulation are in a cylindrical coordinate system, corresponding to the radial direction, r , the vertical direction, z , and the azimuth, θ . Thus, the pseudo-cell has an initially square cross-section and is a toroidal sector in shape (Figure 8.1). The coordinates of a pseudo-cell, at a given time, t , can thus be defined as a matrix, tM :

Table 8.2: Material Model Parameters for Chicxulub simulations. A full list of parameters may be found in Appendix B.

Parameter	Symbol	Unit	Mantle (Dunite)	Crust (Granite)	Sediments (Calcite)
Reference Density	ρ	kg m^{-3}	3320	2630	2600
Poisson's ratio	ν		0.25	0.30	0.30
Intact cohesive strength	Y_0	(MPa)	10	10	5
Intact friction coefficient	μ_i		1.2	2.0	1.0
Intact and damaged strength limit	Y_m	(MPa)	3500	2500	500
Damaged cohesive strength	Y_{d0}	(MPa)	0.01	0.01	0.01
Damaged friction coefficient	μ_{di}		0.6	0.6	0.4
Minimum failure strain for low pressure states	ε_{fb}		1×10^{-4}	1×10^{-4}	1×10^{-4}
Constant of proportionality between failure strain and pressure	B		1×10^{-11}	1×10^{-11}	1×10^{-11}
Pressure above which failure is compressional (Pa)	P_c	(MPa)	300	300	300
Melt Temperature	T_m	(K)	1373	1673	1500
Thermal softening coefficient	ξ		1.2	1.2	1.2
Constant in Simon Approximation	p_{bp}		6×10^9	1.52×10^9	6×10^9
Exponent in Simon Approximation	y_0		3.00	4.05	3.00
Acoustic Fluidisation viscosity constant	γ_η		0.025	0.025	0.025
Acoustic Fluidisation decay time constant	γ_T		150	150	150
Vibrational particle velocity as a fraction of particle velocity	C_{vib}		0.1	0.1	0.1
Maximum vibrational particle velocity	Vib_{max}	(m s ⁻¹)	200	200	200
Time after which no new acoustic vibrations are generated	t_{off}		16	16	16
Maximum dilatancy coefficient	β_{max}		0.09	0.09	0.09
Critical distension	α_c		1.2	1.2	1.2
Critical friction coefficient	μ_c		0.4	0.4	0.4
Initial distension	α_0		1.0	1.0	1.0

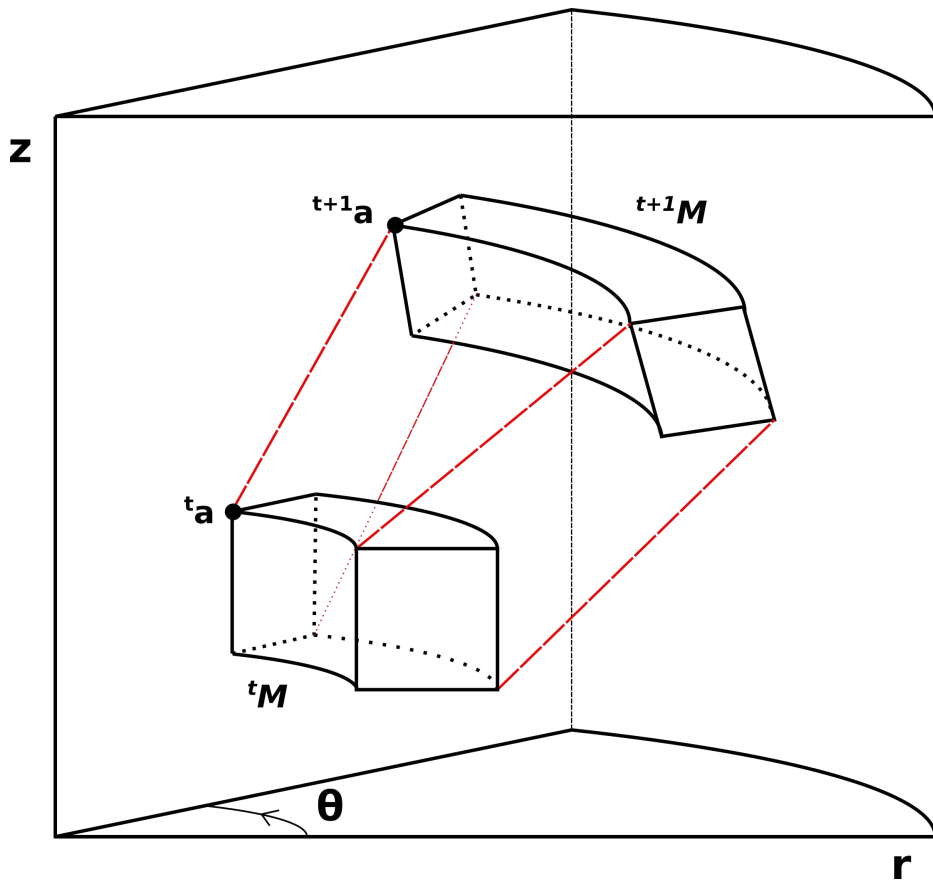


Figure 8.1: Schematic representation of a Lagrangian pseudo-cell at timesteps, t and $t+1$, in black. The coordinates of the tracers within the pseudocell are defined by ${}^t\mathbf{M}$ and ${}^{t+1}\mathbf{M}$, where $\mathbf{a}_{t=i}$ and $\mathbf{a}_{t=i+1}$ are the first columns of the respective matrix. The red lines are a visualisation of the straight-line path along which movement has approximately occurred between the timesteps, it is a visual representation of the displacement gradient tensor (see text).

$${}^t\mathbf{M} = \begin{bmatrix} r_a & r_b & r_c & r_d & r_e & r_f & r_g & r_h \\ z_a & z_b & z_c & z_d & z_e & z_f & z_g & z_h \\ \theta_a & \theta_b & \theta_c & \theta_d & \theta_e & \theta_f & \theta_g & \theta_h \end{bmatrix}, \quad (8.1)$$

where the letters a-h correspond to each individual tracer particle of the pseudo-cell.

The translational part of the deformation between timesteps t and $t + 1$ can be removed by redefining ${}^t\mathbf{M}$ and ${}^{t+1}\mathbf{M}$ such that each component of the matrix is relative to the centroid of the pseudo-cell at the corresponding timestep. Once translations are accounted for by this redefinition, the remaining deformation between timesteps is composed only of a rotation and a strain. Those deformations combined can be characterised by the Deformation Gradient Tensor, ${}^t\mathbf{F}$, which can be calculated by solving the set of simultaneous equations defined by:

$${}^{t+1}\mathbf{M} = {}^t\mathbf{F} \times {}^t\mathbf{M}, \quad (8.2)$$

where ${}^t\mathbf{M}$ and ${}^{t+1}\mathbf{M}$ are known.

By considering the axi-symmetry of the model presented here, it is clear that the θ coordinates of the individual tracer particles can never change between timesteps, consequently, several elements of ${}^t\mathbf{F}$ are zero, meanwhile, though the θ coordinates cannot change, strains may still occur in the θ direction (i.e. hoop direction). For a material that is not undergoing volume change, when translation occurs in the r direction, there must be a corresponding extension or contraction of length in the hoop direction as material diverges, or converges, from the centre respectively. Consequently, if there is ever an r translation, there will always be a strain in the θ direction. Thus, ${}^t\mathbf{F}$ takes the form:

$${}^t\mathbf{F} = \begin{bmatrix} F_{rr} & F_{rz} & 0 \\ F_{rz} & F_{zz} & 0 \\ 0 & 0 & F_{\theta\theta} \end{bmatrix}. \quad (8.3)$$

The deformation gradient field, represented by the deformation gradient tensor, ${}^t\mathbf{F}$, is closely related to the displacement gradient field, represented by the displacement gradient tensor, ${}^t\nabla\mathbf{u}$, by the relation:

$${}^t\nabla\mathbf{u} = {}^t\mathbf{F} - \mathbf{I} = \begin{bmatrix} F_{rr} - 1 & F_{rz} & 0 \\ F_{rz} & F_{zz} - 1 & 0 \\ 0 & 0 & F_{\theta\theta} - 1 \end{bmatrix}, \quad (8.4)$$

where \mathbf{I} is the identity matrix. The displacement gradient tensor is valuable because it describes the displacement vectors that link the pre-deformation state with the post-

deformation state. The velocity gradient tensor, ${}^t\nabla^2\mathbf{u}$, can be calculated from the displacement gradient tensor by dividing each element of ${}^t\nabla\mathbf{u}$ by Δt , this assumes that Δt is sufficiently small that the displacement gradient remains constant over the time increment.

$${}^t\nabla^2\mathbf{u} = \begin{bmatrix} \frac{F_{rr}-1}{\Delta t} & \frac{F_{rz}}{\Delta t} & 0 \\ \frac{F_{rz}}{\Delta t} & \frac{F_{zz}-1}{\Delta t} & 0 \\ 0 & 0 & \frac{F_{\theta\theta}-1}{\Delta t} \end{bmatrix} = \begin{bmatrix} L_{rr} & L_{rz} & 0 \\ L_{rz} & L_{zz} & 0 \\ 0 & 0 & L_{\theta\theta} \end{bmatrix}. \quad (8.5)$$

Strain is a measure that characterises deformation within a body. It can be defined in two ways, according to finite-strain theory or infinitesimal-strain theory. Infinitesimal strain theory makes several assumptions that cannot be made under finite-strain theory. Infinitesimal strains are therefore simpler than finite strains, but rely on the assumption that displacements are insignificantly smaller than the dimension of the body of interest. Specifically, the small angle approximation must apply i.e. solid-body rotations must be less than 10° , to ensure less than 1% error. While impact cratering involves very large strains, this approximation holds to be true in iSALE provided that the time increment between timesteps is suitably small. By the definitions of infinitesimal strain theory, the deformation gradient tensor can be split into an infinitesimal strain tensor, ${}^t\boldsymbol{\epsilon}$, which is symmetrical, and an infinitesimal rotation tensor, ${}^t\boldsymbol{\omega}_i$, which is antisymmetric.

$${}^t\boldsymbol{\epsilon} = \frac{1}{2}({}^t\nabla\mathbf{u} + {}^t\nabla\mathbf{u}^T) = \begin{bmatrix} F_{rr} - 1 & \frac{F_{rz} + F_{zr}}{2} & 0 \\ \frac{F_{rz} + F_{zr}}{2} & F_{zz} - 1 & 0 \\ 0 & 0 & F_{\theta\theta} - 1 \end{bmatrix} = \begin{bmatrix} \epsilon_{rr} & \epsilon_{rz} & 0 \\ \epsilon_{rz} & \epsilon_{zz} & 0 \\ 0 & 0 & \epsilon_{\theta\theta} \end{bmatrix}, \quad (8.6)$$

$${}^t\boldsymbol{\omega}_{ij} = \frac{1}{2}({}^t\nabla\mathbf{u} - {}^t\nabla\mathbf{u}^T) = \begin{bmatrix} 0 & \frac{F_{rz} - F_{zr}}{2} & 0 \\ \frac{F_{rz} - F_{zr}}{2} & 0 & 0 \\ 0 & 0 & 0 \end{bmatrix} = \begin{bmatrix} 0 & \omega_{rz} & 0 \\ -\omega_{rz} & 0 & 0 \\ 0 & 0 & 0 \end{bmatrix}. \quad (8.7)$$

Within the infinitesimal strain tensor, ${}^t\boldsymbol{\epsilon}$; ϵ_{rr} , ϵ_{zz} , and $\epsilon_{\theta\theta}$, represent normal strains, while ϵ_{rz} represents a shear strain contained within the r - z plane. The infinitesimal rotation tensor clearly represents a scalar value, ω_{rz} , which describes the solid-body rotation of the pseudo-cell about the θ axis.

8.2.1.1 Properties of the Strain Tensor

The strain tensor possesses several useful properties that can be used to quantify the state of strain represented by the tensor: principal strains, and strain

invariants. These properties are valuable due to their lack of change if/when the tensor is transformed to a different coordinate system.

For any strain, there exist three orthogonal directions at which there is no shear strain. These are known as the principal strains, and they can be represented by three vectors of a magnitude equal to the strain in that direction. The principal strains of a strain tensor can be found by determining the eigenvalues and eigenvectors of the strain tensor, which respectively, are the magnitudes and orientations of the principal strains. Additionally, the strain tensor possesses three invariant properties, I_1 , I_2 , and I_3 ; known as the first, second, and third strain invariants respectively. These invariants take familiar forms with regards to the strain tensor, ϵ_i :

$$I_1 = \text{tr}(\mathbf{\epsilon}) , \quad (8.8)$$

$$I_2 = \det \begin{bmatrix} \epsilon_{rr} & \epsilon_{rz} \\ \epsilon_{rz} & \epsilon_{zz} \end{bmatrix} + \det \begin{bmatrix} \epsilon_{rr} & 0 \\ 0 & \epsilon_{\theta\theta} \end{bmatrix} + \det \begin{bmatrix} \epsilon_{zz} & 0 \\ 0 & \epsilon_{\theta\theta} \end{bmatrix} , \quad (8.9)$$

$$I_3 = \det(\mathbf{\epsilon}) . \quad (8.10)$$

I_1 and I_2 have important physical interpretations. I_1 is a measure of the hydrostatic part of the strain tensor i.e. it is associated with volumetric strain. I_2 is a measure of the deviatoric part of the strain tensor i.e. it is a measure of the total shear, although here, $\sqrt{I_2}$, will be used, due to its units of linear strain.

A final, useful measure of strain is the kinematic vorticity number, W_k , (Fossen, 2016; Tikoff and Fossen, 1995). W_k has a value of 0 in the case of pure shear, and 1 in the case of simple shear. Values between 0 and 1 denote sub-simple shears. W_k can therefore be thought of as the ratio of simple shear to pure shear. This is of considerable importance when considering the deformation mechanism by which a rock may accommodate strain. The velocity gradient tensor, ${}^t\nabla^2\mathbf{u}$ (Equation 8.5) must be used to calculate W_k , which, in this case, is determined by the simplified expression:

$$W_k = \frac{L_{rz}}{\sqrt{2(L_{\theta\theta}^2 + L_{zz}^2 + L_{rr}^2) + L_{rz}^2}} . \quad (8.11)$$

8.2.2 Stress Quantification

The cause of rock deformation is stress. Stress is the physical quantity that expresses the internal forces that a body experiences due to adjacent material. Similarly

to strain, it is also represented as a tensor quantity, ${}^t\boldsymbol{\sigma}$, and is symmetric. In cylindrical coordinates, it is represented by:

$${}^t\boldsymbol{\sigma} = \begin{bmatrix} \sigma_{rr} & \sigma_{rz} & 0 \\ \sigma_{rz} & \sigma_{zz} & 0 \\ 0 & 0 & \sigma_{\theta\theta} \end{bmatrix}, \quad (8.12)$$

where σ_{rr} , σ_{zz} , and $\sigma_{\theta\theta}$, are normal stresses and σ_{rz} represents a shear stress. The first index indicates that the stress acts on a plane normal to that axis. The second index denotes the direction in which the stress acts. Again, due to the symmetry of the model, σ_{rz} is the only non-zero shear stress.

iSALE calculates the stress tensor as part of its solution cycle for each timestep as an Eulerian field property. Consequently, saving the stress tensor as a Lagrangian tracer particle property requires that the tracer particle saves an interpolated value of the stress tensor within the cell that the tracer particle is within. In order to ensure exact correspondence between the stress tensor and the infinitesimal strain tensor. We linearly interpolate the values of the stress tensor within the Lagrangian pseudo-cell, to make the tensor pseudo-cell centred, and between timesteps, to ensure that the saved stress tensor corresponds to the average stress required to cause the corresponding infinitesimal strain.

8.2.2.1 Properties of the Stress Tensor

The stress tensor possesses several properties that are similar to those of the strain tensor.

Firstly, there exist three principal directions to the stress tensor along which no shear stress is exerted. Similarly to the principal strains, the principal stresses may be determined by calculating the three eigenvalues and eigenvectors of the stress tensor. Principal stresses are represented by the symbols, σ_1 , σ_2 , and σ_3 , which represent the maximum, intermediate, and minimum principal compressive stresses.

Here, I have followed the geological convention and defined the principal stresses as positive when in compression and negative when in tension, n.b. engineering follows the opposite convention, where tensions are positive (Allmendinger et al., 2012). Consequently, for a rock undergoing pure shear, the maximum principal stress will be aligned with the minimum principal strain (i.e. the maximum shortening direction) and the minimum principal stress will be aligned with the maximum principal strain (i.e. the maximum lengthening direction). The principal magnitudes and directions of stress can be determined by obtaining the eigenvalues and eigenvectors of the stress tensor.

The stress tensor can be split into hydrostatic and deviatoric components:

$${}^t\boldsymbol{\sigma} = \begin{bmatrix} P & 0 & 0 \\ 0 & P & 0 \\ 0 & 0 & P \end{bmatrix} + \begin{bmatrix} \sigma_{rr} - P & \sigma_{rz} & 0 \\ \sigma_{rz} & \sigma_{zz} - P & 0 \\ 0 & 0 & \sigma_{\theta\theta} - P \end{bmatrix} = {}^t\mathbf{P} + {}^t\mathbf{s}, \quad (8.13)$$

where ${}^t\mathbf{P}$ is the hydrostatic stress tensor, which contains diagonal elements that each equal to the pressure, $P = \frac{\text{tr}({}^t\boldsymbol{\sigma})}{3}$. ${}^t\mathbf{s}$ is the deviatoric stress tensor. The deviatoric stress tensor possesses eigenvectors that are parallel to those of the stress tensor, and eigenvalues, s_1 , s_2 , and s_3 , that are related to the principal stresses by the relationship:

$$s_{1,2,3} = \sigma_{1,2,3} - P, \quad (8.14)$$

s_1 , s_2 , and s_3 are known as the deviatoric principal stresses.

Furthermore, there are three invariants of the deviatoric stress tensor, denoted J_1 , J_2 , and J_3 . These invariants can be determined following equations similar to Equations (8.8), (8.9), and (8.10), respectively. J_2 is of particular physical significance as it is a measure of the deviatoric part of the stress tensor i.e. it is a measure of the shear stress. Nevertheless, $\sqrt{J_2}$ is commonly used because it has units of Pa.

8.3 Results

The above analysis was used to examine the stress-strain paths of material within a simulation of the Chicxulub impact event. Of the para-autochthonous rocks within a large impact structure, rocks within the peak-ring experience the most extreme deformation during modification. For this reason, and due to the recent IODP-ICDP drilling of the Chicxulub peak-ring, the peak-ring materials will be focussed upon specifically. Here, peak-ring material is defined based on a number of criteria:

1. Peak-ring material in the Chicxulub Crater occurs no further than 45 km from the crater centre and no less than 30 km;
2. Peak-ring material must be solid at the end of the simulation. Melted material is distinguished by peak shock pressures > 60 GPa.
3. Peak-ring material must derive from within the central uplift, this is defined at the time of maximum central uplift (~ 200 s for a Chicxulub-sized simulation on Earth). The central uplift is defined as any material within the trough that surrounds the uplift at this time, and within 10 km of the free surface.

The location of the material that satisfies these three criteria, the peak-ring rocks, is shown on Figure 8.2 throughout the simulation.

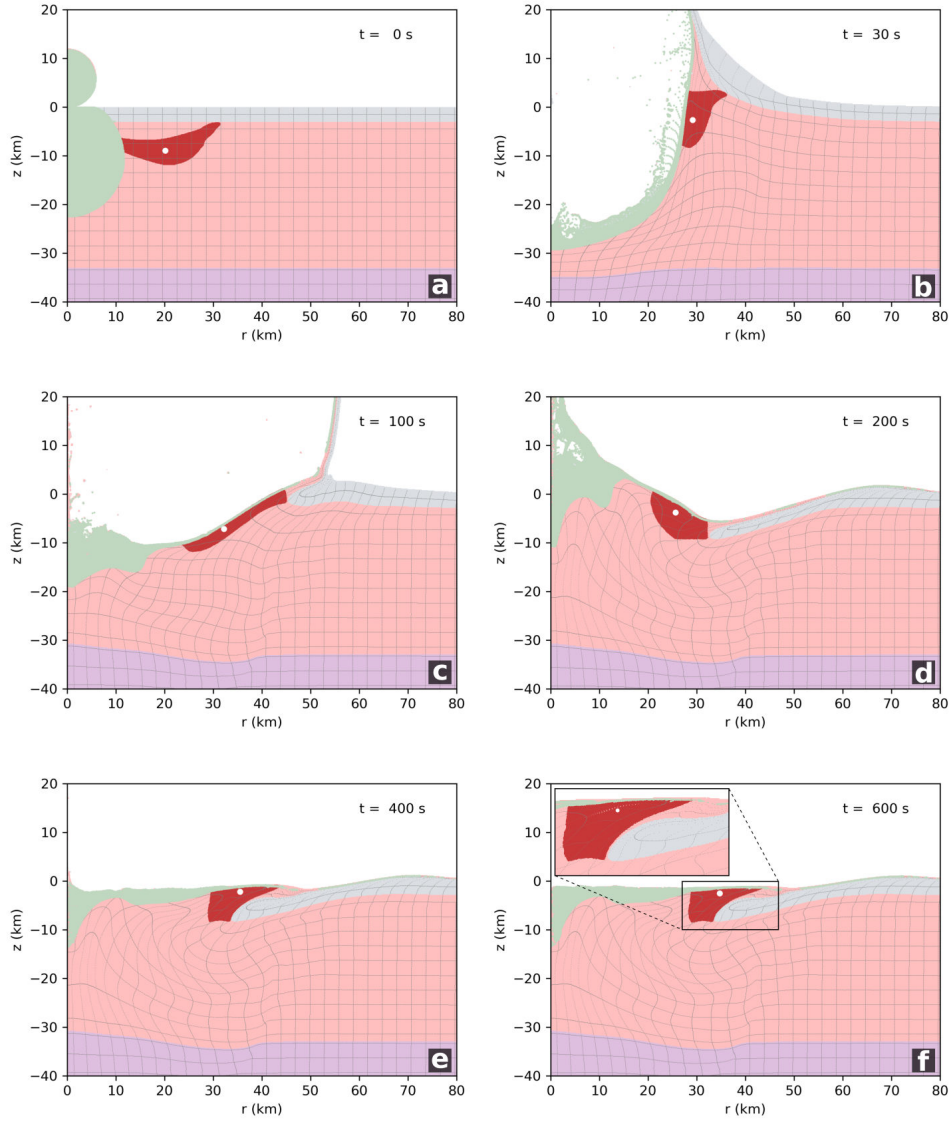


Figure 8.2: Selected timesteps of the presented Chicxulub simulation. The target is comprised of three layers; Sedimentary Rock (Grey), Granitic Basement (Pink), and Mantle (Purple). A grid of tracer particles is shown to highlight the sub-crater deformation. Additionally, in the first frame, a), the provenance of impact melt and the peak-ring is shown in green and red respectively. The impact melt and peak-ring material is then tracked throughout the steps b) - f). The location of a single pseudo-cell (white) is shown throughout the simulation.

The peak-ring originates from 5-12 km depth, and 10-30 km radial distance (Figure 8.2a). After shock, decompression, and transient cavity growth, the material moves outwards, into the transient cavity wall (Figure 8.2b). This material subsequently collapses inwards (Figure 8.2c) and becomes entrained into the flank of the central uplift (Figure 8.2d). At this time, the central uplift is over-heightened, and collapses radially outwards (Figure 8.2e), emplacing the peak-ring on top of the collapsed transient cavity rim (Figure 8.2f). The results presented here will use a single Lagrangian pseudo-cell from within the centre of the peak-ring material, and is thus representative of the stress-strain history of the entire peak-ring. This pseudo-cell originates from 20.2 km radial distance and 8.95 km depth, and ends at 35 km radial distance and 2.5 km depth. The sequence of deformation of this cell will be described chronologically in the following sections.

8.3.1 Shock and Decompression

The first stage of impact related deformation to affect the peak-ring rocks is shock and decompression. The strain pathway of the selected pseudo-cell during this stage is shown in Figure 8.3. Deformation is characterised by an initial, rapid horizontal compression of the material as it is shocked, this results in a sharp reduction in the volume of the material (negative volumetric strains), and a sharp increase in shear strain. During these few milliseconds, strain rate reaches its maximum throughout the entire simulation, 0.17 s^{-1} , n.b. this value may be a slight underestimate due to:

1. Artificial viscosity (see 3.2.1.5);
2. Spatial and temporal resolution;
3. The time interval between saved timesteps, which during this time of the simulation is 0.1 s.

As decompression occurs, the strain rate rapidly drops, volumetric strain increases and becomes positive (due to pressure release). Throughout the entire stage of deformation, there is a negligible amount of rotation of the material from its initial orientation.

During shock and decompression, pressures and shear stresses rapidly increase. For the selected pseudo-cell, the arrival of the stress wave occurs at 2.10 s (Figure 8.4).

Most of the peak-ring material never experiences shock pressures greater than $\sim 40 \text{ GPa}$, therefore the peak-ring material experiences shock metamorphism from a plastic wave with an elastic precursor. The stress wave exceeds the Hugoniot Elastic Limit (HEL; 3.56 GPa for the granite strength properties used here) at 2.43 s where

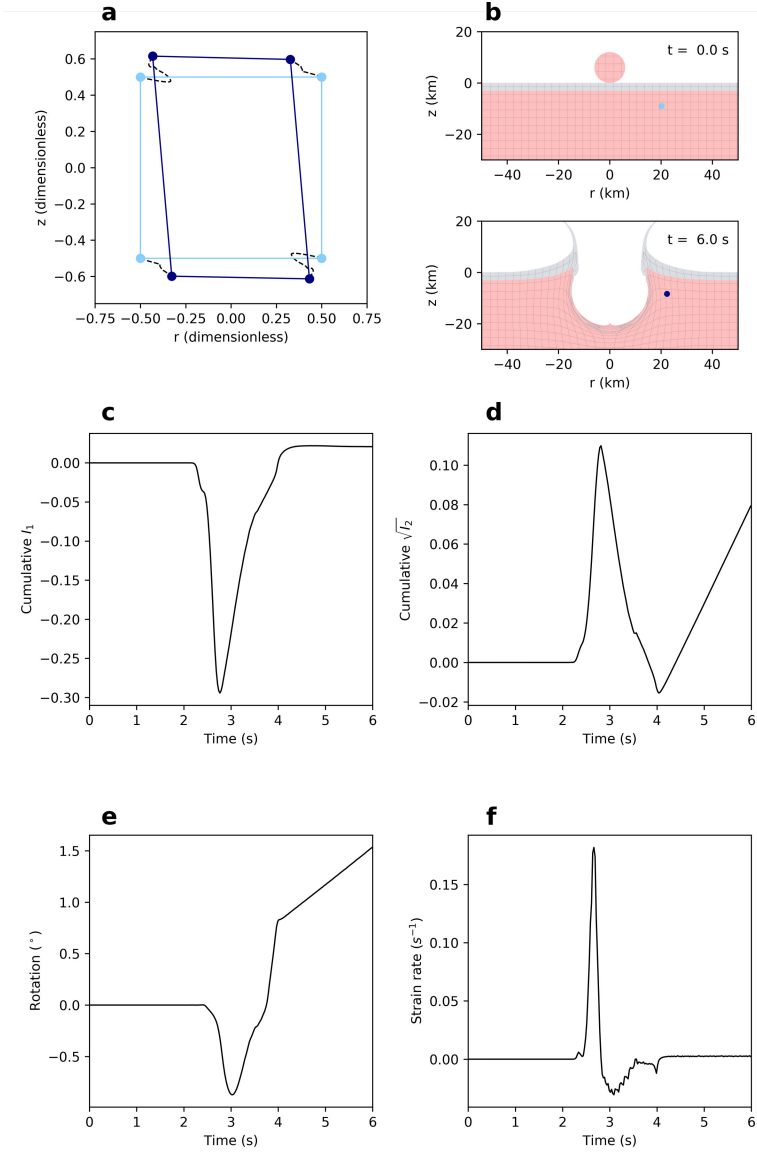


Figure 8.3: Strain path of the Lagrangian pseudo-cell during shock and decompression.
 a) r - z cross-section of the pseudo cell at $t = 0.0\text{ s}$ (Light Blue) and $t = 6.0\text{ s}$ (Dark Blue). The pathway of the individual tracers relative to each other through time is indicated by the dashed lines. b) The initial ($t = 0.0\text{ s}$), and post-shock ($t = 6.0\text{ s}$) arrangement of the simulation, see Figure 8.2. c) The cumulative First Strain Invariant, I_1 . d) The cumulative square root of the Second Strain Invariant $\sqrt{I_2}$. e) Cumulative rotation (i.e. orientation) of the material. f) Strain rate (i.e. the rate of change of $\sqrt{I_2}$ with respect to time).

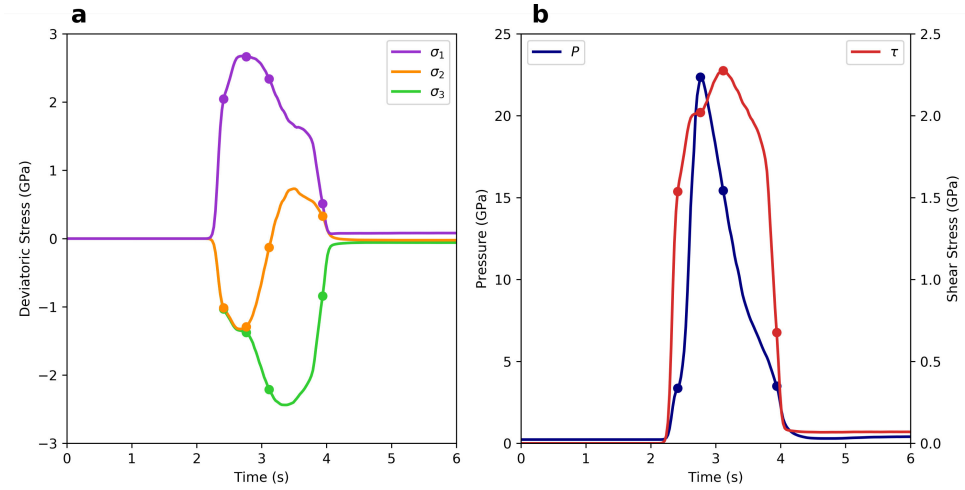


Figure 8.4: Stresses in a shock wave. a) The deviatoric principal stress magnitudes within the pseudo-cell. b) The shock pressure (P) and maximum resolvable shear stress ($\tau = \frac{\sigma_1 - \sigma_3}{2}$) through time during shock and decompression. Points on the curves at $t = 2.43, 2.78, 3.13$, and 3.95 s, refer to the times at which the HEL is exceeded, maximum pressure is reached, maximum τ is reached, and when shock attenuates beneath the HEL, respectively.

the maximum resolvable shear stress is 1.6 GPa. Pressures subsequently increase in the plastic wave up to 22.2 GPa at 2.78 s and where the maximum resolvable shear stress is 2.02 GPa. At this moment of the peak shock condition, the rarefaction wave arrives and subsequently pressure decreases. Nevertheless, the maximum resolvable shear stress increases until 3.13 s, where the pressure is 15.5 GPa, and the maximum resolvable shear stress is 2.28 GPa. The cause of the increase in shear stress as pressure decreases in the wave is the rarefaction wave increasing the intermediate deviatoric principal stress from tensile to compressive values. By 3.95 s, the stress wave possesses a pressure less than the HEL. Nevertheless, after this time, the pressure and shear stress do not return to their pre-stress values, instead, they remain slightly higher as a consequence of the remnant post-shock velocity imparted to the material.

Throughout shock and decompression, the orientations of the principal stresses change. The cause of principal stress rotation is due to the combined effects of refraction, and, later, the interaction of the shock and rarefaction waves. Initially, when the HEL is exceeded ($t = 2.43$ s), the maximum principal stress within peak-ring material plunges inwards (15.2°) while the minimum principal stress is near vertical, and has a similar value to the intermediate principal stress oriented in the hoop direction. By the time of peak shock conditions ($t = 2.78$ s), the maximum principal stress has rotated to become near horizontal (3.2° inwards), while the minimum principal stress becomes vertical. At this time, the intermediate principal stress has a similar magnitude

to the minimum principal stress. By the time of maximum resolvable shear stress ($t = 3.13$ s), the maximum principal stress orientation has continued to rotate and plunges outwards (31.5°). At this time, the intermediate principal stress, s_2 is equal to the pressure (i.e. $s_2 = 0$), and remains in the hoop direction. By the time that the shock pressure decreases to the HEL ($t = 3.95$ s), maximum principal stress is oriented steeply (51.6° outwards). At this time, the intermediate deviatoric principal stress is nearly equal to the maximum principal stress. This history of stress orientations can be seen in Figure 8.4.

8.3.2 Transient Cavity Formation

Following Elbeshausen et al. (2009), the transient crater is defined in numerical simulations as the cavity with the maximum volume. Maximum cavity volume occurs in the simulation presented here at $t = 30$ s, even though maximum cavity depth occurs at $t = 20$ s and rim growth continues beyond $t = 30$ s.

Deformation during transient cavity growth is characterised by continued radial shortening as the transient cavity wall moves outwards (Figure 8.6) due to the remnant velocity of the rocks after shock; i.e., the excavation flow field. Following strain rates on the order of 10^{-1} s $^{-1}$ during shock, strain rates rapidly decrease to values of the order 10^{-3} s $^{-1}$ and these strain rates decrease only slightly throughout transient cavity growth. The kinematic vorticity number during transient cavity growth is always less than 0.3, indicating that deformation is dominated by pure shear. The preceding shock and decompression stage has kinematic vorticity numbers between 0.3 and 0.4, and kinematic vorticity numbers increase towards the end of transient cavity formation. Additionally during this stage of deformation, the material initially rotates clockwise about the hoop direction by approximately 6° before beginning to rotate anti-clockwise from 25 s after impact.

The orientation of stresses during transient cavity growth remains consistent throughout and follows the excavation flow field (Figure 8.7). Initially ($t = 6.0$ s), the pressure and deviatoric stresses are high and the maximum principal stress plunges gently outwards (8.8°), these stresses rapidly decrease until $t = 15$ s, after which, they remain comparatively constant. Nevertheless, the orientation of the maximum principal stress continues to rotate such that by $t = 30$ s, the maximum principal stress plunges gently inwards (10.1°). Throughout this stage of deformation, the intermediate deviatoric principal stress is tensile and is oriented in the hoop direction. Additionally, the proportional difference between σ_1 , σ_2 , and σ_3 remains constant. During this stage of cratering, transient strength reduction has no influence on deformation.

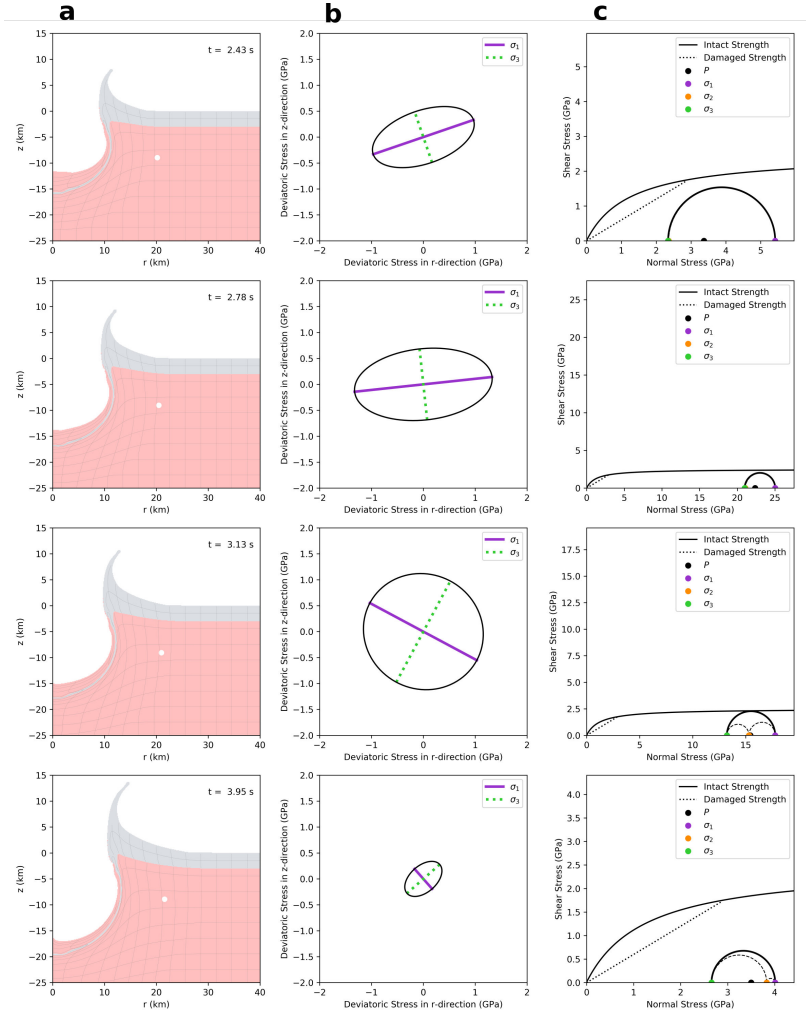


Figure 8.5: Stress orientations and magnitudes during shock and decompression. a) Crater growth at timesteps indicated on Figure 8.4 with location of the pseudo-cell indicated by the white marker. b) Major and minor axes of the r - z cross section of the deviatoric Lamé's stress ellipsoid at corresponding times, solid lines indicate compressive deviatoric stresses, while dashed lines indicate tensile deviatoric stresses. c) Mohr's circle representation of the conditions of stress at corresponding times. Solid and dotted lines indicate the strength envelope of material at standard conditions, intact and damaged respectively, these envelopes are drawn such that shear stress is measured by $\sqrt{J_2}$, rather than $\frac{\sigma_1 - \sigma_3}{2}$. Consequently, material is still at failure even though the Mohr circle may not be in contact with the strength envelopes.

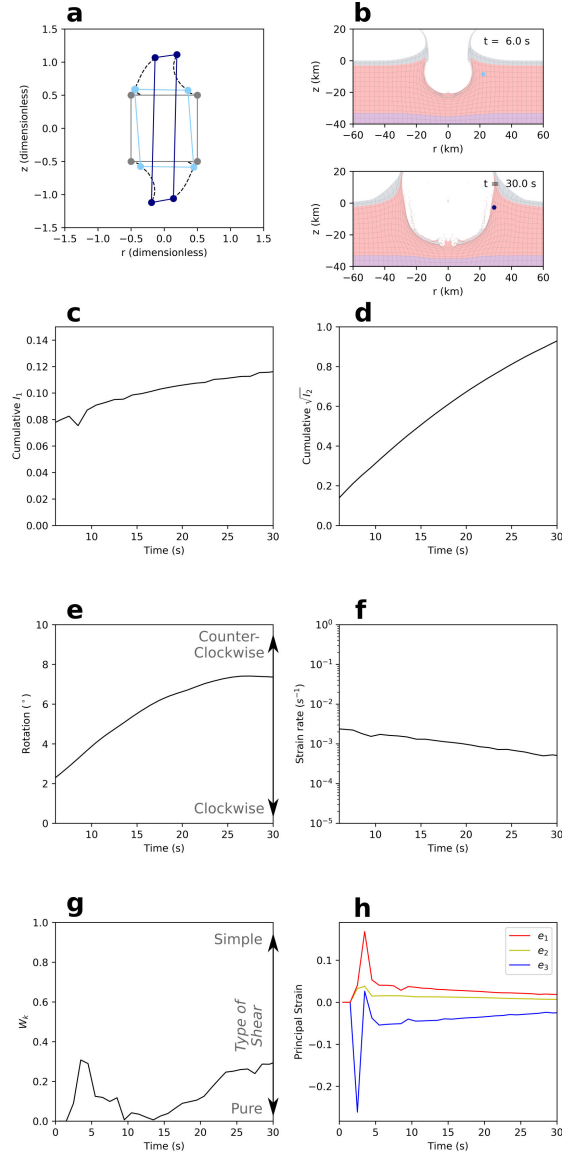


Figure 8.6: Strain path of the Lagrangian pseudo-cell during transient cavity growth. a) r - z cross-section of the pseudo cell at $t = 6.0$ s (Light Blue), $t = 30.0$ s (Dark Blue), and the original pseudo-cell at $t = 0.0$ s (Grey). The pathway of the individual tracers relative to each other through time is indicated by the dashed lines. b) The post-shock ($t = 6.0$ s), and transient crater ($t = 30.0$ s) arrangement of the simulation, see Figure 8.2. c) first strain invariant, I_1 . d) second strain invariant I_2 . e) cumulative rotation (i.e. orientation) of the material. f) strain rate (i.e. the rate of change of I_2 with respect to time). g) kinematic vorticity number. h) principal strain magnitudes.

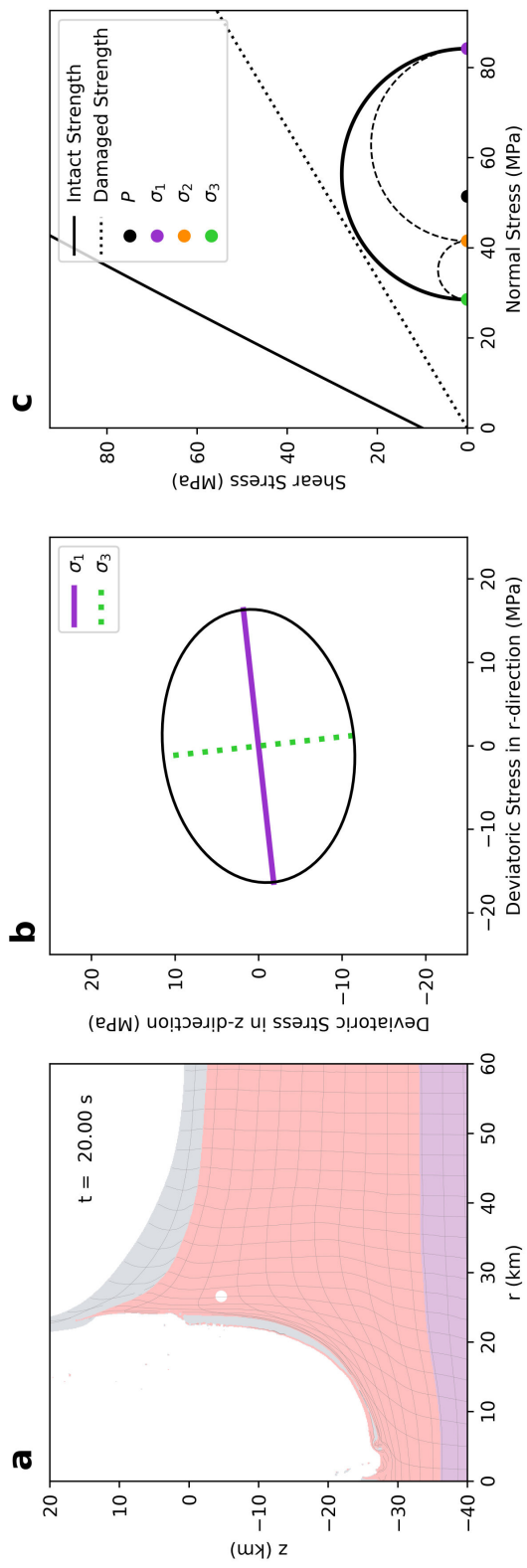


Figure 8.7: Stress orientation and magnitude during transient cavity growth. a) Crater shape at $t = 20$ s, with the location of the pseudo-cell indicated by the white marker. b) Major and minor axes of the r - z cross section of the deviatoric Lamé's stress ellipsoid, solid lines indicate compressive deviatoric stresses, while dashed lines indicate tensile deviatoric stresses. c) Mohr's circle representation of the conditions of stress. Solid and dotted lines indicate the strength envelope of material at standard conditions, intact and damaged respectively.

8.3.3 Modification

The stress-strain-time path during crater modification for peak-ring material is complex (Figure 8.8). Nevertheless, the deformation can be subdivided into 5 qualitatively and quantitatively different phases:

1. Rim Growth ($t = 30\text{--}90\text{ s}$)
2. Inward Transport ($t = 90\text{--}126\text{ s}$)
3. Central Peak Entrainment ($t = 126\text{--}236\text{ s}$)
4. Outward Transport (peak-ring emplacement) ($t = 236\text{--}268\text{ s}$)
5. Relaxation ($t = 268\text{--}600\text{ s}$)

The initial and final timesteps of these phases are shown in Figure 8.8. Quantitative measures of the strain path are shown in Figure 8.9.

8.3.3.1 Strain

The first phase of crater modification, from the perspective of peak-ring material, Rim Growth ($t = 30\text{--}90\text{ s}$), is characterised by the deceleration of the material in the radial direction and the onset of significant clockwise (with respect to the hoop direction) rotation (30°), this rotation occurs as a consequence of the differential velocities of material above and beneath the peak-ring material. Beneath, material is beginning to collapse towards the crater centre, while above, material is still being excavated radially outwards. This differential velocity field also causes an increase in the relative amount of simple shear compared to pure shear; kinematic vorticity numbers increase from 0.3 to 0.95. Throughout this phase, the instantaneous principal strains all decrease in magnitude, and strain rates decrease steadily from 10^{-3} to 10^{-4} s^{-1} (Figure 8.9). The minimum principal strain (e_3) remains perpendicular to the cavity wall while the maximum principal strain (e_1) is also contained within the r-z plane.

The transition to the next phase of crater modification, Inward Transport ($t = 90\text{--}126\text{ s}$), is characterised by the switching of the orientations of the minimum and intermediate principal strains. The minimum principal strain, for the first time in the simulation becomes oriented in the hoop direction, i.e. the maximum shortening direction is concentric. This switch is a result of the inward transport of the peak-ring material as the transient crater wall collapses causing convergence of flow into the centre of the crater. As the material flows inwards, anti-clockwise rotation continues, however, strain rates abruptly decline to 10^{-5} s^{-1} , and thus, this phase of modification is accompanied by comparatively small amounts of non-rigid body deformation (Figure 8.9).

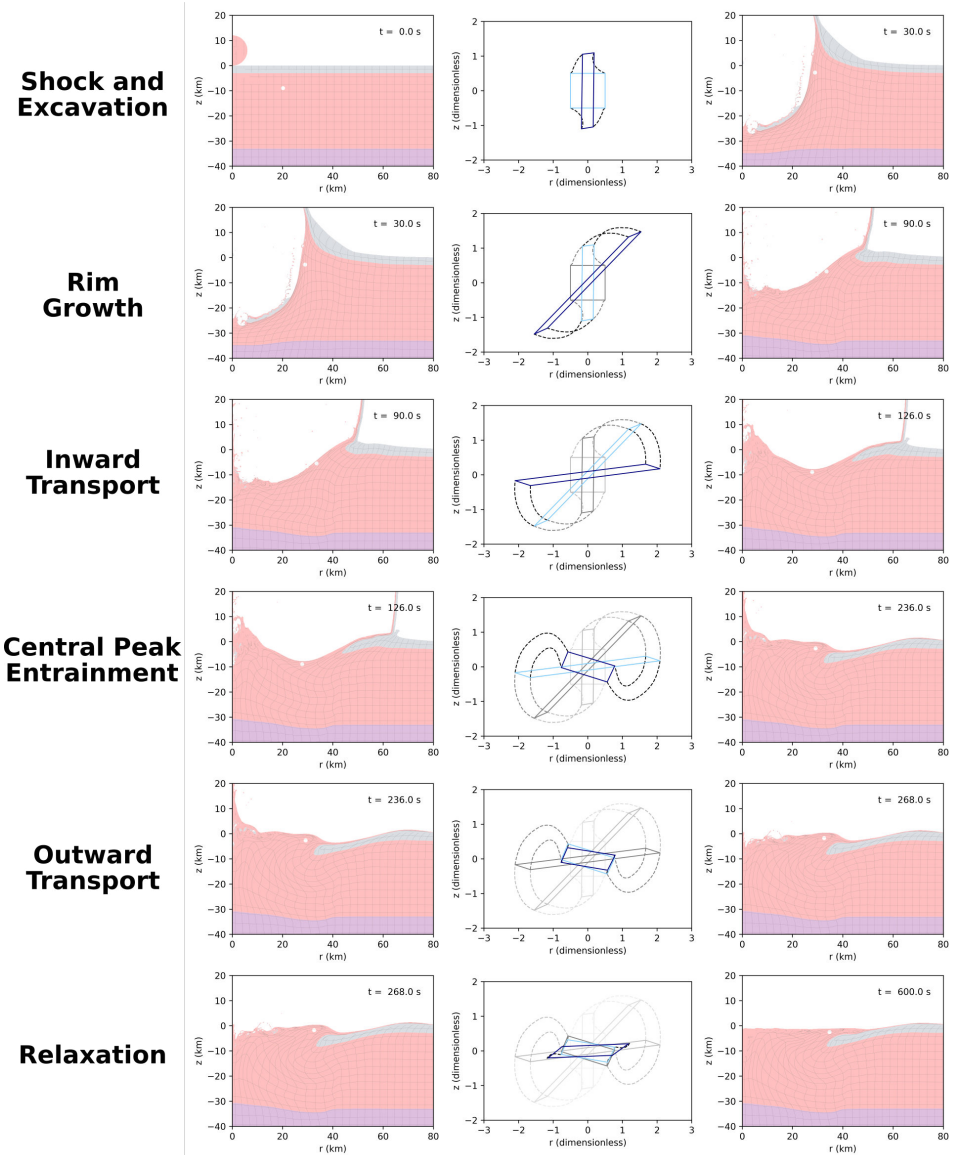


Figure 8.8: Strain stages during modification. Each row shows the first and last arrangement of the crater with the deformation of the indicated Lagrangian pseudo-cell.

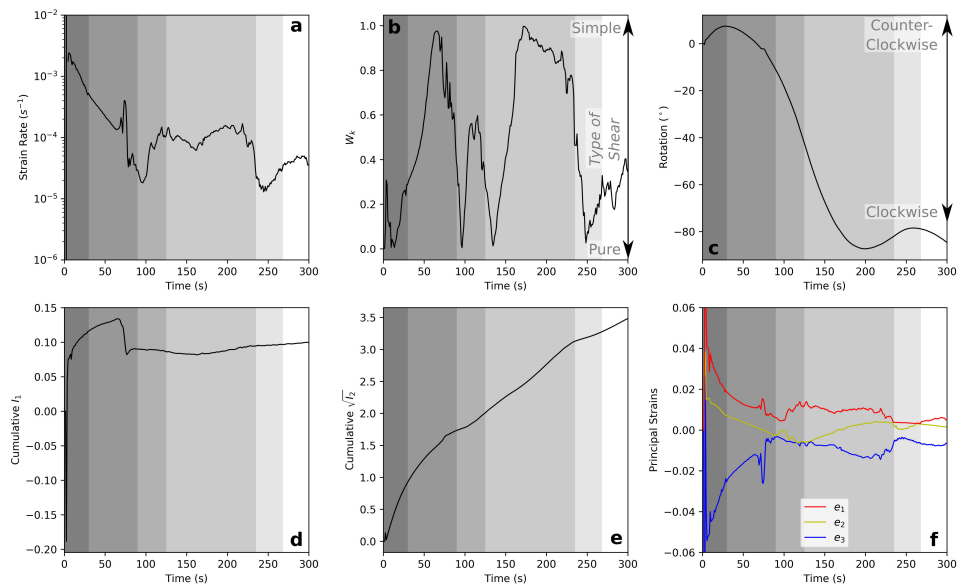


Figure 8.9: Quantification of strain during the phases of crater modification, the duration of each phase is indicated by the grey highlighting beneath the plots. Individual plots show; a) strain rate, b) kinematic vorticity number, c) cumulative material rotation (i.e. orientation), d) cumulative I_1 , e) cumulative $\sqrt{I_2}$, and f) instantaneous principal strains through time.

The inward velocity experienced by the peak-ring material during Inward Transport ceases as the peak-ring material is entrained into the flank of the rising central uplift (Figure 8.2d). Central Peak Entrainment ($t = 126\text{--}236$ s) occurs as the central peak is rising (until $t = 175$ s), and during the initial collapse of the over-heightened central peak. During this phase, and slightly before, for the only time in the simulation after shock, strain rates increase, reaching and maintaining rates of 10^{-4} s $^{-1}$. During this phase, anticlockwise rotation of the peak-ring material continues until slightly after the central peak reaches its maximum height. At this time, the material has reached a total rotation of approximately 90° , such that originally initially horizontal layers would be vertical. Additionally, while the central uplift builds, the maximum principal strain is oriented sub-vertically, while the minimum principal strain (maximum shortening), is oriented sub-horizontally. Later, at the time of maximum central uplift, when the material finally ceases all inward movement and begins to move outwards, the material and the principal strains begin to rotate clockwise (about the hoop direction). By the end of the deformation phase, the minimum principal strain plunges inwards (23.4°), parallel to the direction in which the peak-ring is emplaced. The onset of the central peak collapse also causes an increase in the kinematic vorticity number from 0.1 to 0.9, indicating a transition from pure shear to simple shear.

The transition from the Central Peak Entrainment phase to the Outward Transport phase ($t = 236\text{--}268$ s) is marked by a rapid decrease in strain rate, from 10^{-4} s $^{-1}$ to 10^{-5} s $^{-1}$, and a change in the orientation of the principal strain axes, whereby, the now outwardly directed velocity of the material causes maximum principal extension in the hoop direction. This is the only time in the simulation where the maximum instantaneous stretch is in the hoop direction.

As the peak-ring is emplaced outwards, its radial velocity gradually decreases and the peak-ring comes, on average, to rest. After this occurs, the peak-ring undergoes Relaxation ($t = 268\text{--}600$ s), this phase of deformation occurs at comparatively small strain rates, declining from 10^{-5} s $^{-1}$ to 10^{-8} s $^{-1}$.

The five phases of the modification stage of impact crater formation are marked by distinctly different strain ellipsoids (Figure 8.10). The first phase, Rim Growth, as well as the Contact and Excavation stage, produce oblate strain ellipsoids (flattening). The Inward Transport phase is marked by a moderately prolate strain ellipsoid (constriction). The remaining phases of modification occur under near plane strain conditions, progressing from slightly constrictional to slightly flattening strains as time continues. This indicates that rocks deformed during the earliest stages cratering should have abundantly developed planar fabrics (S-tectonites) while deformation structures developed during later cratering phases should develop some linear fabrics (L-tectonites, or more realistically LS-tectonites).

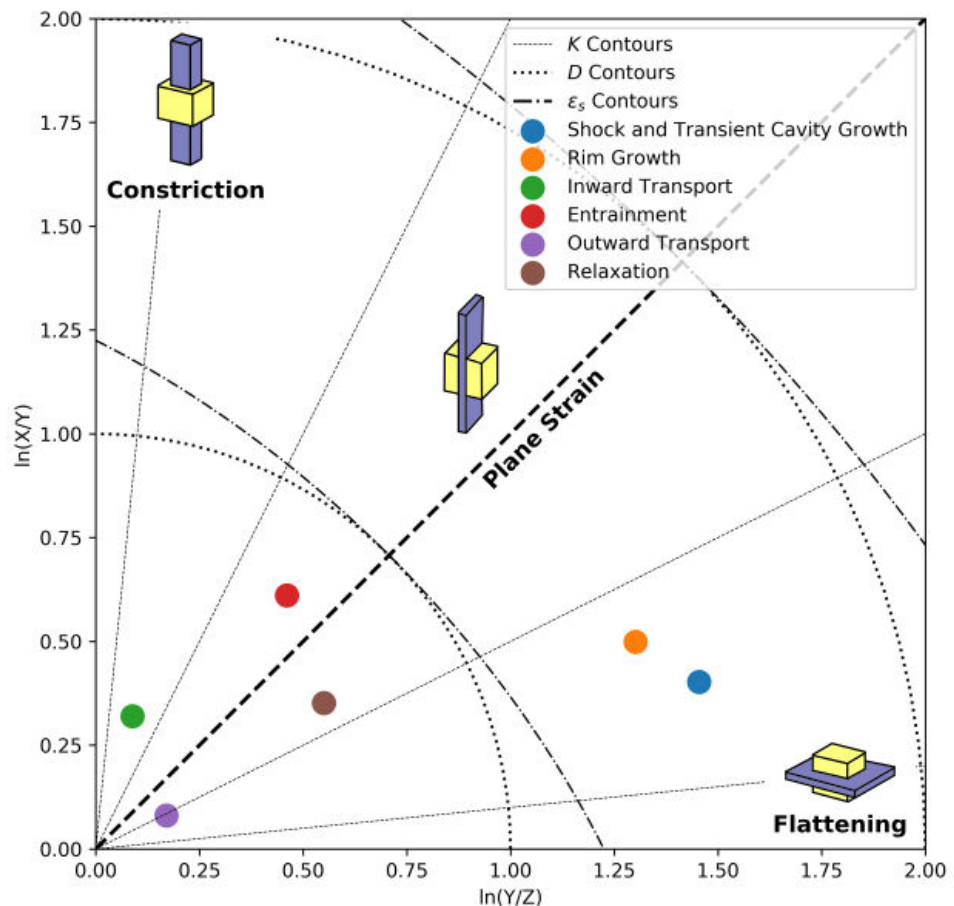


Figure 8.10: Flinn-Ramsay Diagram of strain ellipsoids corresponding to each phase of peak-ring formation. K-numbers and D-numbers/ octahedral shear strain (ε_s), which respectively describe the shape of the strain ellipsoid and the magnitude of strain, are contoured.

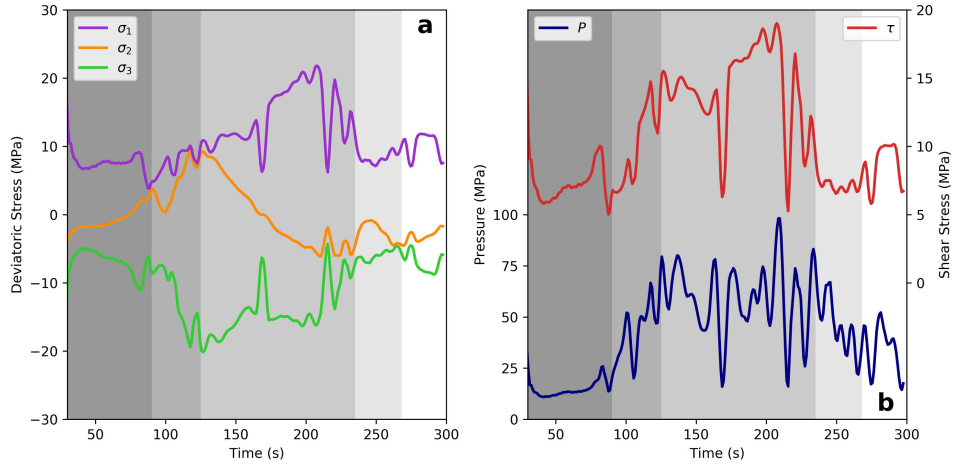


Figure 8.11: Stress magnitudes and pressure through time during crater modification, modification phases are highlighted as grey areas beneath: a) Principal deviatoric stress magnitudes. b) Pressure and maximum resolvable shear stress.

8.3.3.2 Stress

During these phases of deformation, the peak-ring material experiences a sequence of stress states as complex as, and related to, the strain path that the material follows. Figure 8.11 shows the history of deviatoric principal stresses and pressure during the first 4 phases and into the final phase of the crater modification stage.

During the earliest phase of modification, Rim Growth, the peak-ring material experiences pressures from 5 to 25 MPa and shear stresses of approximately 5 to 10 MPa. During this phase, the maximum principal stress orientation plunges inwards, parallel to the cavity wall, consequently, it rotates from steeply to shallowly inclined as the crater rim continues to grow.

Through the Rim Growth phase, the intermediate principal stress, which is oriented in the hoop direction, increases until, as the Inward Transport phase begins, the hoop stress exceeds the wall-parallel stress. This occurs as a result of the inward convergence of the peak-ring material. During this phase, as the material converges into the building central peak, pressures and shear stresses increase to in excess of 50 MPa and 15 MPa respectively.

As the inward transport of material meets increasing resistance against the rising central uplift during entrainment, the radial, wall-parallel stress begins to exceed the hoop stress. Meanwhile, the minimum deviatoric principal stress decreases causing large shear stresses during the central peak entrainment phase. Pressure in the peak-ring material during entrainment reaches up to nearly 100 MPa. During this phase, the

maximum principal stress orientation rotates from plunging gently outwards, through horizontal to plunging inwards until the central uplift reaches its maximum height at $t = 175$ s. Whereupon, the maximum principal stress remains in the same orientation as the central uplift begins to collapse.

As the peak-ring material moves outwards during the collapse of the central peak, the hoop stress, which is intermediate during entrainment, continually decreases and becomes the minimum principal stress as the outward transport phase begins. During this phase, the maximum principal stress plunges inwards. This orientation gradually becomes less steep as the peak-ring is emplaced; simultaneously, pressures in the peak-ring material gradually decrease as the peak-ring loses height due to vertical shortening associated with hoop-directed extensional strains.

The relaxation phase of modification occurs as the stress state of the rocks returns to normal lithostatic conditions. The beginning of this phase is marked by the hoop stress becoming intermediate. As this phase continues, the maximum principal stress rotates to become vertical, i.e. becomes entirely composed of the lithostatic stress. During this phase, all but the most superficial material, melt and high-temperature rocks, of the peak-ring cease to move.

8.3.4 Accumulated Deformation throughout Cratering

Throughout the entire process of peak-ring formation, the peak-ring material accumulates deformation. Deformation can be accommodated in rocks by a variety of different mechanisms depending on, but not limited to, the deviatoric stresses, the strain rate, and the type of shear or change in volume. Shear strain accumulation for the peak-ring occurs in three distinct phases. Firstly, during shock deformation, which occurs in the first few seconds of cratering. Secondly, during transient cavity formation and the growth of the crater rim during modification, which occurs during the first 100 s of cratering. Finally, during the subsequent modification phases, from 100–600 s. The modelled total shear strain is closely related to the total volumetric strain (Figure 8.12), and thus porosity. The simulation presented here suggests that peak-rings accumulate approximately half of their distension during transient cavity formation and rim growth, and the rest during subsequent modification. While accumulating almost no distension during shock deformation.

8.4 Discussion

Before proceeding to compare the observed deformation from the Chicxulub peak-ring, it is necessary to consider the errors associated with analysis of a numerical simulation in this way. Here, we have focussed upon the stress-strain history of just

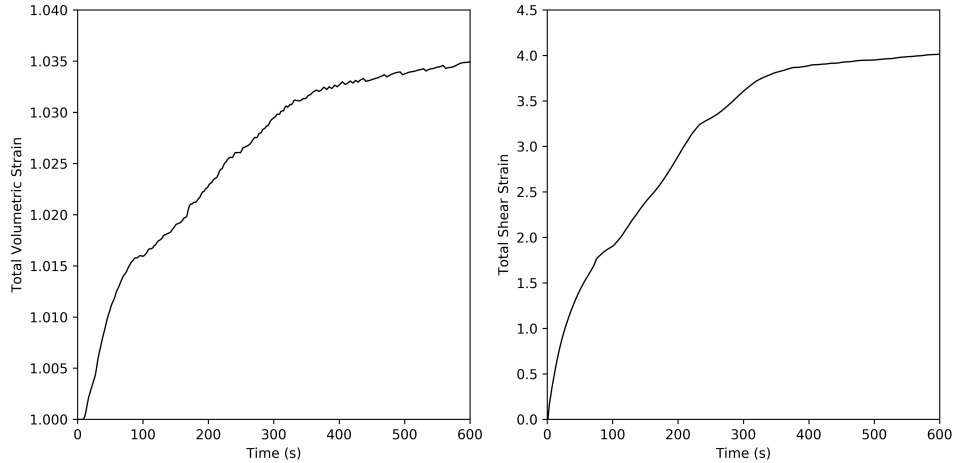


Figure 8.12: Total volumetric and shear strains through time.

one Lagrangian pseudo-cell. The exact location of this pseudo-cell does not directly correspond to the location of the recent IODP-ICDP drill core. The primary reason for this chosen difference is that Lagrangian tracer particles close to the free surface, where there is limited confining pressure can behave without coherency to their neighbouring tracer particles, thus removing any meaning from calculated strain information. Instead the location of the selected pseudo-cell was chosen to be at the centre of the peak-ring material, such that it would be representative of the deformation of the entire peak-ring structure. The stress-strain history of other pseudo-cells within the peak-ring is qualitatively identical, and quantitatively similar, to the one pseudo-cell presented here, with some systematic variations on properties such as material orientation (Appendix G). As a consequence of this similarity between pseudo-cells in the peak-ring, the presented information can be confidently stated to be representative of the deformation of peak-ring material.

8.4.1 Comparison to Observations from the Chicxulub Peak-Ring

Observations of impact-related deformation experienced by peak-ring material in the Chicxulub impact structure have been presented by Riller et al. (in press). In summary, alongside shock deformation, evident by shatter cones, planar deformation features and planar fractures in quartz and feldspars, severe structural modification is evident by brittle and viscous deformation structures. These structures include:

1. Grain-scale fractures;
2. Planar and sub-planar cataclasites and ultra-cataclasites;

3. Foliated cataclasites;
4. Striated fault surfaces;
5. Impact melt rock and suevitic breccia dikes;
6. Brittle-ductile and ductile shear bands.

These macroscopic deformation structures are distributed heterogeneously through the target rocks of the Chicxulub peak-ring. The grain-scale fractures occur pervasively while cataclasites and ultra-cataclasites are spaced every few metres, range in thickness from millimetres to centimetres. Locally, cataclasites grade into, or are truncated by, flow-foliated ultra-cataclasites. 602 open and striated fault surfaces were recorded in the granitic rocks of Hole M0077A, these slip lineations in the target rock form pronounced ridges and grooves of strongly comminuted host rock material. Displacements on these faults may amount to several decimetres. At 1220 to 1316 mbsf in Hole M0077A, the target rocks are strongly deformed, and fragments of it are marginally resorbed and found within dikes of impact melt rock. Highly stretched fragments of target rocks within the melt rocks indicate large ductile strains. Additionally, dikes containing brecciated target rocks host elongate, and frequently wispy, melt-rock fragments, i.e. suevitic breccias. The presence of exotic rock fragments within the suevitic breccias and melt rocks, consisting of gneiss, mafic igneous rocks and various mylonites excludes an in-situ frictional melt origin for the melt rock. This zone of rocks within Hole M0077A contains a large abundance of brittle-ductile and ductile shear bands, commonly expressed in C-S fabrics.

Most importantly, it is possible to determine the relative timing of the various deformation styles. Cataclasites truncate the fragmented geometry of the pervasively fractured target rock. Additionally, some cataclasites and ultra-cataclasites cross-cut other impact-generated cataclasites. Furthermore, the foliated cataclasites appear to have formed by repeated cataclasis associated distinct displacement regimes. The cataclasites and ultra-cataclasites are, in turn, consistently offset by striated fault surfaces. Target rock fragments in impact melt rock dikes are occasionally striated and host cataclasite zones; whereas the impact melt rock itself is devoid of cataclasites and striated shear faults. Suevitic breccia and impact melt rock dikes are found within opened fractures, some of which, possess fault striations. Finally, brittle-ductile shear bands displace zones of cataclasites, foliated cataclasites and the contacts of impact melt rock and breccia dikes. Thus, the sequence of deformation experienced by peak-ring rocks during cratering includes; pervasive fracturing, the formation of cataclasites, ultra-cataclasites, open and striated faults, the emplacement of breccia and impact melt into dilatant fractures, and the formation of brittle-ductile and ductile shear bands.

In this section, it is shown how these observations are consistent with the results presented earlier in this Chapter.

8.4.1.1 Pervasive Fracturing

The rapid, and predominantly pure shear deformation during shock and decompression at strain rates of the order 10^{-1} s^{-1} , is extremely likely to produce pervasive fractures at the sub-grain scale. Following the model presented by Melosh (2005), adapted from Grady and Kipp (1980), the modal fracture spacing, l , is related to the deviatoric strain, ϵ by:

$$l = 4 \left[\frac{(m+1)(m+3)^4}{8\pi k(m+2)^5} \right]^{1/3} \epsilon^{-m/3}, \quad (8.15)$$

where, m and K are the parameters that describe the Weibull distribution of available flaws for fracture nucleation, $N = K e^m$. During shear failure, these parameters have values of $m = \frac{3}{2}$, and $K \approx 2.6 \times 10^9 \text{ m}^{-3}$ (Ramesh et al., 2015). Using these values, and a value of ϵ equal to the cumulative deviatoric shear strain during shock (~ 0.001 ; Figure 8.3) the fracture spacing for the peak-ring rocks, $l = 3.92 \text{ cm}$. This value equates to a scale on the same order as the grain size of the granitic target rocks. Nevertheless, despite the pervasive fracturing that occurs during this stage of crater formation, it is not necessary that the material gains volume by dilatancy. Pressures are extremely high during this stage, therefore fractures will not distend.

8.4.1.2 Cataclasites and Ultra-cataclasites

Following shock and decompression, during crater excavation, the material continues to deform by predominantly pure shear and is horizontally compressed (Figures 8.8a and 8.9b). Consequently, the deformation style during this stage of crater formation is not expected to be any different to that during shock. The low pressure and high strains during excavation are likely to cause the shock-formed fractures to dilate and introduce distension to the rocks. Additionally, as the strain rates are nearly two orders of magnitude lower (Figure 8.9a), displacement is likely to localise onto more widely spaced shock-formed fractures.

Towards the end of excavation and into the rim growth phase of crater modification, deformation becomes increasingly dominated by simple shear (Figure 8.9b). This change in the type of shear is likely to mark a change in deformation style, from pervasive fracture networks, brittlely accommodating a pure shear displacement field, to sub-parallel faults capable of accommodating a simple shear displacement field. Importantly, at the microscopic scale, deformation is never homogeneous, and, during these early stages of cratering is always brittle, occurring by simple shear on fractures. Consequently, macroscale pure shear must be accommodated by more complex fault arrangements than the fracture networks associated with macroscale simple shear. It is therefore during Rim Growth, that cataclasites and ultra-cataclasites are likely to form.

Following Rim Growth, there is a relative hiatus of deformation as peak-ring material is transported inwards towards the crater centre. Nevertheless, as material moves inwards towards the crater centre, a substantial solid-body rotation of the peak-ring material occurs. Additionally, the rearrangement of the orientation of the principal stresses from a reverse stress regime to a transpressional stress regime must cause the rearrangement of fault systems in the deforming peak-ring material such that previously utilised faults are abandoned and new faults form. This phase of deformation may therefore explain the observed cross-cutting between cataclasites.

8.4.1.3 Shear Faults

As the peak-ring material becomes entrained into the central peak, pressures, deviatoric stresses, instantaneous strains, and strain rates substantially increase. Increased strain rates are likely to lead to decreased spacing between deformation structures. Meanwhile, increased pressures from ~ 10 MPa to ~ 100 MPa (respectively, corresponding to ~ 300 m and ~ 3 km depths at normal lithostatic conditions) for rocks that are at ~ 700 K is likely to lead to a change in deformation mechanism. The observations of Riller et al. (in press) indicate that cataclasites and ultra-cataclasites, of which there are 258 occurrences within the recovered core, are truncated by shear faults. The total number of recorded shear faults is 602, i.e. the spacing between the deformation structures formed during Rim Growth and Inward Transport (Cataclasites and Ultra-cataclasites), is more than double the average spacing between the cross-cutting shear faults, which are likely to form during Central Peak Entrainment.

8.4.1.4 Melt Intrusion and Deformation

Once the central peak begins to collapse, peak-ring material moves outwards atop the collapsed transient crater rim, now capped with material originally ejected from the transient cavity, and is itself capped by impact melt. The orientation of principal stresses during this phase is transtensional, which could, potentially, facilitate the intrusion and mixture of impact melt and breccia bodies within the peak-ring material.

The final phase of peak-ring formation, Relaxation, occurs at strain rates approaching conventional tectonic strain rates of 10^{-8} s $^{-1}$ under stress conditions of normal failure; i.e., σ_1 oriented vertically. The shocked target rocks in the peak-ring are at < 700 K, whilst the impact melt rocks and suevitic breccias are likely to be at temperatures exceeding 1000 K. It is therefore no surprise that the last phase of impact deformation is brittle-ductile in the shocked target rocks and is ductile in the suevites and impact melt rocks. Additionally the shear sense of these structures is always normal.

8.5 Conclusions

In this chapter, a new method of tracking material stress and strain during impact cratering simulations. This method provides the opportunity to directly compare structural observations from impact structures with numerical impact simulations. This type of analysis allows for quantitative constraints on the timing of deformation, the orientation and magnitude of strain associated with each stage of the impact cratering process, the orientation and magnitude of stress during shock, crater excavation, and crater modification. The remarkable consistency between the stress-strain-time path of material within the Chicxulub peak-ring during cratering with the complex sequence of observations of deformation from the IODP-ICDP drill core suggests that, kinematically, the dynamic collapse model of peak-ring formation is accurate. The kinematics of the model requires that one or more transient dynamical weakening mechanism operates, and that the total effect of these mechanism(s) must be consistent with the rheological properties of the block model implementation of acoustic fluidisation used here. Consequently, significant predictions can be made by the Dynamic Collapse Model on the properties of rocks around complex craters. The analysis presented here has focussed exclusively on deformation experienced by the peak-ring material during complex crater formation. Primarily, this is due to the recent IODP-ICDP drill core into the peak-ring of the Chicxulub Crater. Nevertheless, this type of analysis is fully applicable to differently sized craters or other locations within a Chicxulub-sized crater.

9 Shock, Fracturing, Porosity, and Gravity at the Chicxulub Impact Structure: Impact Cratering on the μm - km Scale

9.1 Introduction

In the previous chapter, quantitative predictions of the deformation experienced by peak-ring rocks were presented. These predictions were then shown to be consistent with the history of deformation observed in the core, recently recovered by IODP-ICDP expedition 364, from the Chicxulub peak-ring (Riller et al., in press). Nevertheless, the quantitative predictions that can be made based on numerical simulations are capable of much more. It is possible to predict the shock pressure that the peak-ring rocks have experienced, as well as the total dilatancy generated during cratering.

The aim of this chapter is to petrophysically, petrographically, and microstructurally characterise the rocks of the Chicxulub peak-ring; constraining cratering-related deformation and the timing of porosity-generation. The predictive capability of numerical impact simulations to model shock pressure, porosity distribution and fracture orientations will then be tested by comparison with the observational data and, additionally, data from remote geophysical surveys.

9.2 Data Sets

9.2.1 Geophysical and Petrophysical data

9.2.1.1 Gravity Data

Numerous gravity surveys have been acquired at the site of the Chicxulub structure. Data used here were provided by Alan Hildebrand and Mark Pilkington (see Pilkington et al., 1994), supplemented by data acquired during the 2005 seismic surveying of the structure (see Gulick et al., 2008). Comparison between the results of 2D iSALE simulations and gravity data requires the determination of an average gravity profile across the structure, without any regional gravity effects. Following Vermeesch

et al. (2009), data were initially transformed to a cartesian coordinate system with an origin at the crater centre (21.31°N , 270.46°E):

$$X = (101.71 \times \text{Longitude}) + 9107.56 , \quad (9.1)$$

$$Y = (112.02 \times \text{Latitude}) - 2386.67 . \quad (9.2)$$

The gravity data were then corrected to account for the regional variation of the Bouguer gravity field across the site. This was achieved by excluding all data within 100 km of the crater centre, and matching a best-fit plane through the remaining regional data set. The best-fit plane, representing the regional Bouguer gravity field, Z , takes the form:

$$Z = 227.2 + 0.04641X + 0.7371Y . \quad (9.3)$$

After correction of the Bouguer gravity data to account for the regional field. Radial profiles were acquired in 1° intervals, avoiding anomalous regions of the gravity field to the south and north-west of the crater centre (Figure 9.1). Consequently, 232 radial profiles were obtained, and, the median and quartile values of the radial residual gravity field were determined with increasing radial distance (Figure 9.2).

9.2.1.2 Expedition Data

IODP-ICDP Expedition 364 collected density data from cores using two different methods. First, cores were analysed with a Multi-Sensor Core Logger (MSCL) which, alongside other physical property measurements, measured Bulk Density by gamma ray attenuation (GRA), these measurements were acquired at 2 cm intervals where, due to the machine set-up, the individual resolution was 0.5 cm (see Morgan et al., 2017 for details). The second set of density data derives from He-pycnometry measurements of discrete samples taken from the core. Samples had a diameter of 2 cm and an approximate volume of 6 cm^3 . Samples were taken approximately once per core section ($\approx 1.2\text{ m}$). A total of 719 samples were measured. He-pycnometry, in addition to allowing determination of bulk density, also allows the determination of grain density and porosity (see Morgan et al., 2017 for details).

The raw expedition data is shown in Figure 9.3. Here, data acquired during Expedition 364 has been processed in order to facilitate direct comparison between the results of numerical simulations and the observations, and between the two observational methods. Firstly, all data from lithologies that were not granitic target rocks

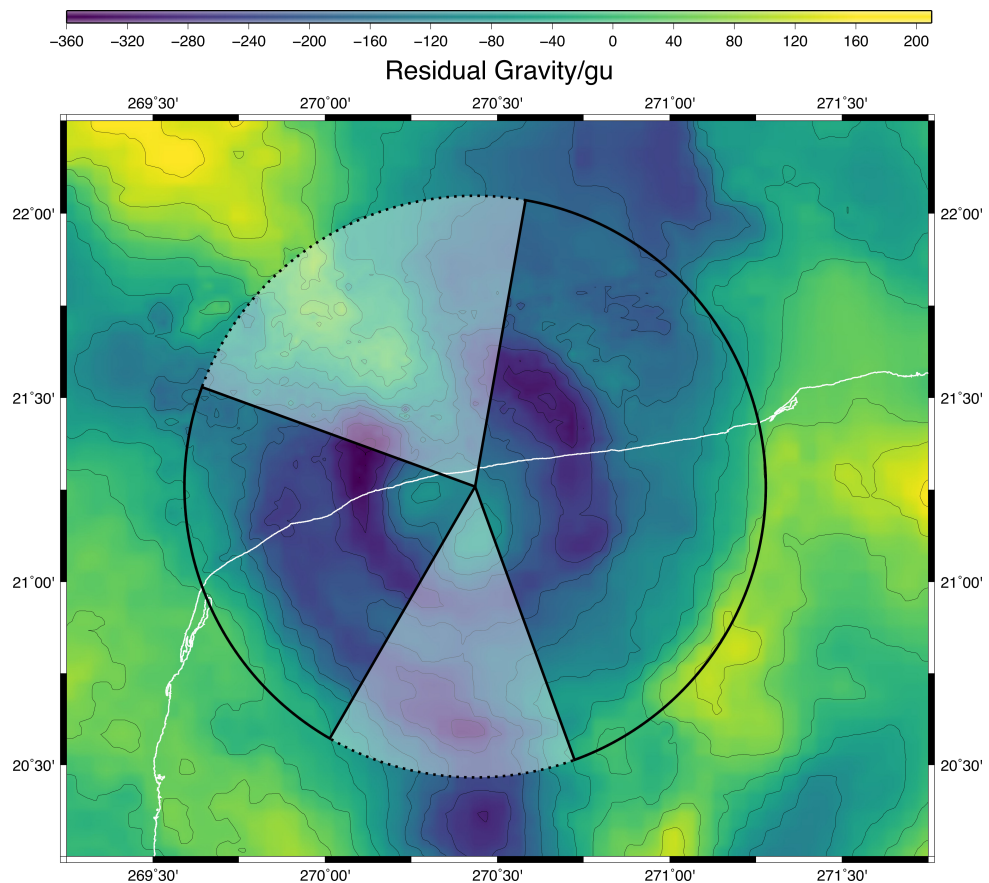
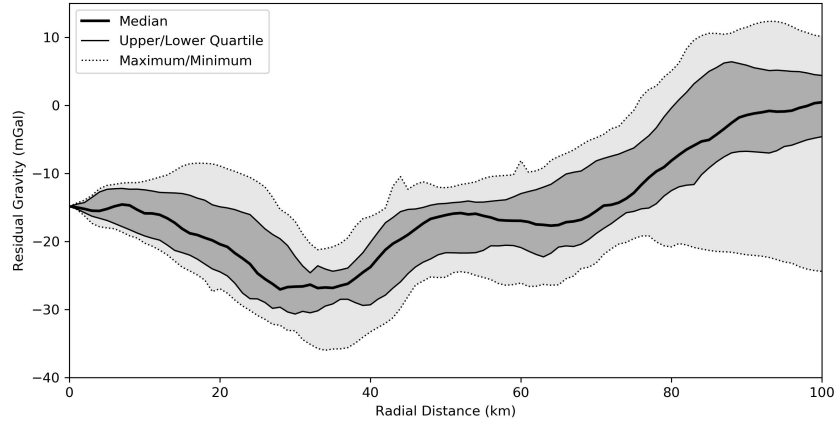


Figure 9.1: Residual Bouguer gravity map of the crater, data is contoured at 50 gu intervals. The circle indicates all points within 100km of the crater centre, shaded sectors indicate the regions from which no gravity profiles were obtained during the calculation of the average radial gravity profile.



*Figure 9.2: Average (median) radial gravity profile of the Chicxulub structure in mGal (1 mGal = 10 *gu*). Upper and Lower Quartiles, and minimum and maximum values are indicated.*

were excluded; numerical simulations are not capable of modelling the injection of allochthonous impactites into the target rocks, nor can they model fine-scale lithological variations between hypabyssal intrusive rocks basement rocks. Subsequent data processing involved the calculation of a running average and standard deviation within ± 6 m of each He-pycnometry sample. Averages and standard deviations were only calculated where 3 or more measurements were acquired within the 12 m wide interval. Comparable measurements from the MSCL data were acquired by taking an average and standard deviation corresponding to the same depth interval for each He-pycnometry sample.

9.2.2 Shock Barometry

The granitic target rocks from Hole M0077A contain abundant quartz with multiple PDF sets (Morgan et al., 2017), this observation has been used to constrain the maximum experienced shock pressure of peak-ring rocks to a range from 10-35 GPa (Morgan et al., 2016). Measuring the orientation of PDFs in quartz using a universal stage microscope allows for a more precise shock pressure estimate. Here, following the methods described in Section 3.1.2.1, 20 thin sections of granitic target rocks from Hole M0077A were investigated with an optical microscope and universal stage. Shock pressure estimates were calculated by averaging the shock pressures assigned to each grain, in turn, based on the PDF orientations that each grain contains.

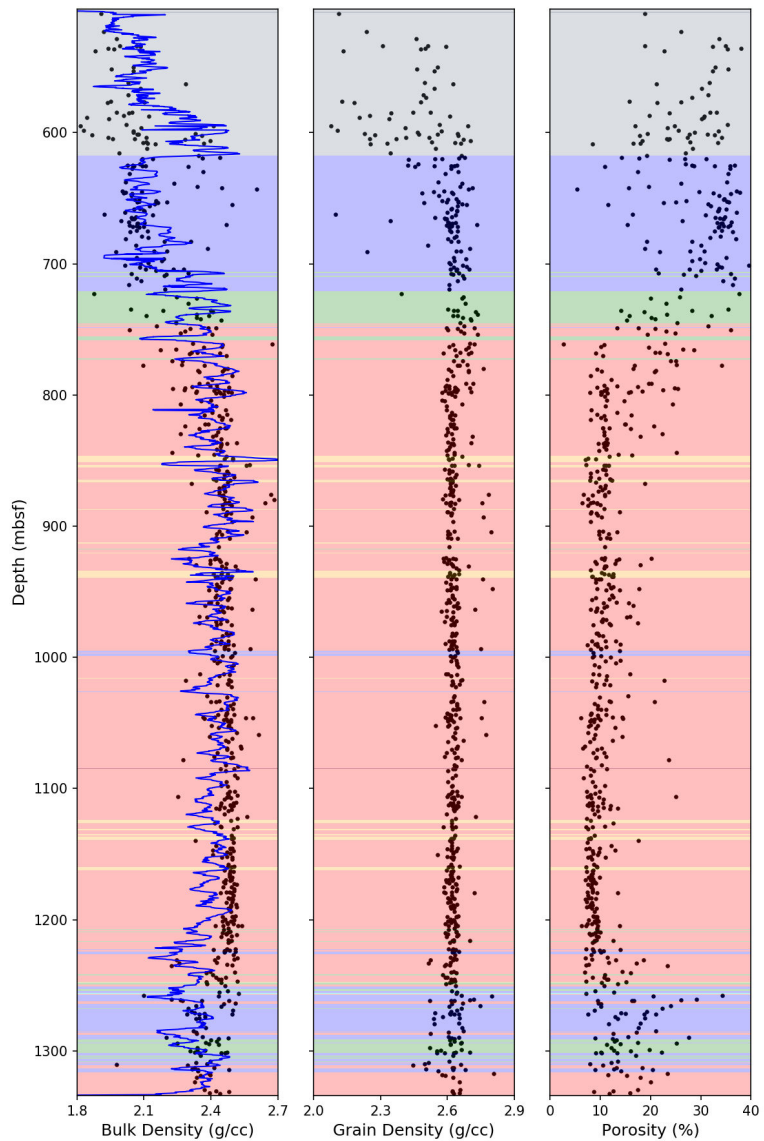


Figure 9.3: IODP-ICDP Expedition 364 density and porosity data, black dots indicate measurements on discrete samples, the blue line indicates MSCL measurements. Background colours indicate the stratigraphy of Hole M0077A (see Figure 7.2). Data from Morgan et al. (2017).

Sample Name	Depth (mbsf)	Notes
364-77-A-095-R-3-27-29	745.16	Fractured Granite
364-77-A-104-R-1-24-26	768.59	Fractured Granite with cataclasite veins
364-77-A-121-R-1-75-77	814.85	Fractured Granite with cataclasite veins
364-77-A-132-R-1-22-24	838.45	Fractured Granite
364-77-A-150-R-1-53-55	884.43	Fractured Granite
364-77-A-204-R-1-07-09	1030.00	Fractured Granite
364-77-A-219-R-1-22-24	1076.15	Fractured Granite
364-77-A-250-R-1-41-43	1169.71	Fractured Granite
364-77-A-276-R-1-17-19	1249.52	Fractured Granite with cataclasite veins
364-77-A-301-R-1-30-32	1326.89	Granitic Breccia

Table 9.1: Imaged thin sections and their depths

9.2.3 SEM Imaging and Analysis

In order to understand the micro-structural cause of the porosity within the granitic basement rocks, 10 thin sections were prepared from samples of the recovered granitic target rocks within Hole M0077A (Table 9.1).

9.2.3.1 Image Acquisition

BSE images of the thin sections were obtained using a Zeiss Ultra Plus Field Emission SEM. Individual images were acquired with a pixel width of 748.9 nm. The individual images were obtained across the entire thin sections under the same conditions and were then stitched together to produce a single greyscale image for each thin-section.

In addition to BSE imaging, thin sections were prepared for EBSD analysis. Data acquisition settings and processing procedures followed that of Timms et al. (2017) and are detailed in Table 9.2.

9.2.3.2 Image Processing

Image processing was carried out in order to analyse and quantify porosity within the thin sections. Processing was achieved using the ImageJ software package (Schindelin et al., 2012).

The first stage required to analyse porosity is image thresholding. The images were deliberately acquired such that there was a significant contrast of greyscale values between pores (black), and mineral phases (grey to white). ImageJ provides several algorithms that automatically thresholds images into objects (pores) and back-

SEM		
Make/model	Tescan Mira3 FEG-SEM	
EBSD acquisition system	Oxford Instruments AZtec	Nordlys EBSD Detector
EDX acquisition system	Oxford Instruments AZtec	XMax 20 mm SDD
EBSD Processing software	Oxford Instruments Channel 5.10	
Acceleration Voltage (kV)	20	
Working Distance (mm)	18.5	
Tilt	70°	
EBSD match units		
Phase	Space Group	β (°)
Titanite	15	113.93
Quartz	152	n/a
Orthoclase	12	116.07
Bytownite	2	115.87
Magnetite		n/a
Calcite	0	n/a
Zircon	141	n/a
Hydroxyapatite	176	n/a
EBSP Acquisition, Indexing and Processing		
EBSP Acquisition Speed (Hz)	40	
EBSP Background (frames)	64	
EBSP Binning	4×4	
EBSP Gain	High	
Hough resolution	60	
Band detection (min / max)	6 / 8	
Mean MAD (all phases)	<1°	
Wildspike correction	Yes	
Nearest neighbour zero solution extrapolation	8	

Table 9.2: Acquisition parameters of EBSD data

ground (solid material), resulting in an image consisting of only binary values, black for pores and white for background. Here, the default ImageJ thresholding algorithm was used, and the result then manually checked and, if required, adjusted. Once pores were thresholded into a binary image file, total porosity estimates could be made by summing the total area of pores and dividing by the total image area. Additionally, the orientation and aspect ratio of each pore were determined by fitting ellipses to each pore, an available function in ImageJ.

9.2.4 The iSALE Shock Physics Code

The formation of the Chicxulub impact structure was simulated using the iSALE shock physics code. Here, the model presented in the Chapter 8 was used.

9.3 Results

9.3.1 Petrophysical Data Sets

The processed 2D gravity profile (Figure 9.2) is broadly consistent with the features seen in previously published individual profiles and average profiles (e.g. Sharpton et al., 1993), with a pronounced gravity low from 30–40 km radial distance, corresponding to a position slightly internal to the topographic peak-ring. In addition, the total mass deficit associated with the Chicxulub impact structure can be calculated from the gravity anomaly by applying Gauss’s theorem (see Campos-Enriquez et al., 1998). The average gravity profile obtained here suggests a total mass deficit of 9.15×10^{15} kg. While suitable upper and lower bounds on the deficit can be made using the upper and lower quartile profiles, which suggest mass deficits of 4.90×10^{15} kg and 1.25×10^{16} kg respectively. These values are consistent with previous estimates Chicxulub mass deficit (Campos-Enriquez et al., 1998). The large range in the data at radial distances beyond 80 km occurs due to the greater thickness of Mesozoic and Cenozoic sediments, with a negative Bouguer gravity contribution, towards the north and north-east of the crater centre (Gulick et al., 2008). Nevertheless, the inter-quartile range remains comparatively constant with increasing radial distance.

The low seismic velocities of the Chicxulub peak-ring rocks, combined with the large gravity low slightly within the peak-ring, had suggested, prior to drilling, that the Chicxulub peak-ring is composed inward dipping, low-density rocks (Morgan et al., 2000). Results from Expedition 364 have shown that the peak-ring is composed of uplifted crystalline target rocks that possess unusually low densities and high porosities (Figure 9.3; Christeson et al., 2018). Processed expedition data are shown in Figure 9.4. The target rocks possess consistent and typical grain densities for granite, averaging 2628 ± 39 kg m⁻³ (1σ), but have remarkable porosities. The average porosity of the

granitic target rocks is $11.5 \pm 4.7\%$, resulting in average bulk densities of 2444 ± 75 kg m⁻³, additionally, the raw porosity measurements show that the granitic target rocks have a pervasive baseline porosity of $\sim 8\%$, where few samples possess less porosity, but where a significant number of samples have excursions to higher porosity values. Nevertheless, there is some heterogeneity of porosity and bulk density with depth in the recovered core; in the upper 100 m, average porosities increase beyond 20% and the variability increases up to $\sigma = 8.1\%$. Additionally, porosities within granitic rocks beneath 1225 mbsf increase from <10% to >10%. Despite some deviation between bulk density measurements by He-pycnometry and the independently measured bulk density by GRA using the MSCL, particularly from depths below 1075 mbsf, the 1σ envelopes of both measurements always overlap, indicating full consistency between the data sets.

9.3.2 Shock Barometry

The thin sections obtained from samples of granitic basement in Hole M0077A display abundant evidence of shock and impact-related deformation. Quartz grains contain multiple PDF, and PF sets each, and occasional quartz grains contain FFs (Figure 9.5a-d). All observed PDFs were decorated. Most quartz grains possessed extremely undulose extinction. Additional deformation within the sections can be seen in all other major phases; folding and fracturing within feldspar grains (Figure 9.5e), and kink banding within biotite (Figure 9.5f).

The crystallographic orientations of PDFs in the 20 granitic samples were obtained by U-stage analysis. Table 9.3 presents the PDF statistics organised by sample. Between 0 and 4 PDF sets were observed per quartz grain with an average number of PDFs per grain in a sample ranging from 1.53 to 2.42. Across all of the thin sections {10̄13} and (0001) PDF orientations were most common, accounting for 32.7% and 31.9% of the total number of measured sets respectively. Additional common PDF sets include {10̄14}, {10̄12}, {10̄11} orientations which account for 12.3%, 7.5%, and 6.7% of the total number of measured sets respectively. 15.0% of the measured sets could not be indexed. This either reflects human error in the original measurements or that there are possible PDF planes not included in the New Stereographic Projection Template (NSPT) (Ferrière et al., 2009). In these particular thin sections, the high unindexed percentage is partially due to extremely undulose extinctions of the quartz grains.

The estimated shock pressures of each sample are shown in Figure 9.6. In general, peak shock pressures are constant with depth, ~ 15 GPa. These pressure estimates are derived by calculating the mean of individually assigned pressures to each crystal, the standard deviation of this average varies between 2.91 GPa and 7.43 GPa, with a mean standard deviation of 5.79 GPa. These standard deviations cannot be thought of directly as an error, but provide measures of the variability of recorded shock pressure within a sample.

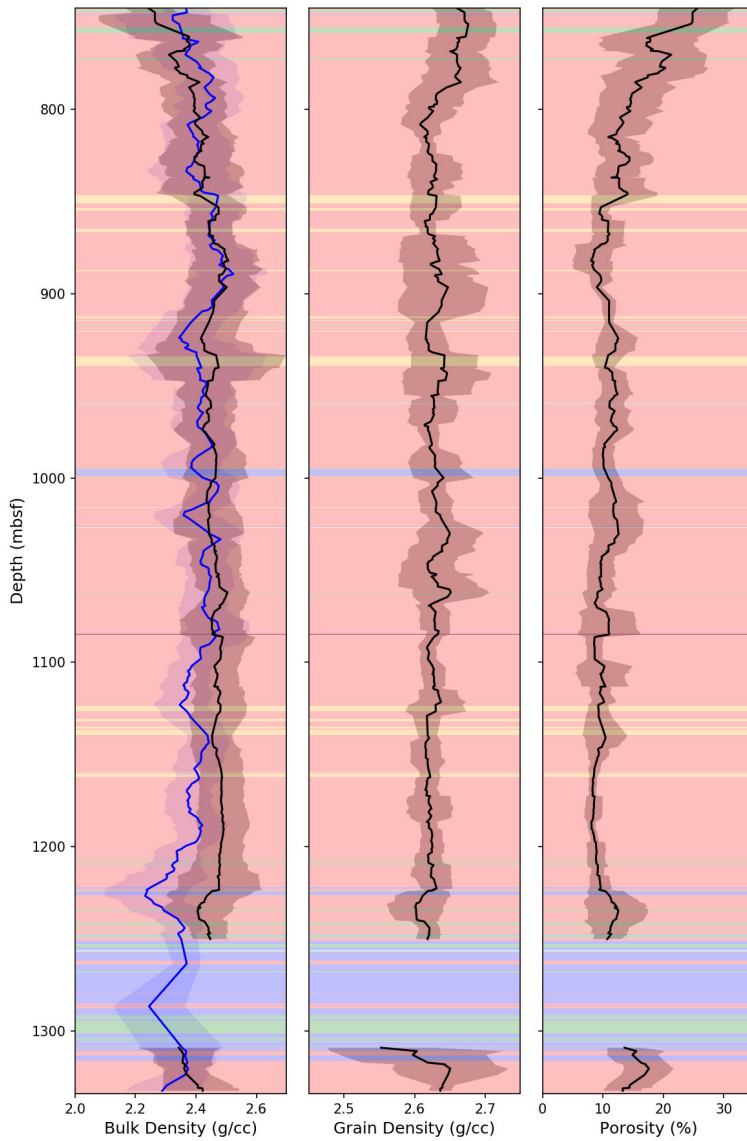


Figure 9.4: Processed physical property measurements of the granitic rocks recovered during Expedition 364. Black lines indicate moving averages of discrete sample measurements within a 12 m window, while 1σ distribution envelopes are indicated by the grey areas. The blue line and area on the bulk density profile (left) indicates the moving average and distribution envelope associated with MSCL measurements of bulk density using GRA. Background colours indicate the stratigraphy of Hole M0077A (see Figure 7.2).

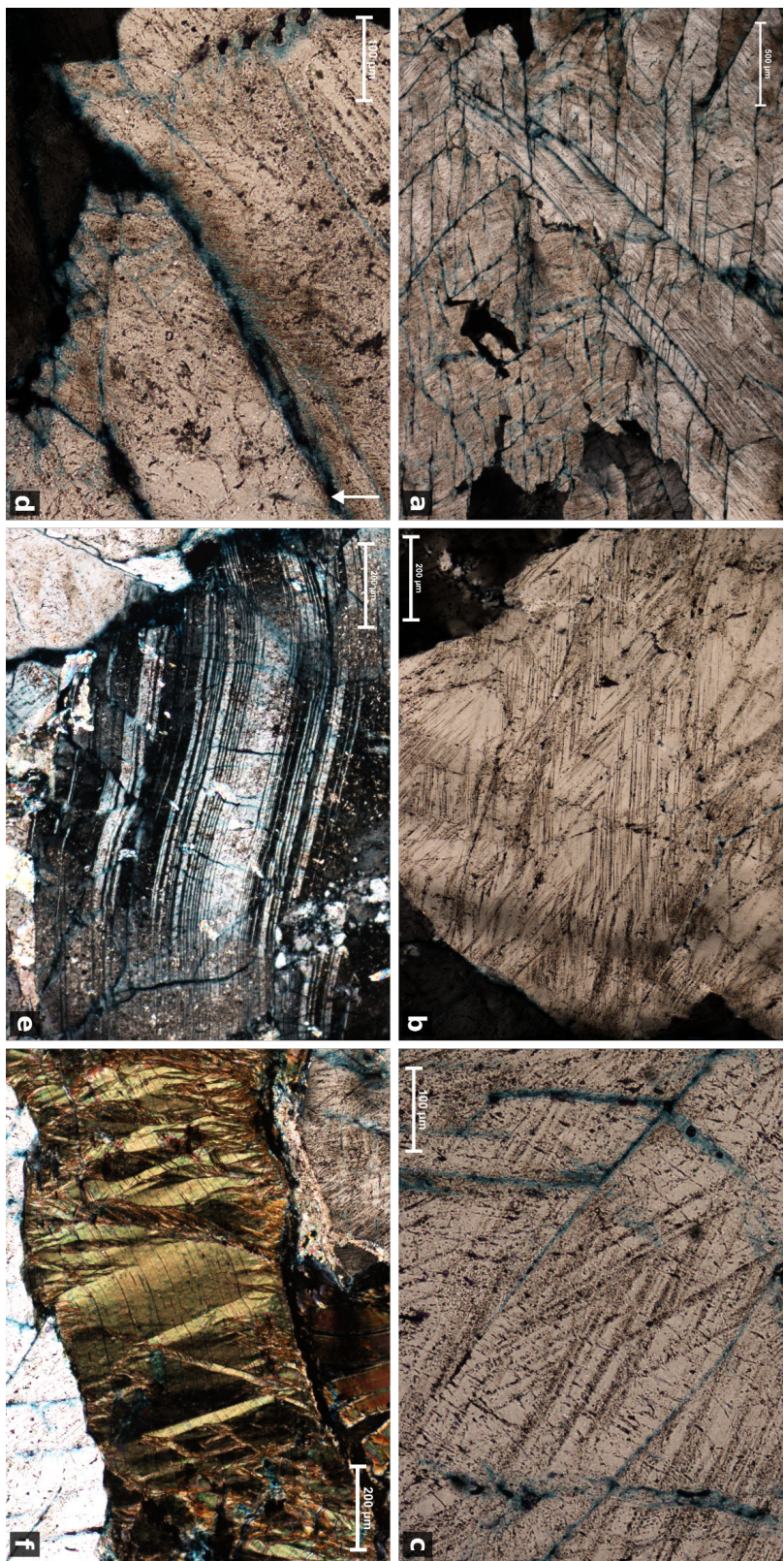


Figure 9.5: Shock deformation at the Chicxulub impact structure. Optical microphotographs under cross-polarised light. a) Multiple PF and PDF sets in quartz. b) Multiple PDF sets in quartz. c) Multiple decorated PDF sets in quartz. d) PFs, PDFs, and FF lamellae in quartz, arrow indicates up direction. e) Folded and micro-faulted plagioclase feldspar. f) Kinked biotite.

Table 9.3: PDF statistics of Chicxulub thin sections, organised by sample.

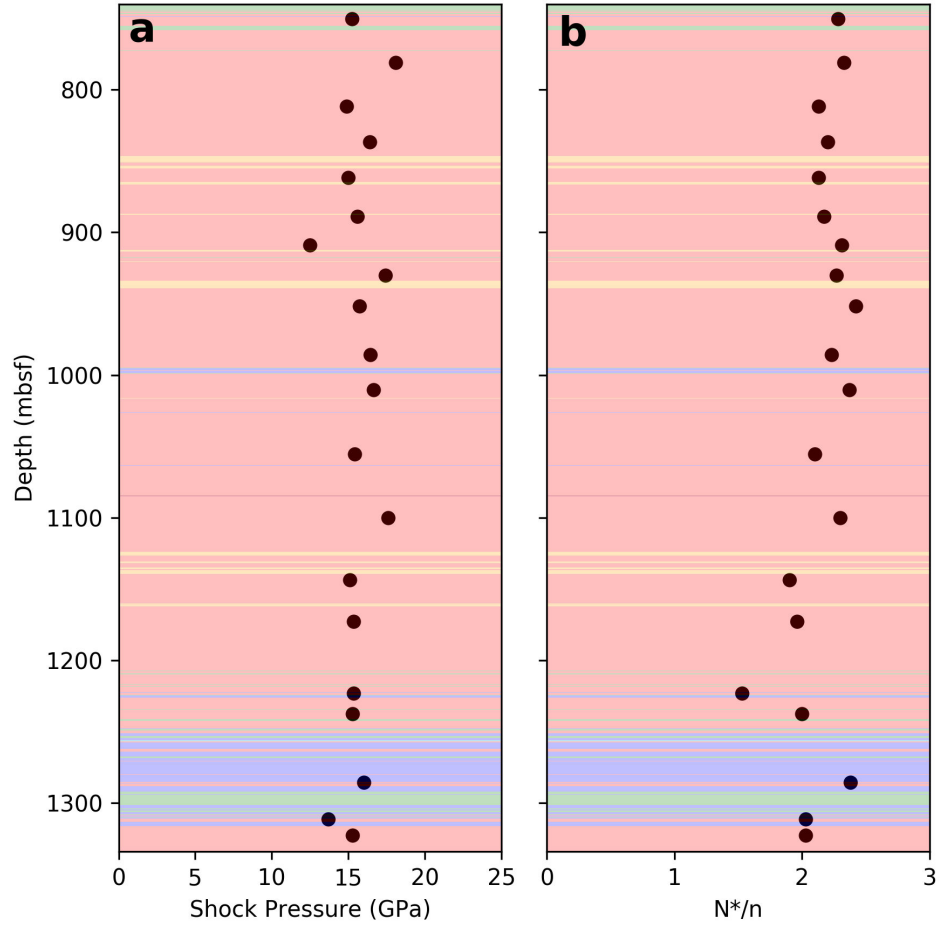


Figure 9.6: Results of universal stage analysis. a) Estimated peak shock pressures and b) the average number of PDFs per grain (N^/n), in Hole M0077A from U-stage analysis of quartz. Background colours indicate the stratigraphy of Hole M0077A (see Figure 7.2).*

9.3.3 SEM Imaging and Analysis

Total porosity measurements made by the analysis of SEM images are shown on Figures 9.7 and 9.10. In general, the estimations from SEM image analysis are consistent with the measurements made by He-pycnometry. All samples excluding the upper-most sample fall within the 1σ envelope of the He-pycnometry porosity measurements. However, most of the samples are offset to lower porosity values compared to the mean measurement from He-pycnometry. Potential errors associated with calculating porosity from SEM images include, under-resolution of small pores, large pores distributed on a scale larger than a thin section (2–3 cm), porosity anisotropy, and sectioning-induced porosity.

Inspection of the SEM images shows that the largest contributor to the total porosity of the granitic target rocks is by intra-granular fracturing, with an additional contribution from cataclasites and large inter-granular pores (Figures 9.7 and 9.8). Cataclasites are easily distinguished by their fine-grain sizes and texture, whilst large inter-granular pores are defined by their anomalous sizes compared to the other porosity types (see Appendix D) Across all the thin sections, the average fraction of the porosity contributed by intra-granular fractures is 0.549, while the average fraction of porosity contributed by inter-granular pores and cataclasites are 0.244 and 0.207, respectively.

Excluding the large inter-granular pores and cataclasites, the average porosity of the intra-granularly fractured granites is 6.4%. This intra-granular fracturing is distributed heterogeneously throughout the thin sections, primarily dependent upon the mineral that is fractured (Figure 9.9). The three major rock-forming minerals within the granites are alkali feldspar, quartz, and plagioclase feldspar. Quartz grains are pervaded by planar fracture (PF) sets which rarely span the entire grain and which occasionally have feather feature (FF) lamellae (Figure 9.9a,e). Additionally, the quartz grains possess occasional individual shear fractures on planar surfaces with observable sub-mm displacements, and rare non-planar fractures which typically contain a gouge of angular to sub-angular quartz fragments. Compared to the feldspars, the quartz grains are more porous. Plagioclase feldspar, whilst also pervasively fractured, possesses a distinctly different fracture pattern to the quartz grains. The fractures are typically closer-spaced than in quartz from the same sample, are rarely planar, and typically branch and converge into other fractures (Figure 9.9b,d). While the plagioclase crystals often have higher fracture densities than the quartz grains, the total dilation on each intra-granular plagioclase fracture is significantly smaller than than the intra-granular fractures in quartz. Compared to the quartz and plagioclase feldspar within the granitic rocks from Hole M0077A, alkali feldspar is remarkably unfractured (Figure 9.9c), possessing only widely-spaced non-planar fractures.

Additional porosity in the granitic rocks is produced by cataclasites. These

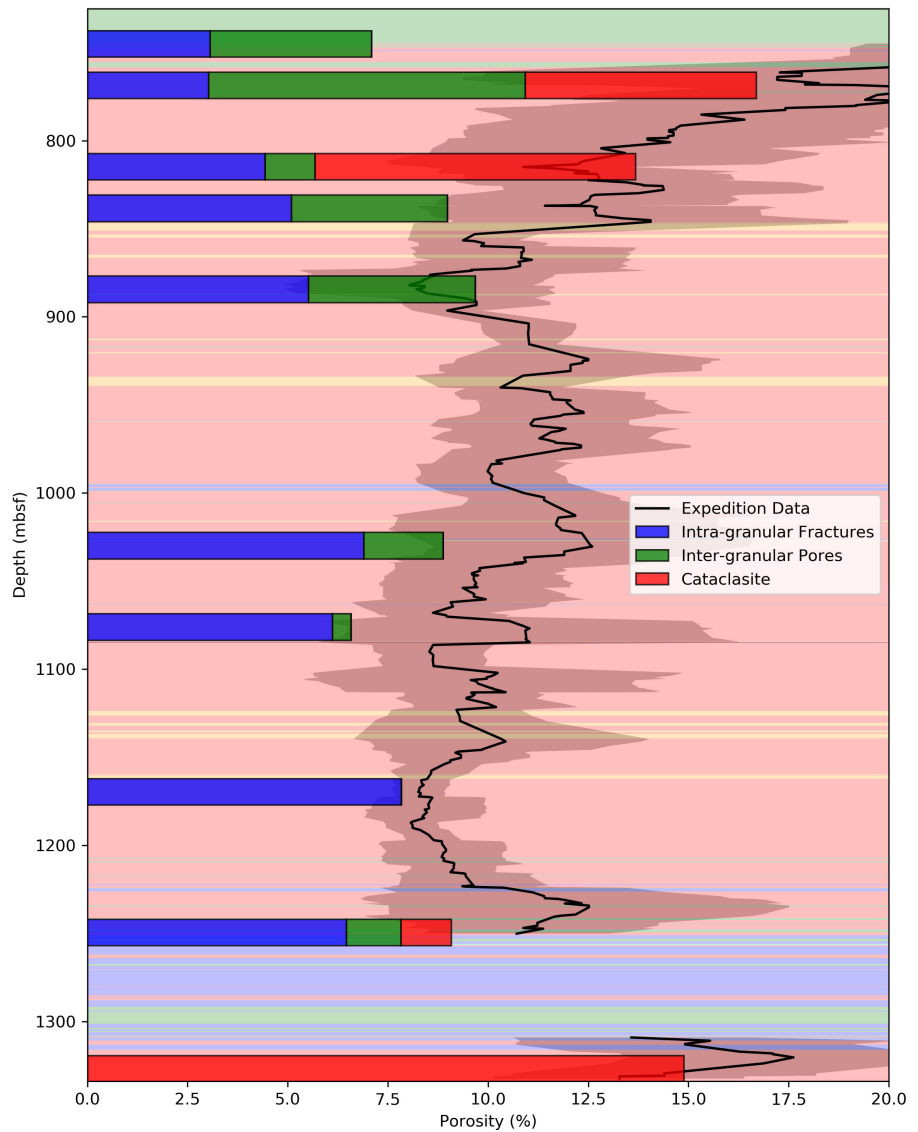


Figure 9.7: Porosities determined by SEM image analysis, subdivided by the type of porosity: intra-granular fractures, inter-granular pores, and cataclasites. Beneath, for comparison, processed expedition data of porosity is shown.

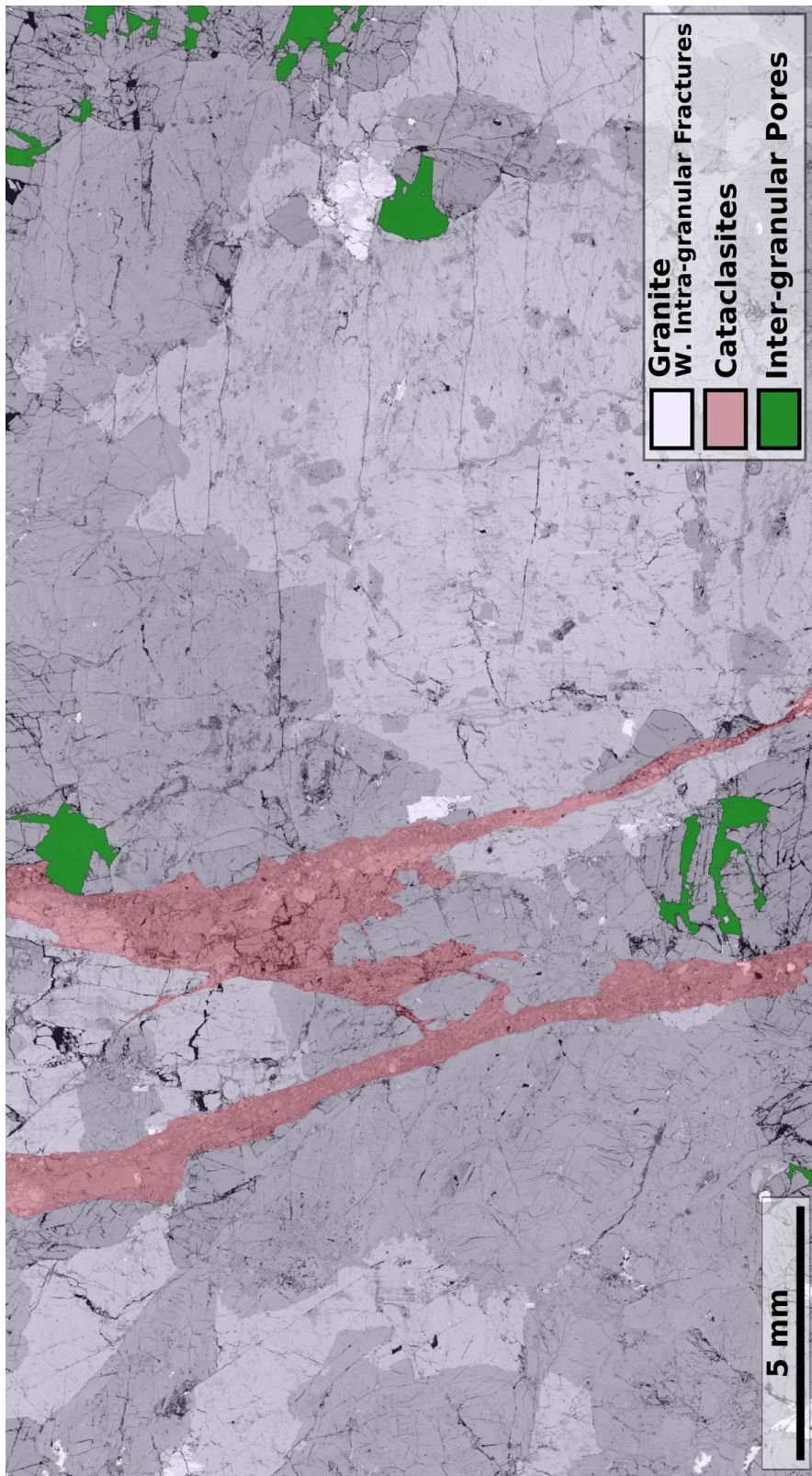


Figure 9.8: Whole thin-section BSE SEM image of Sample 364-77-A-276-R-1-17-19 (1249.52 mbsf), highlighted to distinguish between the three types of porosity. The largest region, highlighted in pale blue, is dominated by intra-granular fractures. The region highlighted in red indicates a cataclasite network. Finally, the pores highlighted in green are the large inter-granular pores.

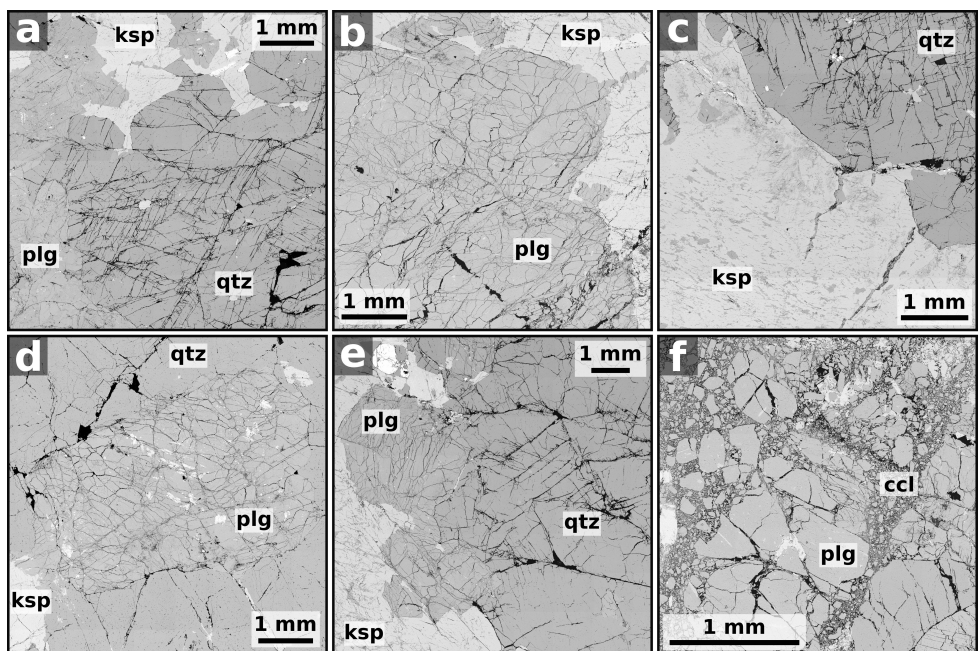


Figure 9.9: Intra-granular fractures within granitic minerals of the Chicxulub peak-ring, qtz = Quartz, ksp = Alkali Feldspar, plg = Plagioclase, and ccl = Cataclasite. a) Strongly dilated fracture network in quartz. b) Poorly dilated, diverging and converging fracture network in plagioclase. c) Poorly fractured alkali feldspar crystal contrasted with heavily fractured quartz. d) High density, poorly dilated, diverging and converging fracture network in a plagioclase grain surrounded by quartz with low density fractures. e) Fractured quartz, plagioclase, and alkali-feldspar with distinctly different fracture patterns. f) Cataclasite partially incorporating a pre-fractured plagioclase grain.

regions of the thin sections have extremely high porosities. Across the 4 thin sections that contain cataclasites, the average porosity of the cataclasite regions is 15.8%. Nevertheless, the cataclasites are only a small volume of the total rock mass (20.0% of the total imaged area) and thus contribute only a small fraction of the total porosity of the thin sections.

The large inter-granular pores observed in the samples may or may not be representative of the in-situ porosity of the granitic target rocks. Their extreme sizes within the pore-size distributions (Appendix D) of each sample could indicate that they are non-natural pores, or that these thin sections are too small to encompass the full pore-size distribution of these rocks. Regardless of their origin, the total contribution of these large inter-granular pores to the total porosity is equal to the average contribution from cataclasites and significantly less than the contribution from intra-granular fractures, and ranges from 0–56.8%, where 4 of the 10 thin sections, which all derive from near to the top of the core, have contributions from the large inter-granular pores that are >42%. The remaining 6 thin sections have significantly lower contributions from large inter-granular pores (Figure 9.7).

Quartz has well-documented shock metamorphic effects (see French and Koeberl, 2010), one of these effects is PFs, which can occur in one or multiple crystallographic orientations. The large abundance of PF sets in quartz from Hole M0077A, together with the inter-connectedness of the intra-granular fractures suggests that most of the intra-granular fracturing is related to deformation during shock (Figure 9.9a,c,e). The partial disaggregation of some grains of quartz and plagioclase feldspar along intra-granular fractures into cataclasites and the matrix of monomict granitic breccias indicates that the formation of cataclasites and brecciation occurred after the formation of intra-granular fractures (Figure 9.9f).

The orientation of pores within the thin sections is generally anisotropic (Figure 9.10). Six thin sections have unimodal pore orientation-frequency distributions while two more thin sections have a bimodal distribution (Table 9.4). Comparing these distributions to the images they derive from (Figure 9.11), indicates that the cause of the dominant orientations is primarily due to the orientation of PFs in quartz.

9.3.4 EBSD Analysis

EBSD analysis of the same thin sections indicates that the granitic rocks have accumulated large amounts of plastic strain on the sub-grain scale (Figure 9.12). The majority of this plastic strain is associated with fractures in the minerals. This relationship is particularly clear in quartz, where pervasive, interconnected planar fracture networks are abundant. In quartz, local disorientation is concentrated against planar fractures, at the terminations of fractures, and most significantly, occur on planes parallel to the orientations of planar fractures (Figure 9.12b,c). Additional examples of this

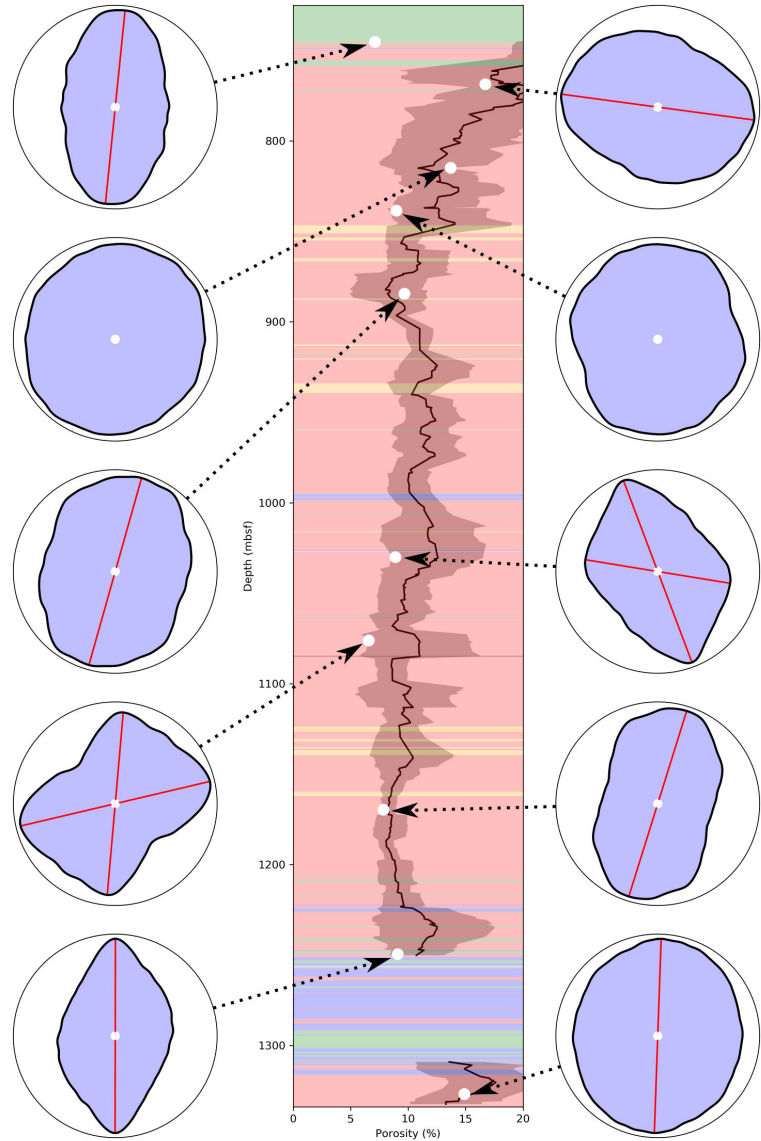


Figure 9.10: Pore orientation-frequency distributions for each of the analysed thin sections. Orientations are measured as apparent dip, where upwards indicates a vertical apparent dip (i.e. 90°), while across indicates a horizontal apparent dip (i.e. 0°). Red lines indicate the significant mode(s) of the distributions. The central column shows the lithology, processed porosity measurements from Expedition 364, and, as white points, the porosities measured by SEM image analysis.

Sample Name	Depth (mbsf)	Distribution Shape	Apparent Dip(s) (°)	Notes
364-77-A-095-R-3-27-29	745.16	Unimodal	84.2	Strong
364-77-A-104-R-1-24-26	768.59	Unimodal	7.7	Moderate
364-77-A-121-R-1-75-77	814.85	Non-modal	—	—
364-77-A-132-R-1-22-24	838.45	Non-modal	—	—
364-77-A-150-R-1-53-55	884.43	Unimodal	74.3	Weak
364-77-A-204-R-1-07-09	1030.00	Bimodal	69.4 & 9.26	Strong & Moderate
364-77-A-219-R-1-22-24	1076.15	Bimodal	13.3 & 85.0	Strong & Strong
364-77-A-250-R-1-41-43	1169.71	Unimodal	72.7	Strong
364-77-A-276-R-1-17-19	1249.52	Unimodal	89.9	Strong
364-77-A-301-R-1-30-32	1326.89	Unimodal	88.0	Very Weak

Table 9.4: Pore orientation distribution descriptions by sample. Most thin sections have Uni- or Bi-modal distributions. A qualitative indication of the relative peak height(s) is indicated in notes. The dominant overall orientation of pores in these samples is at apparent dips $> 69.4^\circ$, with a sub-ordinate orientation at apparent dips $< 13.3^\circ$.

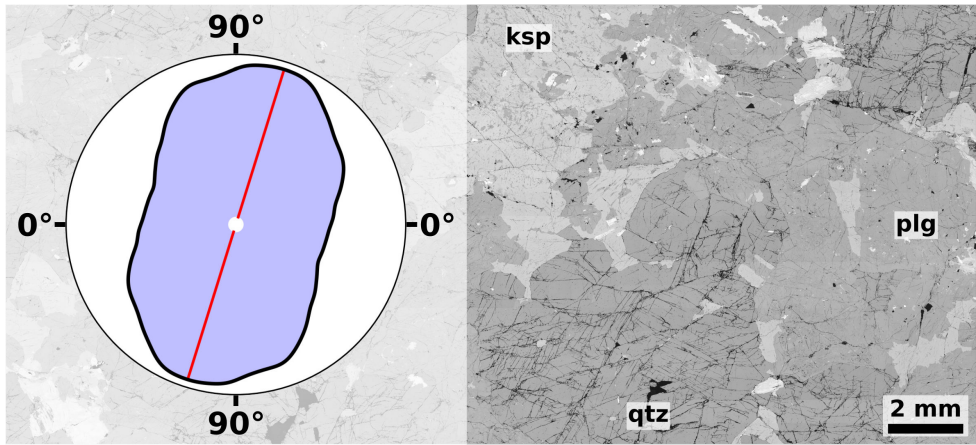


Figure 9.11: BSE image of Sample 364-77-A-250-R-1-41-43 with its pore orientation-frequency distribution. It can be clearly seen that the dominant orientation (72.7° apparent dip) of pores within the distribution is caused by a dominant set of PFs in multiple quartz grains, and that quartz makes the largest contribution to the total porosity of the sample.

behaviour may be seen in Appendix H.

In addition to the variations of local disorientation, deformation has also been accommodated in some quartz grains by the formation of planar deformation bands (PDBs; e.g. Nemchin et al., 2009; Timms et al., 2012, 2018; Figure 9.12d,e). PDBs are effectively box folds within a crystallographic lattice, formed by a pair of tilt planes, accommodated by dislocation migration under deformation. PDBs have not been identified in shocked, or even unshocked, quartz before, however PDBs have been found in both shocked and tectonically deformed zircon (Kovaleva et al., 2015). It is clear that the PDBs have formed after the beginning of shock metamorphism as quartz PDBs are truncated against PFs, thus the PFs must have existed prior to the formation of PDBs.

Finally, it was observed during EBSD acquisition that alkali feldspar was particularly challenging to index. The difficulty of indexing alkali feldspar occurred due to a lack of band contrast in the acquired diffraction patterns. Close inspection of the areas of low band contrast using BSE images indicates an abundance of planar microstructures, here termed generically, 'planar elements' (Figure 9.13). These planar elements are abundant, closely-spaced, and marked by void spaces. Planar elements are often deformed by kink bands within the crystal. The planar elements are generally not continuous across the mineral grain, however, it is likely that these planar elements are PDFs (Stöffler et al., 2018 and refs therein), where the glass in the lamellae has been dissolved due to hydrothermal processes. Alternatively, these features may be a remnant of shock-induced mechanical twins (Huffman et al., 1993). Nonetheless, it is clear that despite the absence of fractures in alkali feldspar grains, significant deformation has still

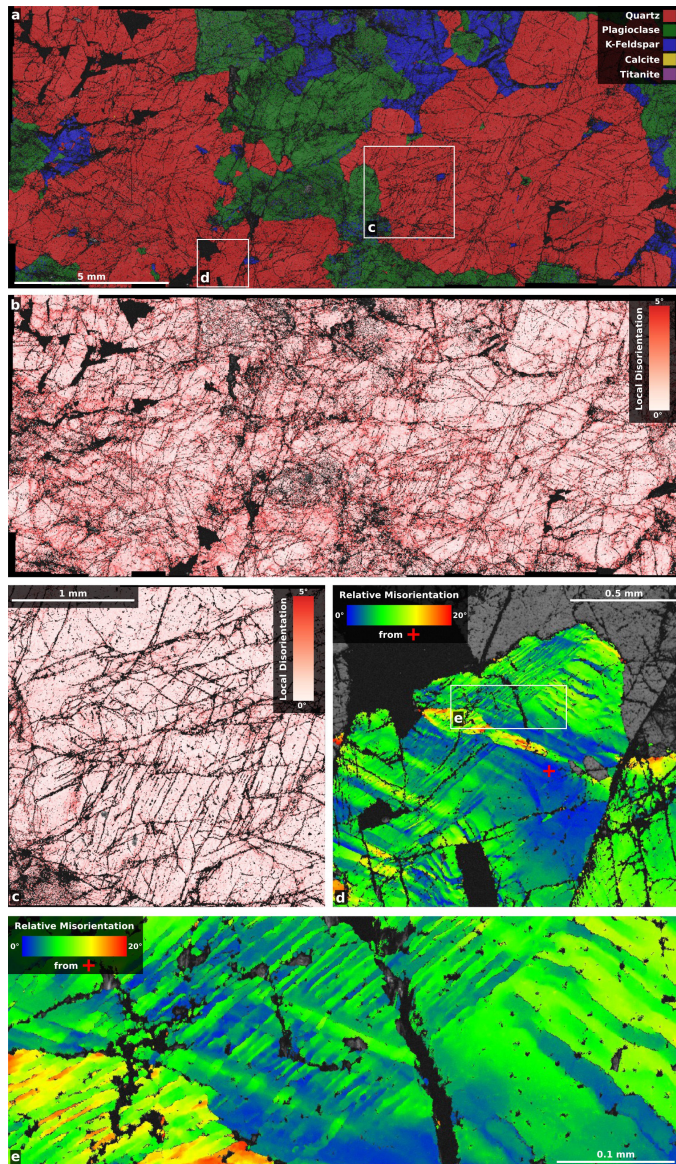


Figure 9.12: Strain on the grain-scale, EBSD analysis of shocked target rocks. a) Phase map of an area of Sample 364-77-A-250-R-1-41-43 (Figure 9.11) overlain on a band contrast map. b) Local disorientation map of target region a) overlain on a band contrast map. Abundant local disorientation, i.e. strain, can be seen accumulated against fractures, at fracture tips, and in planes parallel to the orientation of existing fracture sets. c) Local disorientation map of higher resolution sub-area indicated on a) overlain on a band contrast map. d) Relative misorientation map of a quartz grain in sub area indicated on a) overlain on a band contrast map. This grain possesses planar deformation bands, which are truncated against a PF with FF lamellae. e) Relative misorientation map of higher resolution sub-area indicated on d) overlain on a band contrast map. Two intersecting sets of planar deformation band structures.

been accommodated by all major phases in the granitic rocks of the peak-ring.

9.3.5 Numerical Simulations

The simulated formation of the Chicxulub peak-ring is demonstrated in Figure 8.2, wherein the formation of the peak-ring results from the over-heightening of a central uplift, and its subsequent lateral emplacement over the collapsed transient cavity rim.

Over the course of the simulation, rocks throughout the crater, but particularly the peak-ring rocks, dilate due to shear failure. The final distribution of modelled porosity caused by this dilatancy is shown in Figure 9.14. From the final predicted distribution of porosity in the structure it is possible to produce a vertical profile of porosity in the peak-ring, such that it can be compared to observational results (Figure 9.14). Using $\beta_{max} = 0.045$, these results predict that the porosity of the peak-ring material should be approximately $7 \pm 2\%$, in which the $\pm 2\%$ error is caused by uncertainty in the exact comparative location between the model and the drilled core. Overall, the modelled porosity closely matches the baseline values of porosity in the recovered core, with notable excursions within the top ~ 200 m, from 300–350 m, and at ~ 700 m within the peak-ring. These excursions from the model may be caused by hydrothermal dissolution, and/or localisation of strain.

In addition to the predicted porosity in the peak-ring, a set of predicted Bouguer gravity profiles of the crater were calculated from the iSALE simulation, comparable to the observed local Bouguer gravity anomaly (Figure 9.14). The range of potential profiles results from uncertainties in the assigned reference densities for the materials in the model (Table 9.5).

One significant problem with the calculation of the overall gravity profile comes from the filling of the basin with post-impact sedimentary rocks. In the model, the top of the peak-ring is at 1050 m depth, while in the real crater, the top of the peak-ring is at 618 mbsf. To ensure that the mass-deficit from the post-impact sedimentary rocks is realistic, one of two changes could be made: 1) The thickness of the sediments in the model could be maintained, but the reference density of the sedimentary infill increased such that the mass deficit remains constant, or 2) the reference density of post-impact sediments could be maintained at reasonable values but the thickness of the sedimentary infill reduced such that only 600 m of sedimentary rock overly the peak-ring. Here, the latter approach was adopted because it is more useful for predicting the gravity structure around the crater centre. This approach will result in the model predicting a smaller magnitude anomaly in the terrace zone compared to the observational data due to the lack of low-density sedimentary rock at those radial distances.

The modelled gravity signal possesses a mass deficit in the range of 6.64–

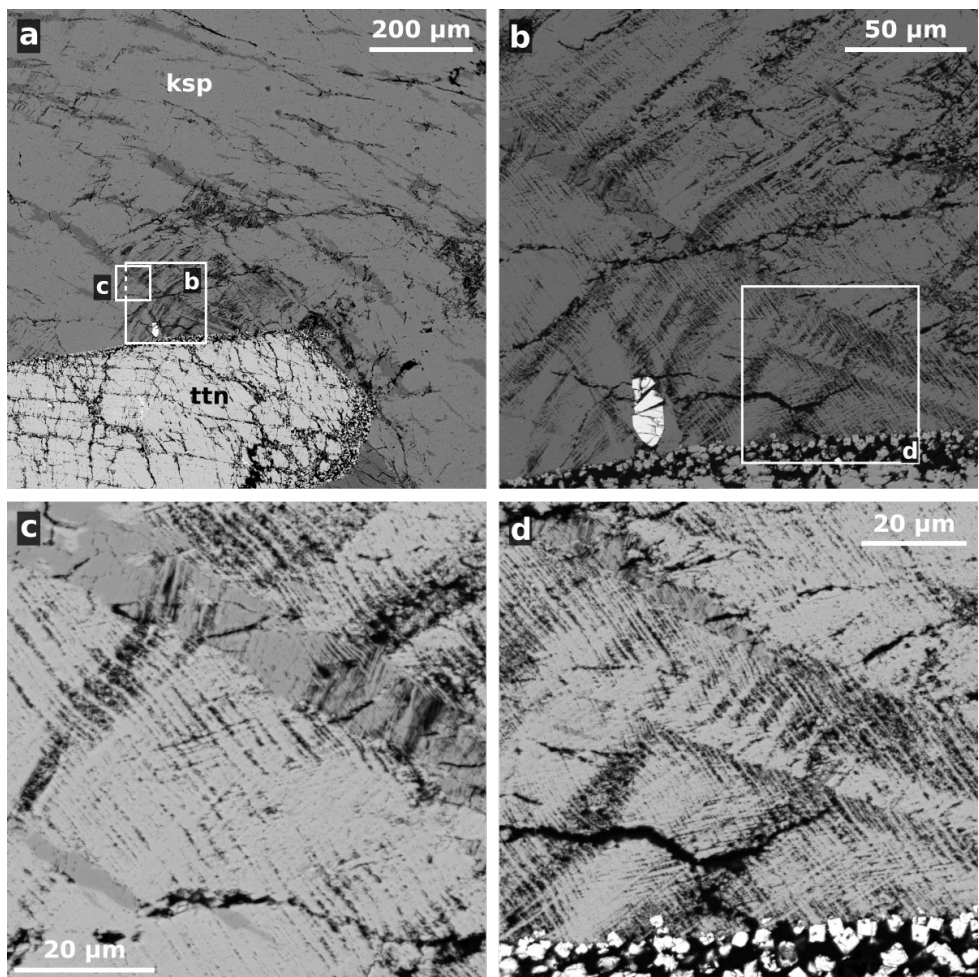


Figure 9.13: Planar elements in alkali feldspar. BSE images of Sample 364-77-A-121-R-1-75-77. a) Low-resolution image of alkali feldspar (ksp) and titanite (ttn). b) High-resolution BSE image of sub-area indicated on a). Multiple, parallel, planar elements in alkali-feldspar. c) High-resolution BSE image of sub-area indicated on a). Multiple, parallel, planar elements, defined most clearly by void spaces, in alkali feldspar. Planar elements in perthitic lamellae are sometimes continue across the lamellae boundaries, and are sometimes truncated at the boundary. Planar elements are deformed by kink bands, which exacerbate void spaces, and which continue with a change of orientation through perthite lamellae. d) High-resolution BSE image of sub-area indicated on b). At least 5 planar element sets in alkali feldspar.

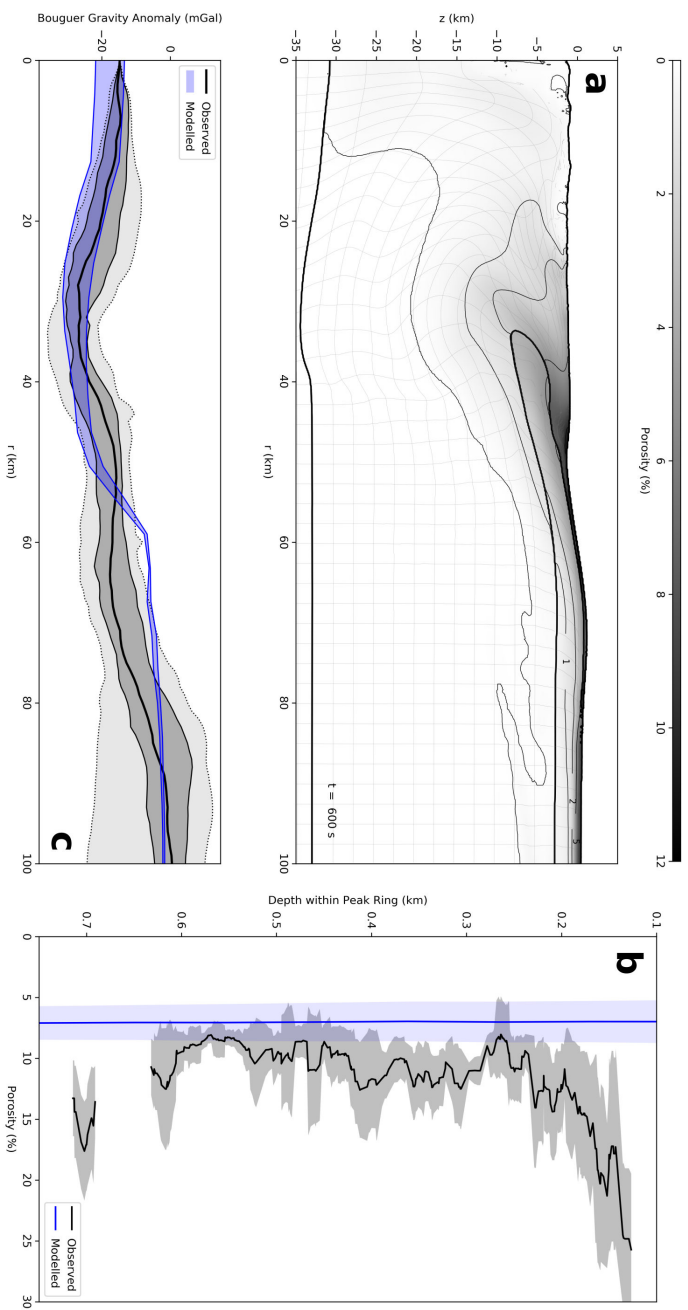


Figure 9.14: Comparison of observed and modelled porosity and gravity signals of the Chicxulub simulation. a) Porosity distribution at the end of the Chicxulub simulation with b) the modelled porosity distribution of Hole M0077A compared to results from IODP-ICDP Expedition 364. The predicted gravity anomaly compared to the observed gravity signal of the Chicxulub structure (see Figures 9.2 and 9.4).

Table 9.5: Range of target material densities used in gravity calculation.

Material	Selected Reference Density (kg m^{-3})	Reported Density (kg m^{-3})	Reference
Pre-impact Sedimentary Rock	2650 ± 50	$2477\text{--}2938$	Elbra and Pesonen (2011)
Crystalline Basement	2628 ± 39	2628 ± 39	This study & Christeson et al. (2018)
Mantle	3320	3320	Benz et al. (1989)
Post-impact Sedimentary Rock*	2200 ± 50	$1960\text{--}2470$	Christeson et al. (2018)
Bouguer Correction Density	2670	2670	Tanner et al. (1988)

*The thickness of post-impact sedimentary rocks above the peak-ring was maintained at 650 m

8.35×10^{15} kg, considering the uncertainties presented in Table 9.5. A slight underestimation of the mass deficit associated with the median gravity signal, 9.15×10^{15} kg, but well within the quartile gravity signals. The magnitude of the modelled anomaly at the crater centre is in a range from 14–22 mGal, consistent with the observed magnitude of approximately 15 mGal. Additionally, the minimum anomaly in the modelled profile occurs between 28 and 40 km radial distance, and has a magnitude of approximately 24–31 mGal, consistent with the observed magnitude of the negative anomaly, 26 mGal, at 35 km radial distance. Beyond the peak-ring, within the annular trough and the terrace zone of the crater, the fit between the modelled and observed gravity profiles is poorer. This can be explained primarily by the oversimplifications associated with the post-impact sedimentary fill; the underestimation of the model at 45–55 km radial distance occurs because of the lack of vertical density variation in the post-impact sediments; the oldest sedimentary rocks, adjacent to the peak-ring within the annular trough, are likely to have greater densities than modelled here, as suggested by the increase in seismic velocity and density with depth (Christeson et al., 2018). Consequently, this would cause a reduction of the size of the gravity anomaly. The overestimation of the observed profile from 55–75 km radial distance occurs, as previously stated, due to the lack of sedimentary infill at these radial distances. Additional causes of discrepancy between the model and observation may include; post-impact compaction/precipitation/dissolution, or a lack of initial porosity in the modelled pre-impact sedimentary rocks.

9.4 Discussion

The rocks of the Chicxulub peak-ring are possess low densities, with porosities of $11.5 \pm 4.7\%$. Compared to shocked target rocks in other craters (Pilkington and Grieve, 1992), and assuming that the granitic rocks of the peak-ring had no porosity prior to impact, the target rocks of the Chicxulub peak-ring have among the highest impact-generated porosities of any impact structure (Table 9.6). Such a result is not unexpected due to the relative size of the Chicxulub impact, and the complex deformation path that peak-ring materials follow during dynamic collapse (Chapter 8).

The results presented here demonstrate that numerical impact simulations are capable of accurately predicting impact-induced porosity within large impact structures and the resultant gravity signal associated with complex impact craters, additional processes such as hydrothermal precipitation/dissolution or post-impact compaction have a comparatively small effect on the total porosity. This porosity is caused by the shear induced failure of target rocks during cratering. Additionally, these results support the recommendation by Collins (2014), that low GSI dilatancy parameters should be used for impact cratering simulations.

The main contributor to the porosity of target rocks in the Chicxulub

Table 9.6: Density contrasts between fractured and undisturbed target rocks at several terrestrial impact structures. From Pilkington and Grieve (1992).

	Target Rocks	$\nabla\rho$ (kg m^{-3})	Reference
Gosses Bluff, Australia	Sedimentary	150	Barlow (1979)
Brent, Canada	Crystalline	170–340*	Millman et al., 1960
Nicholson Lake, Canada	Crystalline	70–140	Dence et al., 1968
West Clearwater Lake, Canada	Crystalline	170	Plante et al., 1990
Holleford, Canada	Crystalline	240*	Beals, 1960
Manicouagan, Canada	Crystalline	130	Sweeney, 1978
Söderfjärden, Finland	Crystalline	160	Lauren et al., 1978
Chicxulub, Mexico	Crystalline	184**	This study

*Values include effects of sediments and breccias

** Assuming initial granitic target rocks had no initial porosity, i.e. that the grain density of the granitic rocks is the same as the initial, pre-impact, bulk density of the granitic rocks

impact structure is shock-induced micro-fracturing. Additional porosity is contributed from cataclasites, which are extremely porous but volumetrically small, and large inter-granular pores. The origin of large inter-granular pores may be due to sectioning-induced damage, or potentially, as the large inter-granular pores are most significant near the top of the granitic rock section, coinciding with the largest deviation between the modelled porosity and observed porosity, these pores may arise as a result of post-impact processes, i.e. hydrothermal dissolution, that are not described by the numerical model.

The rocks of the peak-ring never experience tensile stress regimes during cratering (Chapter 8). Consequently, the shear-induced dilatancy model used here should simulate the production of all styles of primary micro-porosity observed within the peak-ring rocks, although some secondary porosity may be generated by processes such as hydrothermal dissolution, enlarging pre-existing primary pores. The observational evidence shows that the porosity of the peak-ring rocks is primarily hosted in intra-granular fractures formed by shock metamorphism. Nevertheless, the dilatancy model predicts that very minimal amounts of porosity are produced during the passage of the shock wave and rarefaction, instead, it predicts that, for the shallowest rocks in the peak-ring, porosity is generated in two distinct phases, the first during transient cavity formation and rim collapse (0–100 s) and the second during central peak formation and collapse (175–350 s) (Figure 9.15). Deeper material within the peak-ring structure experiences only one distinct phase of dilatancy, which occurs more gradually through transient cavity formation and collapse. One apparent explanation for the discrepancy between the observation of shock-induced micro-fractures dominating porosity and the model prediction of porosity generation through time is that during shock, where pressures are significantly high, fractures are likely to form without any porosity. Those fractures must then open during later phases of crater deformation. Nevertheless, it is possible that the shear-induced dilatancy model used here is an oversimplification of the process that generates porosity in para-autochthonous impactites. A process that may involve two distinct processes; one, a dynamic effect of fracturing during shock, and the second due to true shear-induced dilatancy of a pre-damaged material. If this is the case, the GSI parameters used here for shear-induced dilatancy are too large.

The ability to accurately predict the porosity distribution of complex craters is significant in the understanding of the gravity signal of large impact structures. Here, a close fit to the observed gravity signal of the Chicxulub structure has been obtained, based on the result of a simple dilatancy model. Discrepancies between the modelled and observed gravity signals may be due to the lack of a porous-compaction model in the simulation (Wünnemann et al., 2006), additionally changes to acoustic fluidisation parameters may change the location of down-faulted sedimentary rocks in the collapsed transient cavity rim that underlies the peak-ring, and therefore affect the modelled gravity signature. Nevertheless, the overall consistency between the gravity profiles and porosities between observation and model reinforces the significance of dilatancy on

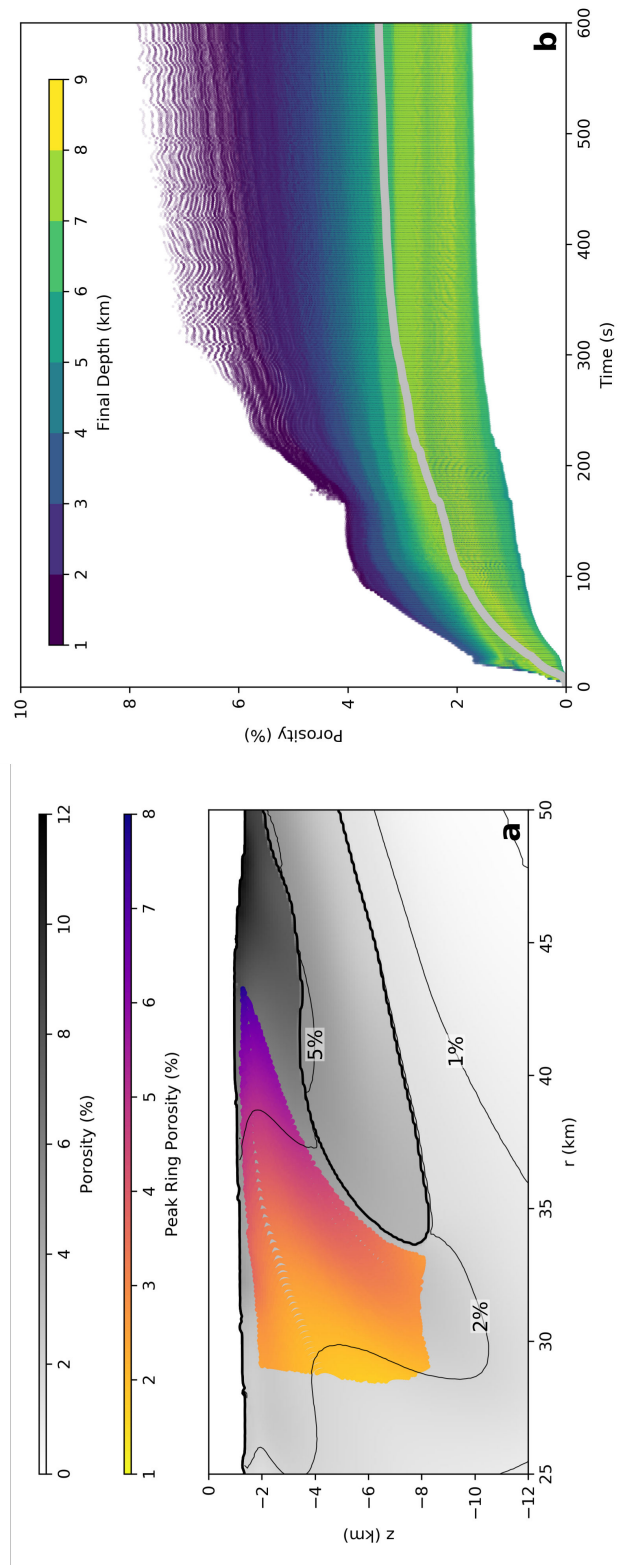


Figure 9.15: The distribution of porosity within the Chicahuah peak-ring, and the timing of its generation. a) Porosity distribution at the final timestep, focussed upon the peak-ring. Shumped sedimentary rocks beneath the peak-ring are distinguished from crystalline rocks by thick black lines, while thin black lines show contours of porosity. Peak-ring material is highlighted by the coloured points. b) porosity of peak-ring material through time, coloured by the material's final depth. The grey line is a mass-weighted average of porosity in the peak-ring through time.

sub-crater structure and deformation.

9.4.1 Orientation of Fractures

The granitic rocks from Hole M0077A have minimal to no grain preferred orientation, consequently, that shock micro-fractures have a preferred orientation across a whole thin section of randomly oriented grains indicates that crystallographic orientation may not have primary control of the orientation of fractures. Canonically, PFs are known to form on rational crystallographic planes (French and Koeberl, 2010), however, EBSD results indicate that fractures within grains are associated with strain (Figure 9.12). Significant plastic strain can only accumulate within crystals due to shear deformation, it is therefore probable that the intra-granular fractures occur within these samples due to shear failure. Thus, the crystallographic orientation of the fracture plane that is activated during shock may be controlled by stress conditions. In addition to the consistency between porosity and gravity measurements with the results of numerical impact simulations, it is also possible to predict the orientation of shock-microfractures in numerical impact simulations (Chapter 8). Predicting the orientation of fractures during cratering requires the assumption of two well-accepted concepts of shock physics and rock mechanics.

Firstly, the orientation of fractures during rock failure is predicted by the canonical model of Mohr-Coulomb rock failure (Anderson, 1905). In low-pressure regimes, rock failure is typically expected at 30° to the orientation of σ_1 , depending on the coefficient of internal friction. However, in a high-pressure regime, greater than the Hugoniot Elastic Limit (HEL), the coefficient of internal friction approaches 0, and consequently, the angle of failure approaches 45° to σ_1 .

Secondly, the formation of PFs during shock occurs during shock loading, i.e. once the HEL is exceeded but before peak pressure conditions are reached (French and Koeberl, 2010; Poelchau and Kenkmann, 2011). Support of this assertion derives from the observation that PFs commonly separate domains within grains that PDFs, which are sensitive to the peak pressure of the shock wave, do not cross.

Using these concepts, by obtaining the orientations and magnitudes of deviatoric principal stresses, following the methodology described in Chapter 8, it is possible to predict shock fracture orientations within target material during shock (Figure 9.17).

During crater excavation and modification, and to a much lesser extent, during shock; material is expected to rotate from its initial orientation. The orientation of material in numerical simulations can be tracked by calculation of infinitesimal strain tensors (see Chapter 8). Here, the Dynamic Collapse Model has been used, and a single tracer selected to represent the recovered core material. This particle rotates by approximately 70° clockwise during cratering. Selecting tracers from deeper, or at

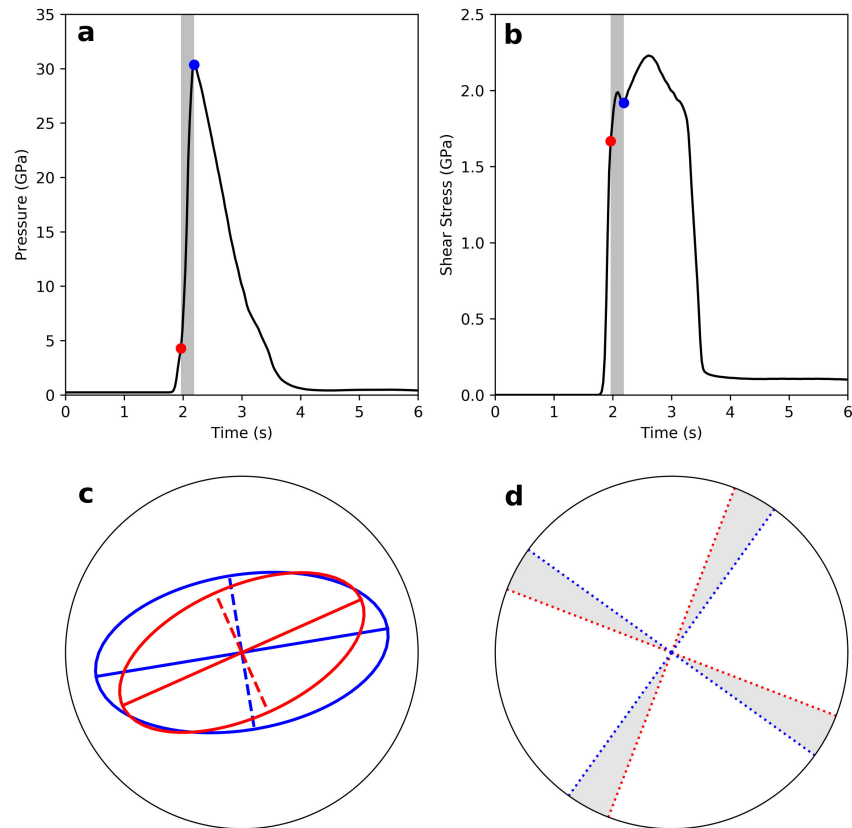


Figure 9.16: Fracture formation during shock. a) Pressure during shock and b) Maximum resolvable shear stress during shock. PF formation is expected to occur between the time at which the HEL is exceeded (red), and the time of maximum pressure (blue). c) Cross-sections of the Lamé stress ellipsoid are shown at the times corresponding to the time points. d) PF formation is expected at 45° to the orientation of σ_1 , therefore PFs are expected to form at orientations within the grey areas. (Note: the highlighted grey areas take into account the rotation of the tracer particle by roughly 1° anti-clockwise during shock).

increasing radial distances within the peak-ring material causes a systematic increase in the total clockwise rotation during cratering by up to an additional 30° (Appendix G). Consequently, the final orientation of shock-related fractures, as predicted by the model is at concentric strikes, dipping at 88° inwards – 78° outwards, and the conjugate set at 12° inwards – 2° outwards. The observed orientations of micro-fractures within the shocked granitic rock samples can be sub-divided into one set of steep apparent dips ($69.4\text{--}89.9^\circ$) and a second set with shallow apparent dips ($7.7\text{--}13.3^\circ$). Despite the observations only being capable of determining apparent dip, without any strike information, the modelled orientations are remarkably consistent with the observed micro-fracture orientations.

This result indicates several significant points; firstly, that the orientation at which shock microfractures (PFs) form may indeed be primarily controlled by the orientation of principal stresses during shock. Secondly, it is clear that a significant rotation of the peak-ring material is required between shock and the final emplacement of the peak-ring. Regardless of the model by which crater collapse occurs by, the orientation of fractures due to shock will always be at moderate dip angles (approximately 45°) immediately after shock. Achieving conjugate sets of planar fractures in sub-vertical and sub-horizontal respective orientations requires either a clockwise rotation of material by approximately $60\text{--}70^\circ$ or an anti-clockwise rotation of $20\text{--}30^\circ$. The dynamic collapse model of peak-ring formation precisely predicts the large clockwise rotation required. Finally, stress-induced fractures significantly affect the permeability anisotropy of rocks. Canonically, the maximum permeability direction of a fault rock is along the intersection of minor-faults, i.e. parallel to the orientation of the σ_2 direction that produced the fractures (Sibson, 2000). Combining this with the fact that shock micro-fracturing produces the dominant pore fabric in these peak-ring rocks leads to possibility that numerical impact simulations may be able to predict the permeability distribution and anisotropy within impact craters, a critical parameter for hydrothermal models of impact structures.

Finally, in addition to the gravity signature, porosity of peak-ring rocks, and orientation of microfractures, numerical impact simulations can predict the shock pressure experienced by peak-ring rocks. Figure 9.18 shows the distribution of shock pressure within the peak-ring of the modelled Chicxulub peak-ring, and a comparison between the observed shock pressures in Hole M0077A with the average shock pressure attenuation pattern within the modelled Chicxulub peak-ring. Similarly to Chapters 5 and 6, the modelled shock pressures overestimate the observed shock pressures by approximately 10 GPa. However, there is some overlap between the 1σ envelopes of the shock pressure estimates and the modelled pressures, thus, bearing in mind the systematic overestimation of shock pressures by numerical simulations, or the underestimation of shock pressures by observational techniques (see Chapters 5 and 6) in other impact structures, the results presented here are not inconsistent.

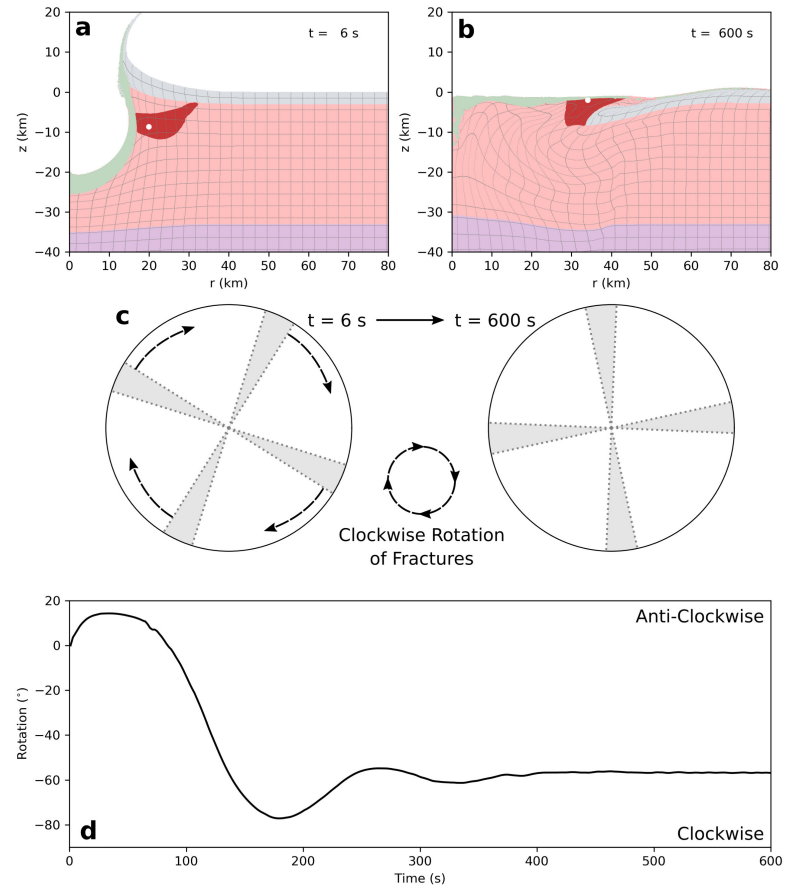


Figure 9.17: Rotation of fractures during modification. Panels of the arrangement of the crater after a) shock passage and b), modification. Peak-ring material is highlighted by the red material while the individual tracer being tracked is highlighted by the white point. c) Orientation of shock microfractures at the timesteps indicated. d) Cumulative orientation of the selected tracer particle throughout all timesteps of the simulation.

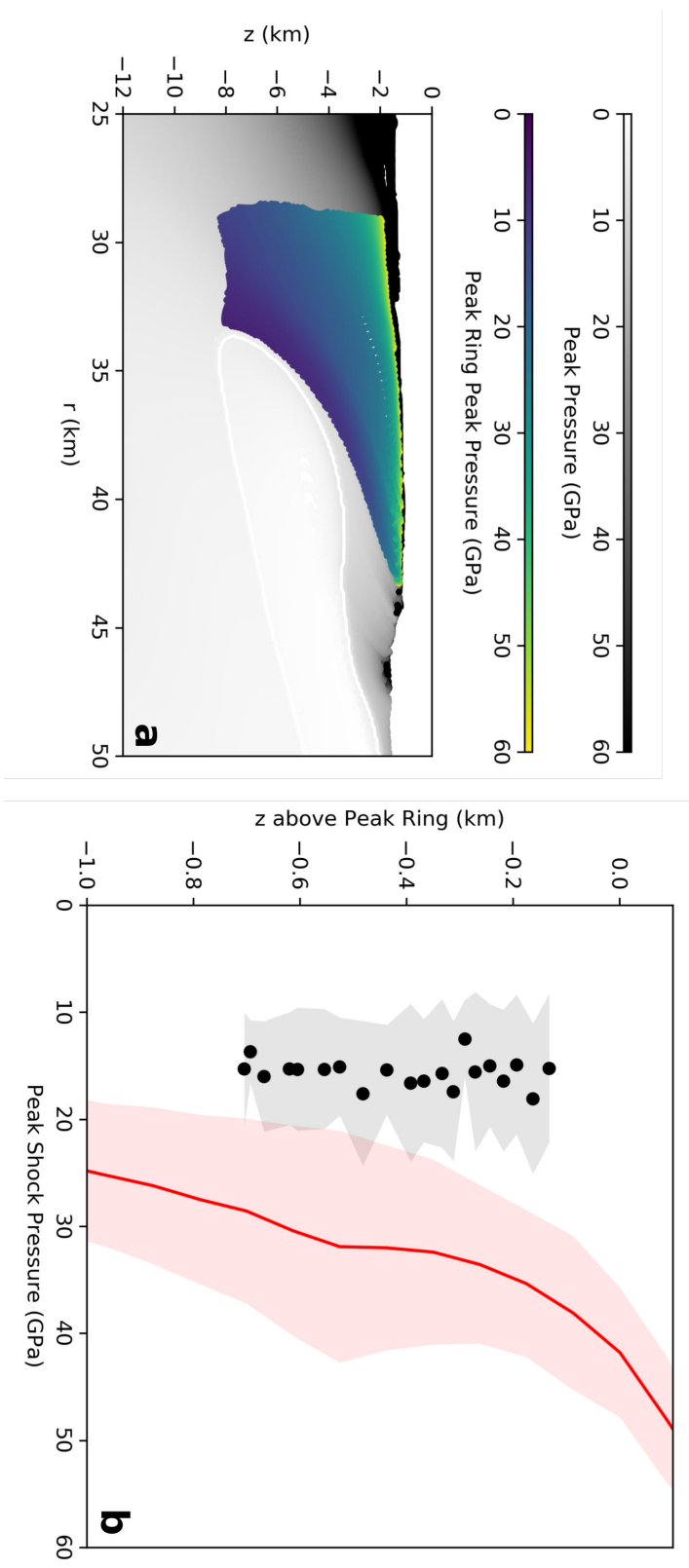


Figure 9.18: The distribution of shock pressure within the Chicxulub peak-ring, and a comparison of observed and modelled shock pressures.
 a) Peak shock pressure distribution at the final timestep, focussed upon the peak-ring. Slumped sedimentary rocks beneath the peak-ring are distinguished from crystalline rocks by thick white lines. Peak-ring material is highlighted by the coloured points. b) Mass-weighted average of peak shock pressures in peak-ring material with depth (red), with 1σ error envelope compared with estimated shock pressures on the basis of petrographic observation (black), with 1σ error envelope.

In addition to constraining the shock pressure at which the Chicxulub peak-ring experienced peak shock conditions (~ 15 GPa), a new shock deformation texture has been identified; PDBs in quartz. These features are unlikely to be unique shock metamorphism indicators, but certainly indicate significant crystal-plastic strain during cratering. Additionally, the occurrence of PDFs in feldspars is often reported, but is rarely imaged in scientific literature. In this chapter, potential PDFs in shocked alkali feldspar have been identified and illustrated. The crystallographic orientation of these features remains to be seen, and would require TEM (Transmission Electron Microscope) analysis.

9.5 Conclusions

In this chapter, it has been shown that within the Chicxulub peak-ring, peak shock metamorphic conditions were around 15 ± 5 GPa, as determined by universal-stage observations of PDFs in quartz. Additionally, the unusually high porosities of the Chicxulub peak-ring reported by Morgan et al. (2017) and Morgan et al. (2016) and Christeson et al. (2018) are caused by pervasive, shock-induced microfracturing. The orientations of the shock micro-fractures are consistent with the Dynamic Collapse Model of peak-ring formation that predicts the experienced shock pressure, and the orientation of shock-induced fractures combined with subsequent rotation of rocks during crater modification (Chapter 8). A significant implication of this work is that PFs in quartz are sensitive to the orientation of principal stresses during shock, in turn, this suggests that porosity and permeability is likely to be anisotropic within craters. Finally, the results presented in this chapter demonstrate that the dilatancy model of Collins (2014) accurately predicts the porosities of peak-ring rocks, and that the predicted gravity anomaly due to dilatancy across the entire structure is consistent with remote geophysical observations, providing a simple gravity model of the Chicxulub structure that accurately constrains all of the important processes that generate mass deficits within craters.

Part IV

Conclusions

10 Conclusions

10.1 Summary of Findings

I have proposed that direct geological observations: macro- and micro-structural observations, shock barometry, and petrophysical measurements, can, and should, be used to place direct constraints on numerical simulations of crater formation. In particular, this thesis has attempted to describe the kinematic process of complex crater collapse, where bowl-shaped transient cavities collapse to form wide terrace zones and structural uplifts composed of central peaks and/or peak-rings. Additionally, work in this thesis has constrained the mechanism that facilitates the collapse of complex craters.

10.1.1 Modification-Related Deformation

Across all three impact structures studied in this thesis, modification-related deformation is primarily accommodated on cataclasites (Chapters 5, 6, and 9). Thus, a significant portion of transient weakening must occur by a “dry” mechanism.

Faulting occurs on all scales within the structural uplifts of craters, from micron-length displacements on grain-scale fractures (Chapters 6 and 9) to field-scale faults accommodating hundreds of meters of displacement (Kenkmann et al., 2014). The concept of a “block size” may therefore be misleading; faults in impact structures possess a fractal-like pattern, it is unclear whether any particular length-scale of fault accommodates more deformation than any other; i.e., the total strain across a central uplift accommodated on grain-scale fractures may be of an order of magnitude similar to the total strain accommodated on field-scale faults. This may explain some of the discrepancies between block sizes measured by field mapping compared to core logging (Ivanov et al., 1996; Kenkmann et al., 2006; Riller et al., in press; Chapter 5; and Chapter 6). To add more complexity, block size varies spatially within a crater (Kenkmann et al., 2006; Chapter 6), and may also vary temporally (Riller et al., in press; Chapter 8). Any “block”-based model of transient weakening should therefore take these observations into account.

Dikes of impact melt rock and melt-bearing breccias are more common in the peak-ring of the Chicxulub structure than observed in cores of smaller structures (Chapters 8), 5, and 6). These “dikes” clearly accommodate modification-related deformation (Riller et al., *in press*; Chapter 8). Thus, it remains possible that weakened faults facilitate late-stage crater collapse in large structures.

10.1.2 Transient Weakening

In this thesis, it has been shown that the block model implementation of acoustic fluidisation produces a rheology for rocks during crater collapse that is consistent with all currently-made observations (Chapters 5, 6, and 9). Nonetheless, the conceptual idea behind the justification of the block model lacks observational support. Large discrete rock blocks do not appear to be separated by significant thicknesses of highly compressible breccia (Chapters 5 and 6). Additionally, unrealistically high quality factors, Q , are required to sustain fluidisation throughout crater collapse (Chapter 5). This may be explained by the regeneration of acoustic energy during collapse and/or a secondary weakening mechanism that continues transient weakening into later phases of the modification stage. One potential mechanism that may operate at this time is the lubrication of faults by impact melts and melt-bearing breccias (Riller et al., *in press*; Chapter 8).

10.1.3 Shock Metamorphism

Observationally determined shock pressures in craters are broadly consistent with the results of numerical impact simulations (Chapters 5, 6, and 9), particularly in terms of the relative patterns of shock attenuation (Chapter 5).

Nevertheless, there is a systematic difference between observationally determined shock pressures and the results of numerical simulations. Observationally estimated shock pressures are always ~ 10 GPa less than those predicted by numerical simulations (Chapters 5, 6, and 9; Holm-Alwmark et al., 2017).

I believe that the systematic offset occurs due to inaccuracies in commonly used shock classification schemes (Table 3.1; Holm-Alwmark et al., 2018; Stöffler and Langenhorst, 1994), and thus, observationally constrained shock pressures are underestimates. The primary problem of the shock classification scheme for ascribing pressures to para-autochthonous rocks is that high pressure (35–60 GPa) features such as diaplectic glasses are extremely uncommon within all crater para-autochthon.

From a simple understanding of the hemispherical attenuation of shock waves in rocks, the volume of rock shocked between 35 and 60 GPa in an impact structure must be of a similar order of magnitude to the volume of impact melt (> 60 GPa; Chapter

5), and becomes more voluminous (in absolute and relative terms) with increasing crater size. Nevertheless, diaplectic glasses can rarely be found in the para-autochthonous rocks of an impact crater, and impact breccias (even including ejecta) contain only a small fraction of the required volume of highly shocked material. It is also implausible that impact melt sheets can assimilate the necessary volume of rock shocked between 35 and 60 GPa. Estimates of impact melt volumes in craters based on a melting criterion of $P > \sim 60$ GPa are one of the most robust results of numerical impact simulations (Pierazzo et al., 1997; Chapter 5). If impact melt sheets were to assimilate most rocks shocked from 35-60 GPa in a crater, melt volume estimates made from numerical impact simulations would all become vast overestimates.

The systematic offset between observations and models could be corrected if shock classification schemes raised the minimum pressures required for each shock feature/ PDF orientation. Such a change could be justified based on the variability of the experimental results on which shock classification schemes are based; for example, Hörz (1968) found in single crystal shock experiments that between 5 and 10 GPa, (0001) and $\{10\bar{1}1\}$ PDF orientations were found. While, in whole rock shock experiments, Huffman and Reimold (1996) did not find any PDFs in samples until shock pressures in excess of 15 GPa (with ambient pre-shock temperatures). Nevertheless, shock classification schemes all place the onset of PDFs in quartz at 5 GPa, and assign pressures from 5-10 GPa for (0001) PDFs. Importantly, the sequence of observed shock features in quartz with increasing pressure across all experiments is robust. Nevertheless it is unclear whether the absolute values ascribed in shock classification schemes (Table 3.1; Holm-Alwmark et al., 2018; Stöffler and Langenhorst, 1994) are accurate. In addition to the importance of using shock features to constrain pressures during metamorphism, this thesis has demonstrated that shock-induced micro-fractures, and PFs in particular, may be influenced by the conditions of shear stress during shock.

10.1.4 Methods to Constrain Numerical Impact Models

It has been shown in this thesis that a wide variety of observations can be used as direct constraints on numerical simulations. Firstly, shock metamorphism can be used and quantified as an observational constraint which traces “stratigraphy” from the transient cavity stage through to the end of modification, accurate constraints from shock pressures alone requires sampling points distributed across a crater (Chapter 5). Additional constraints can be applied on the processes of shock metamorphism, and cratering in general, by the use of observations that constrain the directionality of shock propagation (Chapter 9). More generally, understanding the stress-strain evolution of rocks throughout cratering can provide many valuable constraints on the cratering process. In this thesis, I have developed a new method of tracking stress and strain during cratering simulations, permitting the use of quantitative structural geological observa-

tions as constraints on numerical impact simulations. Combining structural geological observations with numerical models can provide many important insights into the cratering process; e.g., absolute timings of deformation structures, orientations of principal stresses and strains, and accounting for spatial variations of deformation (Chapter 8). Finally, this thesis has demonstrated that the gravity signature of a crater can, and should, be used as a constraint on numerical simulations. This can be achieved by an understanding of the dilatancy of rocks in impacts (Collins, 2014; Chapters 6, and 9).

10.2 Perspectives

The work carried out in this thesis has highlighted several outstanding gaps in our current understanding of impact cratering that should be addressed in future work.

Assigning shock pressures to terrestrial shocked rocks is over-reliant on the shock classification scheme of quartz. An ideal shock classification scheme for rocks would retain the precision of the quartz classification scheme but would account for the shock metamorphism of all (or most) phases within a rock. A significant part of this classification would have to account for the differences between the propagation of shock through a poly-crystalline rock compared to a single crystal. Different minerals may experience different shock pressures depending on their abundance and arrangement within a rock. It is therefore unclear how one may combine shock pressure estimates based on major phases (e.g., quartz) with those based on minor phases (e.g., zircon). Developing new, precise, whole-rock shock classifications would require substantial experimental work.

It is clear at this time that no currently proposed transient weakening model fully accounts for complex crater collapse; the most successful current model is undoubtedly acoustic fluidisation. However, current implementations are overly simplistic. Any new model of transient weakening in craters should account for the spatial and temporal variation of fault block sizes (which likely affects viscosity), and potentially include the effect of fault weakening by frictional melts or by the effect of infiltrating low-strength melts and/or breccias. Frictional melting must be supported by a physically plausibly model that accounts for fault spacing, strain, and strain rate conditions. Accounting for the lubrication of faults by impact melts and/or breccias would require a rheological characterisation of impact melts and/or breccias, in addition to a criterion that describes where the effect may occur. Regardless of the exact mechanism of fault weakening, it can only have a significant effect during the later phases of crater modification. Any model of weakening should, on average, produce the same rheology as the block model implementation of acoustic fluidisation.

Numerical impact simulations are becoming capable of modelling impact craters at very high resolutions, high enough that the behaviour of faults becomes signif-

icant. Accounting for this behaviour is computationally challenging. One of the simplest methods to incorporate faults into continuum numerical impact simulations may be to actively track the active fault spacing, as a function of strain rate, temperature, and other properties, throughout a simulation. The application of this type of model may be important for predicting the occurrence of frictionally-generated pseudotachylites in impact structures, and in the development of fault weakening models.

Bibliography

- Abramov, O. and D. A. Kring (2007). “Numerical modeling of impact-induced hydrothermal activity at the Chicxulub crater”. *Meteoritics & Planetary Science* 42.1, pp. 93–112. ISSN: 1945-5100. DOI: 10.1111/j.1945-5100.2007.tb00220.x.
- Allmendinger, R. W., N. Cardozo, and D. M. Fisher (2012). “Structural Geology Algorithms: Vectors and Tensors”. Cambridge University Press, pp. 60–182. ISBN: 978-1-107-40138-9.
- Amsden, A. A., H. M. Ruppel, and C. W. Hirt (1980). *SALE: A simplified ALE computer program for fluid flow at all speeds*. Tech. rep. LA-8095. New Mexico: Los Alamos National Laboratories, p. 105.
- Anderson, C. E. (1987). “An overview of the theory of hydrocodes”. *International Journal of Impact Engineering* 5.1-4, pp. 33–59.
- Anderson, E. M. (1905). “The dynamics of faulting”. *Transactions of the Edinburgh Geological Society* 8.3, pp. 387–402. ISSN: 0371-6260, 2052-9414. DOI: 10.1144/transed.8.3.387.
- Artemieva, N., K. Wünnemann, F. Krien, W. U. Reimold, and D. Stöffler (2013). “Ries crater and suevite revisited — Observations and modeling Part II: Modeling”. *Meteoritics & Planetary Science* 48.4, pp. 590–627.
- Baker, D. M. H., J. W. Head, S. C. Schon, C. M. Ernst, L. M. Prockter, S. L. Murchie, B. W. Denevi, S. C. Solomon, and R. G. Strom (2011a). “The transition from complex crater to peak-ring basin on Mercury: New observations from MESSENGER flyby data and constraints on basin formation models”. *Planetary and Space Science*. Mercury after the MESSENGER flybys 59.15, pp. 1932–1948. ISSN: 0032-0633. DOI: 10.1016/j.pss.2011.05.010.
- Baker, D. M. H., J. W. Head, C. I. Fassett, S. J. Kadish, D. E. Smith, M. T. Zuber, and G. A. Neumann (2011b). “The transition from complex crater to peak-ring basin on the Moon: New observations from the Lunar Orbiter Laser Altimeter (LOLA) instrument”. *Icarus* 214.2, pp. 377–393. ISSN: 0019-1035. DOI: 10.1016/j.icarus.2011.05.030.
- Baker, D. M. H., J. W. Head, G. S. Collins, and R. W. K. Potter (2016). “The formation of peak-ring basins: Working hypotheses and path forward in using observations to constrain models of impact-basin formation”. *Icarus* 273, pp. 146–163. ISSN: 0019-1035. DOI: 10.1016/j.icarus.2015.11.033.

- Barlow, B. C. (1979). "Gravity investigations of the Gosses Bluff impact structure, central Australia". *BMR Journal of Australian Geology & Geophysics* 4, pp. 323–339.
- Beals, C. S. (1960). "A probable meteorite of Precambrian age at Holleford, Ontario". *Publications of the Dominion Observatory, Ottawa*. 24, pp. 117–142.
- Beals, C. S., G. M. Ferguson, and A. Landau (1956). "A Search for Analogies Between Lunar and Terrestrial Topography on Photographs of the Canadian Shield". *Journal of the Royal Astronomical Society of Canada* 50, pp. 203–250. ISSN: 0035-872X.
- Benz, W., A. G. W. Cameron, and H. J. Melosh (1989). "The origin of the Moon and the single-impact hypothesis III". *Icarus* 81.1, pp. 113–131. ISSN: 0019-1035. DOI: 10.1016/0019-1035(89)90129-2.
- Biren, M. B., M. C. van Soest, J. A. Wartho, K. V. Hodges, and J. G. Spray (2016). "Diachroneity of the Clearwater West and Clearwater East impact structures indicated by the (UTh)/He dating method". *Earth and Planetary Science Letters* 453, pp. 56–66. ISSN: 0012-821X. DOI: 10.1016/j.epsl.2016.07.053.
- Bostock, H. H. (1969). "The Clearwater Complex, New Quebec". *Geological Survey of Canada Bulletin* 178, p. 63.
- Bradley, J. J. and A. N. Fort (1966). "Internal Friction in Rocks". *Handbook of Physical Constants: Geological Society of America Memoir* 97. Ed. by S. P. Clark. Geological Society of America, pp. 173–193.
- Brodie, K, D Fettes, and B Harte (2007). "Structural terms including fault rock terms". *Metamorphic rocks: A classification and glossary of terms, recommendations of the International Union of Geological Sciences*. Ed. by D. Fettes and J. Desmons. Cambridge University Press, pp. 24–31.
- Campos-Enriquez, J., H. Morales-Rodriguez, F. Dominguez-Mendez, and F. Birch (1998). "Gauss's theorem, mass deficiency at Chicxulub crater (Yucatan, Mexico), and the extinction of the dinosaurs". *Geophysics* 63.5, pp. 1585–1594. ISSN: 0016-8033. DOI: 10.1190/1.1444455.
- Carter, N. L. (1965). "Basal quartz deformation lamellae; a criterion for recognition of impactites". *American Journal of Science* 263.9, pp. 786–806. ISSN: 0002-9599, 1945-452X. DOI: 10.2475/ajs.263.9.786.
- Chapman, C. R. and W. B. McKinnon (1986). "Cratering of planetary satellites". *Satellites*. Ed. by J. A. Burns and M. S. Matthews. Tucson: University of Arizona Press, pp. 492–580.
- Christeson, G. L. et al. (2018). "Extraordinary Rocks of the Chicxulub Crater Peak-ring: Physical Property Measurements from IODP/ICDP Expedition 364". *Earth and Planetary Science Letters* 495, pp. 1–11. DOI: 10.1016/j.epsl.2018.05.013.
- Cockell, C. S. (2006). "The origin and emergence of life under impact bombardment". *Philosophical Transactions of the Royal Society of London B: Biological Sciences* 361.1474, pp. 1845–1856. ISSN: 0962-8436, 1471-2970. DOI: 10.1098/rstb.2006.1908.

- Collins, G. S. (2014). "Numerical simulations of impact crater formation with dilatancy". *Journal of Geophysical Research: Planets* 119.12, 2014JE004708. ISSN: 2169-9100. DOI: 10.1002/2014JE004708.
- Collins, G. S., T. Kenkemann, G. R. Osinski, and K. Wünnemann (2008a). "Mid-sized complex crater formation in mixed crystalline-sedimentary targets: Insight from modeling and observation". *Meteoritics & Planetary Science* 43.12, pp. 1955–1977. ISSN: 1945-5100. DOI: 10.1111/j.1945-5100.2008.tb00655.x.
- Collins, G. S. and H. J. Melosh (2003). "Acoustic fluidization and the extraordinary mobility of sturzstroms". *Journal of Geophysical Research: Solid Earth* 108.B10, p. 14.
- Collins, G. S. and K. Wünnemann (2005). "How big was the Chesapeake Bay impact? Insight from numerical modeling". *Geology* 33.12, pp. 925–928. ISSN: 0091-7613, 1943-2682. DOI: 10.1130/G21854.1.
- Collins, G. S., H. J. Melosh, J. V. Morgan, and M. R. Warner (2002). "Hydrocode Simulations of Chicxulub Crater Collapse and Peak-Ring Formation". *Icarus* 157.1, pp. 24–33. ISSN: 0019-1035. DOI: 10.1006/icar.2002.6822.
- Collins, G. S., H. J. Melosh, and B. A. Ivanov (2004). "Modeling damage and deformation in impact simulations". *Meteoritics & Planetary Science* 39.2, pp. 217–231. ISSN: 1945-5100. DOI: 10.1111/j.1945-5100.2004.tb00337.x.
- Collins, G. S., J. V. Morgan, P. Barton, G. L. Christeson, S. P. S. Gulick, J. Urrutia, M. Warner, and K. Wünnemann (2008b). "Dynamic modeling suggests terrace zone asymmetry in the Chicxulub crater is caused by target heterogeneity". *Earth and Planetary Science Letters* 270.3–4, pp. 221–230. ISSN: 0012-821X. DOI: 10.1016/j.epsl.2008.03.032.
- Currie, K. L. (1971). "Geology of the resurgent cryptoexplosion crater at Mistastin Lake, Labrador". *Geological Survey of Canada Bulletin* 207, p. 62.
- Davison, T. M., G. S. Collins, and P. A. Bland (2016). "Mesoscale Modeling of Impact Compaction of Primitive Solar System Solids". *The Astrophysical Journal* 821.1, p. 68. ISSN: 0004-637X. DOI: 10.3847/0004-637X/821/1/68.
- Dence, M. R. (1964). "A Comparative Structural and Petrographic Study of Probable Canadian Meteorite Craters". *Meteoritics* 2, pp. 249–270. ISSN: 1945-5100. DOI: 10.1111/j.1945-5100.1964.tb01432.x.
- Dence, M. R. (1965). "The Extraterrestrial Origin of Canadian Craters". *Annals of the New York Academy of Sciences* 123.2, pp. 941–969. ISSN: 0077-8923. DOI: 10.1111/j.1749-6632.1965.tb20411.x.
- Dence, M. R. (1972). "Meteorite impact craters and the structure of the Sudbury Basin." *New Developments in Sudbury Geology*. Ed. by J. V. Guy-Bray. Geological Association of Canada Special Paper 10. Toronto: Business & Economic Service, pp. 117–124.
- Dence, M. R., M. J. S. Innes, and C. S. Beals (1965). "On the Probable Meteorite Origin of the Clearwater Lakes, Quebec". *Journal of the Royal Astronomical Society of Canada* 59, pp. 13–22. ISSN: 0035-872X.

- Dence, M. R., M. J. S. Innes, and P. B. Robertson (1968). "Recent geological and geo-physical studies of Canadian craters." *Shock Metamorphism of Natural Materials*. Ed. by B. M. French and S. N. M. Baltimore, MD: Mono Book, pp. 339–362.
- Dence, M. R., R. A. F. Grieve, and P. B. Robertson (1977). "Terrestrial impact structures-Principal characteristics and energy considerations". *Impact and Explosion Cratering*. Ed. by D. J. Roddy, R. O. Pepin, and R. B. Merrill. New York: Pergamon Press, pp. 247–275.
- Dence, M. R. (2004). "Structural evidence from shock metamorphism in simple and complex impact craters: Linking observations to theory". *Meteoritics & Planetary Science* 39.2, pp. 267–286. ISSN: 1945-5100. DOI: 10.1111/j.1945-5100.2004.tb00340.x.
- Dietz, R. S. (1959). "Shatter cones in cryptoexplosion structures (meteorite impact?)" *The Journal of Geology* 67.5, pp. 496–505.
- Dressler, B. O. (1990). "Shock metamorphic features and their zoning and orientation in the Precambrian rocks of the Manicouagan Structure, Quebec, Canada". *Tectonophysics* 171.1, pp. 229–245. ISSN: 0040-1951. DOI: 10.1016/0040-1951(90)90101-D.
- Dressler, B. O., V. L. Sharpton, and B. C. Schuraytz (1998). "Shock metamorphism and shock barometry at a complex impact structure: Slate Islands, Canada". *Contributions to Mineralogy and Petrology* 130.3-4, pp. 275–287. ISSN: 0010-7999, 1432-0967. DOI: 10.1007/s004100050365.
- Drucker, D. C. and W. Prager (1952). "Soil mechanics and plastic analysis or limit design". *Quarterly of applied mathematics* 10.2, pp. 157–165.
- Elbeshausen, D., K. Wünnemann, and G. S. Collins (2009). "Scaling of oblique impacts in frictional targets: Implications for crater size and formation mechanisms". *Icarus* 204.2, pp. 716–731. ISSN: 0019-1035. DOI: 10.1016/j.icarus.2009.07.018.
- Elbra, T. and L. J. Pesonen (2011). "Physical properties of the Yaxcopoil-1 deep drill core, Chicxulub impact structure, Mexico". *Meteoritics & Planetary Science* 46.11, pp. 1640–1652. ISSN: 1945-5100. DOI: 10.1111/j.1945-5100.2011.01253.x.
- Engelhardt, W. v and W. Bertsch (1969). "Shock induced planar deformation structures in quartz from the Ries crater, Germany". *Contributions to Mineralogy and Petrology* 20.3, pp. 203–234. ISSN: 0010-7999, 1432-0967. DOI: 10.1007/BF00377477.
- Engelhardt, W. v., F. Hörz, D. Stöffler, and W. Bertsch (1968). "Observations on quartz deformation in the breccias of West Clearwater Lake, Canada and the Ries Basin, Germany." *Shock Metamorphism of Natural Materials*. Ed. by B. M. French and N. M. Short. Baltimore, Maryland: Mono Book Corporation, pp. 475–482.
- Espindola, J. M., M. Mena, M. de La Fuente, and J. O. Campos-Enriquez (1995). "A model of the Chicxulub impact structure (Yucatan, Mexico) based on its gravity

- and magnetic signatures”. *Physics of the Earth and Planetary Interiors* 92.3, pp. 271–278. ISSN: 0031-9201. DOI: 10.1016/0031-9201(95)03022-6.
- Ferrière, L., C. Koeberl, B. A. Ivanov, and W. U. Reimold (2008). “Shock Metamorphism of Bosumtwi Impact Crater Rocks, Shock Attenuation, and Uplift Formation”. *Science* 322.5908, pp. 1678–1681. ISSN: 0036-8075, 1095-9203. DOI: 10.1126/science.1166283.
- Ferrière, L., J. R. Morrow, T. Amgaa, and C. Koeberl (2009). “Systematic study of universal-stage measurements of planar deformation features in shocked quartz: Implications for statistical significance and representation of results”. *Meteoritics and Planetary Science* 44, pp. 925–940. ISSN: 1086-9379. DOI: 10.1111/j.1945-5100.2009.tb00778.x.
- Fossen, H. (2016). “Structural Geology”. 2nd Edition. Cambridge University Press, pp. 25–82.
- Fossen, H. and B. Tikoff (1993). “The deformation matrix for simultaneous simple shearing, pure shearing and volume change, and its application to transpression-transtension tectonics”. *Journal of Structural Geology*. The Geometry of Naturally Deformed Rocks 15.3, pp. 413–422. ISSN: 0191-8141. DOI: 10.1016/0191-8141(93)90137-Y.
- French, B. M. and C. Koeberl (2010). “The convincing identification of terrestrial meteorite impact structures: What works, what doesn’t, and why”. *Earth-Science Reviews* 98.12, pp. 123–170. ISSN: 0012-8252. DOI: 10.1016/j.earscirev.2009.10.009.
- Glass, B. P. and B. M. Simonson (2012). “Distal impact ejecta layers: Spherules and more”. *Elements* 8.1, pp. 43–48.
- Goldin, T. J., K. Wünnemann, H. J. Melosh, and G. S. Collins (2006). “Hydrocode modeling of the Sierra Madera impact structure”. *Meteoritics & Planetary Science* 41.12, pp. 1947–1958. ISSN: 1945-5100. DOI: 10.1111/j.1945-5100.2006.tb00462.x.
- Grady, D. E. and M. E. Kipp (1980). “Continuum modelling of explosive fracture in oil shale”. *International Journal of Rock Mechanics and Mining Sciences & Geomechanics Abstracts* 17.3, pp. 147–157. ISSN: 0148-9062. DOI: 10.1016/0148-9062(80)91361-3.
- Grieve, R. A. F. (1987). “Terrestrial Impact Structures”. *Annual Review of Earth and Planetary Sciences* 15, pp. 245–270. ISSN: 0084-6597. DOI: 10.1146/annurev.ea.15.050187.001333.
- Grieve, R. A. F. and M. J. Cintala (1992). “An analysis of differential impact melt-crater scaling and implications for the terrestrial impact record”. *Meteoritics* 27.5, pp. 526–538.
- Grieve, R. A. F., M. R. Dence, and P. B. Robertson (1976). “The Generation and Distribution of Impact Melts: Implications for Cratering Processes”. *LPI Contributions* 259, pp. 40–42.

- Grieve, R. A. F., P. B. Robertson, and M. R. Dence (1981). "Constraints on the formation of ring impact structures, based on terrestrial data". *Multi-ring basins: Formation and evolution*. Ed. by R. B. Merrill and P. H. Schultz. Vol. 12A. New York: Pergamon Press, pp. 37–57.
- Grieve, R. A. F., D. E. Ames, J. V. Morgan, and N. Artemieva (2010). "The evolution of the Onaping Formation at the Sudbury impact structure". *Meteoritics & Planetary Science* 45.5, pp. 759–782.
- Grieve, R. A. F. (1978). "Meteoritic component and impact melt composition at the lac l'Eau Claire (Clearwater) impact structures, Quebec". *Geochimica et Cosmochimica Acta* 42.4, pp. 429–431. ISSN: 0016-7037. DOI: 10.1016/0016-7037(78)90275-2.
- Grieve, R. A. F. (2005). "Economic natural resource deposits at terrestrial impact structures". *Geological Society, London, Special Publications* 248.1, pp. 1–29. ISSN: 0305-8719, 2041-4927. DOI: 10.1144/GSL.SP.2005.248.01.01.
- Grieve, R. A. F. (2006). *Impact Structures in Canada*. GEOText 5. Geological Association of Canada, p. 210.
- Grieve, R. A. F., F. Langenhorst, and D. Stöffler (1996). "Shock metamorphism of quartz in nature and experiment: II. Significance in geoscience". *Meteoritics & Planetary Science* 31.1, pp. 6–35. ISSN: 1945-5100. DOI: 10.1111/j.1945-5100.1996.tb02049.x.
- Gulick, S. P. S., G. L. Christeson, P. J. Barton, R. A. F. Grieve, J. V. Morgan, and J. Urrutia-Fucugauchi (2013). "Geophysical Characterization of the Chicxulub Impact Crater". *Reviews of Geophysics* 51.1, pp. 31–52. ISSN: 1944-9208. DOI: 10.1002/rog.20007.
- Gulick, S. P. S., P. J. Barton, G. L. Christeson, J. V. Morgan, M. McDonald, K. Mendoza-Cervantes, Z. F. Pearson, A. Surendra, J. Urrutia-Fucugauchi, P. M. Vermeesch, and M. R. Warner (2008). "Importance of pre-impact crustal structure for the asymmetry of the Chicxulub impact crater". *Nature Geoscience* 1.2, p. 131. ISSN: 1752-0908. DOI: 10.1038/ngeo103.
- Hildebrand, A. R., M. Pilkington, M. Connors, C. Ortiz-Aleman, and R. E. Chavez (1995). "Size and structure of the Chicxulub crater revealed by horizontal gravity gradients and cenotes". *Nature* 376.6539, p. 415. ISSN: 1476-4687. DOI: 10.1038/376415a0.
- Hildebrand, A. R., G. T. Penfield, D. A. Kring, M. Pilkington, A. Camargo, S. B. Jacobsen, and W. V. Boynton (1991). "Chicxulub Crater: A possible Cretaceous/Tertiary boundary impact crater on the Yucatán Peninsula, Mexico". *Geology* 19.9, pp. 867–871. ISSN: 0091-7613. DOI: 10.1130/0091-7613(1991)019<0867:CCAPCT>2.3.CO;2.
- Hische, R. (1994). "Geology of the Clearwater impact structure (English translation)". PhD Thesis. Mnster: Westphalian Wilhelm University, p. 200.
- Holm-Alwmark, S, L Ferrière, C Alwmark, and M. H. Poelchau (2018). "Estimating average shock pressures recorded by impactite samples based on universal stage

- investigations of planar deformation features in quartzSources of error and recommendations”. *Meteoritics & Planetary Science* 53.1, pp. 110–130.
- Holm-Alwmark, S., A. S. P. Rae, L. Ferrière, C. Alwmark, and G. S. Collins (2017). “Combining shock barometry with numerical modeling: Insights into complex crater formationThe example of the Siljan impact structure (Sweden)”. *Meteoritics & Planetary Science* 52.12, pp. 2521–2549. ISSN: 1945-5100. DOI: 10.1111/maps.12955.
- Holm, S., C. Alwmark, W. Alvarez, and B. Schmitz (2011). “Shock barometry of the Siljan impact structure, Sweden”. *Meteoritics & Planetary Science* 46.12, pp. 1888–1909. ISSN: 1945-5100. DOI: 10.1111/j.1945-5100.2011.01303.x.
- Holsapple, K. A. and R. M. Schmidt (1979). “A material-strength model for apparent crater volume”. *Lunar and Planetary Science Conference*. Vol. 10, pp. 2757–2777.
- Hörz, F. (1968). “Statistical measurements of deformation structures and refractive indices in experimentally shock loaded quartz”. *Shock Metamorphism of Natural Materials*. Ed. by B. M. French and N. M. Short. Baltimore, Maryland: Mono Book Corporation, pp. 243–253.
- Huber, M. S., L. Ferrière, A. Losiak, and C. Koeberl (2011). “ANIE: A mathematical algorithm for automated indexing of planar deformation features in quartz grains”. *Meteoritics & Planetary Science* 46.9, pp. 1418–1424. ISSN: 1945-5100. DOI: 10.1111/j.1945-5100.2011.01234.x.
- Huffman, A. R. and W. U. Reimold (1996). “Experimental constraints on shock-induced microstructures in naturally deformed silicates”. *Tectonophysics* 256.14, pp. 165–217. ISSN: 0040-1951. DOI: 10.1016/0040-1951(95)00162-X.
- Huffman, A. R., J. M. Brown, N. L. Carter, and W. U. Reimold (1993). “The microstructural response of quartz and feldspar under shock loading at variable temperatures”. *Journal of Geophysical Research: Solid Earth* 98.B12, pp. 22171–22197.
- Ivanov, B. A. (1994). “Geomechanical models of impact cratering Puchezh-Katunki structure”. *Large Meteorite Impacts and Planetary Evolution*. Ed. by B. O. Dressler, R. A. F. Grieve, and V. Sharpton. Vol. 293. Boulder, CO: Geological Society of America Special Paper, pp. 81–81. DOI: 10.1130/SPE293.
- Ivanov, B. A. (2005). “Numerical Modeling of the Largest Terrestrial Meteorite Craters”. *Solar System Research* 39.5, pp. 381–409. ISSN: 0038-0946, 1608-3423. DOI: 10.1007/s11208-005-0051-0.
- Ivanov, B. A. and N. A. Artemieva (2002). “Numerical modeling of the formation of large impact craters”. *Catastrophic Events and Mass Extinctions: Impacts and Beyond*. Ed. by C. Koeberl and K. MacLeod. Vol. 356. Boulder, CO: Geological Society of America Special Paper, pp. 619–630. DOI: 10.1130/0-8137-2356-6.619.
- Ivanov, B. A. and A. Deutsch (1999). “Sudbury impact event: Cratering mechanics and thermal history”. *Large Meteorite Impacts and Planetary Evolution II*. Vol. 339. Boulder, CO: Geological Society of America Special Paper, pp. 389–398. DOI: 10.1130/SPE339.

- Ivanov, B. A. and V. N. Kostuchenko (1997). "Block oscillation model for impact crater collapse". *Lunar and Planetary Science Conference*. Vol. 28. 1655.
- Ivanov, B. A., G. G. Kocharyan, V. N. Kostuchenko, A. F. Kirjakov, and L. A. Pevzner (1996). "Puchezh-Katunki Impact Crater: Preliminary Data on Recovered Core Block Structure". *Lunar and Planetary Science Conference*. Vol. 27, pp. 589–590.
- Ivanov, B. A., D. Deniem, and G. Neukum (1997). "Implementation of dynamic strength models into 2D hydrocodes: Applications for atmospheric breakup and impact cratering". *International Journal of Impact Engineering* 17.1–5, pp. 375–386. ISSN: 0734-743X. DOI: 10.1016/S0734-743X(97)87511-2.
- Ivanov, B. A., H. J. Melosh, and E. Pierazzo (2010). "Basin-forming impacts: Reconnaissance modeling". *Large Meteorite Impacts and Planetary Evolution IV*. Ed. by R. L. Gibson and W. U. Reimold. Vol. 465. Boulder, CO: Geological Society of America Special Paper, pp. 29–49. DOI: 10.1130/SPE465.
- Jourdan, F., W. U. Reimold, and A. Deutsch (2012). "Dating terrestrial impact structures". *Elements* 8.1, pp. 49–53.
- Kenkmann, T., A. Jahn, and K. Wünnemann (2006). "Block Size" in a Complex Impact Crater Inferred from the Upheaval Dome Structure, Utah". *Lunar and Planetary Science Conference*. Vol. 37. 1540.
- Kenkmann, T., G. S. Collins, A. Wittmann, K. Wünnemann, W. U. Reimold, and H. J. Melosh (2009). "A model for the formation of the Chesapeake Bay impact crater as revealed by drilling and numerical simulation". *The ICDP-USGS Deep Drilling Project in the Chesapeake Bay impact structure: Results from the Eyreville Core Holes*. Vol. 458. Boulder, CO: Geological Society of America Special Paper, pp. 571–585. DOI: 10.1130/SPE458.
- Kenkmann, T., G. S. Collins, and K. Wünnemann (2012). "The Modification Stage of Crater Formation". *Impact Cratering*. Ed. by G. R. Osinski and E. Pierazzo. John Wiley & Sons, Ltd, pp. 60–75. ISBN: 978-1-118-44730-7.
- Kenkmann, T., M. H. Poelchau, and G. Wulf (2014). "Structural geology of impact craters". *Journal of Structural Geology* 62, pp. 156–182.
- Koeberl, C. (1994). "Tektite origin by hypervelocity asteroidal or cometary impact". *Large Meteorite Impacts and Planetary Evolution*. Ed. by B. O. Dressler, R. A. F. Grieve, and V. L. Sharpton. Vol. 293. Geological Society of America Special Paper, pp. 133–151. DOI: 10.1130/SPE293.
- Koeberl, C., P. Claeys, L. Hecht, and I. McDonald (2012). "Geochemistry of impactites". *Elements* 8.1, pp. 37–42.
- Kovaleva, E., U. Klötzli, G. Habler, and J. Wheeler (2015). "Planar microstructures in zircon from paleo-seismic zones". *American Mineralogist* 100.8-9, pp. 1834–1847.
- Kranck, S. H. and G. W. Sinclair (1963). "Clearwater Lake, New Quebec." *Geological Survey of Canada Bulletin* 100, p. 25.
- Laurén, L., J. Lehtovaara, R. Bostrom, and R. Tynni (1978). "On the geology of the circular depression at Söderfjärden, western Finland". *Bulletin of the Geological Survey of Finland* 297, pp. 1–38.

- Le Feuvre, M. and M. A. Wieczorek (2011). "Nonuniform cratering of the Moon and a revised crater chronology of the inner Solar System". *Icarus* 214.1, pp. 1–20. ISSN: 0019-1035. DOI: 10.1016/j.icarus.2011.03.010.
- Lundborg, N (1968). "Strength of rock-like materials". *International Journal of Rock Mechanics and Mining Sciences & Geomechanics Abstracts* 5, pp. 427–454.
- McKinnon, W. B. (1978). "An Investigation Into the Role of Plastic Failure in Crater Modification". *Lunar and Planetary Science Conference*. Vol. 9, pp. 3965–3973.
- Melosh, H. J. (1977). "Crater modification by gravity - A mechanical analysis of slumping". *Impact and Explosion Cratering*. Ed. by D. J. Roddy, R. O. Pepin, and R. B. Merrill. New York: Pergamon Press, pp. 1245–1260.
- Melosh, H. J. (1989). *Impact Cratering: A Geologic Process*. Oxford Monographs on Geology and Geophysics 11. New York: Oxford University Press, p. 253.
- Melosh, H. J. (1996). "Dynamical weakening of faults by acoustic fluidization". *Nature* 379.6566, pp. 601–606. DOI: 10.1038/379601a0.
- Melosh, H. J. and B. A. Ivanov (1999). "Impact Crater Collapse". *Annual Review of Earth and Planetary Sciences* 27.1, pp. 385–415. DOI: 10.1146/annurev.earth.27.1.385.
- Melosh, H. J., E. V. Ryan, and E. Asphaug (1992). "Dynamic fragmentation in impacts: Hydrocode simulation of laboratory impacts". *Journal of Geophysical Research: Planets* 97.E9, pp. 14735–14759. ISSN: 2156-2202. DOI: 10.1029/92JE01632.
- Melosh, H. J. (1979). "Acoustic fluidization: A new geologic process?" *Journal of Geophysical Research: Solid Earth* 84.B13, pp. 7513–7520. ISSN: 2156-2202. DOI: 10.1029/JB084iB13p07513.
- Melosh, H. J. (2005). "The Mechanics of Pseudotachylite Formation in Impact Events". *Impact Tectonics*. Ed. by C. Koeberl and H. Henkel. Impact Studies. Berlin, Heidelberg: Springer, pp. 55–80. ISBN: 978-3-540-24181-2 978-3-540-27548-0. DOI: 10.1007/3-540-27548-7__2.
- Millman, P. M., B. A. Liberty, J. F. Clark, P. Willmore, and M. J. S. Innes (1960). "The Brent Crater". *Publications of the Dominion Observatory, Ottawa*. 24, pp. 1–43.
- Morgan, J. V. and M. Rebolledo-Vieyra (2012). "Geophysical studies of impact craters". *Impact Cratering*. Ed. by G. R. Osinski and E. Pierazzo. John Wiley & Sons, Ltd, pp. 60–75. ISBN: 978-1-118-44730-7.
- Morgan, J. V. et al. (1997). "Size and morphology of the Chicxulub impact crater". *Nature* 390.6659, pp. 472–476. ISSN: 0028-0836. DOI: 10.1038/37291.
- Morgan, J. V., M. R. Warner, G. S. Collins, H. J. Melosh, and G. L. Christeson (2000). "Peak-ring formation in large impact craters: geophysical constraints from Chicxulub". *Earth and Planetary Science Letters* 183.3, pp. 347–354. ISSN: 0012-821X. DOI: 10.1016/S0012-821X(00)00307-1.
- Morgan, J. V., S. P. S. Gulick, C. L. Mellett, S. L. Green, and IODP-ICDP Expedition 364 Scientists (2017). *Chicxulub: Drilling the K-Pg Impact Crater*. Vol. 364. Proceedings of the International Ocean Discovery Program. College Station, TX: International Ocean Discovery Program. DOI: 10.14379/iodp.proc.364.2017.

- Morgan, J. V. et al. (2016). "The formation of peak rings in large impact craters". *Science* 354.6314, pp. 878–882. ISSN: 0036-8075, 1095-9203. DOI: 10.1126/science.aah6561.
- Müller, W. F. and M. Defourneaux (1968). "Deformationsstrukturen im Quarz als Indikator für Stosswellen: Eine experimentelle Untersuchung an Quarz-Einkristallen." *Zeitschrift für Geophysik* 34, pp. 483–504.
- Nemchin, A., N Timms, R. Pidgeon, T Geisler, S. Reddy, and C Meyer (2009). "Timing of crystallization of the lunar magma ocean constrained by the oldest zircon". *Nature Geoscience* 2.2, p. 133.
- O'Keefe, J. D. and T. J. Ahrens (1999). "Complex craters: Relationship of stratigraphy and rings to impact conditions". *Journal of Geophysical Research: Planets* 104.E11, pp. 27091–27104. ISSN: 2156-2202. DOI: 10.1029/1998JE000596.
- Osinski, G. R. et al. (2015). "Revisiting the West Clearwater Lake Impact Structure, Canada". *Lunar and Planetary Science Conference*. Vol. 46. 1621.
- Osinski, G. R. (2004). "Impact melt rocks from the Ries structure, Germany: An origin as impact melt flows?" *Earth and Planetary Science Letters* 226.3-4, pp. 529–543.
- Osinski, G. R. and L. Ferrière (2016). "Shatter cones: (Mis)understood?" *Science Advances* 2.8, e1600616. ISSN: 2375-2548. DOI: 10.1126/sciadv.1600616.
- Osinski, G. R., P. Lee, J. G. Spray, J. Parnell, D. S. S. Lim, T. E. Bunch, C. S. Cockell, and B. Glass (2005). "Geological overview and cratering model for the Haughton impact structure, Devon Island, Canadian High Arctic". *Meteoritics & Planetary Science* 40.12, pp. 1759–1776. ISSN: 1945-5100. DOI: 10.1111/j.1945-5100.2005.tb00145.x.
- Palme, H., M. Janssens, H. Takahashi, E. Anders, and J. Hertogen (1978). "Meteoritic material at five large impact craters". *Geochimica et Cosmochimica Acta* 42.3, pp. 313–323. ISSN: 0016-7037. DOI: 10.1016/0016-7037(78)90184-9.
- Penfield, G. T. and Z. A. Camargo (1981). "Definition of a major igneous zone in the central Yucatan platform with aeromagnetics and gravity". *Technical program of the Society of Exploration Geophysicists: Annual International Meeting*. Vol. 51. Los Angeles: Society of Exploration Geophysicists, pp. 37–38.
- Phinney, W. C. and C. H. Simonds (1977). "Dynamical implications of the petrology and distribution of impact melt rocks". *Impact and Explosion Cratering*. Ed. by D. J. Roddy, R. O. Pepin, and R. B. Merrill. New York: Pergamon Press, pp. 771–790.
- Phinney, W. C., C. H. Simonds, A. Cochran, and P. E. McGee (1978). "West Clearwater, Quebec Impact Structure, Part II: Petrology". *Lunar and Planetary Science Conference*. Vol. 9, pp. 2659–2694.
- Pierazzo, E., A. M. Vickery, and H. J. Melosh (1997). "A Reevaluation of Impact Melt Production". *Icarus* 127.2, pp. 408–423. ISSN: 0019-1035. DOI: 10.1006/icar.1997.5713.
- Pierazzo, E. and G. Collins (2004). "A Brief Introduction to Hydrocode Modeling of Impact Cratering". *Cratering in Marine Environments and on Ice*. Ed. by H. Dypvik, M. J. Burchell, and P. Claeys. Berlin, Heidelberg: Springer, pp. 323–340.

- Pike, R. J. (1977). "Size-dependence in the shape of fresh impact craters on the Moon". *Impact and Explosion Cratering*. Ed. by D. J. Roddy, R. O. Pepin, and R. B. Merrill. New York: Pergamon Press, pp. 489–509.
- Pike, R. J. (1980). "Formation of complex impact craters: Evidence from Mars and other planets". *Icarus* 43.1, pp. 1–19.
- Pike, R. J. (1988). "Geomorphology of impact craters on Mercury". *Mercury*. Ed. by F. Vilas, C. R. Chapman, and M. S. Matthews. Space Science. University of Arizona Press, pp. 165–273.
- Pilkington, M. and R. A. F. Grieve (1992). "The geophysical signature of terrestrial impact craters". *Reviews of Geophysics* 30.2, pp. 161–181. ISSN: 1944-9208. DOI: [10.1029/92RG00192](https://doi.org/10.1029/92RG00192).
- Pilkington, M., A. R. Hildebrand, and C. Ortiz-Aleman (1994). "Gravity and magnetic field modeling and structure of the Chicxulub Crater, Mexico". *Journal of Geophysical Research: Planets* 99.E6, pp. 13147–13162. ISSN: 2156-2202. DOI: [10.1029/94JE01089](https://doi.org/10.1029/94JE01089).
- Plante, L., M.-K. Seguin, and J. Rondot (1990). "Étude gravimétrique des astroblèmes du Lac à l'Eau Claire, Nouveau-Québec". *Geoexploration* 26.4, pp. 303–323. ISSN: 0016-7142. DOI: [10.1016/0016-7142\(90\)90010-P](https://doi.org/10.1016/0016-7142(90)90010-P).
- Poelchau, M. H. (2015). "A look at unindexed PDFs: How high should the value be for shocked rocks?" *Lunar and Planetary Science Conference*. Vol. 46. 2473.
- Poelchau, M. H. and T. Kenkmann (2011). "Feather features: A low-shock-pressure indicator in quartz". *Journal of Geophysical Research: Solid Earth* 116.B2, B02201. ISSN: 2156-2202. DOI: [10.1029/2010JB007803](https://doi.org/10.1029/2010JB007803).
- Pohl, J., D. Stöffler, H. v. Gall, and K. Ernstson (1977). "The Ries impact crater". *Impact and Explosion Cratering*. Ed. by D. J. Roddy, R. O. Pepin, and R. B. Merrill. New York: Pergamon Press, pp. 343–404.
- Rae, A. S. P., J. V. Morgan, G. S. Collins, G. R. Osinski, and R. A. F. Grieve (2015a). "Complex Crater Formation: Insights from Combining Observational Constraints with Numerical Models of the West Clearwater Impact Structure". *Bridging the Gap III: Impact Cratering in Nature, Experiments, and Modeling*. 1861, pp. 1031–1032.
- Rae, A. S. P., J. V. Morgan, G. S. Collins, G. R. Osinski, and R. A. F. Grieve (2015b). "Observational Constraints on Structural Uplift Formation: The West Clearwater Impact Structure". *Lunar and Planetary Science Conference*. Vol. 46. 1451.
- Rae, A. S. P., G. S. Collins, R. A. F. Grieve, G. R. Osinski, and J. V. Morgan (2017a). "Complex Crater Formation: Insights from combining observations of shock pressure distribution with numerical models at the West Clearwater Lake impact structure". *Meteoritics & Planetary Science* 52.7, pp. 1330–1350. ISSN: 1945-5100. DOI: [10.1111/maps.12825](https://doi.org/10.1111/maps.12825).
- Rae, A. S. P., J. V. Morgan, G. S. Collins, R. A. F. Grieve, G. R. Osinski, T Salge, B Hall, L Ferrière, M Poelchau, S. P. S. Gulick, and IODP-ICDP Expedition 364 Scientists (2017b). "Deformation, Shock Barometry, and Porosity Within

- Shocked Target Rocks of the Chicxulub Peak Ring: Results from IODP-ICDP Expedition 364.” *Lunar and Planetary Science Conference*. Vol. 48. 1934.
- Rae, A. S. P., R. A. F. Grieve, G. R. Osinski, G. S. Collins, and J. V. Morgan (2017c). “Deformation and Shock Metamorphism in the Central Uplift of the East Clearwater Lake Impact Structure”. *Lunar and Planetary Science Conference*. Vol. 48. 1949.
- Rae, A. S. P., M Poelchau, G. S. Collins, N Timms, A. J. Cavosie, J Lofi, T Salge, U. Riller, L Ferrière, R. A. F. Grieve, et al. (2017d). “On the Magnitude and Orientation of Stress during Shock Metamorphism: Understanding Peak Ring Formation by Combining Observations and Models.” *AGU Fall Meeting Abstracts*. P23H-03.
- Rae, A. S. P., M. H. Poelchau, J Lofi, A Diaw, G. S. Collins, R. A. F. Grieve, G. R. Osinski, and IODP-ICDP Expedition 364 Scientists (2017e). “The History of Deformation during Peak-Ring Emplacement: Linking Observations and Models”. *GSA Annual Meeting*. Vol. 49. 6, pp. 192–1.
- Rae, A. S. P., G. S. Collins, U Riller, M. H. Poelchau, N. Timms, A. Cavosie, T. Salge, J. Lofi, L. Ferrière, G. L. Christeson, R. A. F. Grieve, G. R. Osinski, S. P. S. Gulick, J. V. Morgan, and IODP-ICDP Expedition 364 Scientists (2018). “Quantitative Geological Predictions of the Dynamic Collapse Model of Peak Ring Formation: Comparisons with Observations from the Chicxulub Impact Structure”. *EGU General Assembly*. Vol. 20. 10873.
- Ramesh, K. T., J. D. Hogan, J. Kimberley, and A. Stickle (2015). “A review of mechanisms and models for dynamic failure, strength, and fragmentation”. *Planetary and Space Science*. VIII Workshop on Catastrophic Disruption in the Solar System 107, pp. 10–23. ISSN: 0032-0633. DOI: 10.1016/j.pss.2014.11.010.
- Reimold, W. U., R. A. F. Grieve, and H. Palme (1981). “Rb-Sr dating of the impact melt from East Clearwater, Quebec”. *Contributions to Mineralogy and Petrology* 76.1, pp. 73–76. ISSN: 0010-7999, 1432-0967. DOI: 10.1007/BF00373685.
- Reimold, W. U. and R. L. Gibson (2005). ““Pseudotachylites” in Large Impact Structures”. *Impact Tectonics*. Ed. by C. Koeberl and H. Henkel. Impact Studies. Berlin, Heidelberg: Springer, pp. 1–53. ISBN: 978-3-540-24181-2 978-3-540-27548-0. DOI: 10.1007/3-540-27548-7_2.
- Riller, U., M. H. Poelchau, A. S. P. Rae, F. Schulte, R. A. F. Grieve, J. V. Morgan, G. S. P. S., J. Lofi, N. McCall, D. Kring, G. S. Collins, and IODP-ICDP Expedition 364 Scientists (in press). “Rock fluidization during peak-ring formation in large impact structures”. *Nature*.
- Robertson, P. B. (1975). “Zones of shock metamorphism at the Charlevoix impact structure, Quebec”. *Geological Society of America Bulletin* 86.12, pp. 1630–1638. ISSN: 0016-7606, 1943-2674. DOI: 10.1130/0016-7606(1975)86<1630:ZOSMAT>2.0.CO;2.
- Robertson, P. B. and R. A. F. Grieve (1977). “Shock attenuation at terrestrial impact structures”. *Impact and Explosion Cratering*. Ed. by D. J. Roddy, R. O. Pepin, and R. B. Merrill. New York: Pergamon Press, pp. 687–702.

- Roddy, D. J. (1977). "Large-scale impact and explosion craters-Comparisons of morphological and structural analogs". *Impact and Explosion Cratering*. Ed. by D. J. Roddy, R. O. Pepin, and R. B. Merrill. New York: Pergamon Press, pp. 185–246.
- Rosa, D. F. (2004). "Marble Enclaves in the Melt Sheet at the West Clearwater Lake Impact Crater, Northern Quebec." MSc thesis. McGill University, Montreal, p. 147.
- Rosa, D. F. (2011). "The Sheet of Impact Melt at West Clearwater Lake, Northern Quebec". PhD Thesis. McGill University, Montreal, p. 392.
- Schenk, P. M. and W. B. McKinnon (1985). "Dark halo craters and the thickness of grooved terrain on Ganymede". *Journal of Geophysical Research: Solid Earth* 90.S02, pp. C775–C783. ISSN: 2156-2202. DOI: 10.1029/JB090iS02p0C775.
- Schindelin, J., I. Arganda-Carreras, E. Frise, V. Kaynig, M. Longair, T. Pietzsch, S. Preibisch, C. Rueden, S. Saalfeld, B. Schmid, J.-Y. Tinevez, D. J. White, V. Hartenstein, K. Eliceiri, P. Tomancak, and A. Cardona (2012). "Fiji: an open-source platform for biological-image analysis". *Nature Methods* 9.7, pp. 676–682. ISSN: 1548-7105. DOI: 10.1038/nmeth.2019.
- Schmieder, M., W. H. Schwarz, M. Trieloff, E. Tohver, E. Buchner, J. Hopp, and G. R. Osinski (2015). "New 40Ar/39Ar dating of the Clearwater Lake impact structures (Qubec, Canada) Not the binary asteroid impact it seems?" *Geochimica et Cosmochimica Acta* 148, pp. 304–324. ISSN: 0016-7037. DOI: 10.1016/j.gca.2014.09.037.
- Senft, L. E. and S. T. Stewart (2009). "Dynamic fault weakening and the formation of large impact craters". *Earth and Planetary Science Letters* 287.3, pp. 471–482. ISSN: 0012-821X. DOI: 10.1016/j.epsl.2009.08.033.
- Sharpton, V. L., K. Burke, A. Camargo-Zanoguera, S. A. Hall, D. S. Lee, L. E. Marn, G. Suarez-Reynoso, J. M. Quezada-Mueton, P. D. Spudis, and J. Urrutia-Fucugauchi (1993). "Chicxulub Multiring Impact Basin: Size and Other Characteristics Derived from Gravity Analysis". *Science* 261.5128, pp. 1564–1567. ISSN: 0036-8075, 1095-9203. DOI: 10.1126/science.261.5128.1564.
- Sharpton, V. L., L. E. Marin, J. L. Carney, S. Lee, G. Ryder, B. C. Schuraytz, P. Sikora, and P. D. Spudis (1996). "A model of the Chicxulub impact basin based on evaluation of geophysical data, well logs, and drill core samples". *The Cretaceous-Tertiary Event and Other Catastrophes in Earth History, Spec. Pap.* 307. Ed. by G. Ryder, D. Fastovsky, and S. Gartner. Boulder, CO: Geological Society of America, pp. 55–74. ISBN: 978-0-8137-2307-5.
- Sibson, R. H. (2000). "Fluid involvement in normal faulting". *Journal of Geodynamics* 29.3, pp. 469–499. ISSN: 0264-3707. DOI: 10.1016/S0264-3707(99)00042-3.
- Simonds, C. H., W. C. Phinney, P. E. McGee, and A. Cochran (1978). "West Clearwater, Quebec impact structure, Part I: Field geology, structure and bulk chemistry." *Lunar and Planetary Science Conference*. Vol. 9, pp. 2633–2693.
- Spray, J. G. (1997). "Superfaults". *Geology* 25.7, pp. 579–582. ISSN: 0091-7613. DOI: 10.1130/0091-7613(1997)025<0579:S>2.3.CO;2.

- Stöffler, D (1977). "Research drilling Nördlingen 1973: Polymict breccias, crater base-
ment, and cratering model of the Ries impact structure". *Geologica Bavaria* 75,
pp. 443–458.
- Stöffler, D. and R. A. F. Grieve (2007). "Impactites". *Metamorphic rocks: A classification
and glossary of terms, recommendations of the International Union of Geological
Sciences*. Ed. by D. Fettes and J. Desmons. Cambridge University Press, pp. 82–
92.
- Stöffler, D., L. Bischoff, W. Osierski, and B. Wiest (1988). "Structural deformation,
breccia formation, and shock metamorphism in the basement of complex ter-
restrial impact craters: Implications for the cratering process." *Deep Drilling in
Crystalline Bedrock*. Ed. by A. Boden and K. Eriksson. Vol. 1. Exploration of the
Deep Continental Crust. Berlin, Heidelberg: Springer, pp. 277–297.
- Stöffler, D. and F. Langenhorst (1994). "Shock metamorphism of quartz in nature and
experiment: I. Basic observation and theory". *Meteoritics* 29.2, pp. 155–181. ISSN:
1945-5100. DOI: [10.1111/j.1945-5100.1994.tb00670.x](https://doi.org/10.1111/j.1945-5100.1994.tb00670.x).
- Stöffler, D., N. A. Artemieva, K. Wünnemann, W. U. Reimold, J. Jacob, B. K. Hansen,
and I. A. Summerson (2013). "Ries crater and suevite revisited — Observa-
tions and modeling Part I: Observations". *Meteoritics & Planetary Science* 48.4,
pp. 515–589.
- Stöffler, D., C. Hamann, and K. Metzler (2018). "Shock metamorphism of planetary
silicate rocks and sediments: Proposal for an updated classification system". *Me-
teoritics & Planetary Science* 53.1, pp. 5–49.
- Sweeney, J. F. (1978). "Gravity study of great impact". *Journal of Geophysical Research:
Solid Earth* 83.B6, pp. 2809–2815.
- Tanner, J., C. Aiken, P. Dehlinger, W. Dewhurst, M. de la Fuente, V. Godley, R. Godson,
W. Hanna, T. Hildebrand, M. Kleinkopf, G. McCalpin, R. McConnell, H. Meyers,
N. OHara, A. Palmer, D. Scheibe, R. Sweeney, and L. Thorning (1988). "Gravity
Anomaly Map of North America". *The Leading Edge* 7.11, pp. 15–18. ISSN: 1070-
485X. DOI: [10.1190/1.1439456](https://doi.org/10.1190/1.1439456).
- Thompson, S. L. and H. S. Lauson (1974). *Improvements in the CHART D radiation-
hydrodynamic code III: revised analytic equations of state*. Tech. rep. SC-RR-
710714. Alberquerque, New Mexico: Sandia National Laboratory.
- Tikoff, B. and H. Fossen (1995). "The limitations of three-dimensional kinematic vortic-
ity analysis". *Journal of Structural Geology* 17.12, pp. 1771–1784. ISSN: 0191-8141.
DOI: [10.1016/0191-8141\(95\)00069-P](https://doi.org/10.1016/0191-8141(95)00069-P).
- Timms, N. E., S. M. Reddy, D. Healy, A. A. Nemchin, M. L. Grange, R. T. Pidgeon, and
R. Hart (2012). "Resolution of impact-related microstructures in lunar zircon:
A shock-deformation mechanism map". *Meteoritics & Planetary Science* 47.1,
pp. 120–141.
- Timms, N. E., T. M. Erickson, M. A. Pearce, A. J. Cavosie, M. Schmieder, E. To-
hver, S. M. Reddy, M. R. Zanetti, A. A. Nemchin, and A. Wittmann (2017). "A

- pressure-temperature phase diagram for zircon at extreme conditions”. *Earth-Science Reviews* 165, pp. 185–202.
- Timms, N. E., D. Healy, T. M. Erickson, A. A. Nemchin, M. A. Pearce, and A. J. Cavosie (2018). “Role of elastic anisotropy in the development of deformation microstructures in zircon”. *Microstructural Geochronology: Planetary Records Down to Atom Scale*. Ed. by D. E. Moser, F. Corfu, J. R. Darling, S. M. Reddy, and K. Tait. Vol. 232. Geophysical Monograph. Hoboken, NJ: John Wiley & Sons. Chap. 8, pp. 183–202.
- Vasconcelos, M. A. R., K. Wünnemann, A. P. Crsta, E. C. Molina, W. U. Reimold, and E. Yokoyama (2012). “Insights into the morphology of the Serra da Cangalha impact structure from geophysical modeling”. *Meteoritics & Planetary Science* 47.10, pp. 1659–1670. ISSN: 1945-5100. DOI: 10.1111/maps.12001.
- Vermeesch, P. M., J. V. Morgan, G. L. Christeson, P. J. Barton, and A. Surendra (2009). “Three-dimensional joint inversion of traveltimes and gravity data across the Chicxulub impact crater”. *Journal of Geophysical Research: Solid Earth* 114.B2, B02105. ISSN: 2156-2202. DOI: 10.1029/2008JB005776.
- Vermeesch, P. M. and J. V. Morgan (2008). “Structural uplift beneath the Chicxulub impact structure”. *Journal of Geophysical Research: Solid Earth* 113.B7, B07103. ISSN: 2156-2202. DOI: 10.1029/2007JB005393.
- Waters, K. H. (1981). *Reflection Seismology — a Tool for Energy Resource Exploration*. 2nd Edition. New York: John Wiley & Sons, Ltd, p. 453. ISBN: 9780471082248.
- Wilks, R. P. A. and G. R. Osinski (2015). “Impact Melt Veins in the Central Uplift of the West Clearwater Lake Impact Structure, Northern Quebec, Canada”. *Lunar and Planetary Science Conference*. Vol. 46. 1397.
- Woodcock, N. H. and K. Mort (2008). “Classification of fault breccias and related fault rocks”. *Geological Magazine* 145.3, pp. 435–440.
- Wünnemann, K. and B. A. Ivanov (2003). “Numerical modelling of the impact crater depth-diameter dependence in an acoustically fluidized target”. *Planetary and Space Science* 51.13, pp. 831–845. ISSN: 0032-0633. DOI: 10.1016/j.pss.2003.08.001.
- Wünnemann, K. and M. Lange (2002). “Numerical modeling of impact-induced modifications of the deep-sea floor”. *Deep Sea Research Part II: Topical Studies in Oceanography* 49.6, pp. 969–981.
- Wünnemann, K., J. V. Morgan, and H. Jödicke (2005). “Is Ries crater typical for its size? An analysis based upon old and new geophysical data and numerical modeling”. *Large Meteorite Impacts III*. Ed. by T. Kenkemann, F. Hötz, and A. Deutsch. Vol. 384. Boulder, CO: Geological Society of America Special Paper, pp. 67–83. DOI: 10.1130/SPE384.
- Wünnemann, K., G. S. Collins, and H. J. Melosh (2006). “A strain-based porosity model for use in hydrocode simulations of impacts and implications for transient crater growth in porous targets”. *Icarus* 180.2, pp. 514–527. ISSN: 0019-1035. DOI: 10.1016/j.icarus.2005.10.013.

- Zuber, M. T., D. E. Smith, M. M. Watkins, S. W. Asmar, A. S. Konopliv, F. G. Lemoine, H. J. Melosh, G. A. Neumann, R. J. Phillips, S. C. Solomon, M. A. Wieczorek, J. G. Williams, S. J. Goossens, G. Kruizinga, E. Mazarico, R. S. Park, and D.-N. Yuan (2013). “Gravity Field of the Moon from the Gravity Recovery and Interior Laboratory (GRAIL) Mission”. *Science* 339.6120, pp. 668–671. ISSN: 0036-8075, 1095-9203. doi: [10.1126/science.1231507](https://doi.org/10.1126/science.1231507).
- Zwiessler, R., T. Kenkmann, M. H. Poelchau, S. Nau, and S. Hess (2017). “On the use of a split Hopkinson pressure bar in structural geology: High strain rate deformation of Seeberger sandstone and Carrara marble under uniaxial compression”. *Journal of Structural Geology* 97, pp. 225–236.

Appendices

A The Universal Stage and Shocked Quartz

Measuring the orientations of planar deformation features (PDFs) in quartz (Figure A.1) is an exacting and precise skill. The description here is based on a set-up with a Zeiss 4-axis universal stage and Olympus BH2 polarising microscope, however the process should be similar using any 4-axis universal stage.

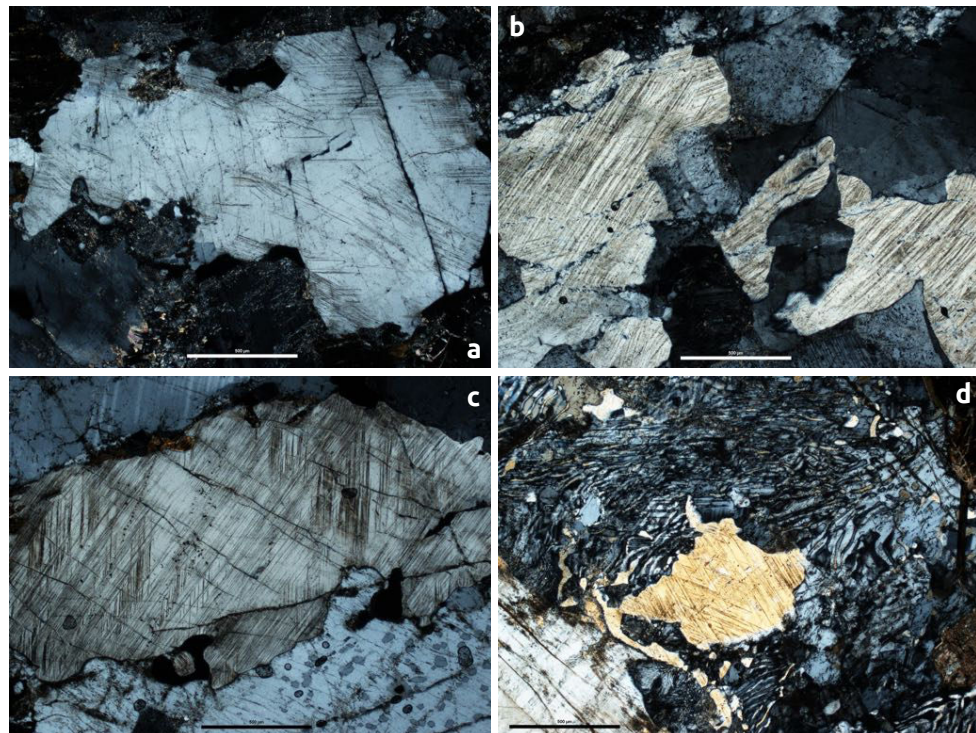


Figure A.1: Transmitted cross-polarised light photomicrographs of quartz PDFs from the West Clearwater Lake Impact Structure.

A.1 The Basics

A schematic diagram of a 4-axis universal stage is shown in Figure A.2. The stage itself comprises of 4 rotation axes (A1-4), with a further axis (A5) corresponding to the microscope rotation axis. A1 and A2 respectively control the azimuth and declination of the inner ring; A1 is measured on the graduated ring on the outside edge of the inner ring, A2 is measured using the Wright's scale arms that can be raised from their position on the outer ring. A3 and A4 respectively control the azimuth and declination of the outer ring; A3 is measured on the graduated ring at the outer edge of the outer ring, A4 is measured using the dial attached to the axis, opposite the screw to fix the axis in place.

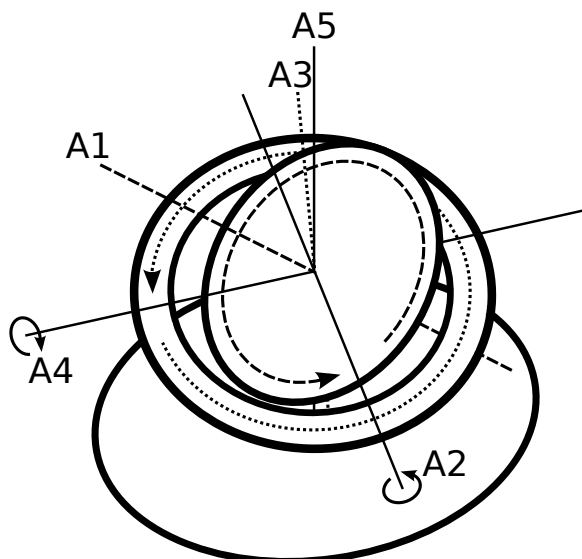


Figure A.2: Schematic diagram of a universal stage. All rotation axes, including the microscope axis, A5, are noted.

A.2 Preparing the Microscope for U-Stage Installation

1. Remove all standard microscope objective lenses.
2. Lower the microscope stage to its lowest setting.
3. Set the A5 axis to 0/360.
4. Mount the U-stage such that the A4 axis is running E-W on the microscope stage and fix in place (with screws if you have a compatible microscope and stage, if not, double-sided tape will do!).

5. Install Long Working Distance U-stage objective lens(es).

A.3 Setting a Thin Section

The U-stage will come with several pairs of glass hemispheres. They are paired by refractive index. There are also two types of hemisphere; the smaller type are used for conoscopic viewing, the larger hemispheres, which will be used exclusively here, are for orthoscopic viewing. For investigating quartz, the $n=1.554$ hemispheres will need to be used (these are chosen to match the refractive index of quartz).

1. Place the lower glass hemisphere onto the centre of the U-stage.
2. If they are not already installed, mount the parallel guides to the stage, these will ensure that the slide stays orientated when moved.
3. Put a drop of oil/glycerine on the centre of the lower hemisphere
4. Place the slide gently onto the lower hemisphere, ensure that there are no bubbles of air trapped beneath the slide.
5. Put another drop of oil/glycerine onto the centre of the slide.
6. Place upper hemisphere onto the top of the slide, ensure that there are no bubbles of air trapped beneath the upper hemisphere, and then screw the upper hemisphere to the stage.

A.4 Calibration of the U-Stage

1. Set all axes to zero, The inner and outer ring should be horizontal where the A2 and A4 axes should be orthogonal and oriented N-S and E-W respectively.
2. Centre the objective lenses with the U-stage.
 - (a) The objective of this is to ensure that rotation about the microscope axis, A5, does not cause the centre of the cross-hairs to move over the slide.
 - (b) Depending on the microscope used, this can mean centering the objectives individually using screws at the objective mounting, or centering the microscope stage using screws attached to the sub-stage array.
3. Centre the U-stage on the microscope.
 - (a) The objective of this is to ensure that rotation about the A2 (and A4) axes does not cause the centre of the cross-hairs to move over the slide.

- (b) This process is achieved by using the two screws at the base of the U-stage, each screw will push the A2 and A4 rotation axes away/towards the screw. To achieve centering, move the cross-hairs halfway between the points marked by the position of the crosshairs when A2 (or A4) is at 0, and where the A2 axis is at 180.
4. Adjust the height of the A2 axis
 - (a) Try rotating about the A2 axis (which should be oriented N-S, such that the inner ring will now be dipping in the E-W direction).
 - (b) Keeping your eye down the microscope, you will notice that the extreme E-W edges of the slide go out of focus as the inner ring is inclined, whilst a line orientated N-S remains perfectly focused. By rotating the A2 axis back and forth, you may notice that this focused line moves from left to right, if this is the case, the height of the A2 axis needs to be adjusted.
 - (c) The height of the A2 axis is controlled by a threaded ring underneath the specimen and hemispheres, by rotating the threaded ring, the A2 axis can be raised and lowered such that the A2 axis is at exactly the focal length of the objective.

A.5 Measuring Quartz PDFs and Peak Shock Pressure

1. Identify a quartz crystal in a thin section of a shocked rock.
2. Determine the c-axis of the quartz crystal. Quartz belongs to the trigonal crystal system (possessing two identical a-axes at 120 degrees, and a c-axis perpendicular to the a-axes).
 - (a) Rotate the crystal about the A1 axis until the crystal goes into extinction (under crossed-polarised light).
 - (b) Trial rotate about the A2 axis.
 - i. If the crystal illuminates, rotate the A1 axis by 90 degrees so that the crystal is in the alternative extinction position, then step 2b).
 - ii. If the crystal remains in extinction, the c-axis is contained within the E-W plane, continue to step 2c).
 - (c) Rotate about the A4 axis until the grain illuminates (~30 degrees) and fix the A4 axis at this position.
 - (d) Rotate about the A2 axis until the grain becomes extinct and fix the axis at this position.
 - (e) Return the A4 axis to zero rotation, the c-axis is now either vertically orientated or horizontally orientated.

- (f) Trial rotate about the A5 axis (i.e. the microscope stage).
 - i. If the crystal illuminates, the c-axis is horizontal.
 - ii. If the crystal remains in extinction, the c-axis is vertical.
 - (g) Note the inclination of the A1 and A2 axes and whether the c-axis is horizontal or vertical. (IMPORTANT NOTE: Ensure that you know in which direction the inner ring is dipping, either to the E or to the W.)
 - (h) Return all axes to zero.
3. Measure the orientations of all PDFs within the oriented crystal
- (a) Rotate the crystal around the A1 axis such that the first PDF set contains the N-S vector.
 - (b) Rotate about the A2 axis until the PDFs become sharp, the PDF sets are now parallel to the N-S plane. The pole to the PDF plane is horizontal and in the E-W orientation.
 - (c) Note the inclination of the A1 and A2 axes. (IMPORTANT NOTE: Ensure that you know in which direction the inner ring is dipping, either to the E or to the W.)
 - (d) Repeat for all PDF sets.
4. Uniquely assign PDF sets. (This can also be carried out using ANIE, a mathematical algorithm for automated indexing of PDFs (Huber et al., 2011))
- (a) Plot the orientation of the crystal and all PDF poles on a Wulff stereonet. Plot A1 as the azimuth co-ordinate and A2 as the declination co-ordinate.
 - (b) Rotate the c-axis to the vertical position and move all PDF poles relative to the c-axis.
 - (c) Overlay plotted PDF poles onto the new stereographic projection template (NSPT) (Ferrière et al., 2009).
 - (d) Rotate the PDF poles about the vertical axis (also the c-axis) until the maximum number of PDF poles lie within the orientation envelopes.
 - (e) Note the indexed PDF sets, and the number of unindexed PDF sets.
5. Repeat for at least 20 randomly selected crystals, preferably 30 randomly selected crystals, within the slide.
6. Using a shock classification scheme for indexed PDFs (There are several to choose from: e.g. Engelhardt and Bertsch (1969), Grieve et al. (1996), Holm-Alwmark et al. (2018), Robertson and Grieve (1977), and Stöffler and Langenhorst (1994)), assign a shock pressure for each crystal.
7. The determined peak shock pressure is the arithmetic mean of the assigned shock pressures.

A.6 Notes and Troubleshooting

Unable to determine the c-axis of a crystal - The method described of determining the c-axis of a quartz grain will only work for minerals with a uniaxial indicatrix. Other minerals with non-uniaxial indicatrices, particularly the feldspars, also develop PDFs. The existence of PDFs does not make it quartz!

Uncertainty in whether a feature is a PDF - PDFs are planar elements in a crystal that are closely spaced, they can exist as either undecorated (amorphous planes) or decorated (inclusion-rich narrow planes). If in doubt, return to that crystal at the end of your analysis and see if it is consistent with other PDFs in the sample. If still uncertain, don't measure it, it could easily be planar fractures (PFs), Boehm lamellae (a signature of tectonic deformation), or another type of microfracture.

Only one PDF set per grain - In an ideal world, grains with only one PDF set (unless it is a basal plane PDF) in them would not be indexed. This is because the solution is non-unique with free rotation of the PDF pole about the c-axis. Realistically, one is likely to need to include the statistics of grains with only one PDF set. However, it is worth noting the difficulty in single PDF set grains.

Large numbers of unindexed PDFs - According to Poelchau (2015), Unindexed PDF percentages should be lower than 16% for shocked rocks. Values higher than this need to be critically discussed. Firstly, before starting to measure PDFs in a grain, ensure that PDFs are only being measured from the domain of the crystal where the c-axis was measured. A few degrees of error, particularly when there are large numbers of PDFs in the crystal, can be highly significant. The larger the number of PDFs, the fewer the degrees of freedom there will be in the optimal solution. If there are still high numbers of unindexed PDFs, try the following steps:

1. After noting the orientations of A1 and A2 after measuring the c-axis and/or PDF orientation, rotate the A1 axis by 180 degrees.
2. Adjust A2 such that the c-axis/PDF pole returns to the horizontal.
3. If measured correctly, A1 measurement will be 180 degrees greater than or less than before and the A2 measurement will be the same magnitude but in the opposite direction. If not, you have spotted your error...
4. This acts as a sanity check on your measurements. Without increasing the time taken to do the measurements by that much. It is very easy to make mistakes, particularly when measuring the A2 axis.

An unusually large number of high angle PDF sets - Be aware that there if you are measuring a lot of vertically oriented c-axes, there is a selective bias (due to

the blind spot of the U-stage set-up) to measure high angle PDF sets. Correspondingly, many horizontally orientated c-axes create a bias towards low angle PDF sets. If all quartz grains are truly randomly orientated, 29% of quartz grains should have c-axes oriented at greater than 45 degrees to the surface of the section.

B iSALE inputs

In this appendix, full lists of input parameters for the iSALE simulations presented in thesis are shown. Tables B.1 and B.2 list the parameters used in Chapter 5 to model the West Clearwater Lake impact structure. Tables B.3 and B.4 list the parameters used in Chapter 6 to model the East Clearwater Lake impact structure. Tables B.5 and B.6 list the parameters used in Chapter 8 to model the Chicxulub impact structure.

Table B.1: Full global model parameters for West Clearwater Lake simulations.

Parameter	Symbol (units)	Value
Cell resolution	(m)	30
Cells per impactor radius		50
Horizontal cells in high resolution zone		800
Horizontal cells in outer extension zone		200
Vertical cells in high resolution zone		750
Vertical cells in upper extension zone		75
Vertical cells in lower extension zone		175
Extension factor in extension zone		1.05
Maximum grid spacing in extension zone		600
Impactor velocity	v_i (km s ⁻¹)	15
Impactor density	ρ_i (kg m ⁻³)	2630
Impactor damage		1
Acceleration due to gravity	g (m s ⁻²)	9.81
Surface temperature	T_{surf} (K)	273
Surface temperature gradient	T_{grad} (K m ⁻¹)	0.0051
Lithospheric thickness	d_{lith} (km)	200
Initial time increment	(s)	0.001
Maximum time increment	(s)	1
Save interval	(s)	1
End time	(s)	150.1
Linear artificial viscosity term		0.24
Quadratic artificial viscosity term		1.2
Tracer moving algorithm		Material

Table B.2: Full material model parameters for West Clearwater Lake simulations.

Parameter	Symbol (units)	Crust (Granite)
Reference Density	ρ (kg m^{-3})	2630
Poisson's ratio	ν	0.30
Intact cohesive strength	Y_0 (MPa)	10
Intact friction coefficient	μ_i	2.0
Intact and damaged strength limit	Y_m (MPa)	2500
Damaged cohesive strength	Y_{d0} (MPa)	0.01
Damaged friction coefficient	μ_{di}	0.6
Minimum failure strain for low pressure states	$\varepsilon_j b$	1×10^{-4}
Constant of proportionality between failure strain and pressure	B	1×10^{-11}
Pressure above which failure is compressional (Pa)	P_c (MPa)	300
Melt Temperature	T_m (K)	1673
Specific Heat Capacity	C ($\text{J K}^{-1} \text{kg}^{-1}$)	1000
Thermal softening coefficient	ξ	1.2
Constant in Simon Approximation	p_{bp}	1.52×10^9
Exponent in Simon Approximation	y_0	4.05
Vibrational particle velocity as a fraction of particle velocity	C_{vib}	0.1
Maximum vibrational particle velocity	Vib_{max} (m s^{-1})	200
Time after which no new acoustic vibrations are generated	t_{off} (s)	16
Maximum dilatancy coefficient	β_{max}	0.09
Dilatancy pressure limit	p_{lim} (MPa)	200
Critical distension	α_c	1.2
Critical friction coefficient	μ_c	0.4
Initial distension	α_0	1.0
Minimum distension	α_{min}	1.0

Table B.3: Full global model parameters for East Clearwater Lake simulations.

Parameter	Symbol (units)	Value
Cell resolution	(m)	30
Cells per impactor radius		25
Horizontal cells in high resolution zone		500
Horizontal cells in outer extension zone		200
Vertical cells in high resolution zone		400
Vertical cells in upper extension zone		40
Vertical cells in lower extension zone		80
Extension factor in extension zone		1.05
Maximum grid spacing in extension zone		600
Impactor velocity	v_i (km s ⁻¹)	15
Impactor density	ρ_i (kg m ⁻³)	2630
Impactor damage		1
Acceleration due to gravity	g (m s ⁻²)	9.81
Surface temperature	T_{surf} (K)	273
Surface temperature gradient	T_{grad} (K m ⁻¹)	0.0051
Lithospheric thickness	d_{lith} (km)	200
Initial time increment	(s)	0.001
Maximum time increment	(s)	1
Save interval	(s)	1
End time	(s)	150.1
Linear artificial viscosity term		0.24
Quadratic artificial viscosity term		1.2
Tracer moving algorithm	Material	

Table B.4: Full material model parameters for East Clearwater Lake simulations.

Parameter	Symbol (units)	Crust (Granite)
Reference Density	ρ (kg m^{-3})	2630
Poisson's ratio	ν	0.30
Intact cohesive strength	Y_0 (MPa)	10
Intact friction coefficient	μ_i	2.0
Intact and damaged strength limit	Y_m (MPa)	2500
Damaged cohesive strength	Y_{d0} (MPa)	0.01
Damaged friction coefficient	μ_{di}	0.6
Minimum failure strain for low pressure states	$\varepsilon_f b$	1×10^{-4}
Constant of proportionality between failure strain and pressure	B	1×10^{-11}
Pressure above which failure is compressional (Pa)	P_c (MPa)	300
Melt Temperature	T_m (K)	1673
Specific Heat Capacity	C ($\text{J K}^{-1} \text{kg}^{-1}$)	1000
Thermal softening coefficient	ξ	1.2
Constant in Simon Approximation	p_{bp}	1.52×10^9
Exponent in Simon Approximation	y_{t0}	4.05
Acoustic Fluidization viscosity constant	γ_η	0.025
Acoustic Fluidization decay time constant	γ_T	125
Vibrational particle velocity as a fraction of particle velocity	C_{vib}	0.1
Maximum vibrational particle velocity	V_{vibmax} (m s^{-1})	200
Time after which no new acoustic vibrations are generated	t_{off} (s)	16
Maximum dilatancy coefficient	β_{max}	0.09
Dilatancy pressure limit	p_{lim} (MPa)	200
Critical distension	α_c	1.2
Critical friction coefficient	μ_c	0.4
Initial distension	α_0	1.0
Minimum distension	α_{min}	1.0

Table B.5: Global model parameters for Chicxulub simulations.

Parameter	Symbol (units)	Value
Cell resolution	(m)	100
Cells per impactor radius		60
Horizontal cells in high resolution zone		1000
Horizontal cells in outer extension zone		200
Vertical cells in high resolution zone		800
Vertical cells in upper extension zone		0
Vertical cells in lower extension zone		200
Impactor velocity	v_i (km s ⁻¹)	15
Impactor density	ρ_i (kg m ⁻³)	2670
Acceleration due to gravity	g (m s ⁻²)	9.81
Surface temperature	T_{surf} (K)	288
Surface temperature gradient	T_{grad} (K m ⁻¹)	0.01
Lithospheric thickness	d_{lith} (km)	100
Linear artificial viscosity term		0.24
Quadratic artificial viscosity term		1.2
Tracer moving algorithm	Velocity	

Table B.6: Material model parameters for Chucruth simulations.

Parameter	Symbol (units)	Mantle (Dunite)	Crust (Granite)	Sediments (Calcite)
Reference Density	ρ (kg m^{-3})	3320	2630	2600
Poisson's ratio	ν	0.25	0.30	0.30
Intact cohesive strength	Y_0 (MPa)	10	10	5
Intact friction coefficient	μ_i	1.2	2.0	1.0
Intact and damaged strength limit	Y_m (MPa)	3500	2500	500
Damaged cohesive strength	Y_{d0} (MPa)	0.01	0.01	0.01
Damaged friction coefficient	μ_{di}	0.6	0.6	0.4
Minimum failure strain for low pressure states	$\varepsilon_f b$	1×10^{-4}	1×10^{-4}	1×10^{-4}
Constant of proportionality between failure strain and pressure	B	1×10^{-11}	1×10^{-11}	1×10^{-11}
Pressure above which failure is compressional (Pa)	P_c (MPa)	300	300	300
Melt Temperature	T_m (K)	1373	1673	1500
Thermal softening coefficient	ξ	1.2	1.2	1.2
Constant in Simon Approximation	p_{bp}	6×10^9	1.52×10^9	6×10^9
Exponent in Simon Approximation	y_0	3.00	4.05	3.00
Acoustic Fluidization viscosity constant	γ_η	0.025	0.025	0.025
Acoustic Fluidization decay time constant	γ_T	150	150	150
Vibrational particle velocity as a fraction of particle velocity	C_{vib}	0.1	0.1	0.1
Maximum vibrational particle velocity	V_{ibmax} (m s^{-1})	200	200	200
Time after which no new acoustic vibrations are generated	t_{off} (s)	16	16	16
Maximum dilatancy coefficient	β_{max}	0.09	0.09	0.09
Dilatancy pressure limit	p_{dm} (MPa)	200	200	200
Critical distension	α_c	1.2	1.2	1.2
Critical friction coefficient	μ_c	0.4	0.4	0.4
Initial distension	α_0	1.0	1.0	1.0
Minimum distension	α_{min}	1.0	1.0	1.0

C Supplementary Universal-Stage Data

C.1 West Clearwater Lake

In this section of the appendix, summarised thin section descriptions and universal stage data, organised by sample, for samples from the West Clearwater Lake structure are provided (Chapter 5). The methods by which data were acquired are described in Chapters 3 and 5. Thin section descriptions were only acquired from samples in Holes 1-63 and 5-63. Universal-stage data were acquired for samples from all holes and the field.

C.2 East Clearwater Lake

In this section of the appendix, summarised thin section descriptions and universal stage data, organised by sample, for samples from the East Clearwater Lake structure are provided (Chapter 6). The methods by which data were acquired are described in Chapters 3 and 6. Thin section descriptions and universal-stage data were acquired from samples in Hole 1-64.

Depth (ft)	Sample Info	Modal Mineralogy											Avg. Grain Size (mm)	Notes
		Qtz	Ksp	Plag	Bi	Amph	Cpx	Op	Gmass	Cc	Chl	Gt		
62	18.91	n.d.	n.d.	n.d.	n.d.	n.d.	n.d.	n.d.	n.d.	n.d.	n.d.	n.d.	n.d.	n.d.
63.4	19.337	20	50	20	5	0	0	0	0	5	0	0	0	1
65.5	19.9775	35	20	35	8	0	0	1	0	1	0	0	0	1
68	20.74	40	15	35	8	0	0	1	0	1	0	0	0	1
72	21.96	40	15	35	8	0	0	1	0	1	0	0	0	3
80	24.4	40	15	35	8	0	0	1	0	1	0	0	0	3
88.6	27.023	40	15	40	0	0	0	2	0	3	0	0	0	1
110	33.55	40	35	20	3	0	0	1	0	1	0	0	0	1
150	45.75	35	35	20	8	0	0	2	0	0	0	0	0	1
166.2	50.691	18	7	37	30	0	3	2	0	3	0	0	0	0.5
185	56.425	40	30	28	0	0	0	2	0	0	0	0	0	1
220	67.1	35	15	30	8	0	10	2	0	0	0	0	0	3
241	73.505	30	20	35	7	0	7	1	0	0	0	0	0	1
274.5	83.725	40	30	20	0	0	0	0	0	0	0	0	0	2
284	86.62	n.d.	n.d.	n.d.	n.d.	n.d.	n.d.	n.d.	n.d.	n.d.	n.d.	n.d.	n.d.	n.d.
330	100.05	n.d.	n.d.	n.d.	n.d.	n.d.	n.d.	n.d.	n.d.	n.d.	n.d.	n.d.	n.d.	n.d.
348	106.14	55	20	5	0	0	0	0	0	0	0	0	0	1
366	111.63	40	30	20	0	0	0	0	0	0	0	0	0	n.d.
377	114.985	30	35	30	4	0	0	1	0	0	0	0	0	1
422.3	128.8015	40	25	30	4	0	0	1	0	0	0	0	0	1
507	134.635	0	25	60	0	0	14	1	0	0	0	0	0	n.d.
548	167.14	50	30	0	0	0	15	0	0	0	5	0	0	1
616	187.88	0	0	40	10	20	30	0	0	0	0	0	0	0.5
661.4	201.727	0	0	40	5	40	12	0	0	0	0	3	0	0.1
752.5	229.5125	0	0	30	15	40	10	0	0	0	0	0	0	n.d.
781	238.205	50	40	10	0	0	0	0	0	0	0	0	0	4
786	239.73	70	30	0	0	0	0	0	0	0	0	0	0	n.d.
789	240.645	45	50	5	0	0	0	0	0	0	0	0	0	n.d.
814	248.27	50	40	10	0	0	0	0	0	0	0	0	0	4
814.1	248.3005	50	37	8	0	0	5	0	0	0	0	0	0	n.d.
859	261.995	0	0	20	20	60	0	0	0	0	0	0	0	n.d.
900.5	274.6525	0	0	20	20	60	0	0	0	0	0	0	0	n.d.
954	290.97	n.d.	n.d.	n.d.	n.d.	n.d.	n.d.	n.d.	n.d.	n.d.	n.d.	n.d.	n.d.	n.d.
964	294.02	55	40	0	0	0	0	0	5	0	0	0	0	n.d.
989	301.645	0	0	20	20	60	0	0	0	0	0	0	0	n.d.
1083	330.315	2	0	25	0	25	0	40	0	8	0	0	0	n.d.
1100	335.5	n.d.	n.d.	n.d.	n.d.	n.d.	n.d.	n.d.	n.d.	n.d.	n.d.	n.d.	n.d.	n.d.
1126	343.43	60	40	0	0	0	0	0	0	0	0	0	0	4
1141.5	348.1375	0	0	30	0	60	10	0	0	0	0	0	0	n.d.
1182	360.51	0	0	35	10	40	15	0	0	0	0	0	0.5	n.d.
1191	363.295	n.d.	n.d.	n.d.	n.d.	n.d.	n.d.	n.d.	n.d.	n.d.	n.d.	n.d.	n.d.	n.d.
1208	368.44	0	0	30	10	55	5	0	0	0	0	0	0	n.d.

Table C.1: Summary of thin section descriptions from Core 1-63 of West Clearwater Lake. “n.d.” indicates a measurement that was not made.

Qtz - Quartz, Ksp - Alkali Feldspar, Plag - Plagioclase, Bi - Biotite, Amph - Amphibole, Cpx - Clinopyroxene, Op - Opaque Phases, Gmass - Groundmass, Cc - Calcite, Chl - Chlorite, Gt - Garnet, ? - Unidentified Phase.

Depth (ft)	Depth (m)	Depth (m)	N	N*	n	P	N*	n	O	A	B	C	D	X	0001	1013	1012	1011	1010	1122	1121	2131	5161	1120	2241	3141	4041	5160	1014	Unindexed	1013+1014
62.0	-18.9	18.9	56	50	23	15.54	2.17	0.0%	21.1%	60.9%	17.4%	0.0%	0.0%	21	14	4	0	0	0	1	0	0	0	0	0	0	5	6	5	5	
63.4	-18.3	19.3	43	40	1.7	4.20%	52.1%	4.3%	0.0%	13.3%	46.7%	23.3%	0.0%	16.7%	22	16	7	1	0	0	1	0	0	0	0	0	4	4	2	2	
65.5	-20.0	20.0	74	60	30	12.50	1.74	0.0%	13.3%	50.0%	10.0%	0.0%	26.7%	16	17	3	1	0	1	1	0	0	1	0	0	11	14	1	1		
68.0	-20.7	20.7	67	57	30	15.34	1.90	0.0%	13.3%	50.0%	10.0%	0.0%	13.3%	16	25	2	0	1	0	2	1	1	1	0	1	9	10	4	4		
72.0	-22.0	22.0	69	57	30	15.67	1.90	0.0%	13.3%	50.0%	10.0%	0.0%	13.3%	16	25	2	0	1	0	0	0	0	0	0	1	5	12	3	3		
80.0	-24.4	24.4	58	54	30	15.19	1.80	0.0%	20.0%	53.3%	13.3%	0.0%	13.3%	24	18	4	0	0	0	0	0	0	0	0	0	0	6	4	2	2	
88.6	-27.0	27.0	71	58	30	15.77	1.93	0.0%	13.3%	60.0%	10.0%	0.0%	13.3%	13	17	4	1	0	2	1	0	1	13	13	4	4	4	4	4	4	4
110.0	-33.6	33.6	64	53	30	16.15	1.77	0.0%	26.7%	30.0%	23.3%	0.0%	20.0%	20	10	7	1	2	0	0	1	1	0	0	0	9	11	1	1	1	1
150.0	-45.8	45.8	58	48	30	15.96	1.60	0.0%	80.0%	66.7%	0.0%	0.0%	13.3%	15	22	2	0	0	0	0	0	0	0	0	0	0	10	2	2	2	
166.2	-50.7	50.7	63	52	30	15.77	1.73	0.0%	13.3%	60.0%	13.3%	0.0%	13.3%	20	17	4	3	0	2	0	0	0	0	0	0	2	11	2	2	2	
185.0	-56.4	56.4	70	64	30	16.81	2.13	0.0%	10.0%	66.7%	20.0%	0.0%	3.3%	27	20	6	0	0	1	0	0	1	0	0	1	0	2	6	4	4	
220.0	-67.1	67.1	68	55	30	14.70	1.83	0.0%	20.0%	53.3%	10.0%	0.0%	16.7%	14	16	3	0	1	3	0	1	2	1	1	0	0	2	7	7	4	
241.0	-75.5	73.5	66	59	30	13.27	1.97	0.0%	20.0%	66.7%	0.0%	0.0%	13.3%	21	16	0	1	0	0	0	1	0	0	0	0	0	14	7	5	5	
274.5	-83.7	83.7	73	59	30	13.70	1.97	0.0%	13.3%	63.3%	0.0%	0.0%	23.3%	18	19	0	0	0	0	0	0	0	0	0	0	0	12	14	7	7	
281.0	-86.6	86.6	67	57	30	16.74	1.90	0.0%	16.7%	66.7%	6.7%	0.0%	10.0%	25	16	2	0	0	0	0	0	0	0	0	0	0	7	10	7	7	
330.0	-100.7	100.7	74	65	30	15.63	2.17	0.0%	10.0%	60.0%	10.0%	0.0%	20.0%	21	17	3	4	0	0	0	1	1	1	0	0	9	9	5	5		
348.0	-106.1	106.1	71	60	30	17.21	2.00	0.0%	13.3%	50.0%	23.3%	0.0%	13.3%	16	15	7	1	0	3	1	0	2	1	1	0	0	8	11	3	3	
366.0	-111.6	111.6	67	55	30	17.40	1.83	0.0%	13.3%	43.3%	23.3%	0.0%	20.0%	15	16	7	2	0	2	0	1	0	1	0	1	4	12	4	4		
377.0	-115.0	115.0	50	43	30	14.17	1.43	0.0%	13.3%	53.3%	3.3%	0.0%	30.0%	14	14	1	0	1	0	1	0	0	0	0	0	0	4	7	3	3	
422.3	-128.8	128.8	66	53	30	14.44	1.87	0.0%	23.3%	56.7%	10.0%	0.0%	10.0%	22	15	3	0	0	0	1	0	0	0	0	0	0	8	10	5	5	
507.0	-154.6	154.6	n.d.	n.d.	n.d.	n.d.	n.d.	n.d.	n.d.	n.d.	n.d.	n.d.	n.d.	n.d.	n.d.	n.d.	n.d.	n.d.	n.d.	n.d.	n.d.	n.d.	n.d.	n.d.	n.d.	n.d.	n.d.	n.d.	n.d.	n.d.	
548.0	-167.1	167.1	n.d.	n.d.	n.d.	n.d.	n.d.	n.d.	n.d.	n.d.	n.d.	n.d.	n.d.	n.d.	n.d.	n.d.	n.d.	n.d.	n.d.	n.d.	n.d.	n.d.	n.d.	n.d.	n.d.	n.d.	n.d.	n.d.	n.d.	n.d.	n.d.
616.0	-187.9	187.9	n.d.	n.d.	n.d.	n.d.	n.d.	n.d.	n.d.	n.d.	n.d.	n.d.	n.d.	n.d.	n.d.	n.d.	n.d.	n.d.	n.d.	n.d.	n.d.	n.d.	n.d.	n.d.	n.d.	n.d.	n.d.	n.d.	n.d.	n.d.	n.d.
661.4	-201.7	201.7	n.d.	n.d.	n.d.	n.d.	n.d.	n.d.	n.d.	n.d.	n.d.	n.d.	n.d.	n.d.	n.d.	n.d.	n.d.	n.d.	n.d.	n.d.	n.d.	n.d.	n.d.	n.d.	n.d.	n.d.	n.d.	n.d.	n.d.	n.d.	n.d.
752.5	-229.5	229.5	n.d.	n.d.	n.d.	n.d.	n.d.	n.d.	n.d.	n.d.	n.d.	n.d.	n.d.	n.d.	n.d.	n.d.	n.d.	n.d.	n.d.	n.d.	n.d.	n.d.	n.d.	n.d.	n.d.	n.d.	n.d.	n.d.	n.d.	n.d.	n.d.
781.0	-238.2	238.2	30	26	18	12.31	1.44	5.6%	16.7%	5.6%	0.0%	55.6%	4	4	1	3	0	2	1	0	1	0	1	0	0	2	1	0	4	4	
786.0	-239.7	239.7	32	32	17	10.96	1.88	0.0%	41.2%	35.3%	0.0%	0.0%	28.5%	12	5	0	3	0	1	1	0	0	1	0	0	1	4	4	4	4	
789.0	-240.6	240.6	25	27	19	13.54	1.42	0.0%	21.1%	36.8%	5.3%	0.0%	36.8%	7	6	1	1	0	2	1	0	1	0	0	2	1	0	5	1	1	
814.0	-248.3	248.3	43	36	24	14.38	1.50	0.0%	12.5%	50.0%	4.2%	0.0%	33.3%	11	10	1	0	0	1	0	0	0	0	0	0	3	0	0	0	0	
814.1	-248.3	248.3	43	36	24	14.38	1.50	0.0%	12.5%	50.0%	4.2%	0.0%	33.3%	4	5	2	0	0	2	0	0	1	0	0	0	5	4	0	0	0	
859.0	-262.0	262.0	n.d.	n.d.	n.d.	n.d.	n.d.	n.d.	n.d.	n.d.	n.d.	n.d.	n.d.	n.d.	n.d.	n.d.	n.d.	n.d.	n.d.	n.d.	n.d.	n.d.	n.d.	n.d.	n.d.	n.d.	n.d.	n.d.	n.d.	n.d.	
900.5	-274.7	274.7	n.d.	n.d.	n.d.	n.d.	n.d.	n.d.	n.d.	n.d.	n.d.	n.d.	n.d.	n.d.	n.d.	n.d.	n.d.	n.d.	n.d.	n.d.	n.d.	n.d.	n.d.	n.d.	n.d.	n.d.	n.d.	n.d.	n.d.	n.d.	n.d.
954.0	-291.0	291.0	48	43	30	14.43	1.43	6.7%	13.3%	60.0%	10.0%	0.0%	10.0%	15	17	3	0	0	0	0	0	0	0	0	0	0	6	5	2	2	
964.0	-294.0	294.0	41	36	30	11.22	1.20	10.0%	23.3%	43.3%	0.0%	0.0%	23.3%	11	13	0	0	2	0	1	0	0	0	1	0	8	5	0	0	0	
989.0	-301.6	301.6	n.d.	n.d.	n.d.	n.d.	n.d.	n.d.	n.d.	n.d.	n.d.	n.d.	n.d.	n.d.	n.d.	n.d.	n.d.	n.d.	n.d.	n.d.	n.d.	n.d.	n.d.	n.d.	n.d.	n.d.	n.d.	n.d.	n.d.	n.d.	
1083.0	-330.3	330.3	26	22	22	11.33	1.00	22.7%	9.1%	0.0%	31.8%	4	5	2	0	0	3	2	0	0	1	0	0	5	4	0	0	0	0		
1100.0	-335.5	335.5	43	35	30	11.76	1.17	0.0%	30.0%	23.3%	3.3%	0.0%	43.3%	12	7	1	0	0	0	0	0	0	0	0	0	14	8	1	1	1	
1126.0	-343.4	343.4	48	42	24	14.65	1.75	0.0%	12.5%	41.7%	16.7%	0.0%	16.7%	12	10	5	3	0	1	0	2	1	0	0	1	6	1	1	1	1	
1141.5	-348.2	348.2	n.d.	n.d.	n.d.	n.d.	n.d.	n.d.	n.d.	n.d.	n.d.	n.d.	n.d.	n.d.	n.d.	n.d.	n.d.	n.d.	n.d.	n.d.	n.d.	n.d.	n.d.	n.d.	n.d.	n.d.	n.d.	n.d.	n.d.	n.d.	
1182.0	-360.5	360.5	n.d.	n.d.	n.d.	n.d.	n.d.	n.d.	n.d.	n.d.	n.d.	n.d.	n.d.	n.d.	n.d.	n.d.	n.d.	n.d.	n.d.	n.d.	n.d.	n.d.	n.d.	n.d.	n.d.	n.d.	n.d.	n.d.	n.d.	n.d.	
1191.0	-363.3	363.3	52	43	30	13.74	1.43	0.0%	13.3%	56.7%	3.3%	0.0%	23.3%	14	15	1	0	0	0	0	0	0	0	0	0	11	9	1	1	1	
1208.0	-368.4	368.4	n.d.	n.d.	n.d.	n.d.	n.d.	n.d.	n.d.	n.d.	n.d.	n.d.	n.d.	n.d.	n.d.	n.d.	n.d.	n.d.	n.d.	n.d.	n.d.	n.d.	n.d.	n.d.	n.d.	n.d.	n.d.	n.d.	n.d.	n.d.	

Table C.2: PDF statistics of thin sections from West Clearwater Lake, organised by sample. “n.d.” indicates a measurement that was not made due to a lack of quartz.

Depth (ft)	Depth (m)	Depth (m)	N	N*	n	P	N*/n	O	A	B	C	D	X	0001	1013	1012	1011	1010	1122	1121	2131	5101	1120	2241	3141	4041	5100	1014	Unindexed	1013+1014		
87.0	-26.5	26.5	50	48	30	10.98	1.60	3.3%	46.7%	46.7%	0.0%	0.0%	3.3%	27	11	0	0	0	0	0	1	0	0	0	0	0	0	6	2	3		
199.0	-60.7	60.7	22	22	17	11.30	1.29	11.8%	35.3%	35.3%	5.9%	0.0%	11.8%	12	5	1	0	0	0	0	0	0	0	0	0	0	0	3	1	1		
294.5	-80.8	80.8	57	55	30	11.64	1.83	3.3%	36.7%	53.3%	0.0%	0.0%	6.7%	27	14	0	1	0	0	1	0	0	0	0	0	0	0	8	2	4		
302.0	-92.1	92.1	41	38	23	14.39	1.65	4.3%	21.7%	43.5%	13.1%	0.0%	17.4%	12	8	3	0	1	1	0	0	0	2	0	0	0	0	8	3	3	3	
302.0	-92.1	92.1	62	61	30	14.23	2.03	0.0%	20.4%	60.0%	6.7%	0.0%	13.3%	24	14	2	1	1	2	0	0	0	0	0	0	0	1	7	1	5		
302.0	-92.1	92.1	64	60	30	12.62	2.00	3.3%	36.7%	50.0%	6.7%	0.0%	3.3%	28	14	2	0	1	0	1	0	0	0	0	0	0	0	3	4	3		
302.0	-92.1	92.1	64	63	30	12.76	2.10	0.0%	40.0%	50.0%	6.7%	0.0%	3.3%	27	16	2	0	1	2	1	0	0	0	0	0	0	0	9	1	0		
425.0	-129.6	129.6	8	8	30	4.68	0.27	76.7%	20.0%	3.3%	0.0%	0.0%	0.0%	7	1	0	0	0	0	0	0	0	0	0	0	0	0	0	0	0	0	
427.0	-145.5	145.5	25	25	30	6.53	0.83	40.0%	53.3%	0.0%	3.3%	0.0%	0.0%	17	0	1	2	0	0	1	0	0	0	0	0	0	0	0	0	0	0	
477.5	-146.6	145.6	13	13	30	5.10	0.43	60.0%	40.0%	0.0%	0.0%	0.0%	0.0%	12	0	0	0	0	0	0	0	0	0	0	0	0	0	0	0	0	0	
482.0	-147.0	147.0	23	23	30	6.77	0.77	43.3%	33.3%	13.3%	0.0%	0.0%	0.0%	17	1	0	0	0	0	0	0	0	0	0	0	0	0	0	0	0	0	
516.9	-157.7	157.7	15	15	30	5.02	0.50	60.0%	23.3%	3.3%	0.0%	0.0%	0.0%	7	1	0	0	0	0	1	1	0	0	0	0	0	0	0	0	0	0	
580.0	-176.9	176.9	6	6	30	4.17	0.20	83.3%	16.7%	0.0%	0.0%	0.0%	0.0%	5	0	0	0	0	0	0	0	0	0	0	0	0	0	0	0	0	0	
580.0	-176.9	176.9	23	23	30	6.52	0.77	30.0%	63.3%	3.3%	0.0%	0.0%	0.0%	20	1	0	0	0	0	0	0	0	0	0	0	0	0	0	0	0	0	
586.0	-178.7	178.7	11	11	30	5.62	0.37	70.0%	23.3%	3.3%	0.0%	0.0%	0.0%	9	1	0	0	0	0	0	0	0	0	0	0	0	0	0	0	0	0	
592.0	-180.6	180.6	4	4	30	4.03	0.13	86.7%	13.3%	0.0%	0.0%	0.0%	0.0%	4	0	0	0	0	0	0	0	0	0	0	0	0	0	0	0	0	0	
592.0	-180.6	180.6	n.d.	n.d.	n.d.	n.d.	n.d.	n.d.	n.d.	n.d.	n.d.	n.d.	n.d.	n.d.	n.d.	n.d.	n.d.	n.d.	n.d.	n.d.	n.d.	n.d.	n.d.	n.d.	n.d.	n.d.	n.d.	n.d.	n.d.	n.d.		
592.0	-180.6	180.6	24	24	30	6.92	0.80	33.3%	56.7%	10.0%	0.0%	0.0%	0.0%	20	3	0	0	0	0	0	0	0	0	0	0	0	0	0	0	0	0	0
692.0	-211.1	211.1	25	25	30	7.57	0.83	40.0%	43.3%	3.3%	0.0%	0.0%	0.0%	18	4	1	0	1	1	0	0	0	0	0	0	0	0	0	0	0	0	0
785.0	-239.4	239.4	11	11	30	5.00	0.37	66.7%	26.7%	3.3%	0.0%	0.0%	0.0%	9	1	0	0	0	1	0	0	0	0	0	0	0	0	0	n.d.	n.d.	n.d.	
811.8	-247.6	247.6	n.d.	n.d.	n.d.	n.d.	n.d.	n.d.	n.d.	n.d.	n.d.	n.d.	n.d.	n.d.	n.d.	n.d.	n.d.	n.d.	n.d.	n.d.	n.d.	n.d.	n.d.	n.d.	n.d.	n.d.	n.d.	n.d.	n.d.	n.d.		
818.5	-249.6	249.6	n.d.	n.d.	n.d.	n.d.	n.d.	n.d.	n.d.	n.d.	n.d.	n.d.	n.d.	n.d.	n.d.	n.d.	n.d.	n.d.	n.d.	n.d.	n.d.	n.d.	n.d.	n.d.	n.d.	n.d.	n.d.	n.d.	n.d.	n.d.		
832.4	-253.9	253.9	n.d.	n.d.	n.d.	n.d.	n.d.	n.d.	n.d.	n.d.	n.d.	n.d.	n.d.	n.d.	n.d.	n.d.	n.d.	n.d.	n.d.	n.d.	n.d.	n.d.	n.d.	n.d.	n.d.	n.d.	n.d.	n.d.	n.d.	n.d.		
1014.0	-309.3	309.3	40	40	30	10.38	1.33	10.0%	53.3%	23.3%	6.7%	0.0%	6.7%	25	7	2	2	0	1	0	0	0	0	0	0	0	0	0	0	0	0	0
1144.5	-339.9	339.9	22	22	30	6.55	0.73	46.7%	46.7%	3.3%	0.0%	0.0%	0.0%	16	0	1	2	0	0	0	0	0	0	0	0	0	0	0	2	0	0	
1162.0	-354.4	354.4	26	25	30	8.02	0.83	26.7%	63.3%	3.3%	6.7%	0.0%	0.0%	22	1	2	0	0	0	0	0	0	0	0	0	0	0	0	1	0	0	
1164.0	-355.0	355.0	28	27	30	6.91	0.90	20.0%	70.0%	3.3%	0.0%	0.0%	0.0%	22	1	0	3	0	0	0	0	0	0	0	0	0	0	0	1	1	0	
1192.0	-363.6	363.6	21	21	30	8.02	0.70	43.3%	10.0%	3.3%	0.0%	0.0%	0.0%	17	1	3	0	0	0	0	0	0	0	0	0	0	0	0	0	0	0	
1194.0	-364.2	364.2	18	18	30	6.10	0.60	60.0%	26.7%	13.3%	0.0%	0.0%	0.0%	11	4	0	0	0	1	0	0	0	0	0	0	0	0	0	1	0	0	
1258.5	-383.8	383.8	12	12	30	5.22	0.40	63.3%	33.3%	3.3%	0.0%	0.0%	0.0%	11	1	0	0	0	0	0	0	0	0	0	0	0	0	0	0	0	0	

Table C.3: PDF statistics of thin sections from Hole 3-63 from West Clearwater Lake, organised by sample. “n.d.” indicates a measurement that was not made due to a lack of quartz.

Sample Info		Modal Mineralogy							Notes		
Depth (ft)	Depth (m)	Qtz	K-spar	Plag	Bi	Amph	Op	Gmass	Cc	Chl	Max Grain Size (mm)
105	32.025	35	0	15	0	0	0	50	0	0	n.d.
117	35.085	5	5	5	1	0	0	84	0	0	n.d.
117	35.085	10	10	10	5	0	0	65	0	0	n.d.
137	41.785	45	30	20	4	0	1	0	0	0	1
148	45.14	60	25	10	0	0	0	0	5	0	2
158.5	48.3425	n.d.	n.d.	n.d.	n.d.	n.d.	n.d.	n.d.	n.d.	n.d.	n.d.
170	51.85	60	25	10	0	3	0	0	2	0	2
180	54.9	n.d.	n.d.	n.d.	n.d.	n.d.	n.d.	n.d.	n.d.	n.d.	n.d.
234	71.37	60	25	10	0	10	0	0	15	0	2
262	79.91	n.d.	n.d.	n.d.	n.d.	n.d.	n.d.	n.d.	n.d.	n.d.	n.d.
289	88.145	50	25	15	0	7	3	0	0	0	3
395	120.475	40	45	10	0	4	0	0	1	1	2
430	131.15	n.d.	n.d.	n.d.	n.d.	n.d.	n.d.	n.d.	n.d.	n.d.	n.d.
491	149.755	25	50	20	1	0	0	0	4	0	n.d.
554	168.97	n.d.	n.d.	n.d.	n.d.	n.d.	n.d.	n.d.	n.d.	n.d.	n.d.
700	213.5	0	20	20	0	60	0	0	0	0	n.d.

Table C.4: Summary of thin section descriptions from Core 5-63 of West Clearwater Lake. "n.d." indicates a measurement that was not made.
Qtz - Quartz, Ksp - Alkali Feldspar, Plag - Plagioclase, Bi - Biotite, Amph - Amphibole, Op - Opaque Phases, Gmass - Groundmass, Cc - Calcite, Chl - Chlorite.

Depth (ft)	Depth (m)	Depth (m)	N	N*	n	P	N*/n	O	A	B	C	D	X	0001	1013	1012	1011	1010	1122	1121	2131	5161	1120	2241	3141	4041	5160	1014	Unindexed	1013+1014	
105.0	-32.0	32.0	55	45	30	16.70	1.50	0.0%	0.0%	63.3%	10.0%	0.0%	26.7%	8	19	3	1	0	0	1	1	1	0	0	9	10	1	n.d.	n.d.		
117.0	-35.7	35.7	n.d.	n.d.	n.d.	n.d.	n.d.	n.d.	n.d.	n.d.	n.d.	n.d.	n.d.	n.d.	n.d.	n.d.	n.d.	n.d.	n.d.	n.d.	n.d.	n.d.	n.d.	n.d.	n.d.	n.d.	n.d.	n.d.			
117.0	-35.7	35.7	n.d.	n.d.	n.d.	n.d.	n.d.	n.d.	n.d.	n.d.	n.d.	n.d.	n.d.	n.d.	n.d.	n.d.	n.d.	n.d.	n.d.	n.d.	n.d.	n.d.	n.d.	n.d.	n.d.	n.d.	n.d.	n.d.	n.d.		
137.0	-41.8	41.8	36	32	30	9.00	1.07	20.0%	33.3%	26.7%	0.0%	0.0%	20.0%	15	6	0	2	1	0	1	0	0	0	0	0	3	4	2	n.d.	n.d.	
148.0	-45.1	45.1	37	32	30	9.67	1.07	23.3%	26.7%	26.7%	3.3%	0.0%	20.0%	11	8	1	0	0	0	1	1	0	0	0	0	9	5	1	1	1	
158.5	-48.3	48.3	40	34	24	16.62	1.42	0.0%	12.5%	41.7%	16.7%	0.0%	29.2%	8	12	3	0	0	1	1	1	3	0	0	0	4	6	6	1	1	
170.0	-51.9	51.9	31	26	30	9.52	0.87	26.7%	20.0%	36.7%	0.0%	0.0%	16.7%	8	11	0	0	1	0	0	0	0	0	0	0	6	5	0	n.d.	n.d.	
189.0	-54.9	54.9	34	30	21	13.93	1.43	4.8%	38.1%	33.3%	19.0%	0.0%	4.8%	14	8	4	0	0	0	0	0	0	0	0	0	1	3	4	0	n.d.	n.d.
234.0	-71.4	71.4	31	27	30	8.87	0.90	26.7%	30.0%	30.0%	0.0%	0.0%	13.3%	14	8	0	0	0	0	0	0	0	0	0	0	0	0	0	4	4	1
262.0	-79.9	79.9	52	47	30	11.70	1.57	0.0%	36.7%	46.7%	0.0%	0.0%	16.7%	21	14	0	0	1	0	0	0	0	0	0	0	5	1	1	n.d.	n.d.	
289.0	-88.1	88.1	26	24	30	8.54	0.80	26.7%	36.7%	26.7%	0.0%	0.0%	10.0%	14	6	0	0	0	0	1	0	0	0	0	0	0	0	2	2	1	
395.0	-120.5	120.5	3	3	30	4.15	0.10	90.0%	6.7%	3.3%	0.0%	0.0%	2	1	0	0	0	0	0	0	0	0	0	0	0	0	0	0	0	0	
439.0	-131.2	131.2	25	22	30	7.92	0.73	50.0%	23.3%	3.3%	0.0%	0.0%	12	7	1	0	0	0	0	0	0	0	0	0	0	0	0	1	3	1	
491.0	-149.8	149.8	1	1	30	3.50	0.03	96.7%	0.0%	0.0%	3.3%	0	0	0	0	0	1	0	0	0	0	0	0	0	0	0	0	0	0		
554.0	-169.0	169.0	16	15	30	5.34	0.50	56.7%	33.3%	3.3%	0.0%	0.0%	6.7%	11	0	0	0	1	0	0	0	0	0	0	2	1	1	1	n.d.	n.d.	
700.0	-213.5	213.5	n.d.	n.d.	n.d.	n.d.	n.d.	n.d.	n.d.	n.d.	n.d.	n.d.	n.d.	n.d.	n.d.	n.d.	n.d.	n.d.	n.d.	n.d.	n.d.	n.d.	n.d.	n.d.	n.d.	n.d.	n.d.	n.d.			

Table C.5: PDF statistics of thin sections from Hole 5-63 from West Clearwater Lake, organised by sample. “n.d.” indicates a measurement that was not made due to a lack of quartz.

Table C.6: Sample location and PDF statistics of thin sections from field samples from West Clearwater Lake, organised by sample. “n.d.” indicates a measurement that was not made due to a lack of quartz. The initials within the sample name indicate the collector of the sample:
 AR – Auriol Rae, MK – Mary Kerrigan, AEB – Anna E. Brunner.

Depth (ft)	Depth (m)	Sample Info		Qtz	Ksp	Plag	Bt	Modal Mineralogy							Max Grain Size (mm)	Notes
		Sample	Loc					Amph	Cpx	Op	Gmass	Cc	Chl			
412.0	-125.7	50.0	30.0	10.0	0	0	0	0	0	0	0	0	0	0	3.0	Heavily fractured; lots of cataclasis.
415.0	-126.6	50.0	30.0	15.0	2.0	0	0	0	0	0	0	0	0	0	3.0	
419.0	-127.8	60.0	10.0	10.0	0	0	0	0	0	0	0	0	0	0	3.0	Strong cataclasis; calcite fills pore space in cataclasitic and felsic veins. Compositionally banded; biotite very rich in bands.
422.0	-128.7	60.0	18.0	15.0	2.0	0	0	0	0	0	0	0	0	0	3.0	
426.5	-130.1	40.0	35.0	20.0	3.0	0	0	0	0	0	0	0	0	0	2.0	
431.0	-131.5	40.0	35.0	20.0	3.0	0	0	0	0	0	0	0	0	0	3.0	
444.0	-135.4	50.0	25.0	20.0	5.0	0	0	0	0	0	0	0	0	0	3.0	Extensive Cataclasis
453.0	-138.2	40.0	18.0	2.0	0	0	0	0	0	0	0	0	0	0	3.0	Common Cataclasis
456.5	-139.2	20.0	50.0	10.0	20.0	0	0	0	0	0	0	0	0	0	3.0	Extensive Cataclasis
465.0	-141.8	30.0	30.0	10.0	0	0	0	0	0	0	0	0	0	0	3.0	
472.0	-144.0	40.0	30.0	20.0	10.0	0	0	0	0	0	0	0	0	0	0.5	
472.3	-144.1	30.0	40.0	25.0	5.0	0	0	0	0	0	0	0	0	0	10.0	
472.3	-144.1	20.0	50.0	25.0	5.0	0	0	0	0	0	0	0	0	0	4.0	
478.0	-145.8	30.0	35.0	5.0	0	0	0	0	0	0	0	0	0	0	2.0	
494.6	-150.9	40.0	35.0	5.0	0	0	0	0	0	0	0	0	0	0	0	Extensive Cataclasis
498.0	-151.9	30.0	30.0	10.0	10.0	0	0	0	0	0	0	0	0	0	3.0	Extensive Cataclasis
504.0	-153.7	40.0	15.0	0	0	0	0	0	0	0	0	0	0	0	0	Extensive Cataclasis
509.2	-155.3	40.0	30.0	25.0	5.0	0	0	0	0	0	0	0	0	0	3.0	Weak Foliation
516.5	-157.5	50.0	25.0	5.0	0	0	0	0	0	0	0	0	0	0	0	
521.5	-159.1	50.0	25.0	5.0	0	0	0	0	0	0	0	0	0	0	0	
531.0	-162.0	50.0	30.0	15.0	4.0	0	0	0	0	0	0	0	0	0	1.0	
540.5	-164.9	40.0	30.0	20.0	8.0	0	0	0	0	0	0	0	0	0	0	
543.3	-165.7	35.0	15.0	10.0	0	0	0	0	0	0	0	0	0	0	0	
543.7	-165.8	20.0	50.0	8.0	0	0	0	0	0	0	0	0	0	0	0	
568.5	-173.4	20.0	58.0	20.0	0	0	0	0	0	0	0	0	0	0	0	
587.0	-179.0	30.0	30.0	2.0	0	0	0	0	0	0	0	0	0	0	0	
603.7	-184.1	45.0	20.0	30.0	2.0	0	0	0	0	0	0	0	0	0	3.0	
650.0	-198.3	5.0	20.0	20.0	20.0	0	0	0	0	0	0	0	0	0	0	
655.0	-199.8	25.0	30.0	25.0	15.0	0	0	0	0	0	0	0	0	0	5.0	
710.0	-216.0	50.0	20.0	4.0	0	0	0	0	0	0	0	0	0	0	1.0	
740.0	-225.7	40.0	35.0	20.0	1.0	0	0	0	0	0	0	0	0	0	1.0	
768.8	-234.5	35.0	30.0	30.0	5.0	0	0	0	0	0	0	0	0	0	0	
818.5	-240.6	30.0	30.0	35.0	5.0	0	0	0	0	0	0	0	0	0	0	
876.0	-267.2	30.0	50.0	10.0	0	0	0	0	0	0	0	0	0	0	0	
941.0	-274.5	25.0	50.0	20.0	5.0	0	0	0	0	0	0	0	0	0	0	
1536.5	-403.6	40.0	15.0	5.0	0	0	0	0	0	0	0	0	0	0	0	
1600.0	-468.6	30.0	50.0	10.0	0	0	0	0	0	0	0	0	0	0	0	
1683.0	-513.3	35.0	35.0	20.0	10.0	0	0	0	0	0	0	0	0	0	0	
1750.0	-533.8	35.0	35.0	20.0	10.0	0	0	0	0	0	0	0	0	0	0	
1835.0	-550.7	35.0	35.0	20.0	10.0	0	0	0	0	0	0	0	0	0	0	
1949.0	-594.4	50.0	30.0	10.0	5.0	0	0	0	0	0	0	0	0	0	0	
2024.0	-617.3	50.0	30.0	10.0	5.0	0	0	0	0	0	0	0	0	0	0	
2162.9	-650.7	30.0	35.0	4.0	1.0	0	0	0	0	0	0	0	0	0	0	
2276.0	-694.2	50.0	25.0	25.0	0	0	0	0	0	0	0	0	0	0	3.0	
2354.0	-718.0	35.0	35.0	20.0	10.0	0	0	0	0	0	0	0	0	0	0	
2462.0	-748.0	40.0	19.0	1.0	0	0	0	0	0	0	0	0	0	0	10.0	
2514.0	-766.8	25.0	50.0	20.0	3.0	0	0	0	0	0	0	0	0	0	0	
2613.7	-797.2	40.0	40.0	19.0	1.0	0	0	0	0	0	0	0	0	0	0	
2655.5	-809.9	30.0	50.0	19.0	1.0	0	0	0	0	0	0	0	0	0	0	
2752.0	-838.4	35.0	35.0	8.0	0	0	0	0	0	0	0	0	0	0	0	
2849.0	-868.9	30.0	30.0	10.0	0	0	0	0	0	0	0	0	0	0	0	
2947.0	-898.8	15.0	40.0	35.0	10.0	0	0	0	0	0	0	0	0	0	0	
3062.5	-934.1	30.0	35.0	30.0	5.0	0	0	0	0	0	0	0	0	0	0	
3182.5	-961.5	10.0	65.0	5.0	0	0	0	0	0	0	0	0	0	0	0	
3225.5	-983.8	10.0	25.0	10.0	0	0	0	0	0	0	0	0	0	0	10.0	
3276.0	-999.2	25.0	25.0	9.0	0	0	0	0	0	0	0	0	0	0	0	
General Comments		Abundant PDFs in Qtz, Ksp-spar often perthitic; Plag occasionally myrmekitic; Cc and Chl occur as secondary minerals, often within cataclasites and veins.														

Table C.7: Summary of thin section descriptions from East Clearwater Lake. Qtz - Quartz, Ksp - Alkali Feldspar, Plag - Plagioclase, Bi - Biotite, Amph - Amphibole, Cpx - Clinopyroxene, Op - Opaque Phases, Gmass - Groundmass, Cc - Calcite, Chl - Chlorite.

Table C.8: PDF statistics of East Clearwater Lake thin sections, organised by sample.

D Supplementary BSE Images and Analysis

D.1 East Clearwater Lake

In this section of the appendix, BSE maps, analysis by location within a transect of a deformation feature, grain size-frequency distributions, and pore size-frequency distributions in samples from Hole 1-64 are provided (Chapter 6). The methods by which images were acquired and processed are described in Chapters 3 and 6. A list of the acquired and analysed images can be found in Table D.1.

Hole	Depth (ft)	Depth (mbls)	Description
1-64	544a	166	Cataclasite (with veins) → Granite
1-64	544b	166	Granite → Cataclasite
1-64	972	296	Granite → Cataclasite → Granite
1-64	1090	332	Granite → Cataclasite → Granite
1-64	1223	373	Granite
1-64	1617	493	Granite → Cataclasite → Granite
1-64	2140	652	Cataclasite
1-64	2206a	672	Cataclasite → Granite
1-64	2206b	672	Cataclasite → Granite
1-64	2763a	842	Granite → Cataclasite (with veins)
1-64	2763b	842	Granite → Cataclasite (with veins)

Table D.1: List of BSE imaged and analysed samples from East Clearwater Lake.

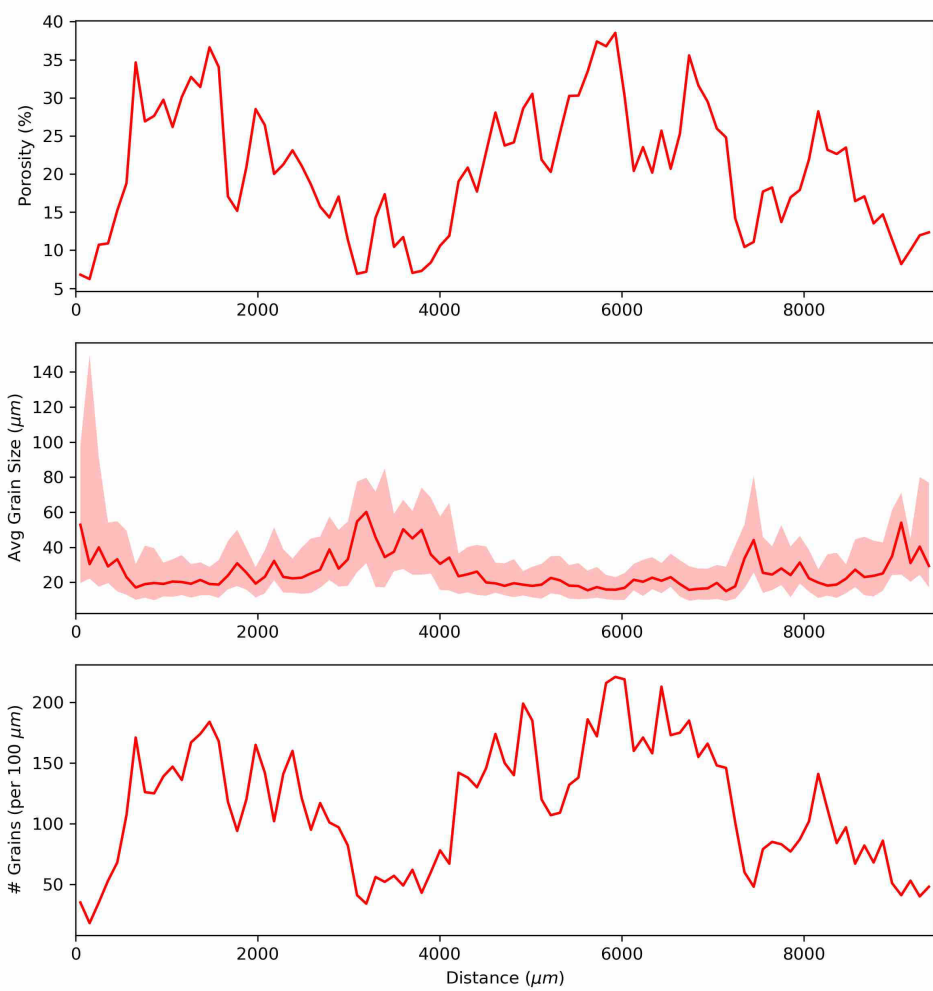
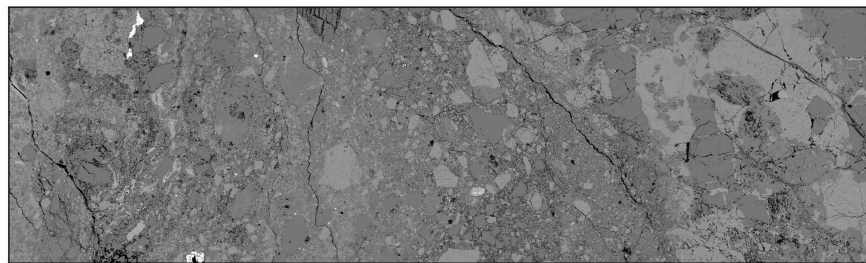


Figure D.1: Transect analysis of 1-64-544a

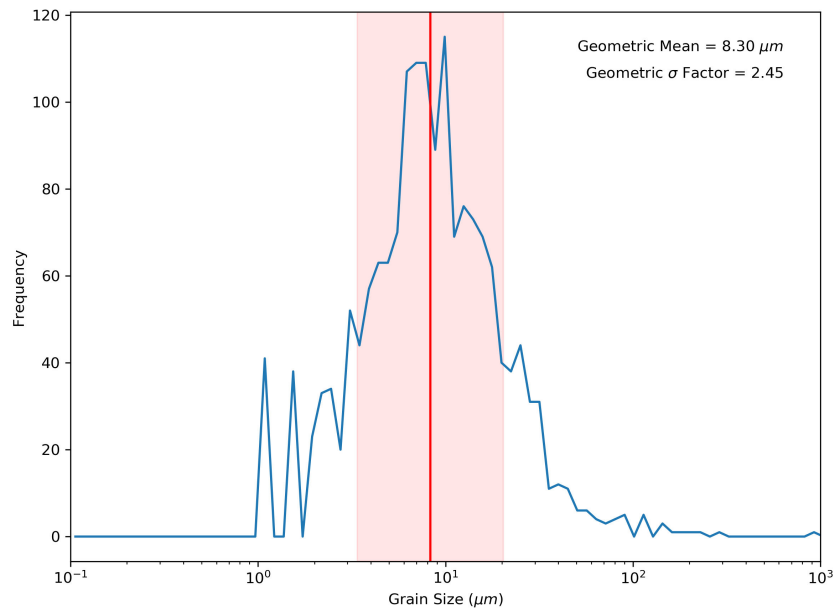


Figure D.2: Grain size-frequency distribution of 1-64-544a

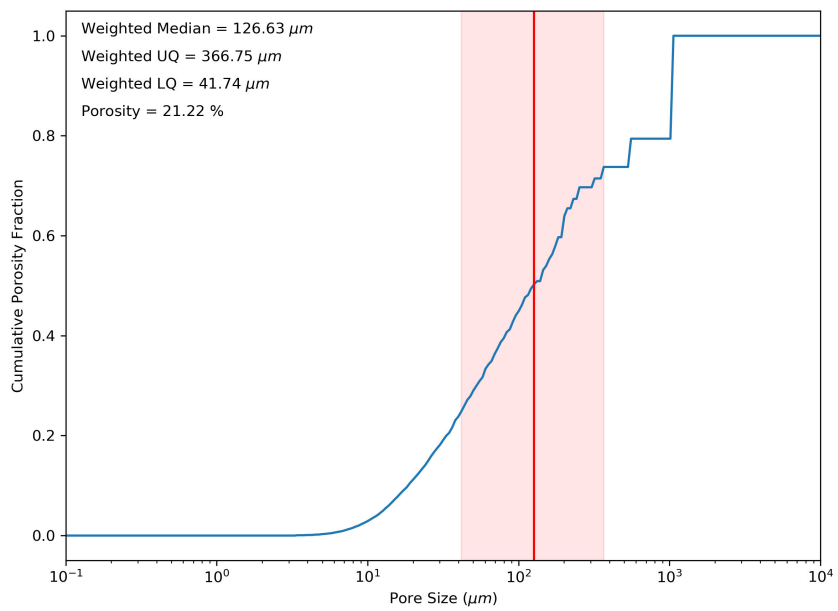


Figure D.3: Pore size-frequency distribution of 1-64-544a

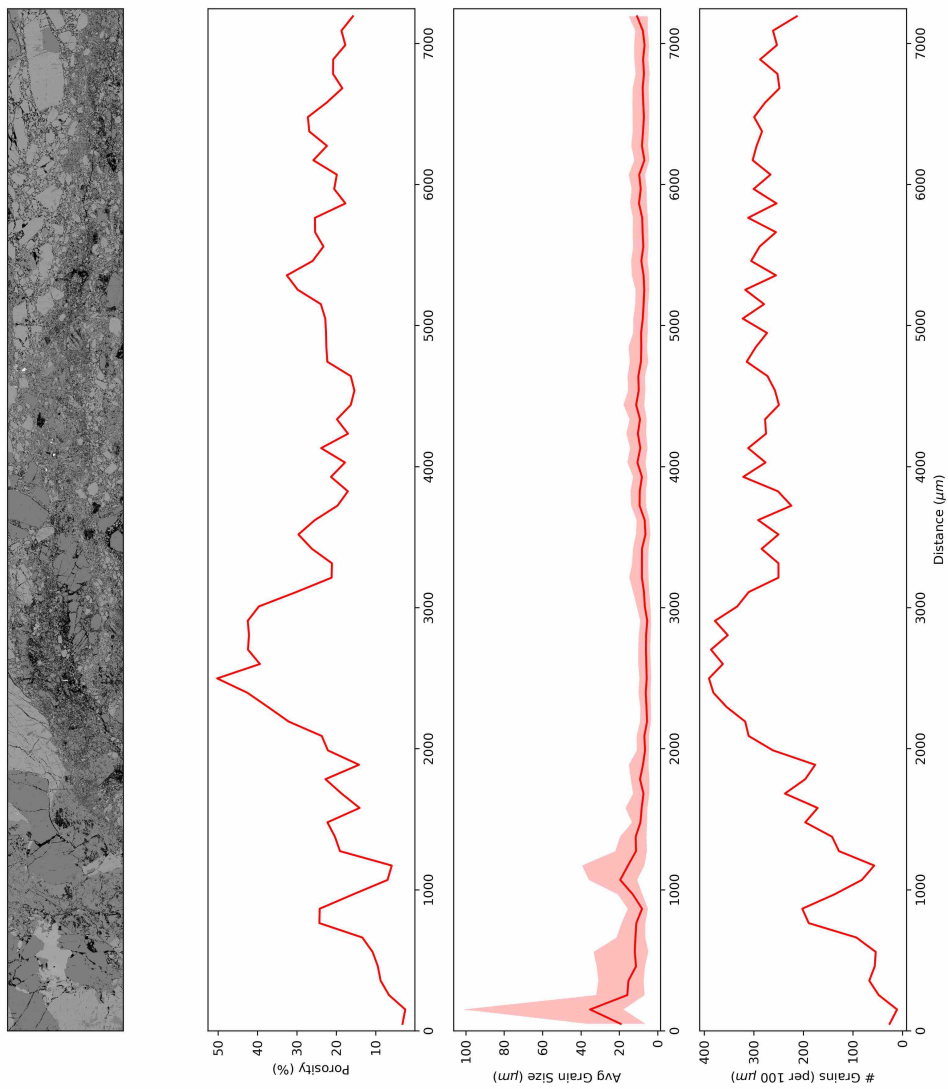


Figure D.4: Transect analysis of 1-64-54b

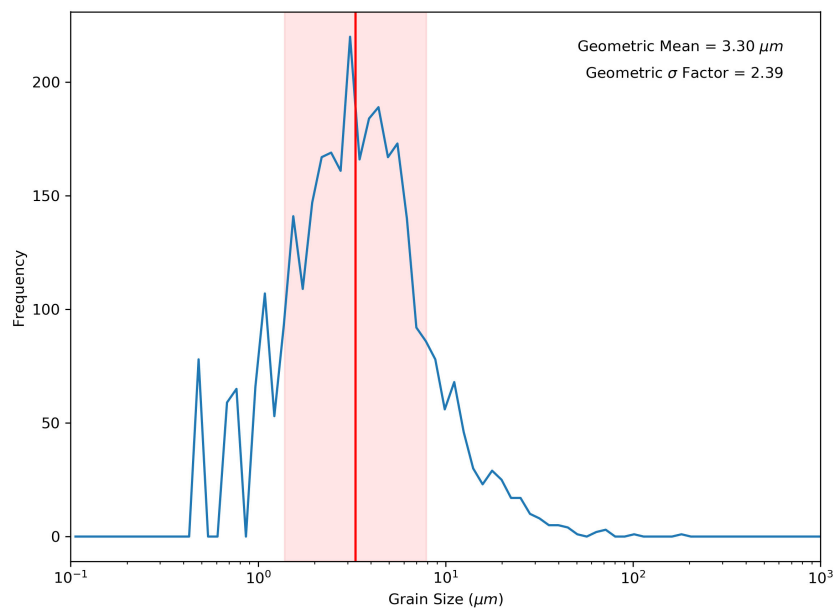


Figure D.5: Grain size-frequency distribution of 1-64-544b

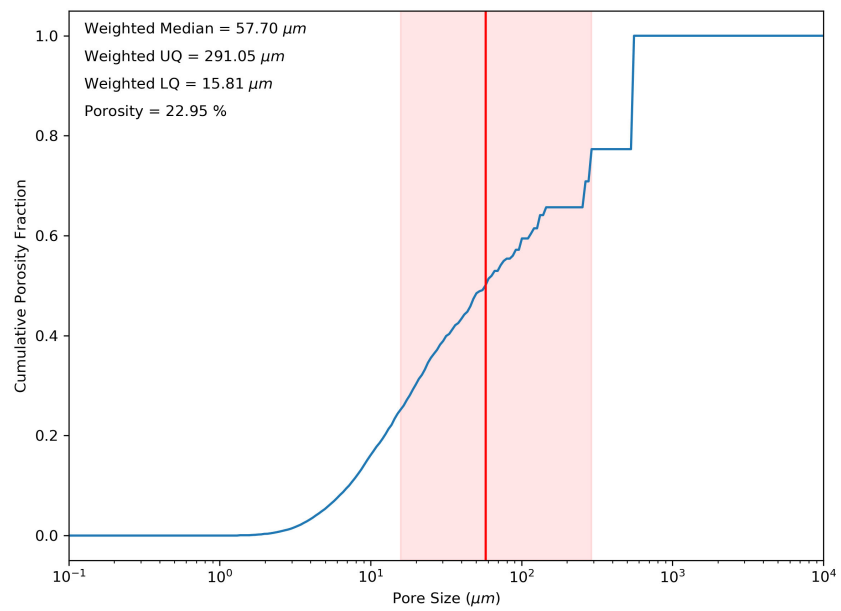


Figure D.6: Pore size-frequency distribution of 1-64-544b

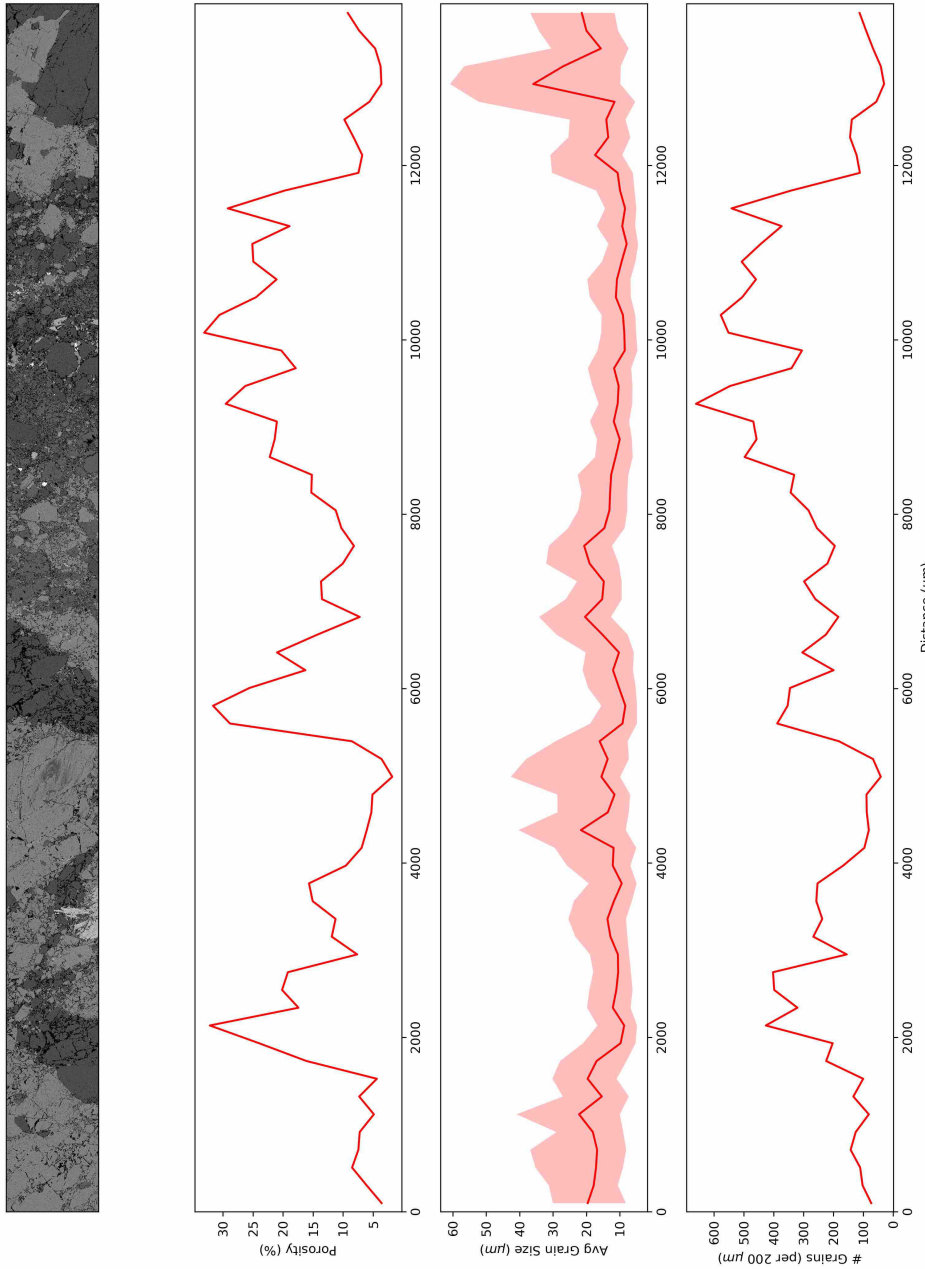


Figure D.7: Transect analysis of 1-64-972

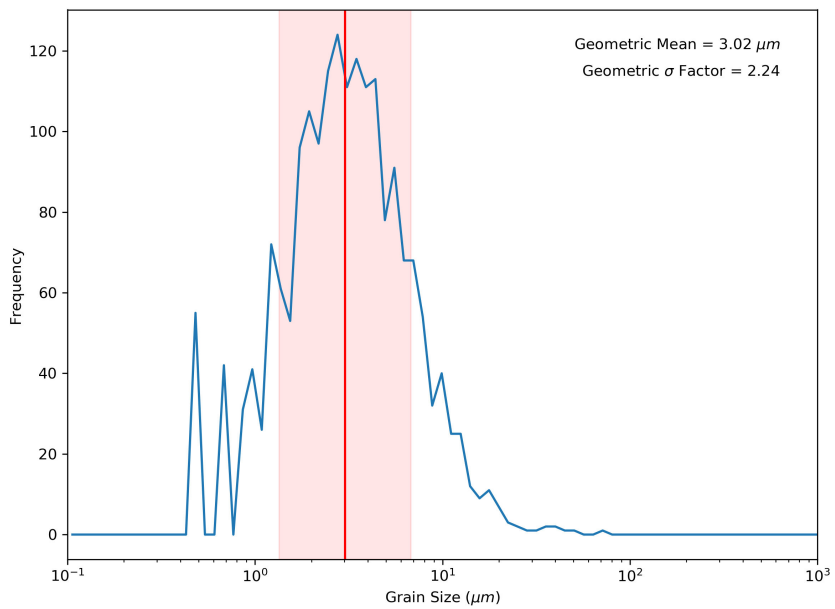


Figure D.8: Grain size-frequency distribution of 1-64-972

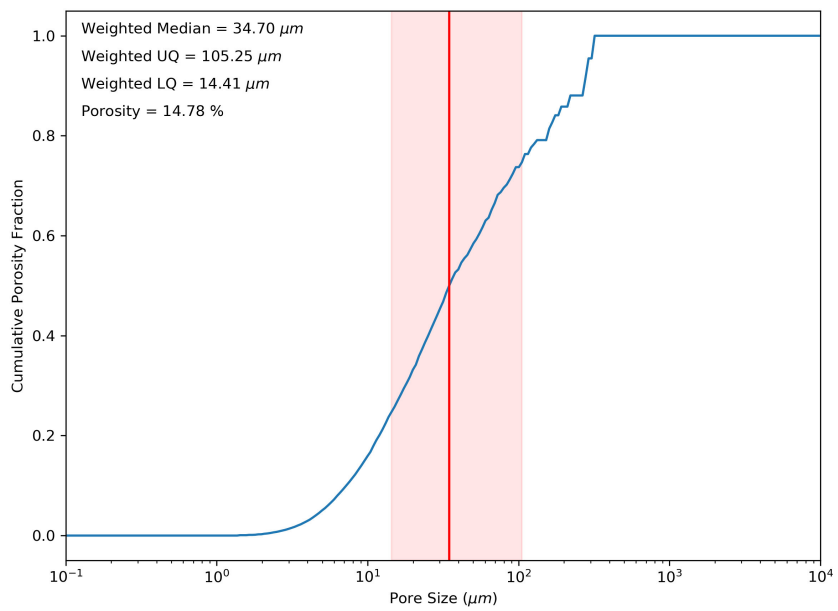


Figure D.9: Pore size-frequency distribution of 1-64-972

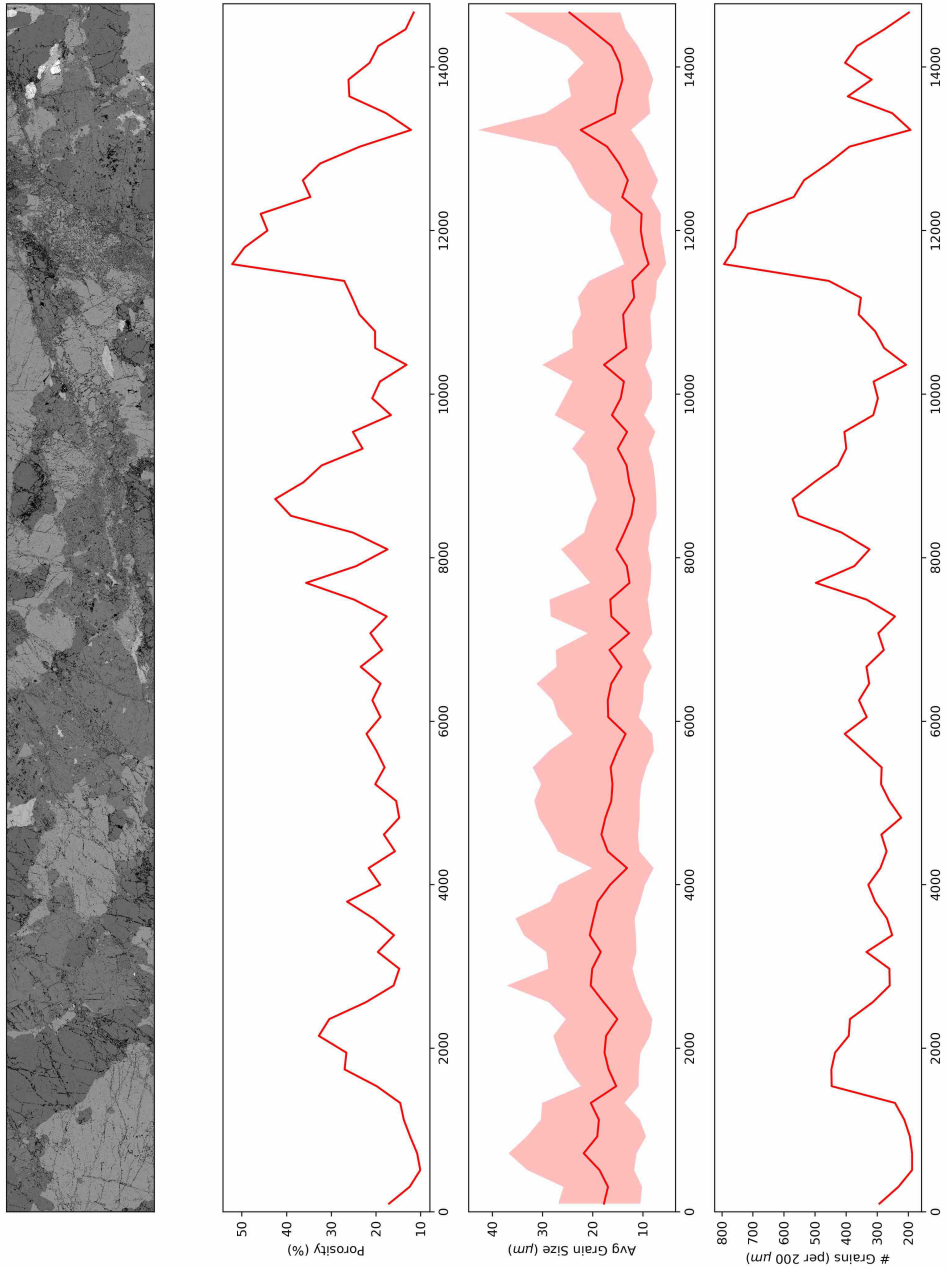


Figure D.10: Transect analysis of 1-64-1090

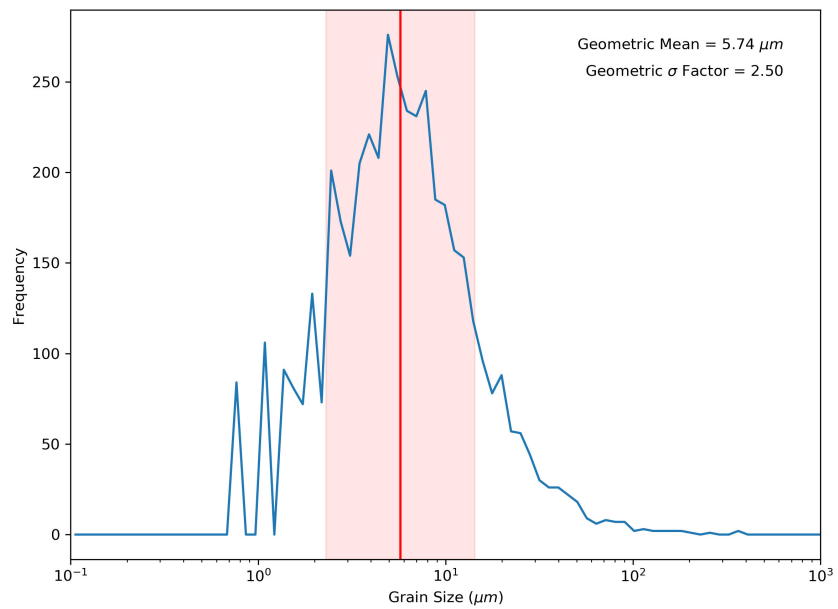


Figure D.11: Grain size-frequency distribution of 1-64-1090

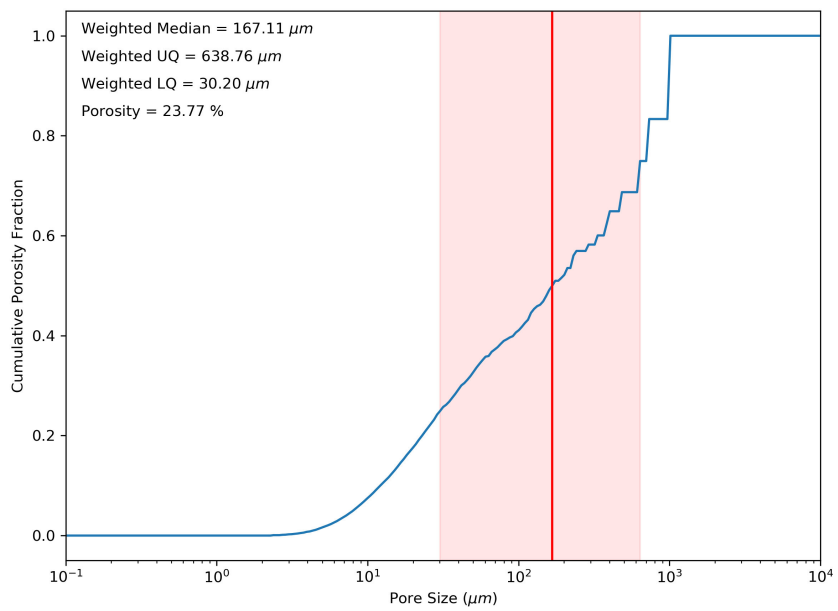


Figure D.12: Pore size-frequency distribution of 1-64-1090

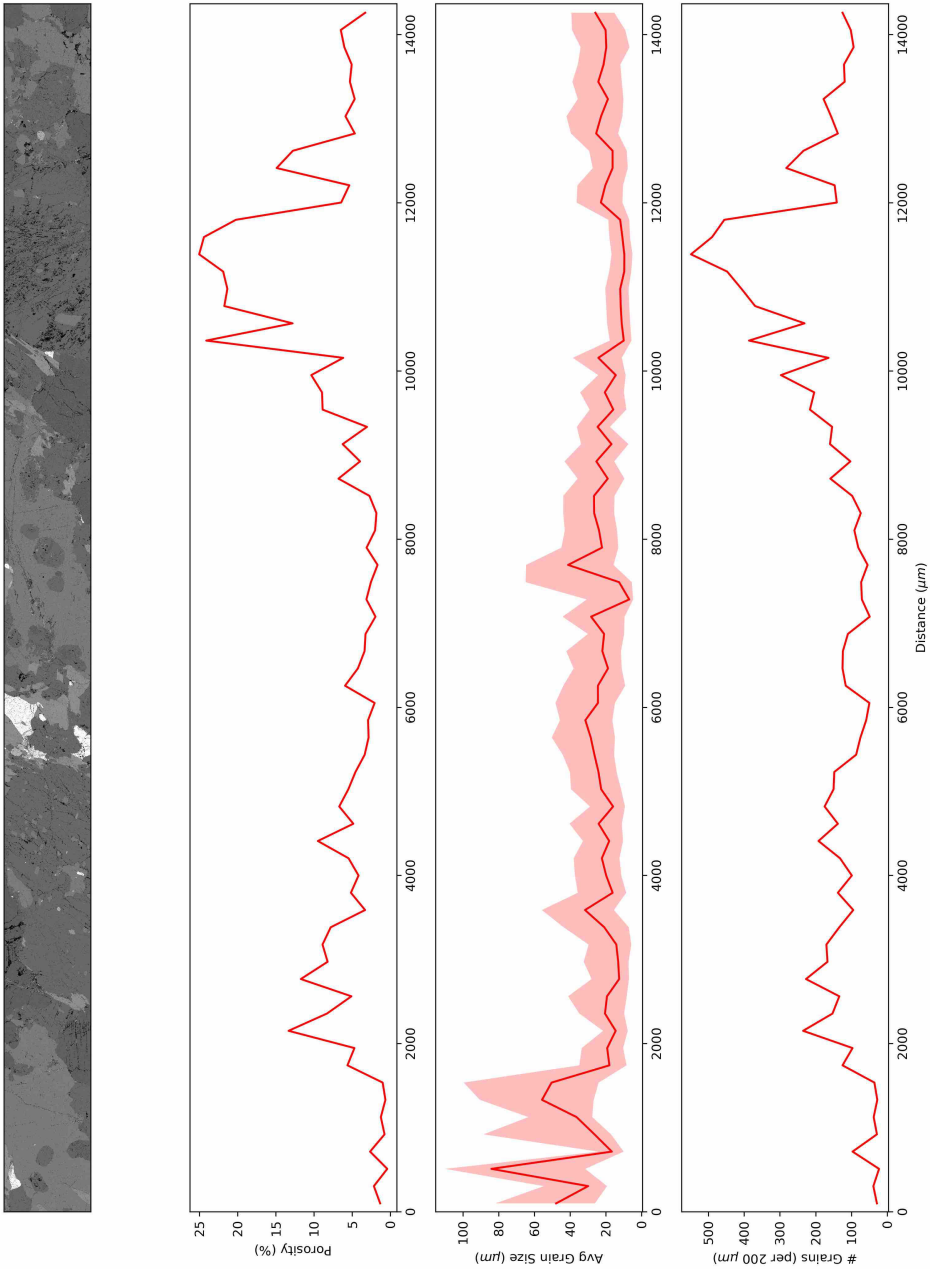


Figure D.13: Transect analysis of 1-64-1223

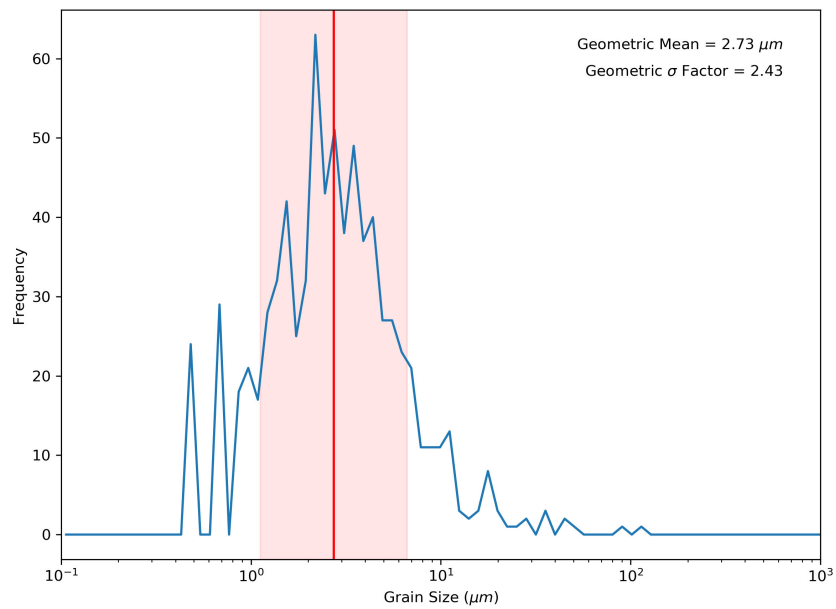


Figure D.14: Grain size-frequency distribution of 1-64-1223

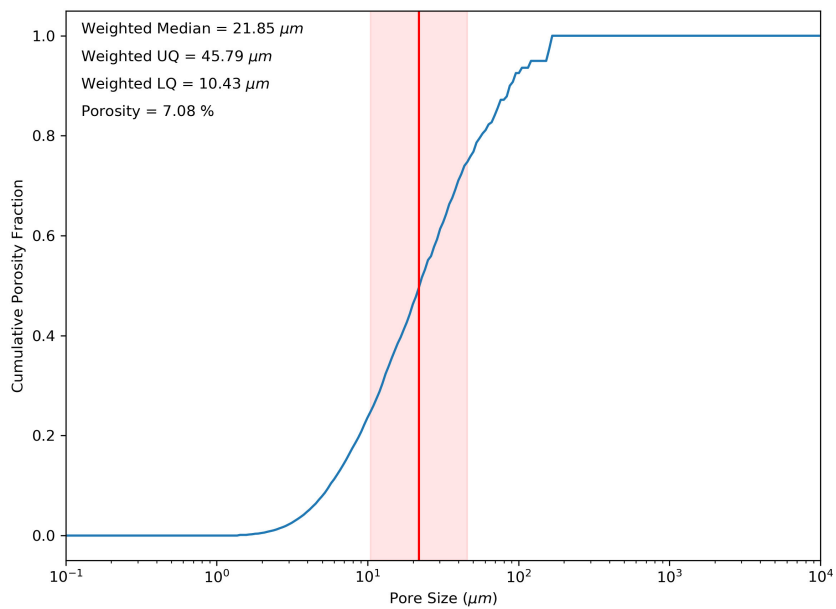


Figure D.15: Pore size-frequency distribution of 1-64-1223

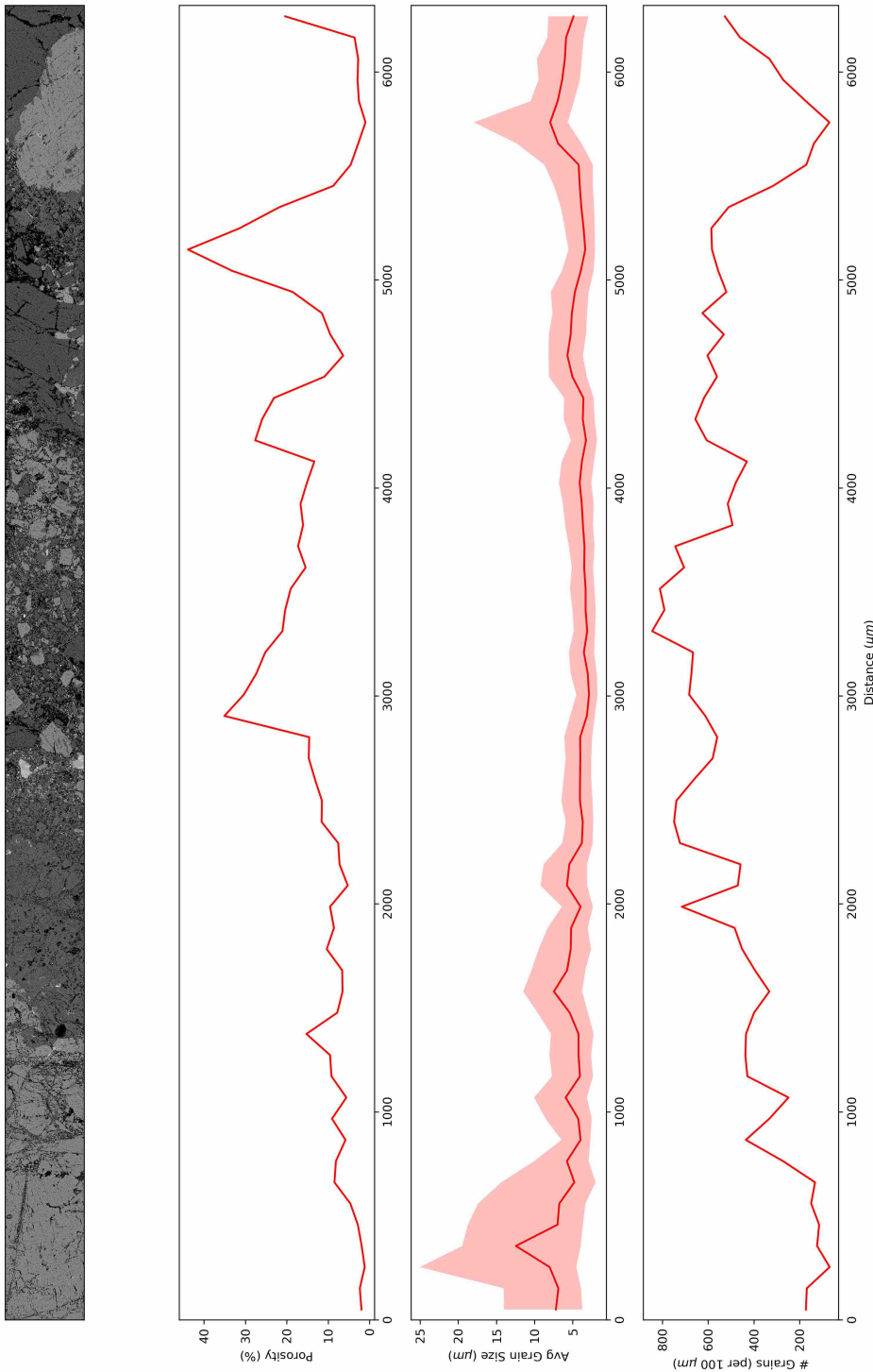


Figure D.16: Transect analysis of 1-64-1617

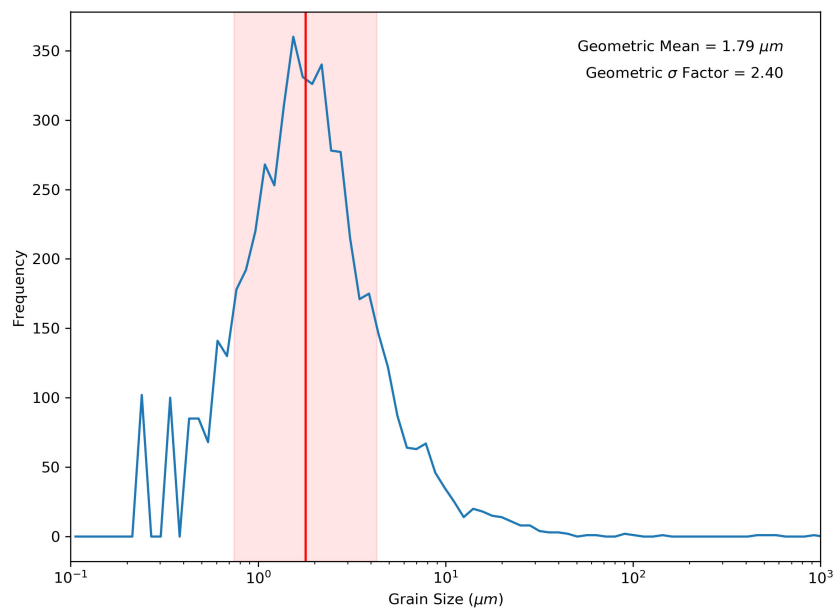


Figure D.17: Grain size-frequency distribution of 1-64-1617

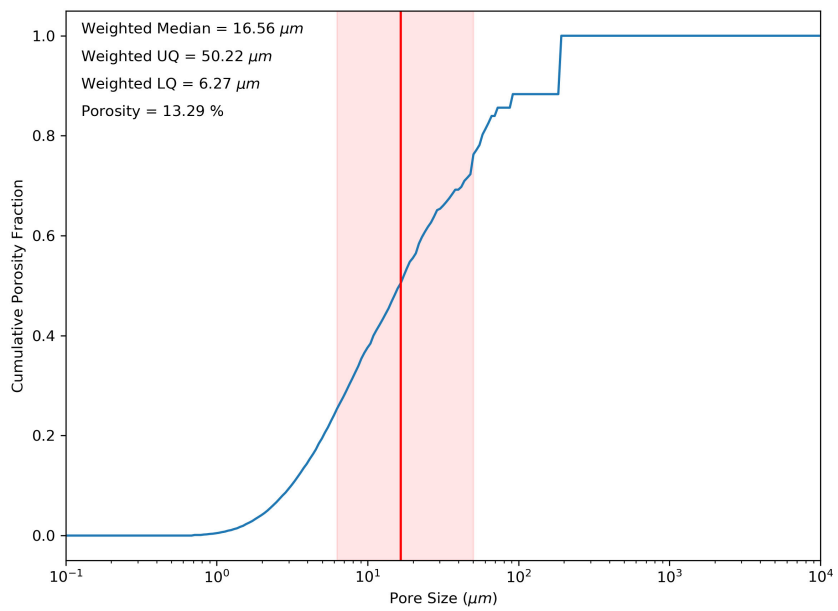


Figure D.18: Pore size-frequency distribution of 1-64-1617

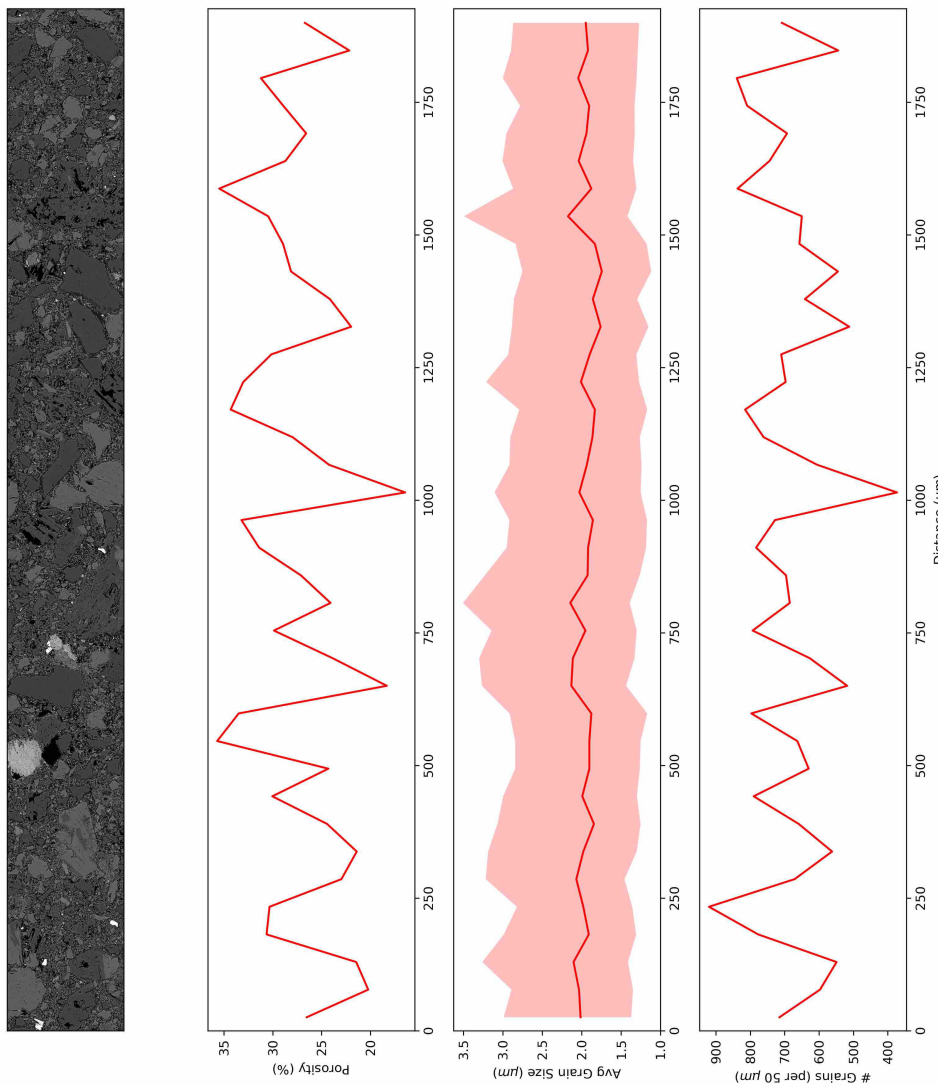


Figure D.19: Transect analysis of 1-64-2140

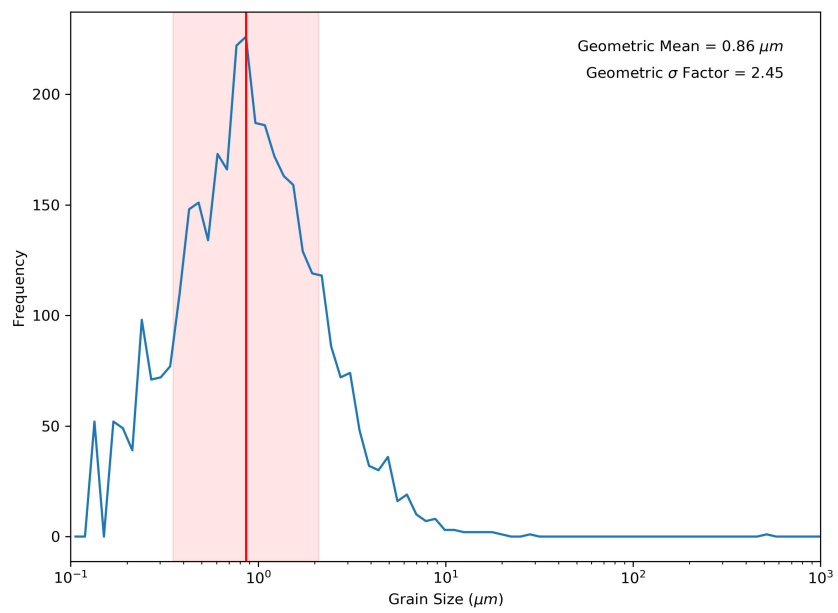


Figure D.20: Grain size-frequency distribution of 1-64-2140

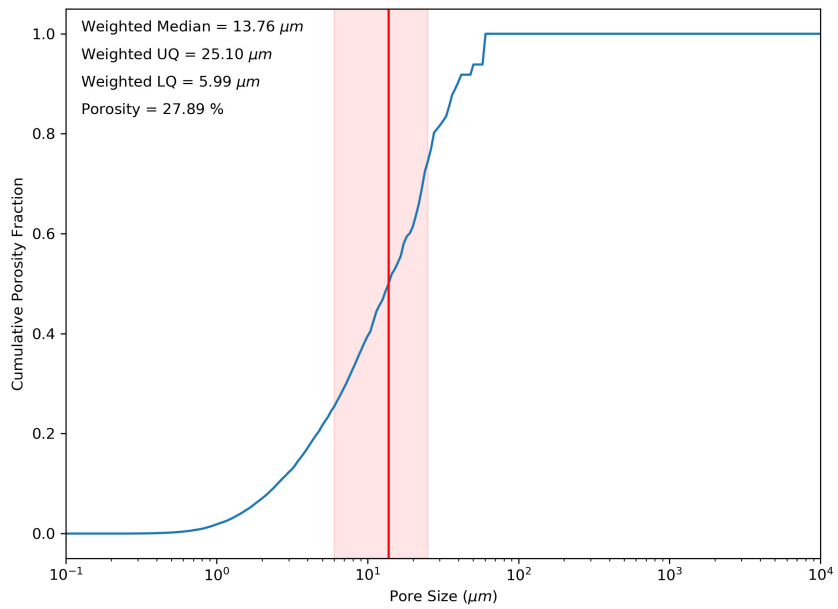


Figure D.21: Pore size-frequency distribution of 1-64-2140

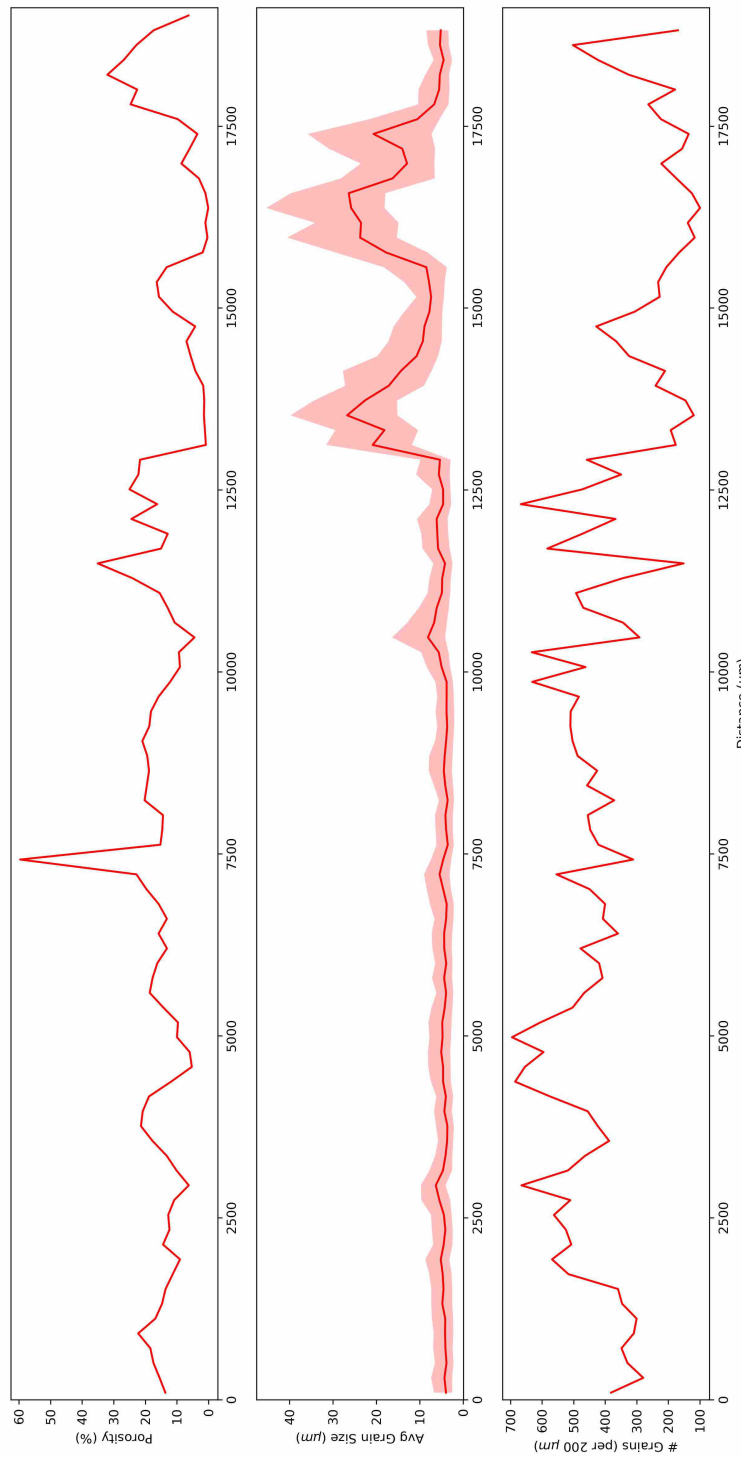
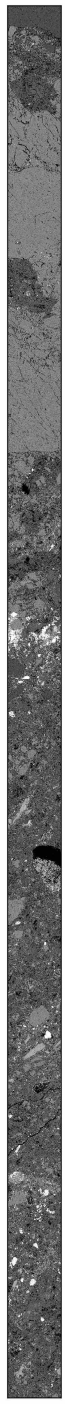


Figure D.22: Transect analysis of 1-64-2206a

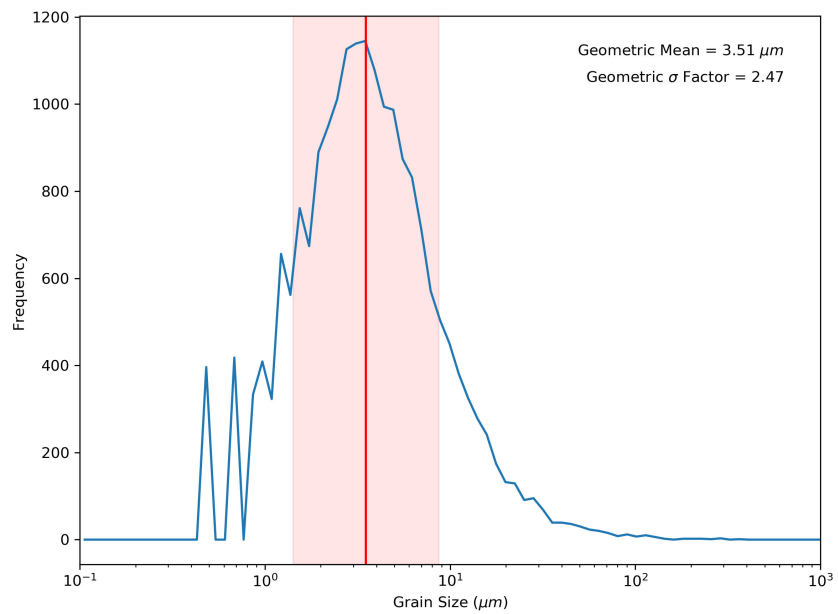


Figure D.23: Grain size-frequency distribution of 1-64-2206a

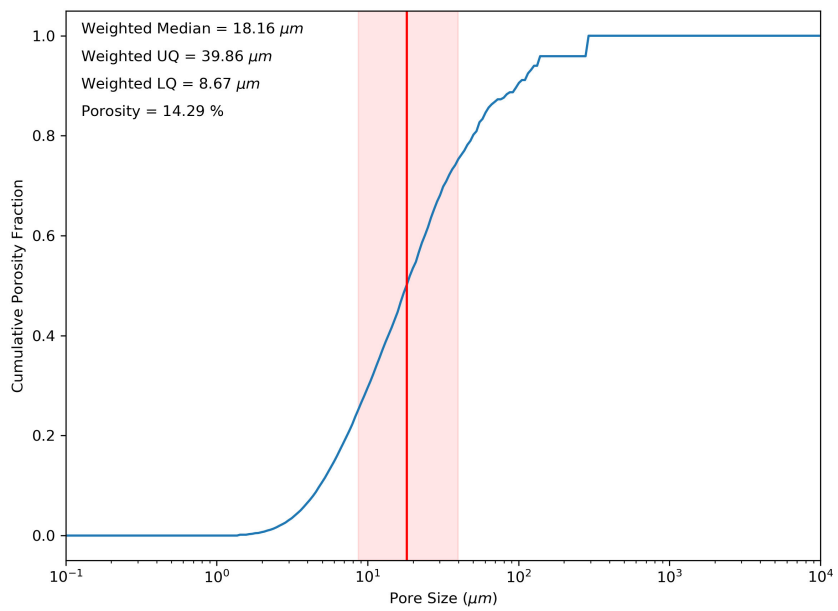


Figure D.24: Pore size-frequency distribution of 1-64-2206a

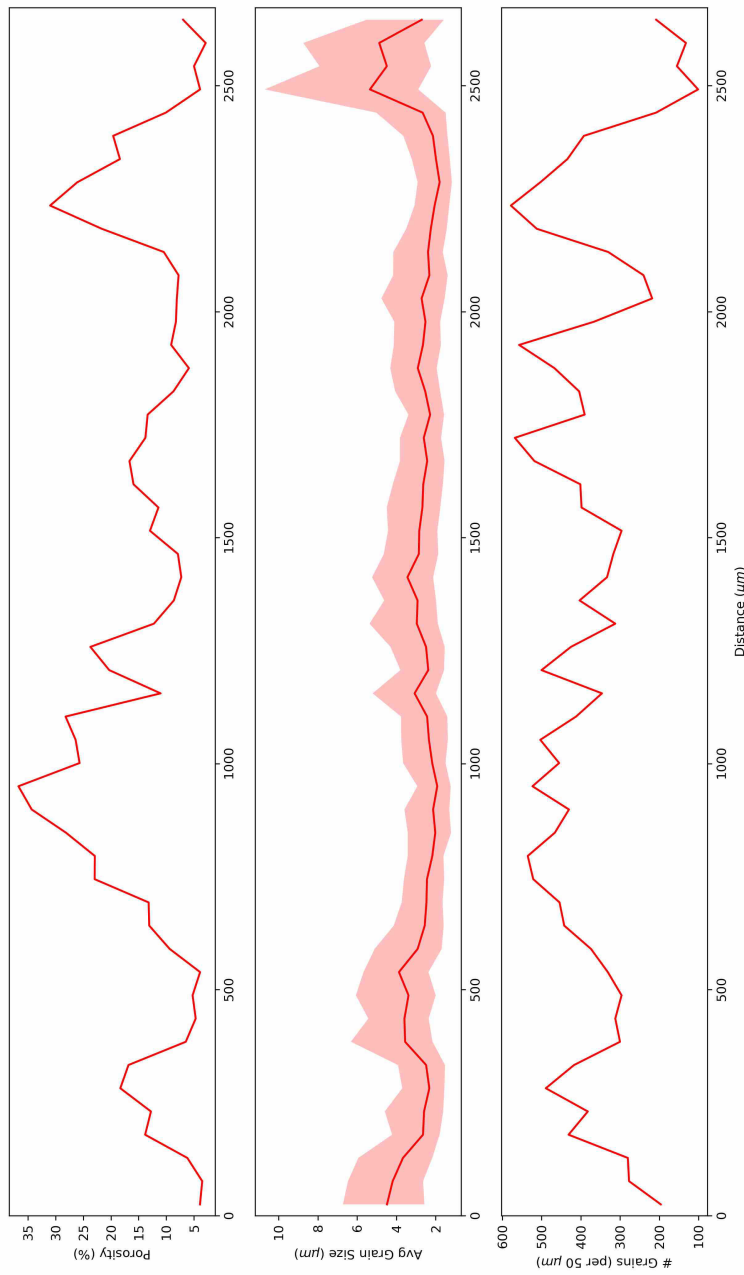
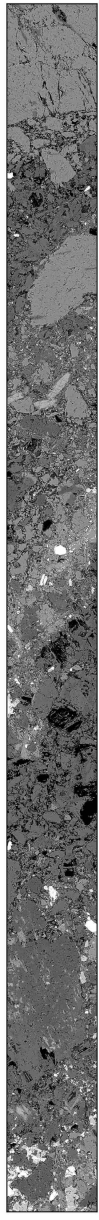


Figure D.25: Transect analysis of 1-64-2206b

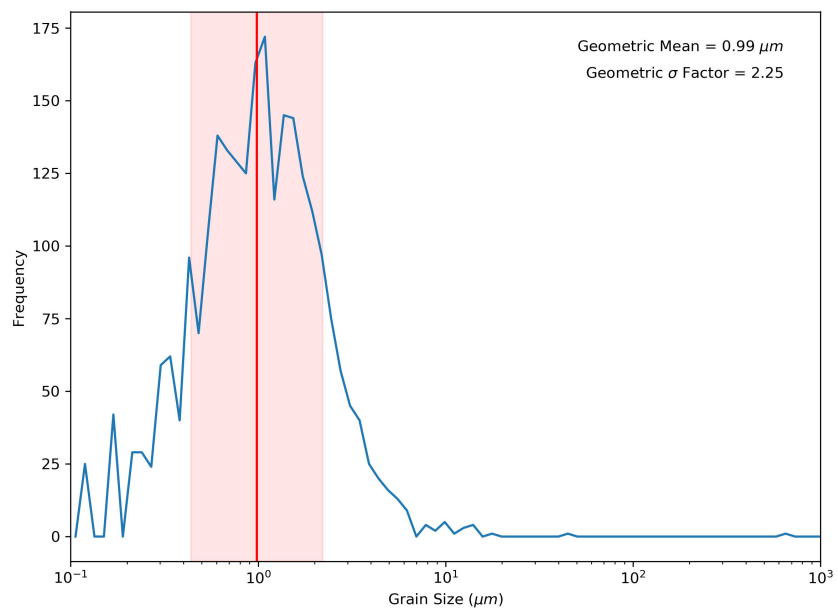


Figure D.26: Grain size-frequency distribution of 1-64-2206b

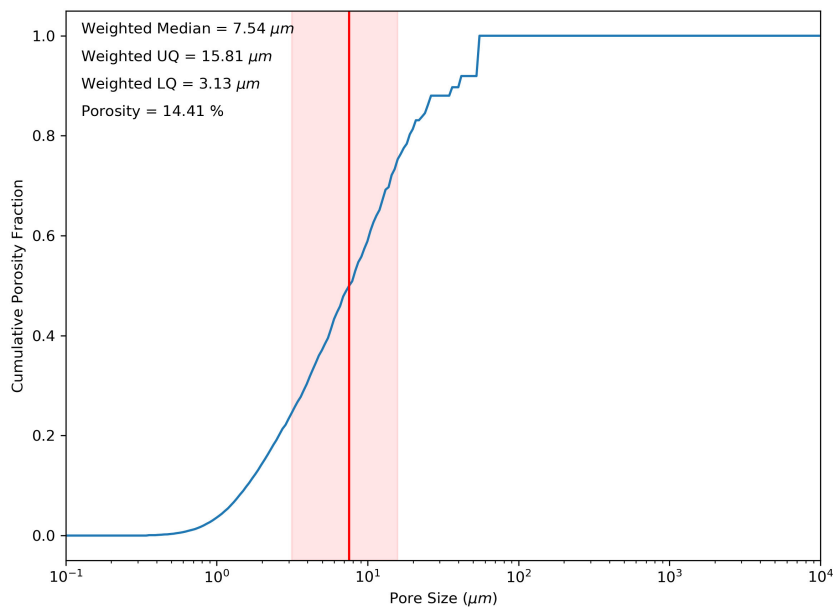


Figure D.27: Pore size-frequency distribution of 1-64-2206b

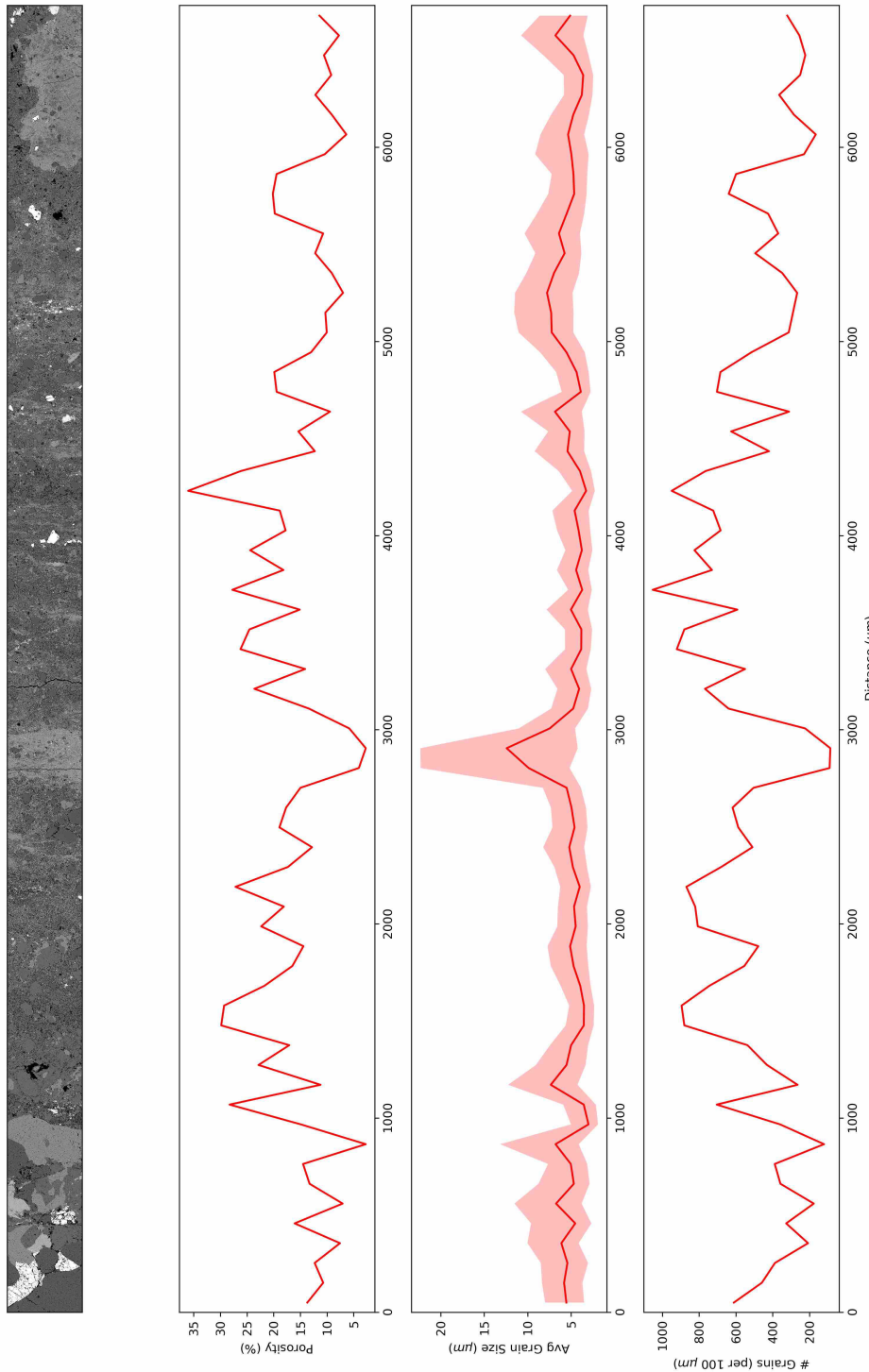


Figure D.28: Transect analysis of 1-64-2763a

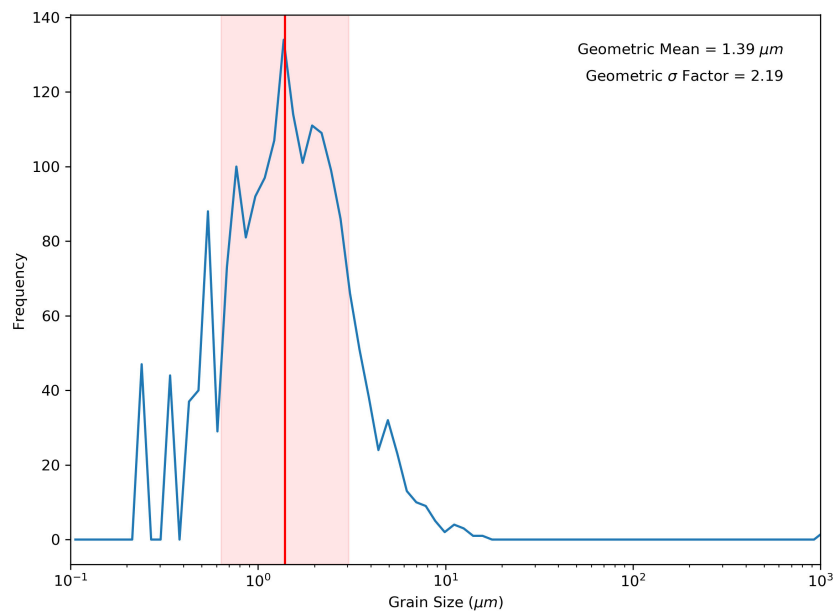


Figure D.29: Grain size-frequency distribution of 1-64-2763a

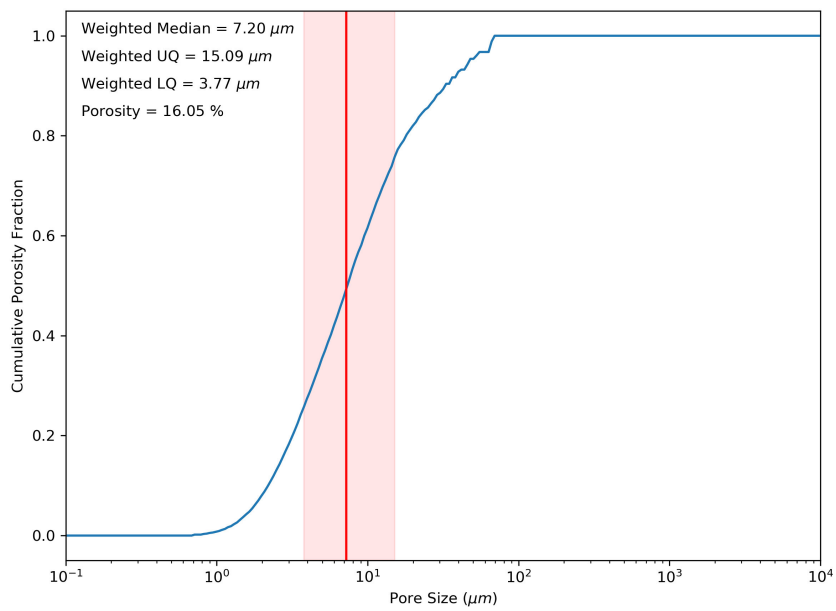


Figure D.30: Pore size-frequency distribution of 1-64-2763a

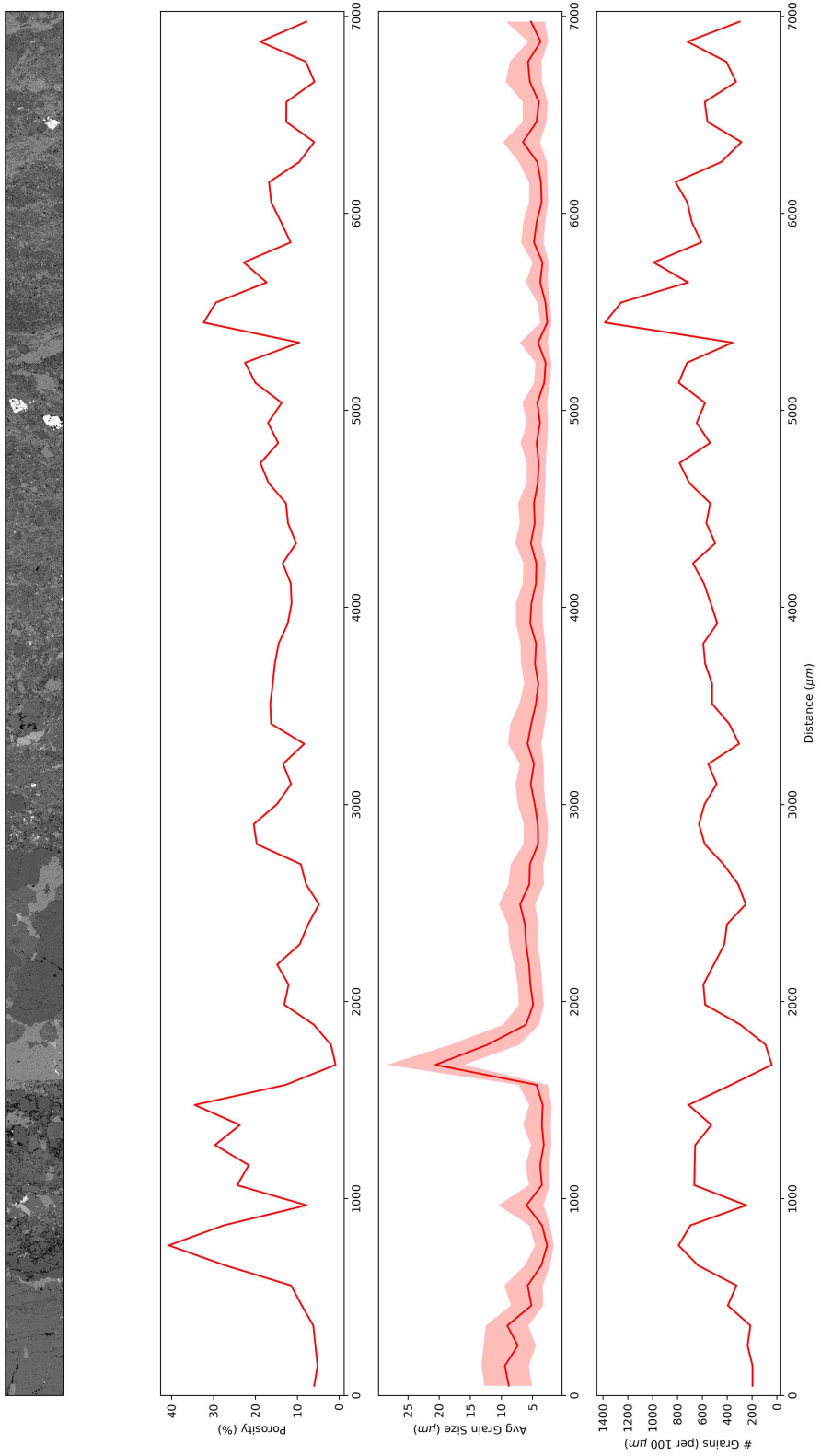


Figure D.31: Transect analysis of 1-64-2763b

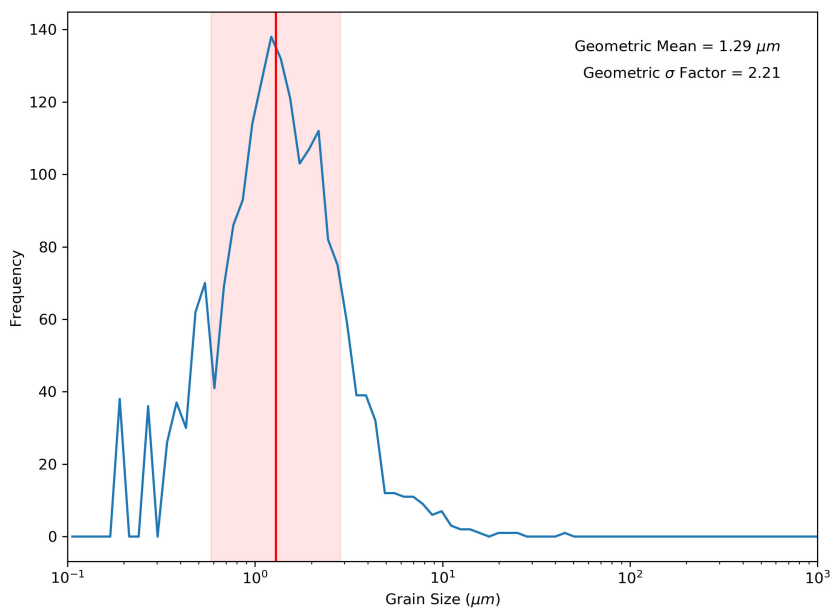


Figure D.32: Grain size-frequency distribution of 1-64-2763b

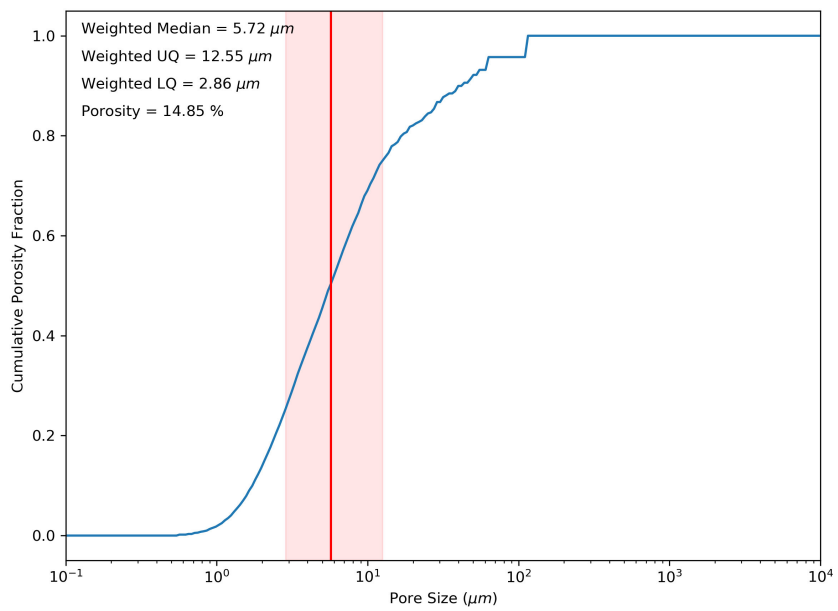


Figure D.33: Pore size-frequency distribution of 1-64-2763b

D.2 Chicxulub

In this section of the appendix, BSE maps, pore-size frequency distributions, and pore orientation distributions in samples from Hole M0077A are provided (Chapter 9). The methods by which images were acquired and processed are described in Chapters 3 and 9. A list of the samples imaged and analysed in this manner can be found in Table 9.1.

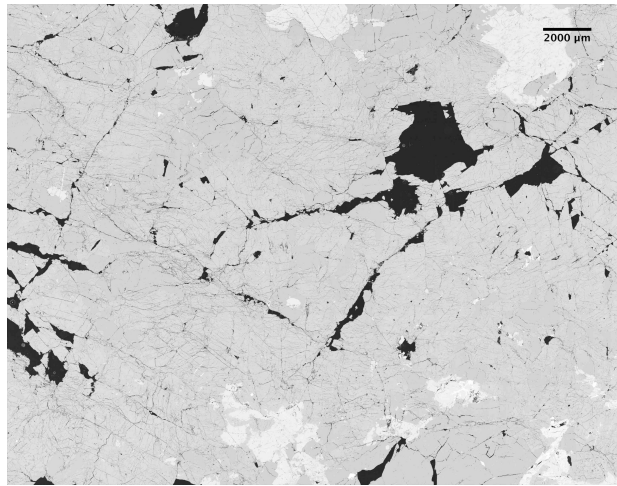


Figure D.34: Stitched BSE image of Sample 364-77-A-95-R-3-27-29.

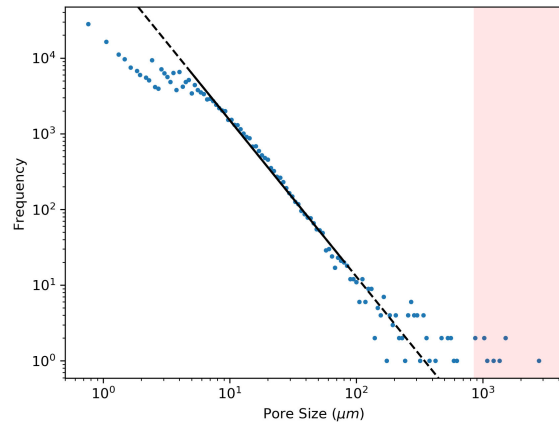


Figure D.35: Pore size-frequency distribution of Sample 364-77-A-95-R-3-27-29.

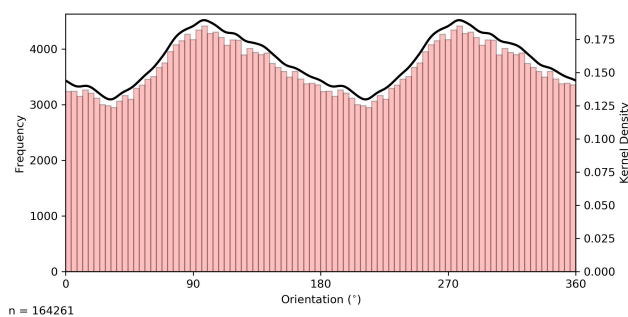


Figure D.36: Pore orientation distribution of Sample 364-77-A-95-R-3-27-29.

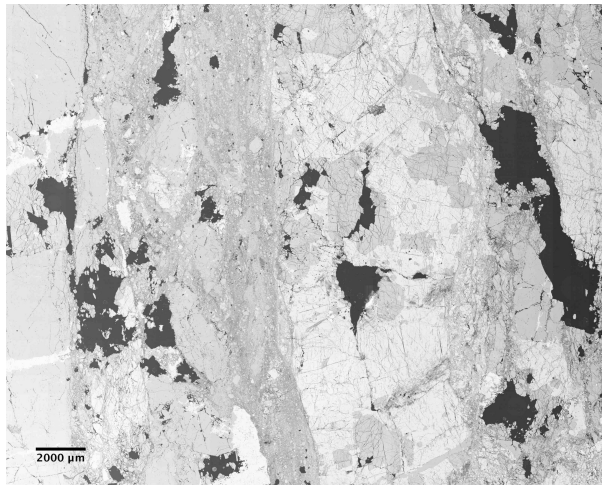


Figure D.37: Stitched BSE image of Sample 364-77-A-104-R-1-24-26.

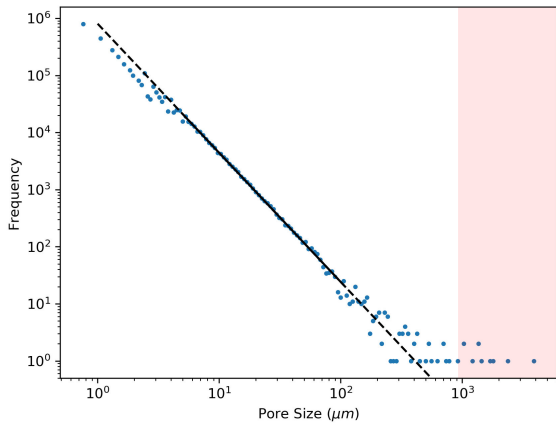


Figure D.38: Pore size-frequency distribution of Sample 364-77-A-104-R-1-24-26.

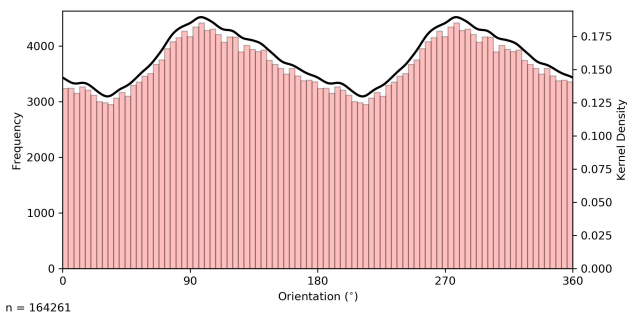


Figure D.39: Pore orientation distribution of Sample 364-77-A-104-R-1-24-26.

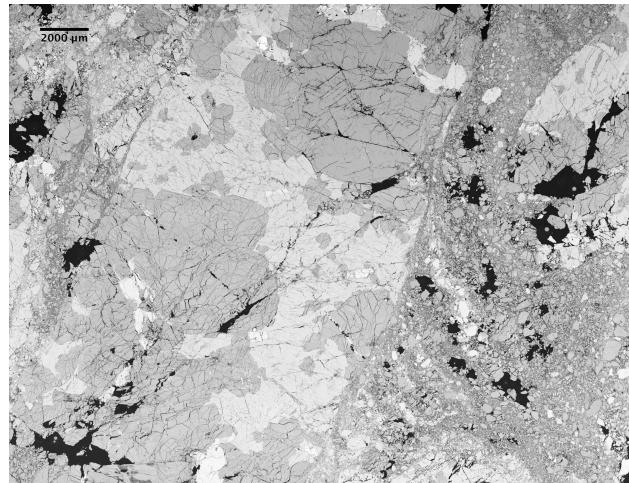


Figure D.40: Stitched BSE image of Sample 364-77-A-121-R-1-75-77.

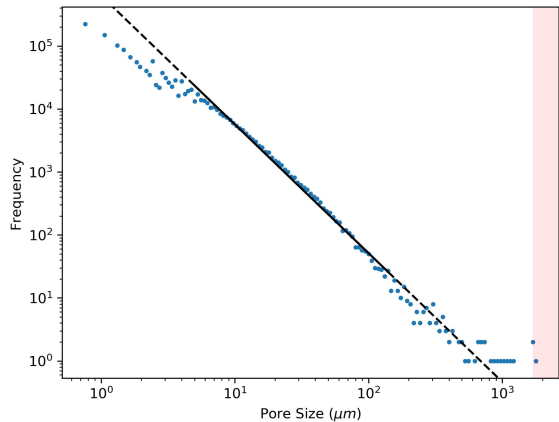


Figure D.41: Pore size-frequency distribution of Sample 364-77-A-121-R-1-75-77.

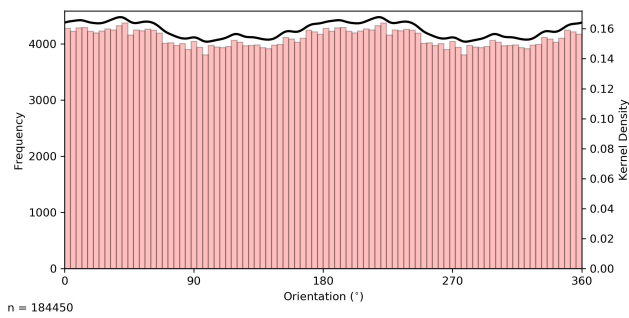


Figure D.42: Pore orientation distribution of Sample 364-77-A-121-R-1-75-77.

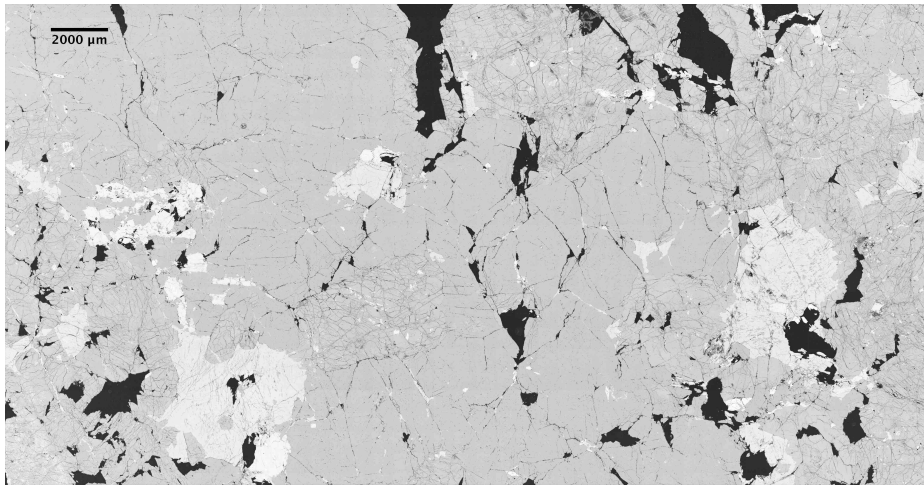


Figure D.43: Stitched BSE image of Sample 364-77-A-132-R-1-22-24.

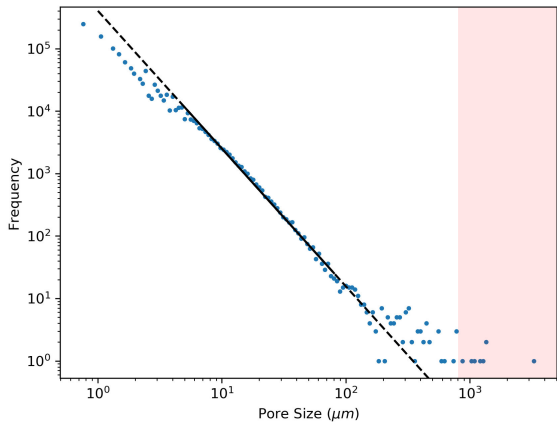


Figure D.44: Pore size-frequency distribution of Sample 364-77-A-132-R-1-22-24.

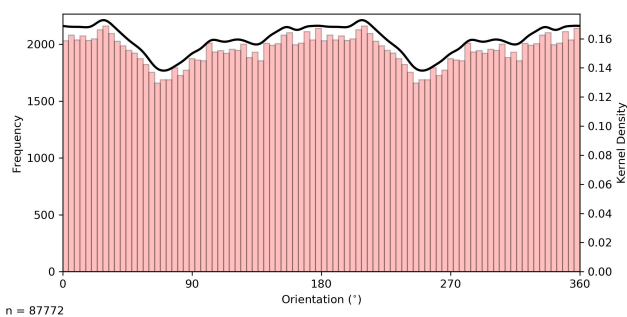


Figure D.45: Pore orientation distribution of Sample 364-77-A-132-R-1-22-24.

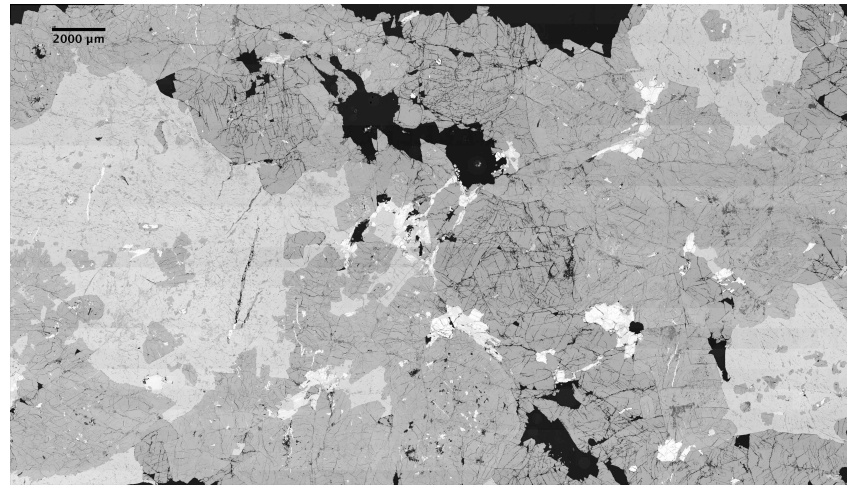


Figure D.46: Stitched BSE image of Sample 364-77-A-150-R-1-53-55.

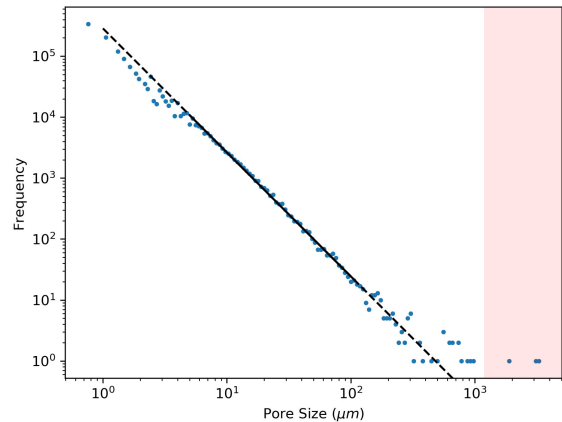


Figure D.47: Pore size-frequency distribution of Sample 364-77-A-150-R-1-53-55.

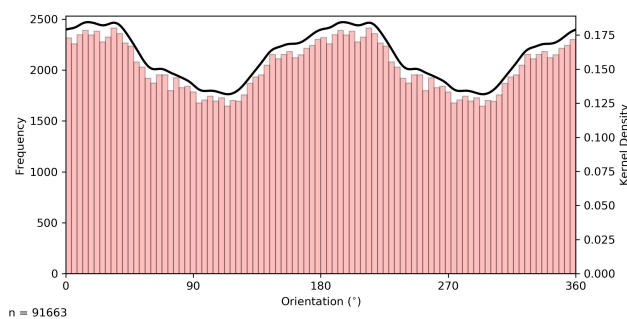


Figure D.48: Pore orientation distribution of Sample 364-77-A-150-R-1-53-55.

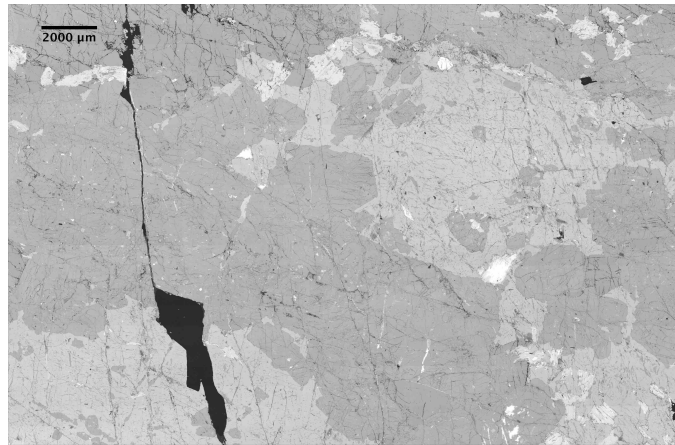


Figure D.49: Stitched BSE image of Sample 364-77-A-204-R-1-07-09.

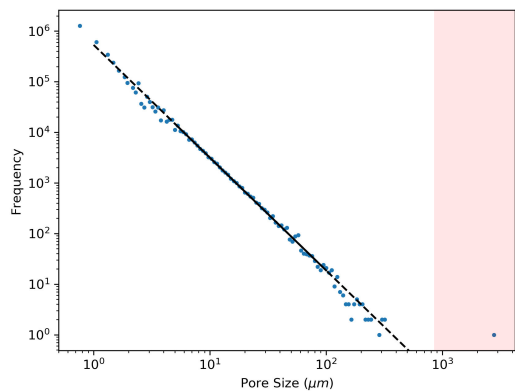


Figure D.50: Pore size-frequency distribution of Sample Pore orientation distribution of Sample 364-77-A-204-R-1-07-09.

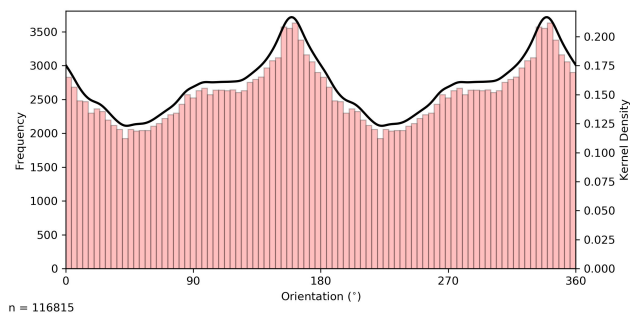


Figure D.51: Pore orientation distribution of Sample 364-77-A-204-R-1-07-09.

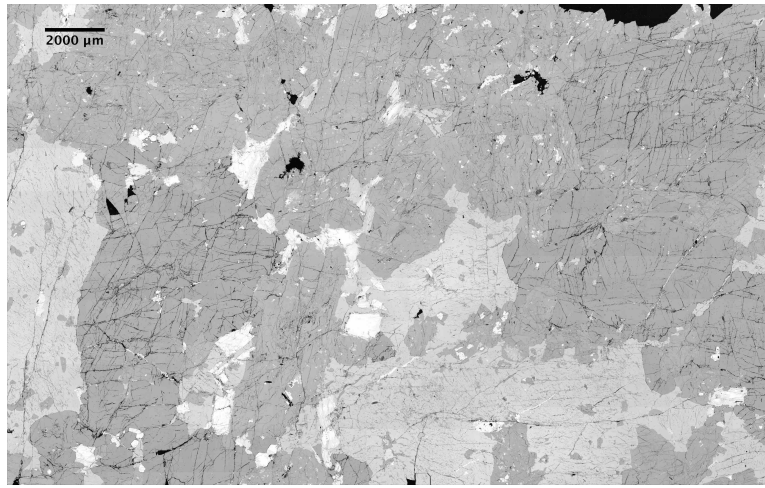


Figure D.52: Stitched BSE image of Sample 364-77-A-219-R-1-22-24.

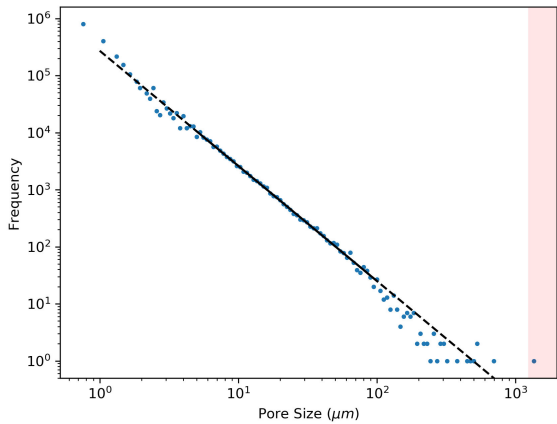


Figure D.53: Pore size-frequency distribution of Sample 364-77-A-219-R-1-22-24.

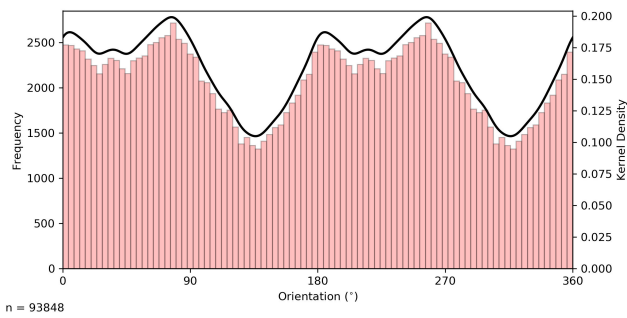


Figure D.54: Pore orientation distribution of Sample 364-77-A-219-R-1-22-24.

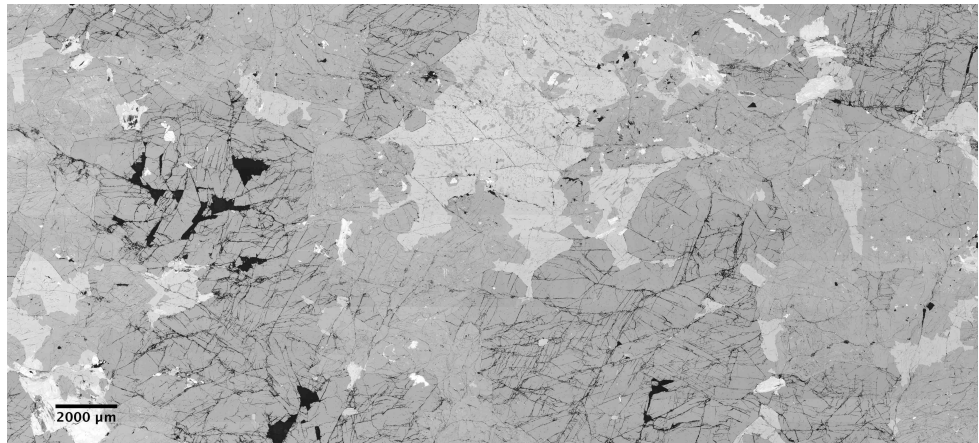


Figure D.55: Stitched BSE image of Sample 364-77-A-250-R-1-41-43.

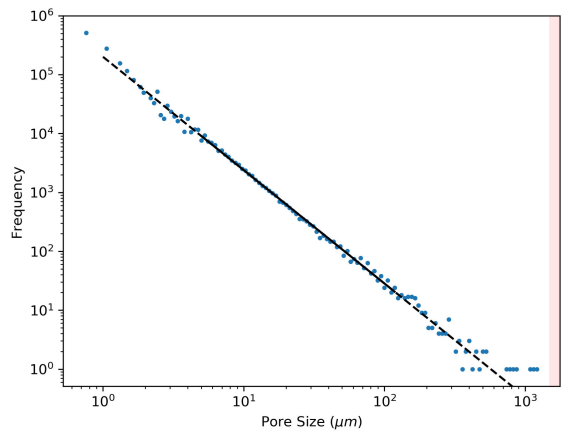


Figure D.56: Pore size-frequency distribution of Sample 364-77-A-250-R-1-41-43.

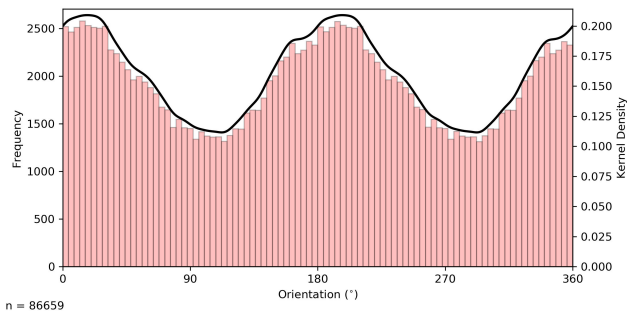


Figure D.57: Pore orientation distribution of Sample 364-77-A-250-R-1-41-43.

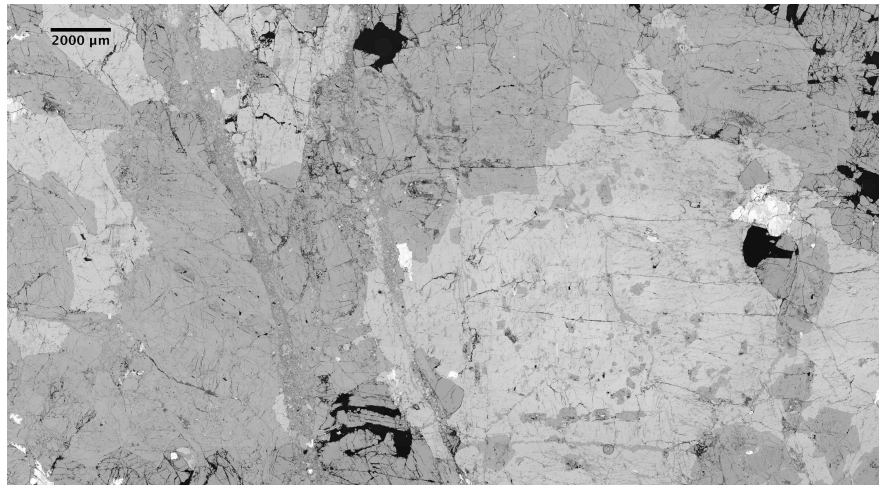


Figure D.58: Stitched BSE image of Sample 364-77-A-276-R-1-17-19.

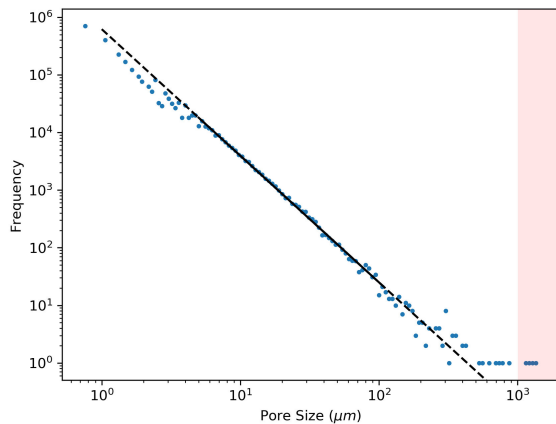


Figure D.59: Pore size-frequency distribution of Sample 364-77-A-276-R-1-17-19.

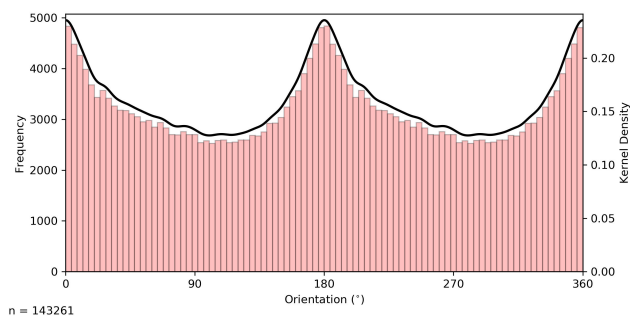


Figure D.60: Pore orientation distribution of Sample 364-77-A-276-R-1-17-19.

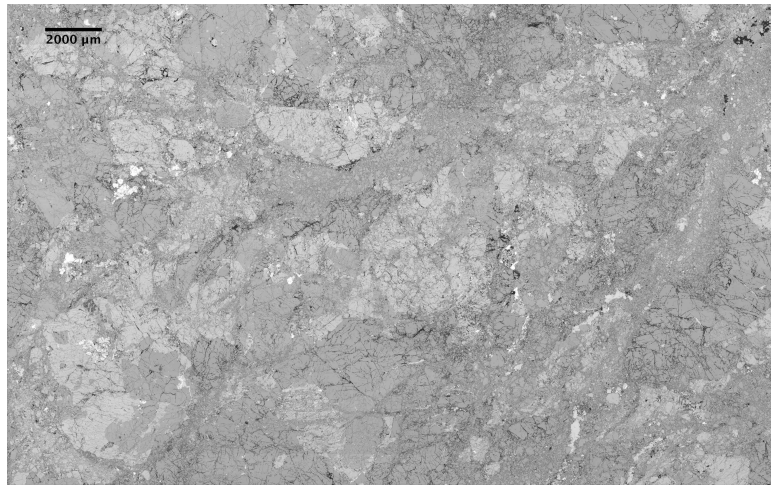


Figure D.61: Stitched BSE image of Sample 364-77-A-301-R-2-30-32.

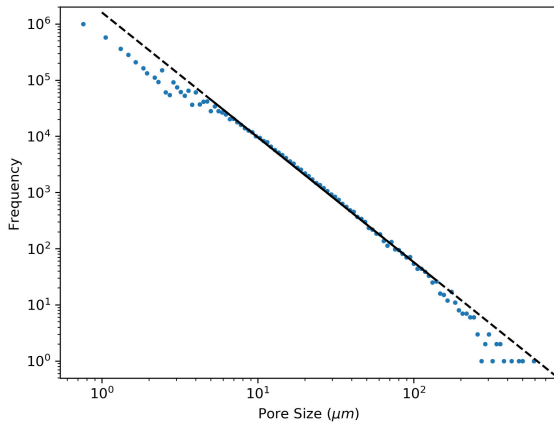


Figure D.62: Pore size-frequency distribution of Sample 364-77-A-301-R-2-30-32.

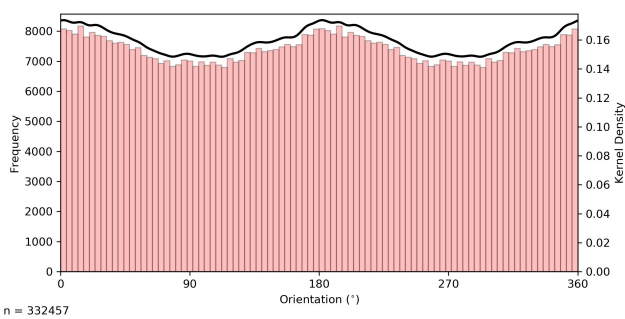


Figure D.63: Pore orientation distribution of Sample 364-77-A-301-R-2-30-32.

E Supplementary EDS Results

In this appendix, EDS analysis of deformation structures within Hole 1-64 of the East Clearwater Lake structure are presented. In particular, the results illustrate the textures and composition of 'melt veins' within the cores. The data were acquired using the methods described in Chapters 3 and 6.

543_Melt_ZoomIn

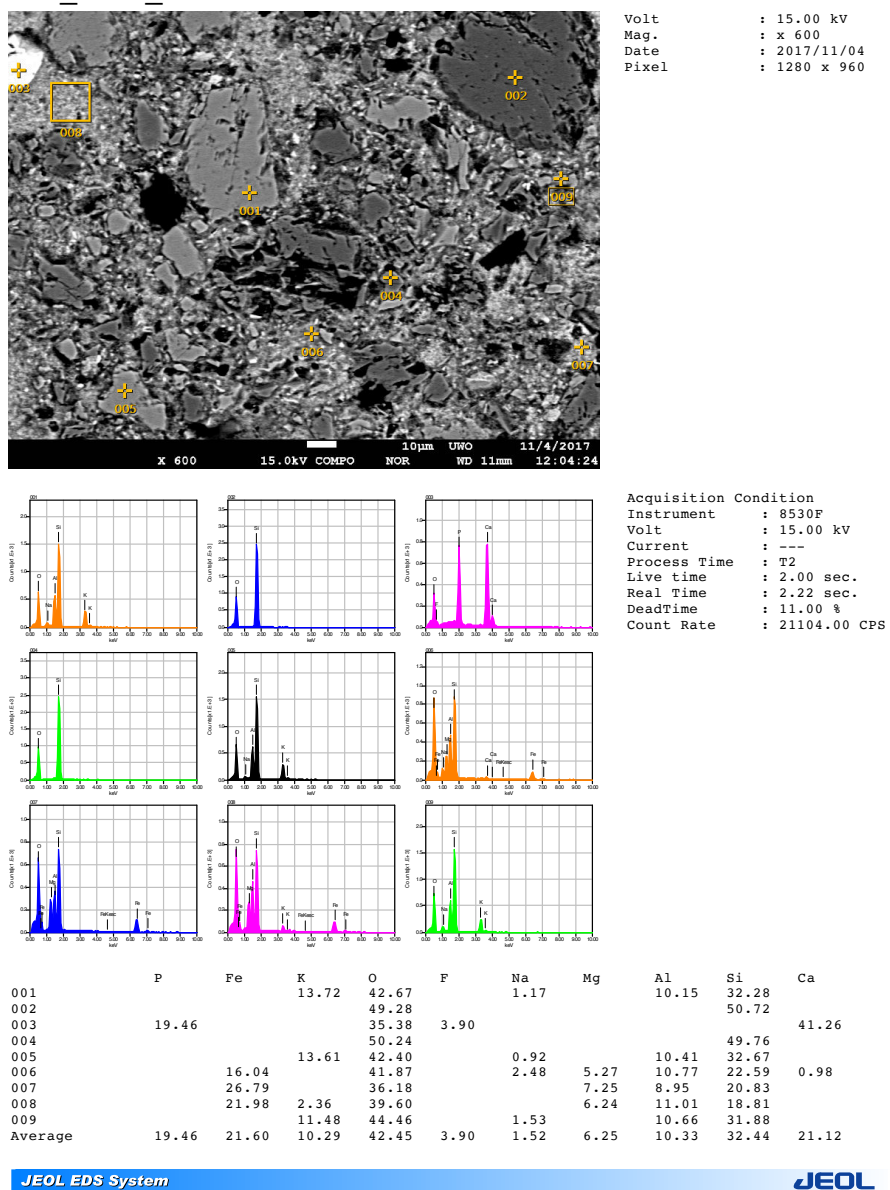


Figure E.1: EDS data from Sample 1-64-543a.

543_Melt2

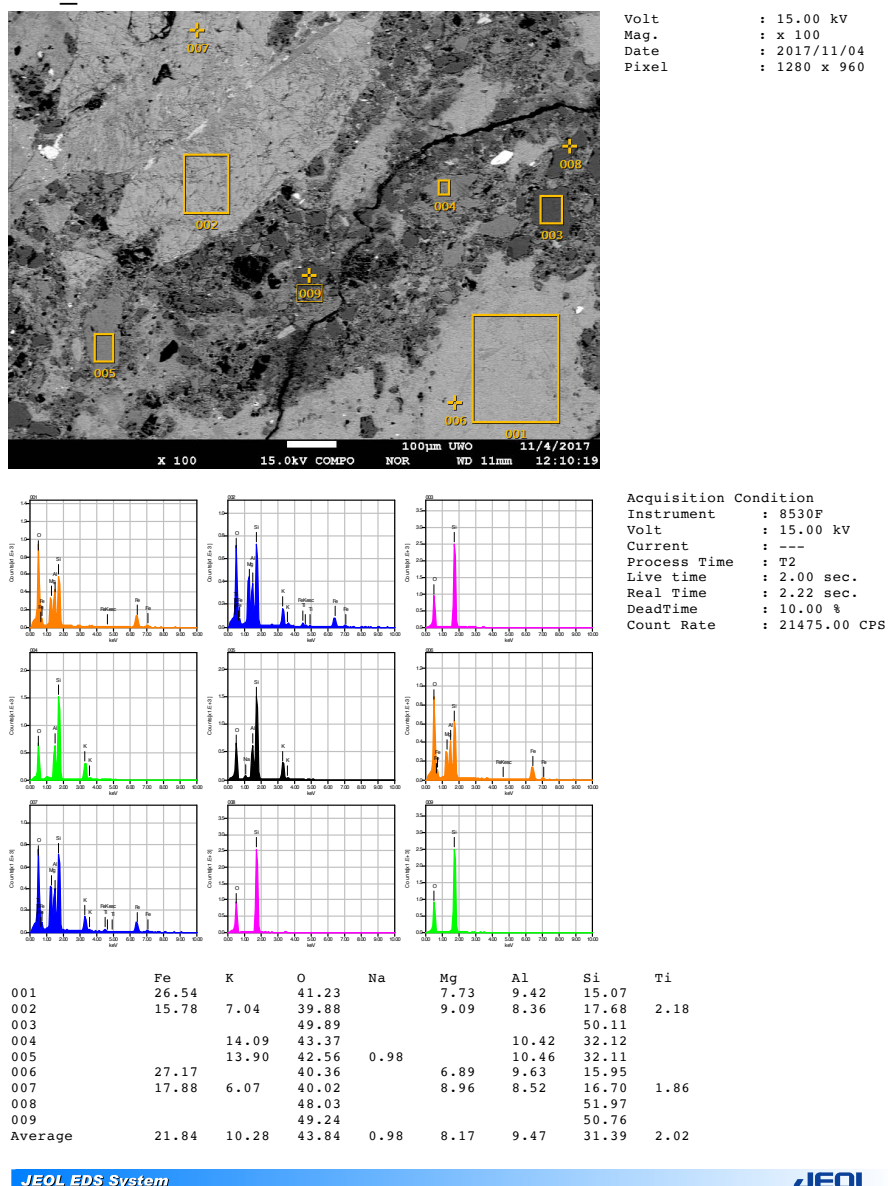


Figure E.2: EDS data from Sample 1-64-543b.

543_Melt3

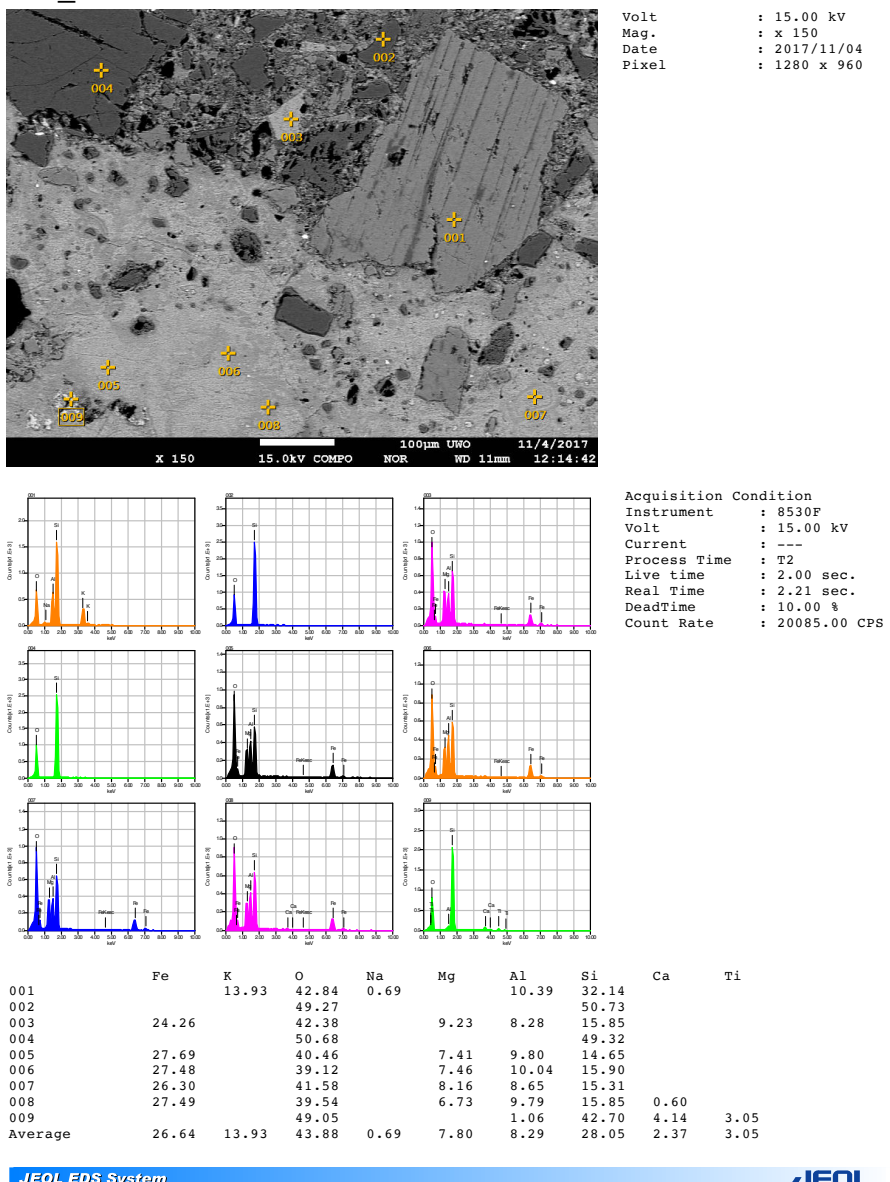


Figure E.3: EDS data from Sample 1-64-543c.

544_BrecciaMelt_Stitch3

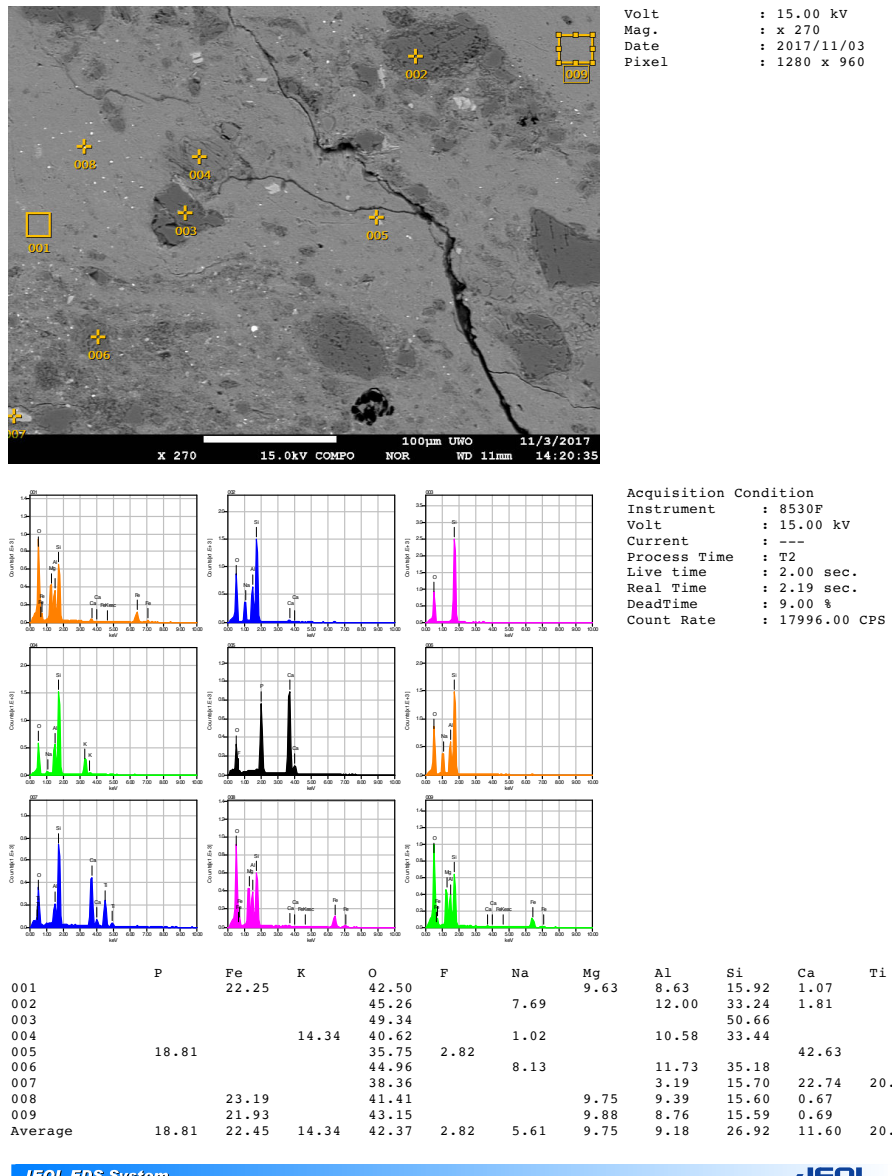


Figure E.4: EDS data from Sample 1-64-544a.

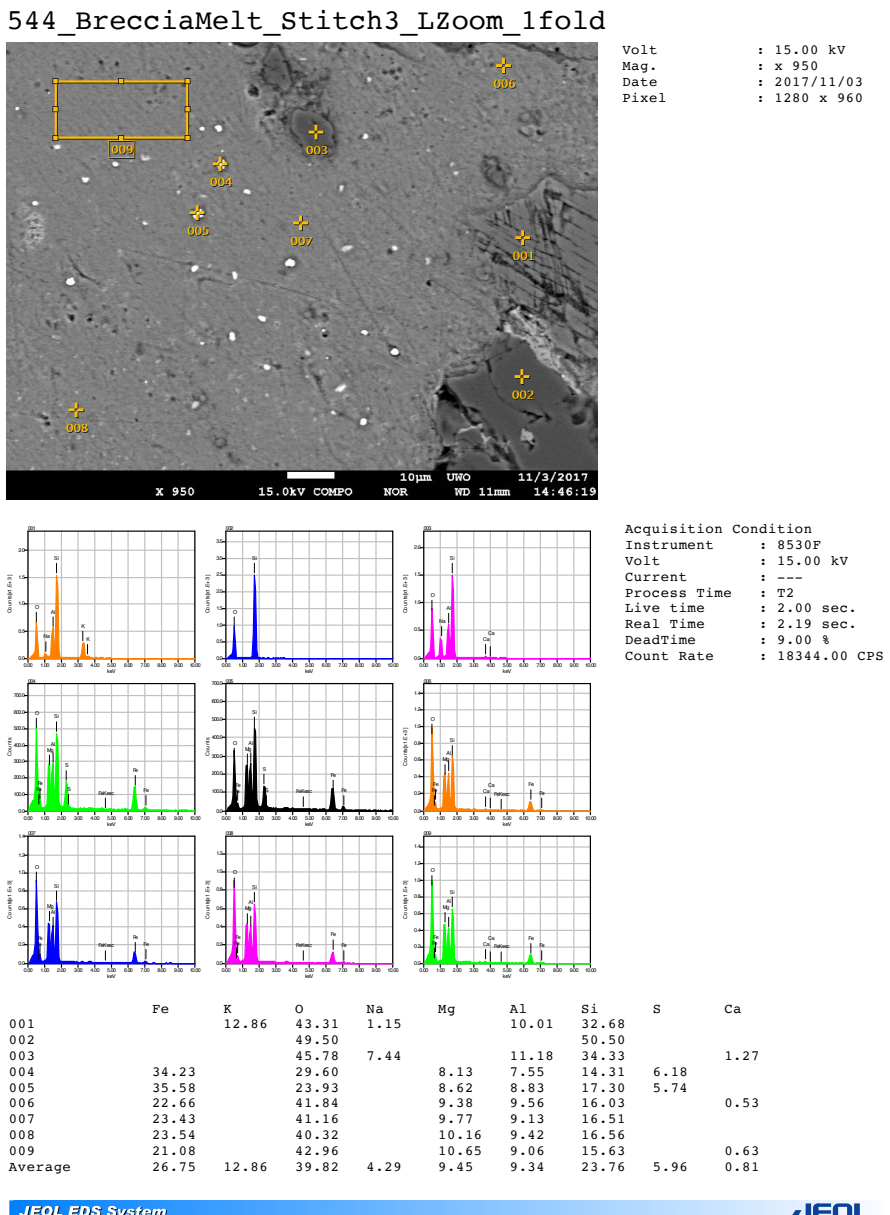


Figure E.5: EDS data from Sample 1-64-544b. Close-up of Figure E.5.

544_BrecciaMelt_Stitch5_CZoom_2fold

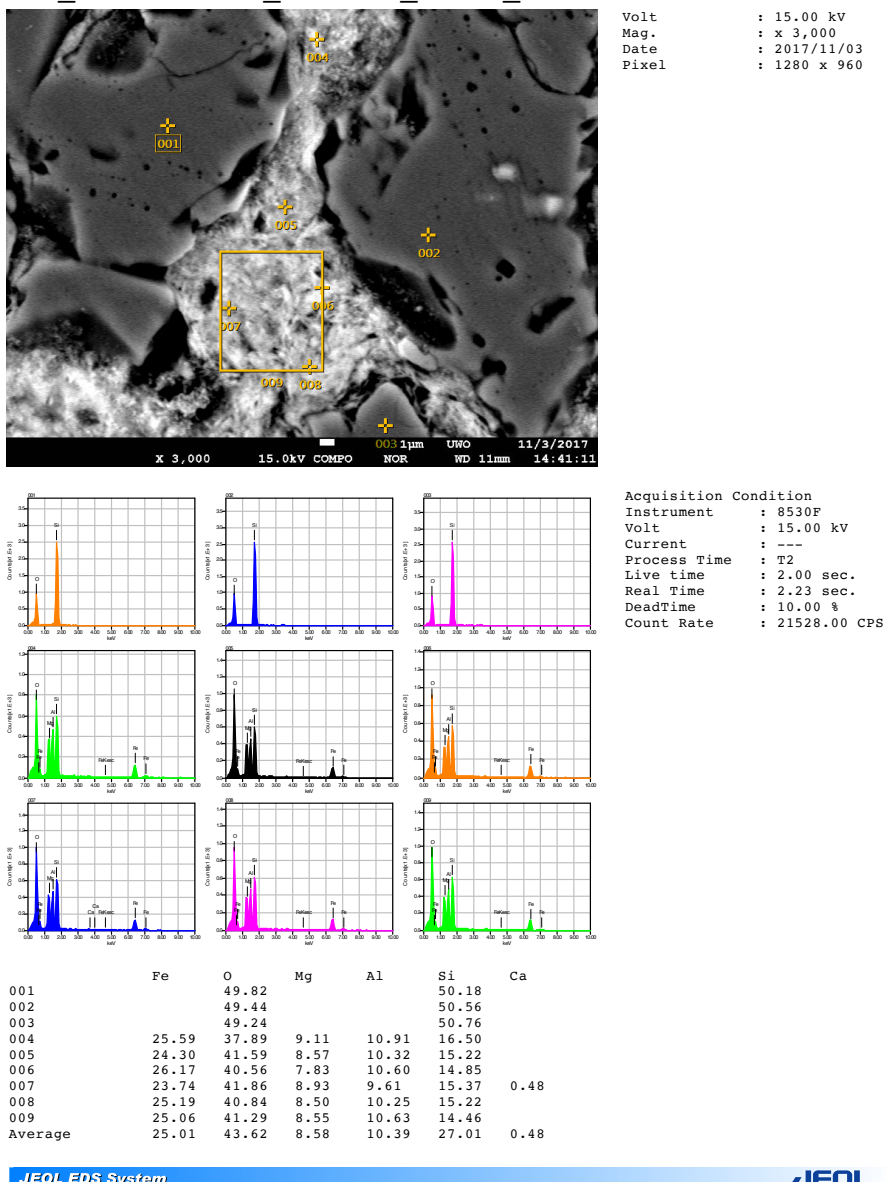


Figure E.6: EDS data from Sample 1-64-54c.

544_GraniteBrecciaContact_Stitch6

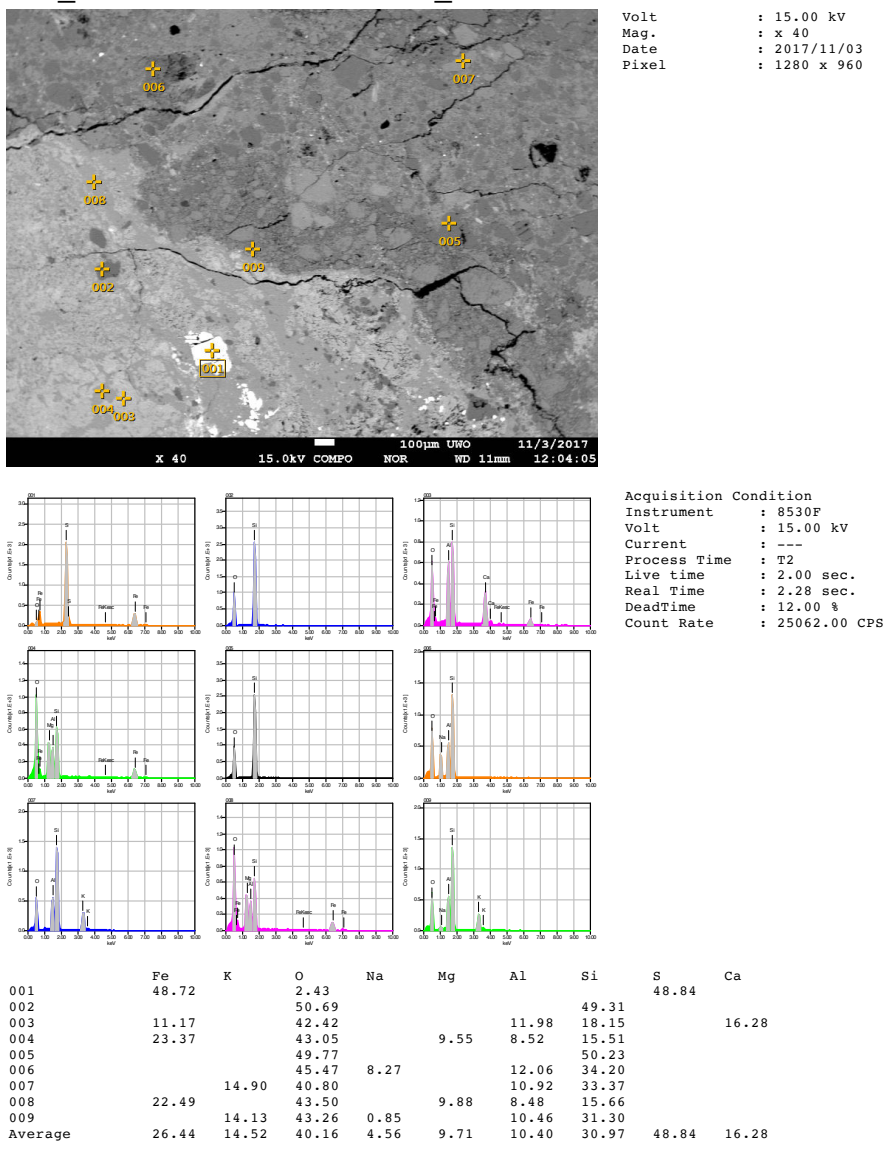


Figure E.7: EDS data from Sample 1-64-544d.

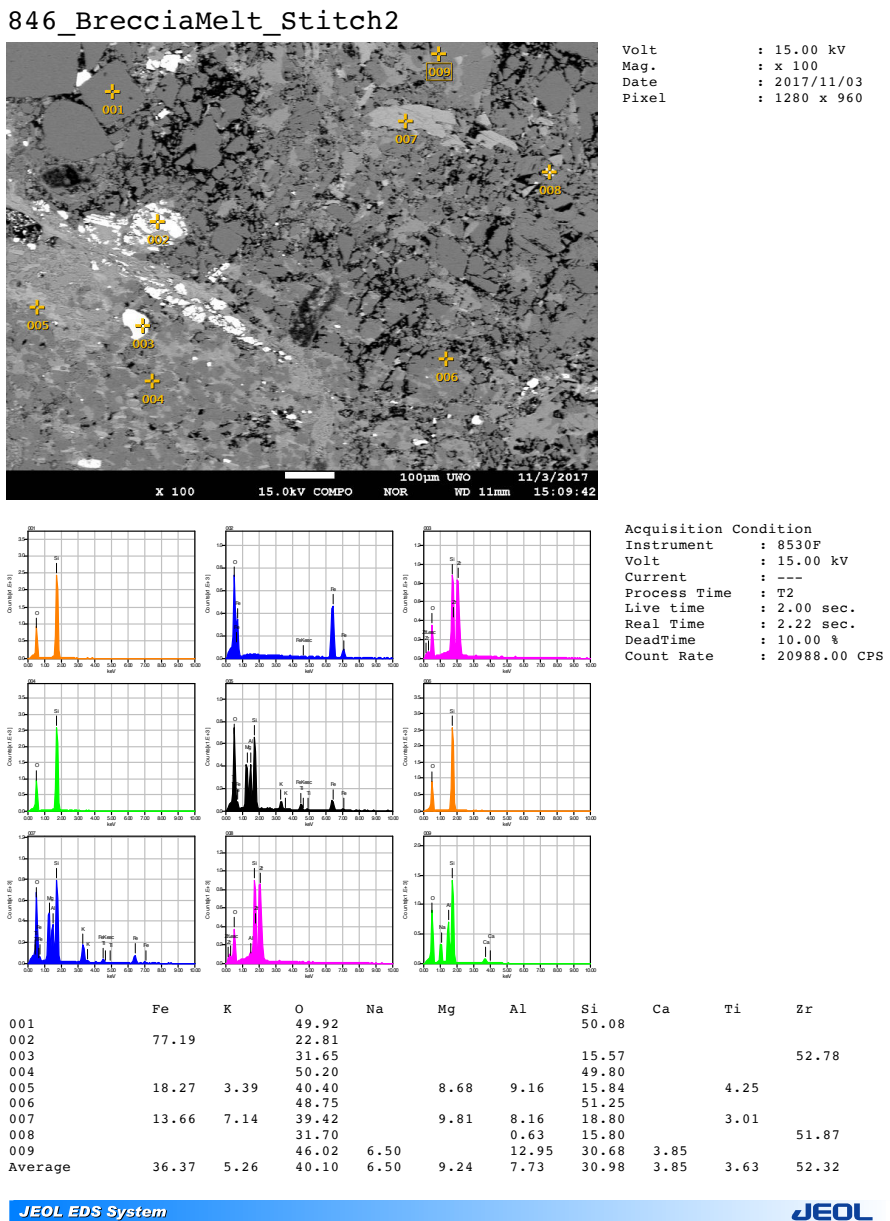


Figure E.8: EDS data from Sample 1-64-846a.

846_BrecciaMelt2_Stitch21

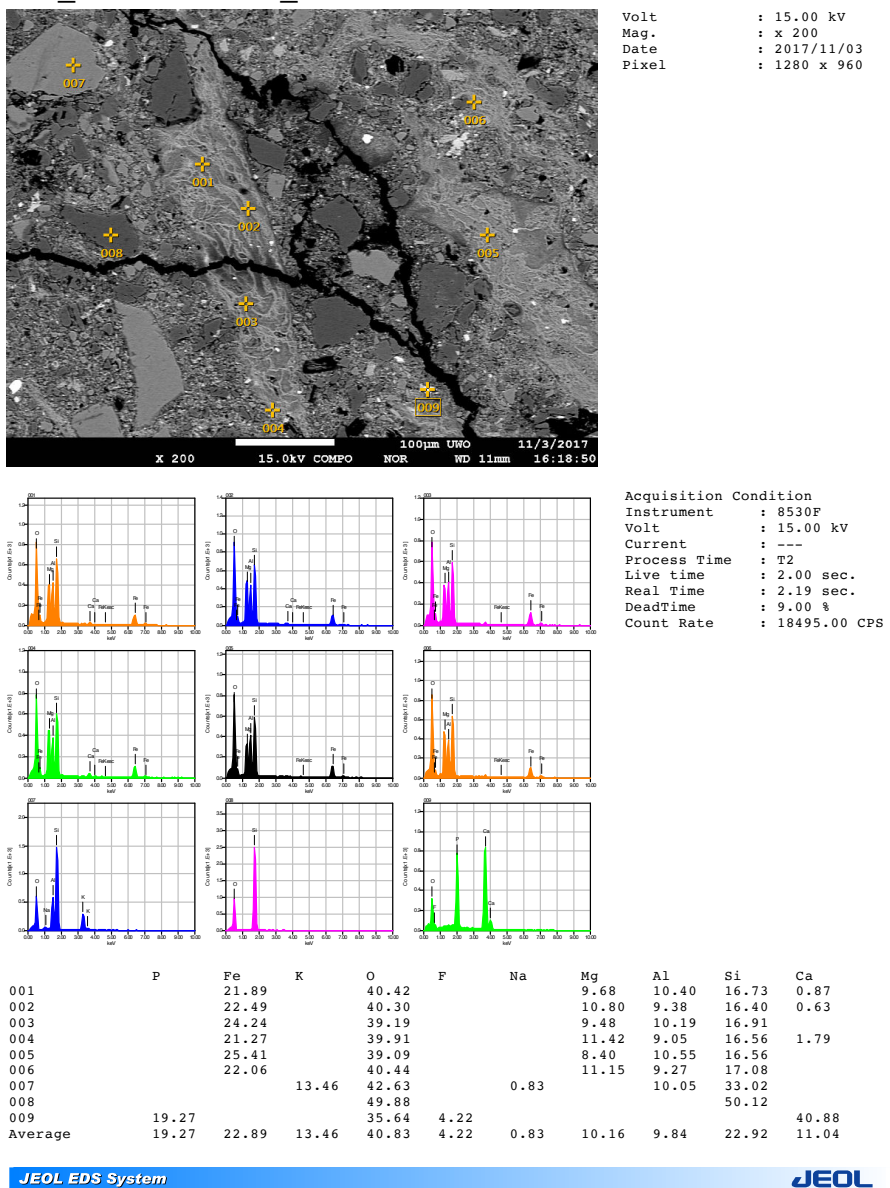
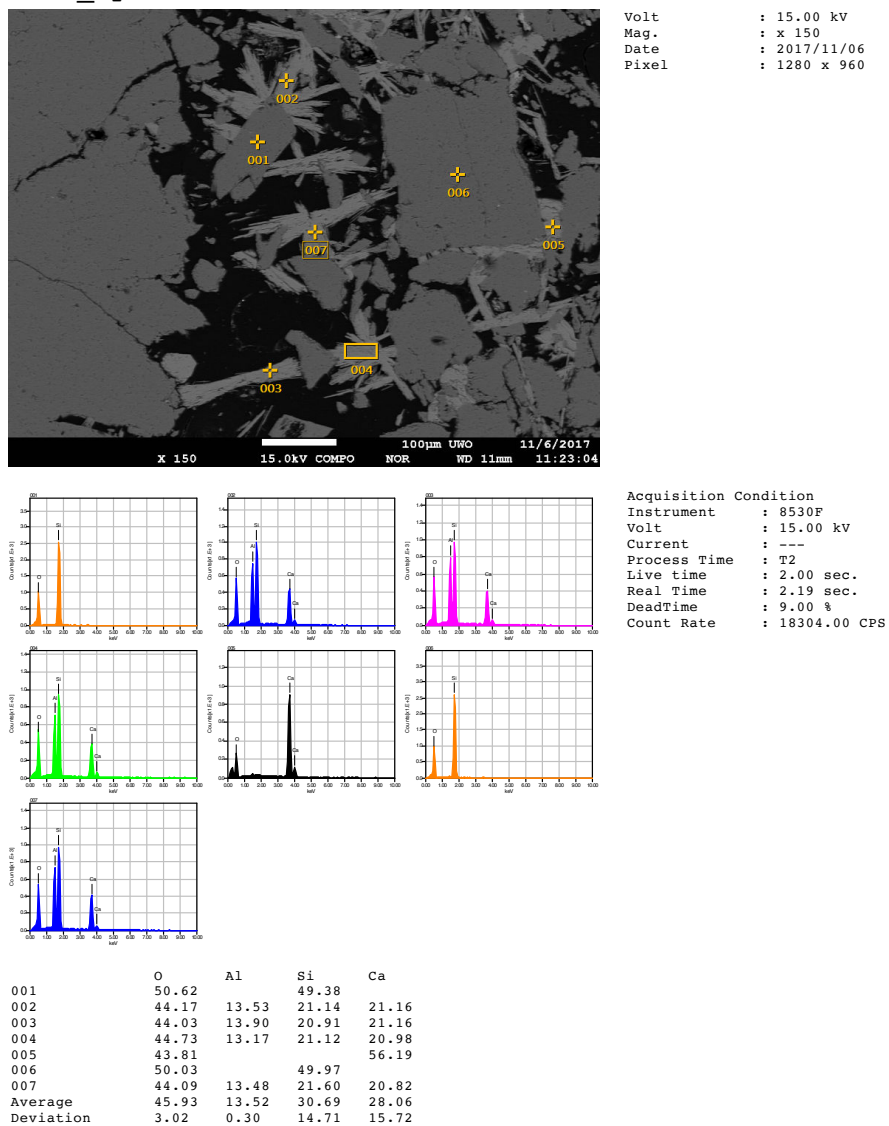


Figure E.9: EDS data from Sample 1-64-846b.

1357_Hydrothermal



JEOL EDS System

JEOL

Figure E.10: EDS data from Sample 1-64-1357.

1617_SrSO₃

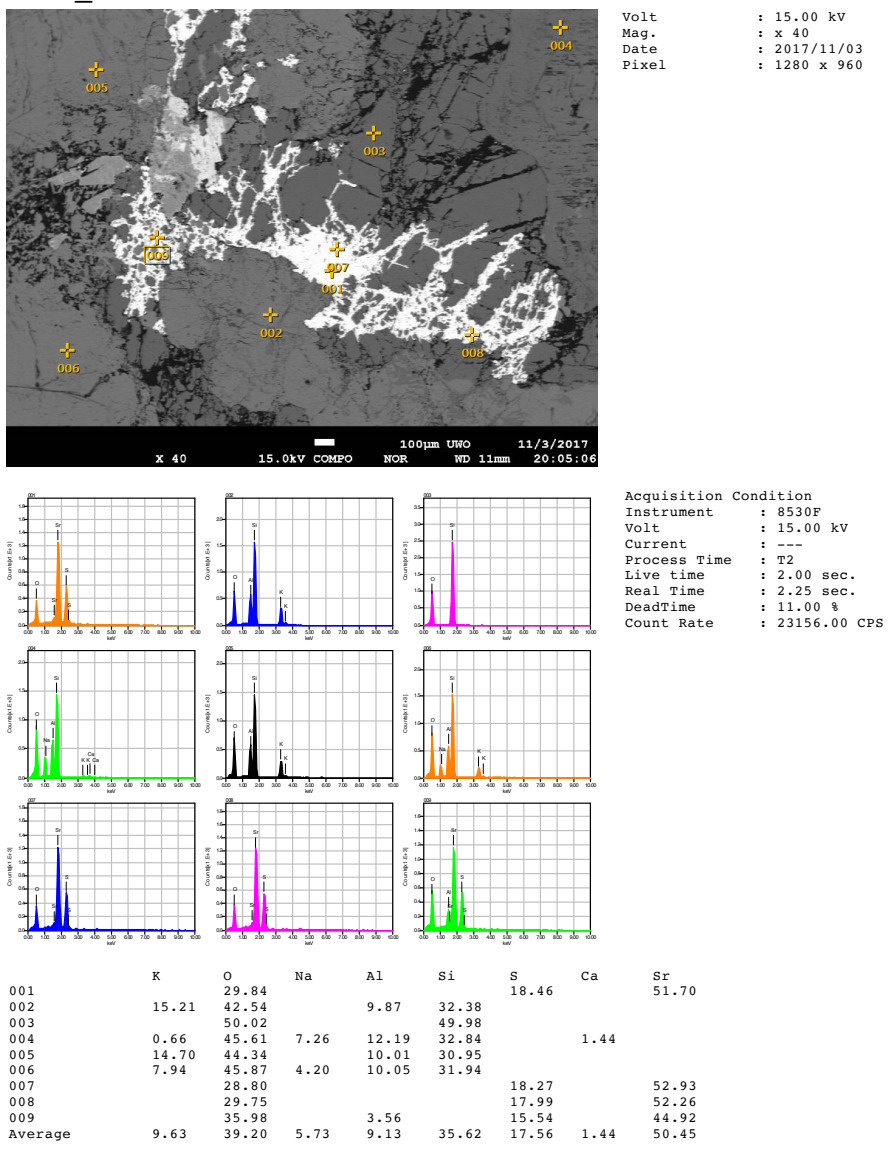


Figure E.11: EDS data from Sample 1-64-1617.

2763_Cataclasite2_Stitch16_CZoomIn_2fold

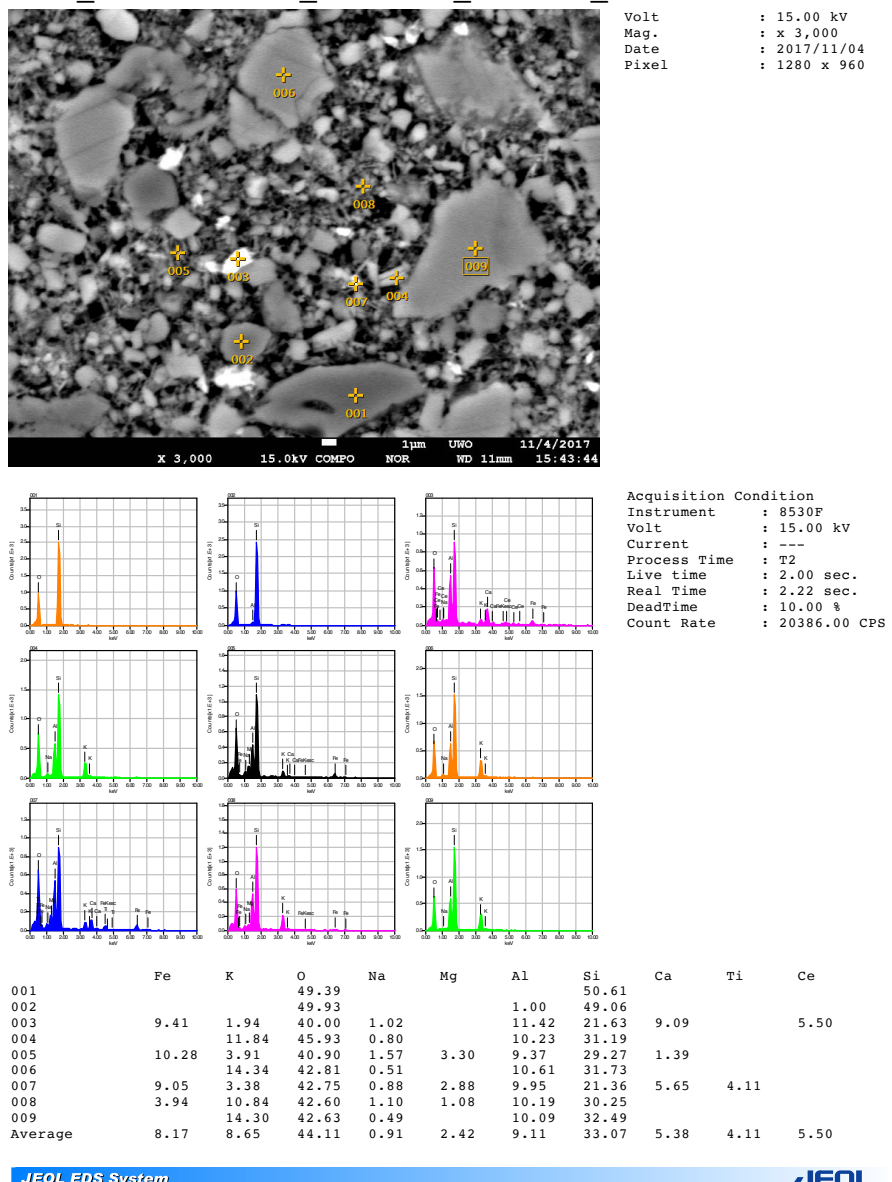


Figure E.12: EDS data from Sample 1-64-2763a.

2763_Cataclasite2_Stitch16_CZoomInBR_2fold

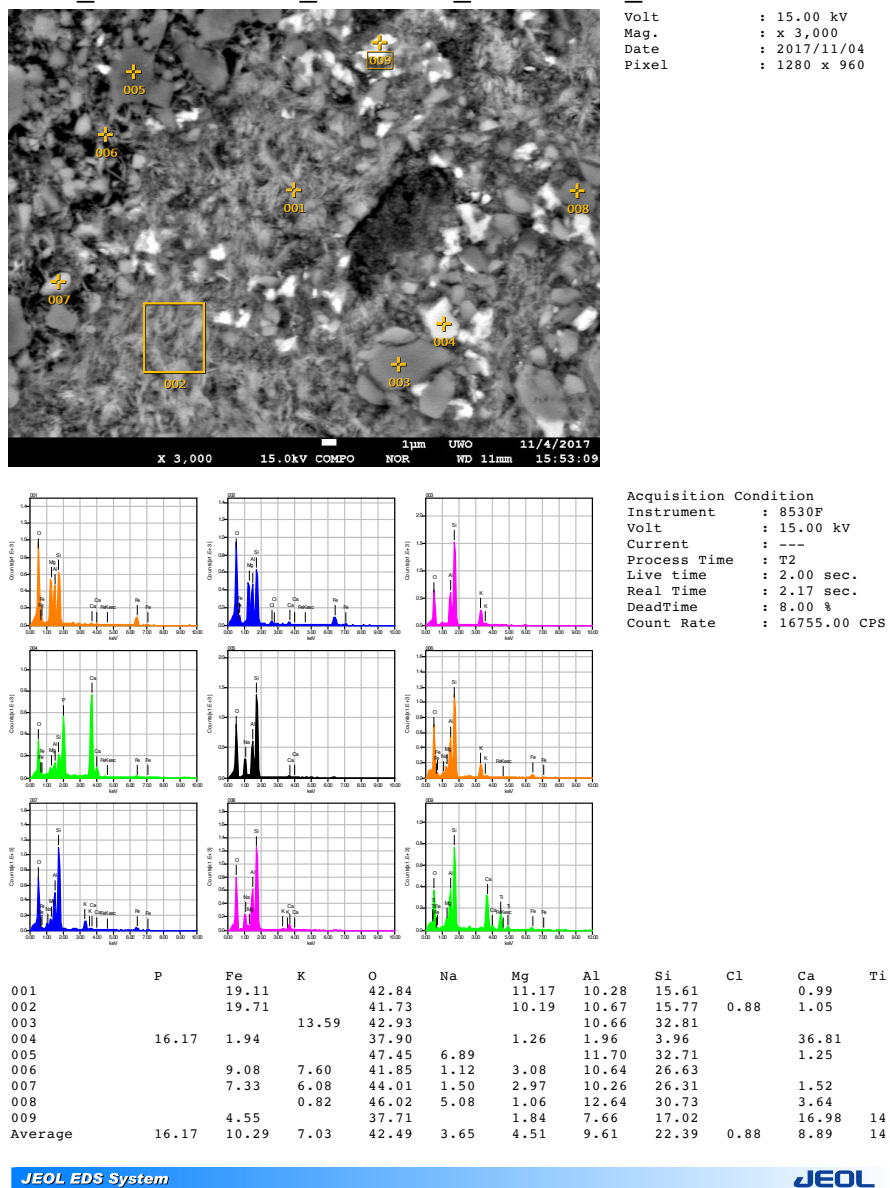


Figure E.13: EDS data from Sample 1-64-2763b.

F Comparison of Chicxulub Numerical Simulations

In this appendix, three iSALE simulations of the Chicxulub impact event are compared, both between themselves (Figure F.1), and with a geophysically constrained cross-section of the Chicxulub structure based on Vermeesch and Morgan (2008). In summary, the updated simulation presented in this thesis (Figure F.1a) is not substantially different to previously published models (e.g. Figure F.2c; Morgan et al. 2016). Nevertheless, there are several distinct improvements:

1. The impact velocity has been increased to a more realistic value of 15 km s^{-1} .
2. The depth of the modelled crater is considerably closer to the true depth of the Chicxulub Crater, although the model remains around 400 m too deep. At this point, it is worth noting that all published numerical impact simulations predict craters that are too deep (see references within the main body), this fact is rarely addressed in published work.
3. The impact melt volume remains consistent with the geophysically constrained volume.
4. The topography of the rim of the crater is less extreme.
5. The new model has increased spatial resolution.

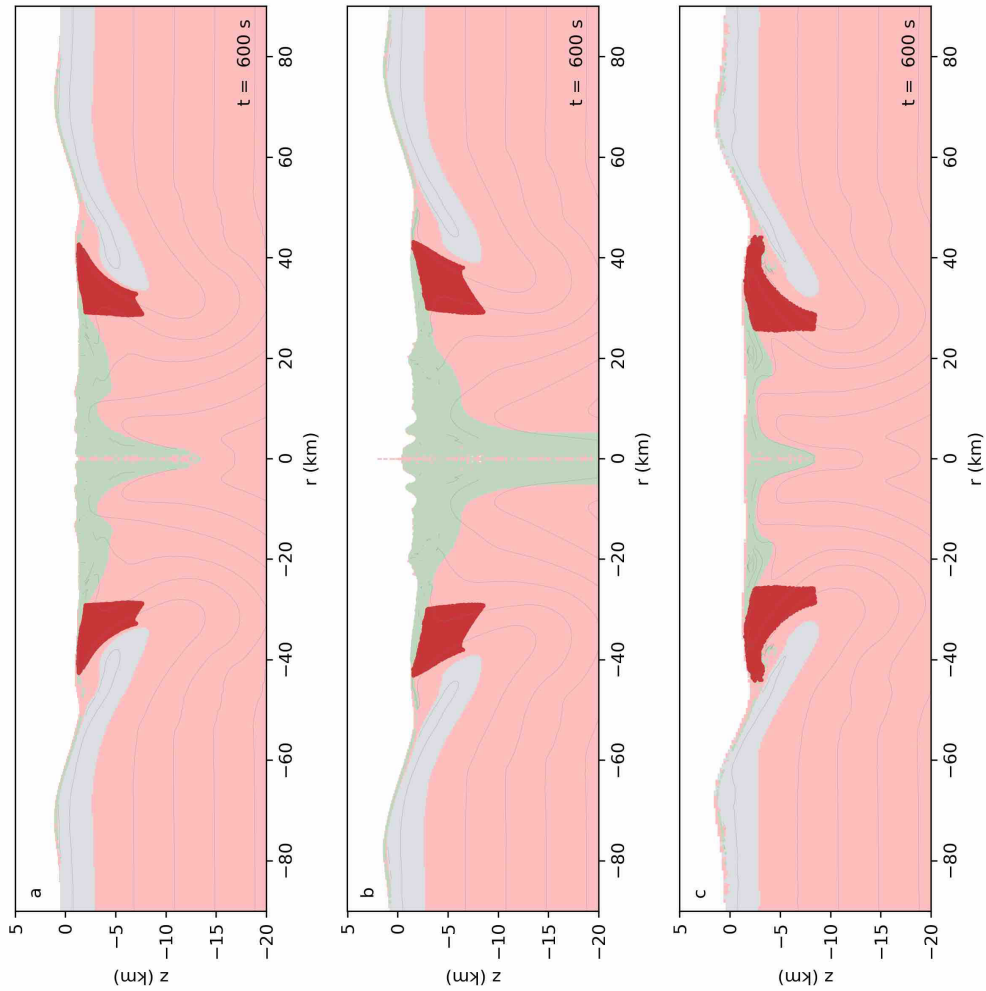


Figure F.1: Comparison of iSALE Chicxulub simulations: a) The model presented in Chapter 8, with an impactor diameter of 12 km, and velocity of 15 km s^{-1} . b) A model with an impactor diameter of 14 km, and velocity of 15 km s^{-1} , all other parameters are consistent with the model presented in Chapter 8. c) A Chicxulub simulation presented in Morgan et al. (2016), with an impactor diameter of 14 km, and velocity of 12 km s^{-1} , the model is fully described in Morgan et al. (2016).

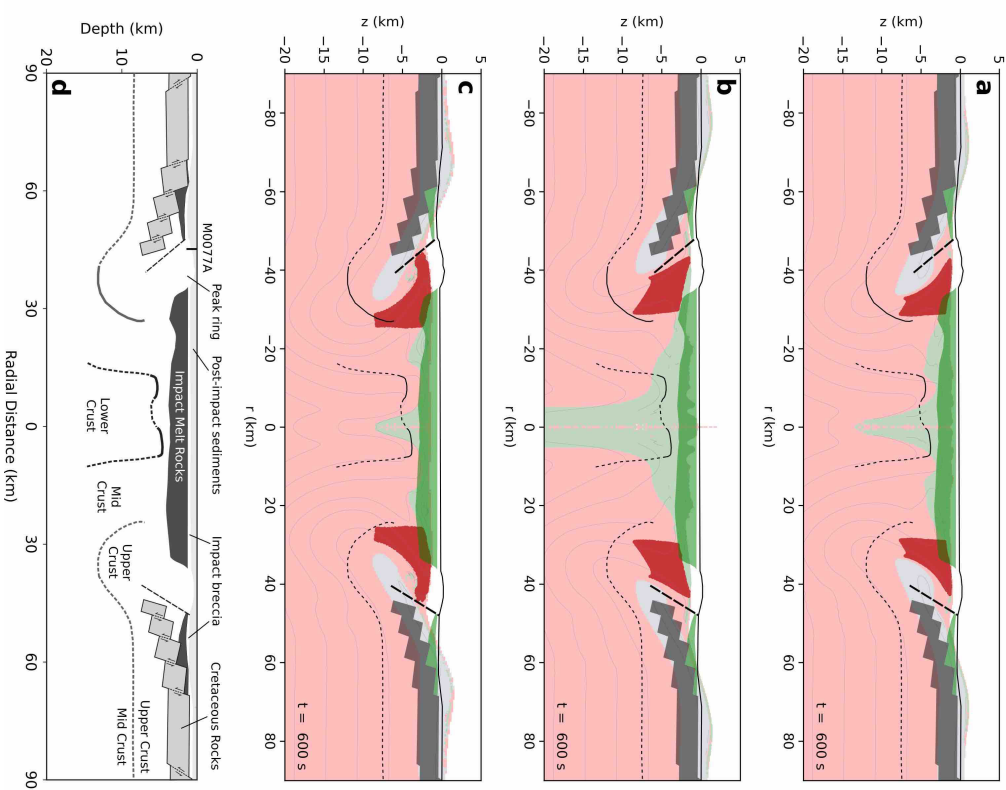


Figure F.2: Comparison of iSALE Chicxulub simulations with previously published cross-section. a)-c) are the same simulations seen in Figure F.1, d) Geophysically constrained cross section of upper 20 km of the Chicxulub impact structure. Modified from Vermeesch and Morgan (2008) (Reproduction of Figure 7.1.) A simplified, though still accurate version of this cross-section is overlain on models a)-c).

G Comparison of Stress-Strain Paths of Lagrangian Pseudo-Cells within the Chicxulub Peak-Ring

In this appendix, data presented in Chapter 8 on the stress-Strain evolution of a single Lagrangian pseudo-cell are compared to other Lagrangian pseudo-cells within the Chicxulub peak-ring. In summary, the Lagrangian pseudo-cell chosen in Chapter 8 represents an “average” parcel of peak-ring material. The patterns of stress-strain evolution in all pseudo-cells are qualitatively similar, where deformation in a cell may be displaced temporally to another cell, as a consequence of the spatial difference between them. Additionally, there are some quantitative variations between pseudo-cells that vary systematically, associated with location in the peak-ring e.g. cumulative rotation, which varies by $\pm 30^\circ$ (see Chapter 9).

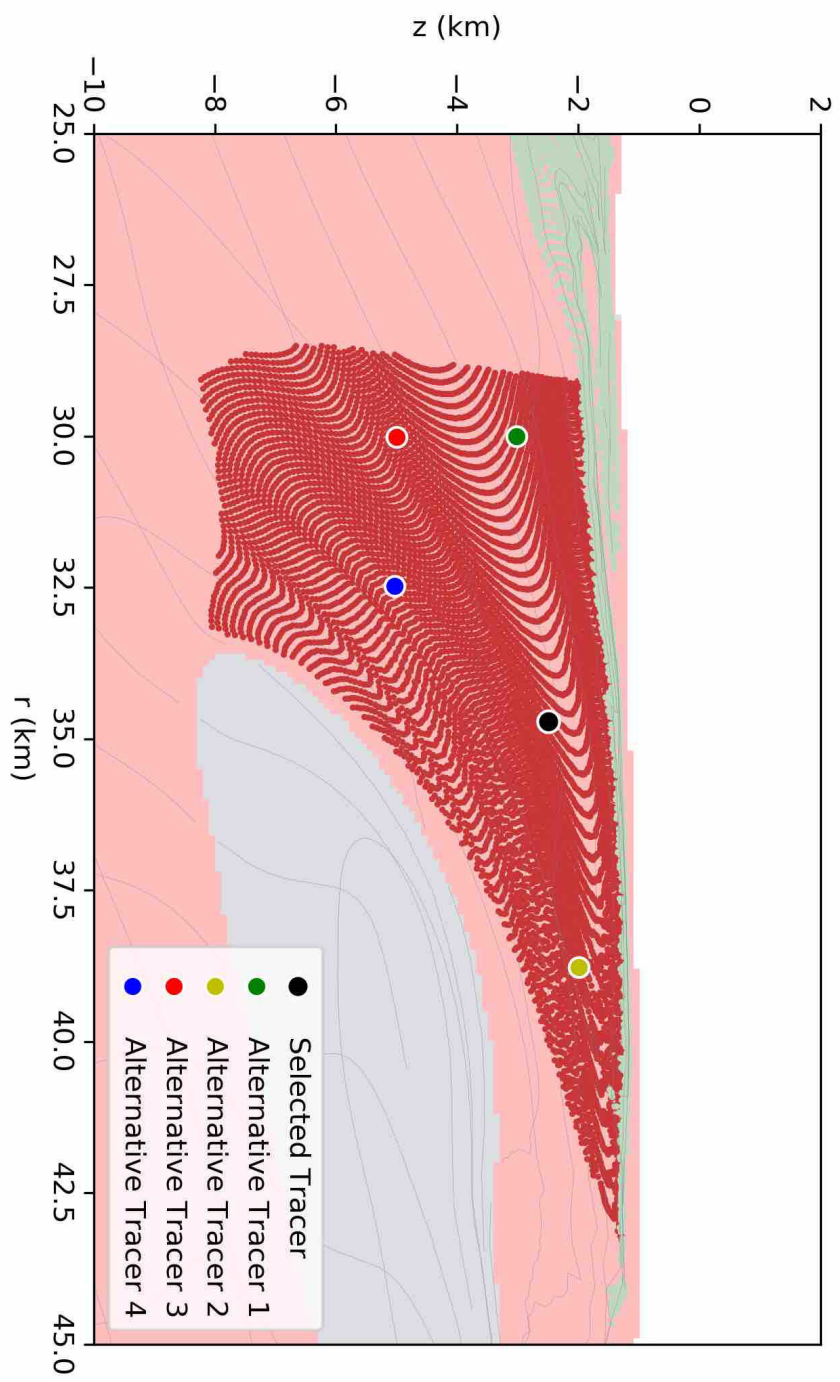


Figure G.1: Locations of selected and alternative Lagrangian pseudo-cells within the modelled Chicxulub peak-ring. The colour scheme for the Lagrangian pseudo-cells will be used in Figures G.2 and G.3

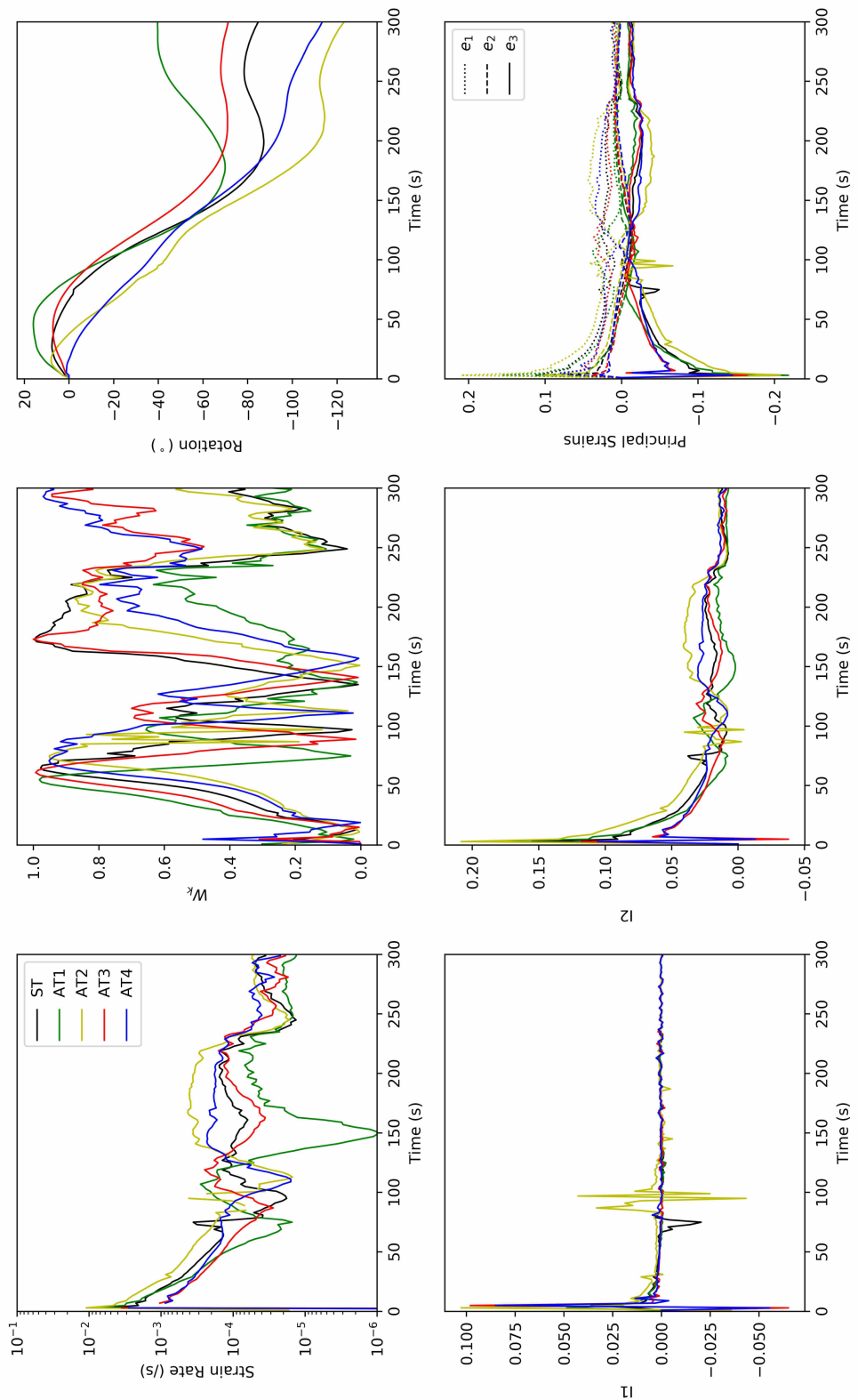


Figure G.2: Comparison between strains recorded by alternative Lagrangian pseudo-cells.

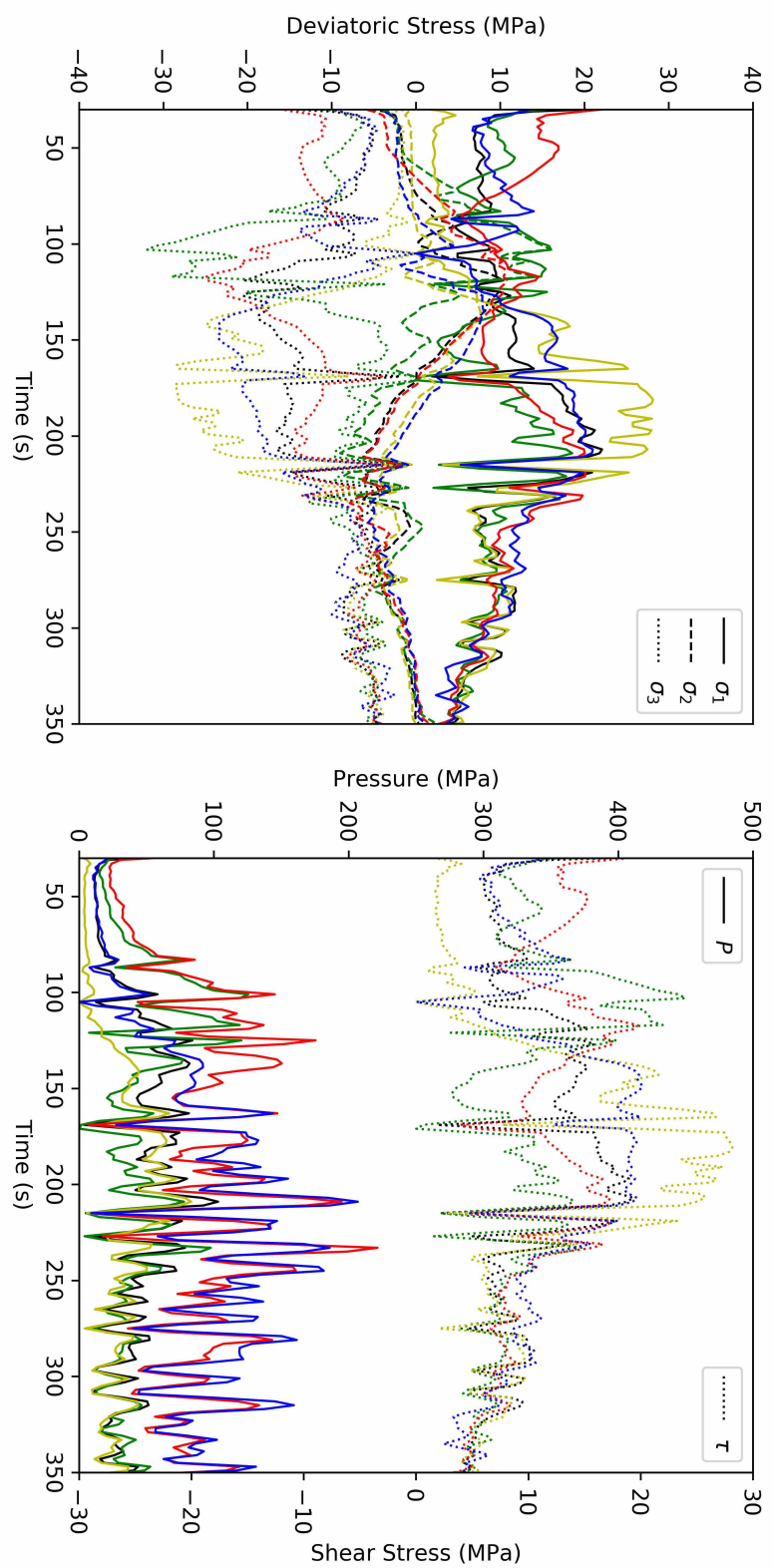


Figure G.3: Comparison of stresses recorded by alternative Lagrangian pseudo-cells.

H Supplementary EBSD Maps

In this appendix, EBSD maps providing additional examples grain-scale deformation in samples from Hole M0077A are provided (Chapter 9). The maps were acquired using the methods described in Chapters 3 and 9. A list of the samples analysed using EBSD and presented in this thesis is presented in Table H.1.

Exp.	Site	Hole	Core	Section	Top (cm)	Bottom (cm)	Sample Depth (mbsf)
364	77	A	104	1	24	26	768.59
364	77	A	132	1	22	24	838.46
364	77	A	204	1	7	9	1030.00
364	77	A	219	1	22	24	1076.15
364	77	A	250	1	41	43	1169.71
364	77	A	288	1	59	61	1287.14

Table H.1: Sample names and depths of EBSD maps presented here and in Chapter 9.

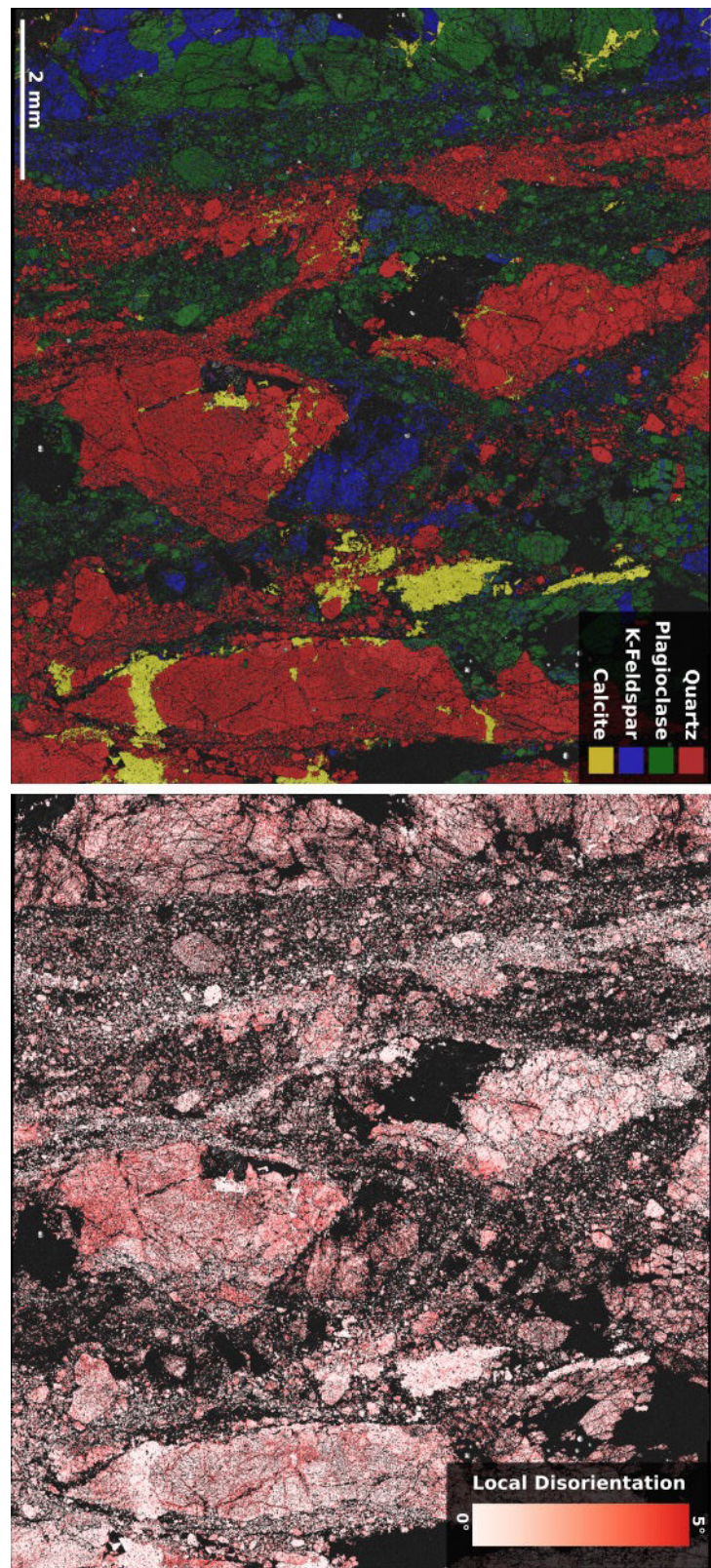


Figure H.1: EBSD maps of Sample 364-77-A-104-R-1-24-26.

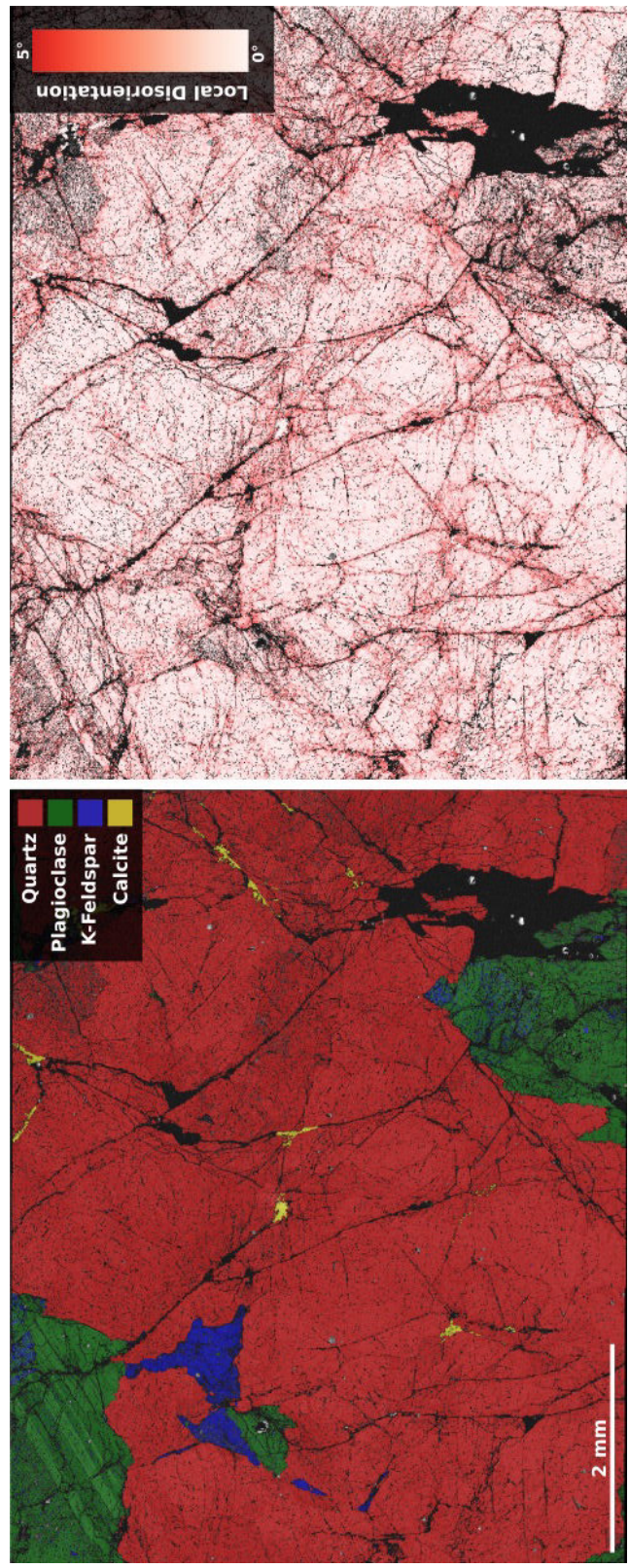


Figure H.2: EBSD maps of Sample 364-77-A-132-R-1-22-24.

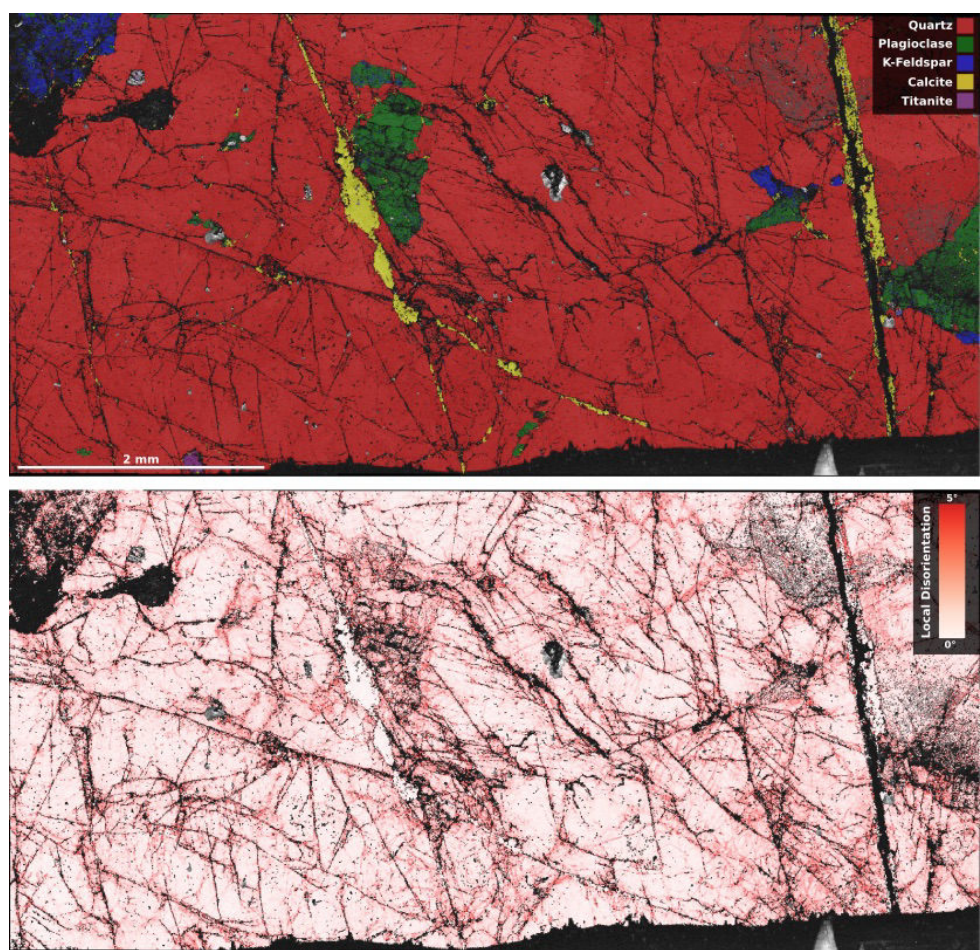


Figure H.3: EBSD maps of Sample 364-77-A-204-R-1-07-09.

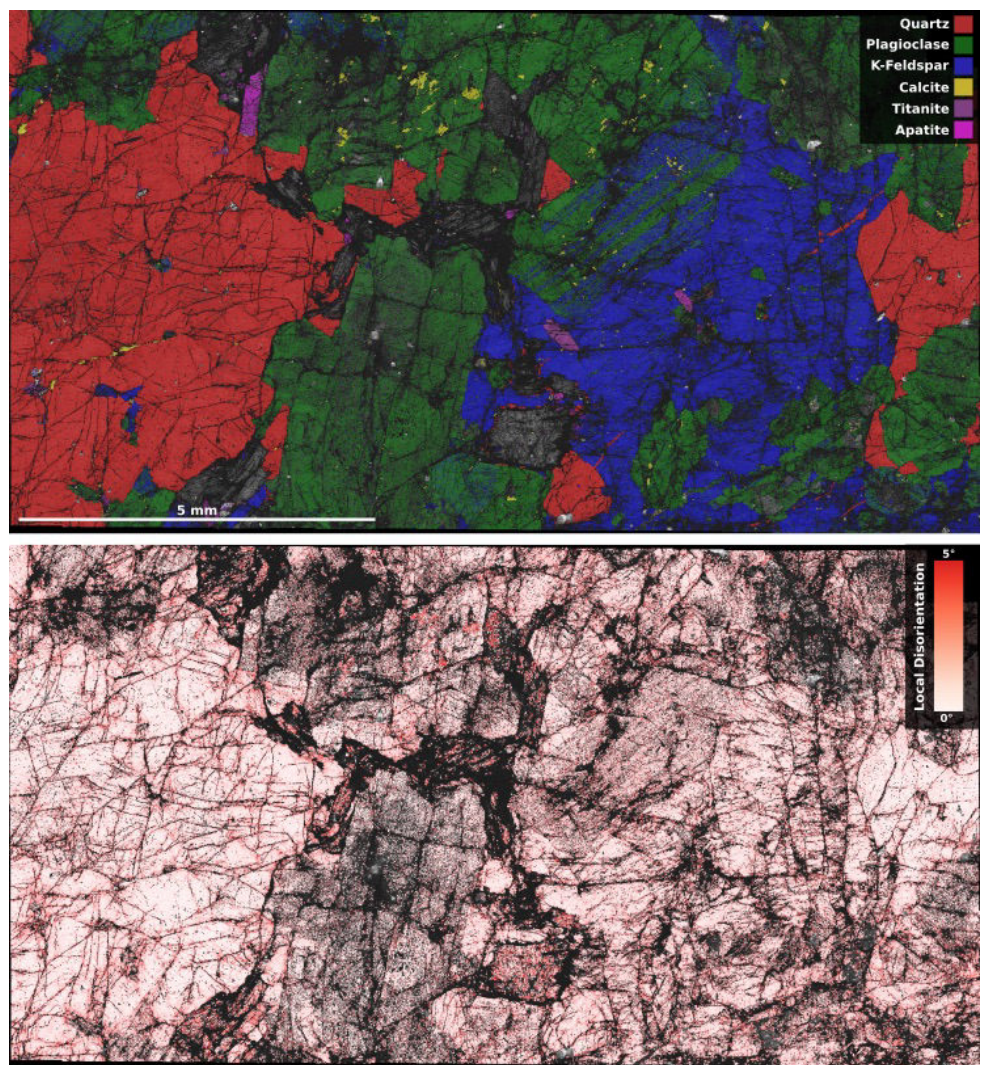


Figure H.4: EBSD maps of Sample 364-77-A-219-R-1-22-24.

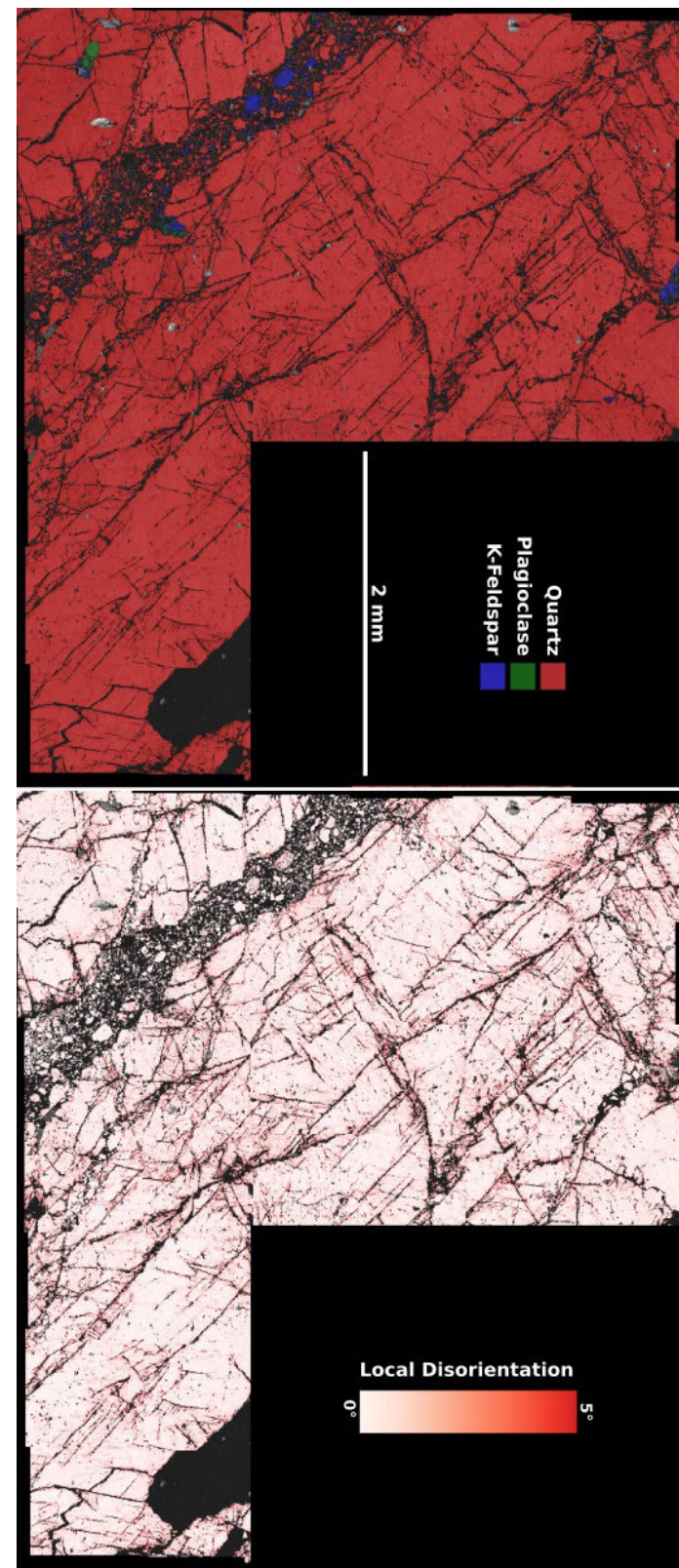


Figure H.5: EBSD maps of Sample 364-77-A-288-R-1-59-61.